

Unclassified

SECURITY CLASSIFICATION OF THIS PAGE (When Data Entered)

REPORT DOCUMENTATION PAGE		READ INSTRUCTIONS BEFORE COMPLETING FORM
1. REPORT NUMBER NAVENVPREDRSCHFAC Contractor Report CR 82-02	2. GOVT ACCESSION NO.	3. RECIPIENT'S CATALOG NUMBER
4. TITLE (and Subtitle)  Final Report on A.R.A.P.'s Model for the Atmospheric Marine Environment		5. TYPE OF REPORT & PERIOD COVERED Final 12 Nov. 1980 - 18 Sept. 1981
		6. PERFORMING ORG. REPORT NUMBER A.R.A.P. Report No. 457
7. AUTHOR(s)  W.S. Lewellen, D.A. Oliver, and R.I. Sykes		8. CONTRACT OR GRANT NUMBER(s)  N00019-80-C-0617
9. PERFORMING ORGANIZATION NAME AND ADDRESS Aeronautical Research Associates of Princeton, Inc 50 Washington Road, P.O. Box 2229 Princeton, New Jersey 08540		10. PROGRAM ELEMENT, PROJECT, TASK AREA & WORK UNIT NUMBERS PE 62759N PN WF59-551 NEPRF WU 6.2-4
11. CONTROLLING OFFICE NAME AND ADDRESS Naval Air Systems Command Department of the Navy Washington, DC 20361		12. REPORT DATE January 1982
		13. NUMBER OF PAGES 178
14. MONITORING AGENCY NAME & ADDRESS (if different from Controlling Office) Naval Environmental Prediction Research Facility Monterey, California		15. SECURITY CLASS. (of this report)  Unclassified
		15a. DECLASSIFICATION/DOWNGRADING SCHEDULE
16. DISTRIBUTION STATEMENT (of this Report)  Approved for public release; distribution unlimited.		
17. DISTRIBUTION STATEMENT (of the abstract entered in Block 20, if different from Report)		
18. SUPPLEMENTARY NOTES		
19. KEY WORDS (Continue on reverse side if necessary and identify by block number)  Atmospheric Boundary Layer Turbulence Modeling Fog Modeling Kelvin-Helmholtz Wave Breaking		
20. ABSTRACT (Continue on reverse side if necessary and identify by block number)  This report presents the results for the past year's developments to A.R.A.P.'s program for computing the detailed low-level atmospheric distribution of velocity, temperature, moisture, refractive index, and the turbulent variances of these quantities. A critical review of the present status of the model is presented along with results of new calculations. A calculation of fog evolution is presented to show a cold-water fog evolving into a warm-water fog as a result of radiational cooling.		

The evolution of breaking Kelvin-Helmholtz waves is also followed in a series of calculations which should lead to a better understanding of the dynamics of the inversion layer at the top of the atmospheric boundary layer. Detailed derivations of two proposed extensions to the model are presented. One involves a hybrid integral-differential description to permit approximate solutions to be obtained with less numerical effort, and the second involves the incorporation of precipitation into the two-phase representation of water in the atmospheric.



NAVENVPREDRSCHFAC CR 82-02

LIBRARY  
RESEARCH REPORTS DIVISION  
NAVAL POSTGRADUATE SCHOOL  
MONTEREY, CALIFORNIA 93940

NAVENVPREDRSCHFAC  
CONTRACTOR REPORT  
CR 82-02

# FINAL REPORT ON A.R.A.P.'s MODEL FOR THE ATMOSPHERIC MARINE ENVIRONMENT

Prepared By:

W. S. Lewellen, D. A. Oliver, and R. I. Sykes

Aeronautical Research Associates of Princeton, Inc.  
Princeton, New Jersey 08540

A.R.A.P. report ~~457~~ 457

Contract No. N00019-80-C-0617

JANUARY 1982

APPROVED FOR PUBLIC RELEASE  
DISTRIBUTION UNLIMITED



Prepared For:

NAVAL AIR SYSTEMS COMMAND  
WASHINGTON, D. C., 20361

QUALIFIED REQUESTORS MAY OBTAIN ADDITIONAL COPIES  
FROM THE DEFENSE TECHNICAL INFORMATION CENTER.  
ALL OTHERS SHOULD APPLY TO THE NATIONAL TECHNICAL  
INFORMATION SERVICE.

# TABLE OF CONTENTS

	<u>Page</u>
Table of Contents	1
List of Figures	3
List of Tables	7
1. Introduction	9
2. Fog Evolution Study	11
3. Hybrid Integral-Differential Description Of The Planetary Boundary Layer Using Second-Order Closure Turbulence Theory	19
3.1 Introduction	19
3.2 Concept of the Hybrid Method	19
3.3 Integral Constraints and Their Incorporation Into the Hybrid Method	21
3.3.1 Governing Equations of the Horizontally Homogeneous PBL	21
3.3.2 Integral Parameters and Integral Constraints	24
3.3.3 Structure Function Approach to the Surface Flux Laws and the Integral Parameters	28
3.3.4 Transfer Coefficients	35
3.3.5 Surface Layer Depth	38
3.3.6 Energy Thickness and the Dynamic Equation for the PBL Thickness	39
3.3.7 Average Scale and Integral Scale Equation	42
3.3.8 Linearized Forms of the Integral Equations	45
3.3.9 Coupling of the Integral and Differential Systems	47
3.4 Illustrations	49
3.4.1 PBL Subjected to Unsteady Forcing	49
3.4.2 Stable PBL Illustrations	57
4. The Interaction of Turbulence with Precipitation: Formulation of A Precipitation Model for The Planetary Boundary Layer	65
4.1 Introduction	65
4.2 Condensation, Evolution of the Cloud Droplet Spectrum, and Precipitation	66

	<u>Page</u>
4.3 Turbulence and the Collisional/Coalescence Process	67
4.4 The Cloud Precipitation (CP) Model	71
4.4.1 The Division of Liquid Water Into Cloud and Precipitation Groups	71
4.4.2 Cloud and Precipitation Variables and Conservation Equations	72
4.4.3 The Cloud Conversion to Precipitation (CP) Process	73
4.4.4 The Cloud Collection (CC) Process	75
4.4.5 The Precipitation Evaporation Process	75
4.5 Illustration of the CP Model for the Homogeneous Cloud	76
5. A.R.A.P. Model Problems	97
5.1 Turbulent Transport Model	97
5.2 Uncertain Physical Processes	99
5.3 Numerical Difficulties	99
6. Future Plans	101
References	103
Appendix A: A Numerical Study of Breaking Kelvin-Helmholtz Billows Using a Reynolds-Stress Turbulence Closure Model	A-1

## LIST OF FIGURES

	<u>Page</u>
Figure 2.1 - Schematic showing the air relative humidity and air-sea temperature differences required for pure advective fogs.	12
Figure 2.2 - Evolution of air virtual potential temperature following a drop of 5°C in the sea surface temperature.	14
Figure 2.3 - Evolution of the turbulent heat flux following a drop of 5°C in the sea surface temperature.	15
Figure 2.4 - Evolution of the liquid water content following a drop of 5°C in the sea surface temperature.	16
Figure 2.5 - Evolution of the radiative cooling rate following a drop of 5°C in the sea surface temperature.	17
Figure 3.1 - Information flow in hybrid integral-differentiation description of the PBL.	48
Figure 3.2(a) - Surface RMS turbulence response to unsteady forcing of the PBL. Period of outflow acceleration is from $t = 0$ to $t = 1$ . Standard ARAP finite difference model.	51
Figure 3.2(b) - Cross isobaric angle for conditions of Figure 3.2(a).	52
Figure 3.3(a) - Surface RMS turbulence response corresponding to Figure 3.2(a) but with purely integral form of hybrid procedure.	53
Figure 3.3(b) - Cross isobaric angle for conditions of Figure 3.3(a).	54
Figure 3.4(a) - Surface RMS turbulence response corresponding to Figure 3.2(a) but with 5 grid level hybrid procedure.	55
Figure 3.4(b) - Cross isobaric angle for conditions of Figure 3.4(a).	56
Figure 3.5(a) - Boundary layer thickness of response following onset of a constant surface cooling rate corresponding to the condition of Table 3.4.2.	59
Figure 3.5(b) - Surface shear velocity corresponding to Figure 3.5(a).	60



	<u>Page</u>
Figure 3.5(c) - Cross-isobaric angle response corresponding to Figure 3.5(a).	61
Figure 3.5(d) - Monin-Obukhov length corresponding to Figure 3.5(a).	62
Figure 3.5(e) - Zilitinkevich scaling parameter $d$ corresponding to Figure 3.5(a).	63
Figure 4.1(a) - Evolution of precipitation water mixing ratio $H_p$ for a homogeneous cloud with all water existing as cloud water $H_c$ at time $t = 0$ . Lowest turbulence level of these illustrations, $\epsilon = .001 \text{ m}^2/\text{sec}^3$ .	79
Figure 4.1(b) - Evolution of average precipitation drop radius corresponding to Figure 4.1(a).	80
Figure 4.1(c) - Evolution of precipitation flux corresponding to Figure 4.1(a).	81
Figure 4.2(a) - Evolution of precipitation water mixing ratio $H_p$ . Turbulence level $\epsilon = 0.01 \text{ m}^2/\text{sec}^3$ .	82
Figure 4.2(b) - Evolution of average precipitation drop radius corresponding to Figure 4.2(a).	83
Figure 4.2(c) - Evolution of precipitation flux corresponding to Figure 4.2(a).	84
Figure 4.3(a) - Evolution of precipitation mixing ratio $H_p$ for turbulence level $\epsilon = 0.1 \text{ m}^2/\text{sec}^3$ .	85
Figure 4.3(b) - Evolution of precipitation drop water average radius corresponding to Figure 4.3(a).	86
Figure 4.3(c) - Evolution of precipitation flux corresponding to Figure 4.3(a).	87
Figure 4.4(a) - Evolution of precipitation water mixing ratio $H_p$ for turbulence level $\epsilon = 1.0 \text{ m}^2/\text{sec}^3$ .	88
Figure 4.4(b) - Evolution of precipitation drop average radius corresponding to Figure 4.4(a).	89
Figure 4.4(c) - Evolution of precipitation flux corresponding to Figure 4.4(a).	90



	<u>Page</u>
Figure 4.5(a) - Evolution of precipitation water mixing ratio $H_p$ for turbulence level $\epsilon = 10 \text{ m}^2/\text{sec}^3$ .	91
Figure 4.5(b) - Evolution of precipitation drop average radius corresponding to Figure 4.5(a).	92
Figure 4.5(c) - Evolution of precipitation flux corresponding to Figure 4.5(a).	93
Figure 4.6(a) - Evolution of the precipitation water mixing ratio for the homogeneous cloud evolution conditions of Figures 1-4 as predicted by the Kessler model (Reference 42). There is no dependence upon turbulence in the Kessler model.	94
Figure 4.6(b) - Evolution of the average precipitation drop radius as predicted by the Kessler model corresponding to Figure 4.6(a).	95
Figure 4.6(c) - Evolution of the precipitation flux as predicted by the Kessler model corresponding to Figure 4.6(a).	96

## LIST OF TABLES

	<u>Page</u>
Table 3.4.1 - Conditions for Neutral PBL Subjected to Ramp Transition	50
Table 3.4.2 - Conditions for Constant Surface Cooling Rate Stable PBL Illustration	57
Table 4.1 - Turbulence Length, Time, and Acceleration Scales in the Atmosphere for Dissipation Scale Eddies	68
Table 4.2 - Conditions For Illustration of the CP Model For a Homogeneous Cloud	78

## 1. INTRODUCTION

For the past seven years, A.R.A.P., Inc. has had a series of contracts from the Naval Air Systems Command to develop a computer model for determining the detailed low-level atmospheric distributions of velocity, temperature, moisture, refractive index, and the turbulent variances of these quantities for marine environments. In addition to appropriately modeling the turbulent transport of momentum, heat, and moisture, it was necessary to incorporate moisture change of phase and the physics of thermal radiation into this model since low-level clouds or fog are a frequent occurrence in the marine atmospheric boundary layer. The development and a number of sample calculations exemplifying different phenomena are detailed in References 1-17. Reference 18 which accompanies this report provides a detailed review of modeling the atmospheric boundary layer using turbulent transport theory. It includes a review of the status of our understanding of atmospheric boundary layer dynamics, as well as a review of the modeling of the three physical processes most critical for determining the atmospheric marine boundary layer. These three are turbulent transport, thermal radiation, and change of phase of atmospheric water. Reference 18 also provides a review of many of the sample calculations made with the A.R.A.P. model which successfully illustrates features expected in the atmospheric marine boundary layer. Section 5 of the present report counterbalances those "successes" by detailing some problem areas of the current model. Together they provide the detailed critical review specified in the past years contract.

Two model calculations performed during the past year are detailed in Section 2 and in Appendix A. The fog calculation presented in the next section gives one possible reason why the surface air in fogs is generally found to be cooler than the ocean surface. By following the evolution of a fog which is formed by warm air passing over colder water under nocturnal radiation conditions, it is shown that the enhanced radiational cooling induced by the fog is sufficient to reduce the surface air temperature relatively rapidly to below that of the water surface. During the past year we have had discussions with E. Mack and W. Rodgers of Calspan regarding the forthcoming fog model evaluation study. We look forward to exercising our model as part of this study.

Appendix A details a calculation of the detailed mechanism of Kelvin-Helmholtz wave breaking. The turbulent breaking process is modeled using our second-order closure model to describe the small-scale turbulence, while the large scale billow itself is calculated explicitly as a two-dimensional flow. This calculation was partially supported by an ONR contract which called for examining trackable clear-air, radar signals. The large values of  $C_N^2$ , which can occur when this phenomenon occurs at the top of a relatively moist boundary layer when the air above the inversion is much dryer, makes this a likely candidate. This type of calculation can also be used to investigate the detailed interaction of waves and turbulence along the inversion and possibly lead to improved parameterization of this interaction in the one-dimensional models.

Model development during the past year has concentrated on deriving a hybrid integral-differential description of the planetary boundary layer which would allow approximate solutions to be obtained using far fewer numerical calculations, and on deriving a capability for incorporating precipitation as a possibility in our two-phase representation of atmospheric water. Neither of these developments have reached the point of being fully integrated into our general model. Sections 3 and 4 detail the derivation and current status of each.

## 2. FOG EVOLUTION STUDY

Our purpose in this section is to demonstrate the mechanism by which a fog generated by a decrease in surface temperature can relatively rapidly invert its internal temperature gradient so that the surface becomes warmer than the air in the fog. This mechanism is, of course, radiative cooling of the fog top which then quickly moves down through the fog layer by convective overturning. We present a case study of a fog produced by warm airflow over a cold surface illustrating the phenomenon; we have considered the horizontally homogeneous, time-dependent problem, but this is closely related to steady-state advection with time corresponding to downstream distance.

In order to generate a cold water fog, we take an initially fog-free boundary layer, and suddenly reduce the surface temperature. The magnitude of the temperature change,  $\Delta T$ , which is needed to produce a fog depends on the initial relative humidity of the boundary layer near the surface. In the absence of radiation effects, the surface layer analysis (Reference 10) can be used to give the relationship between the critical  $\Delta T$  and the critical relative humidity. The relationship depends on the absolute temperature of the surface, and the result is shown graphically in Figure 2.1. It is clear that relative humidities below 95% will require a substantial change in temperature to produce a fog. It should be noted that radiative effects will change this result to an extent which depends on the relative magnitudes of radiative and turbulent heat transfer.

Since we are dealing with surface temperature changes of only a few degrees, this restriction on initial relative humidity causes problems if we are trying to study the fog evolution in isolation. We need to set the initial humidity very close to saturation, which means that a fog is about to form even in the absence of our applied temperature change at the surface. Thus, the generation of the fog depends as much on the precise initial state of the boundary layer as on the externally applied forcing. We have therefore not attempted any extensive study of the fog evolution from different initial states with different surface temperature changes, but instead present a single case study and use the integration as an illustrative example.

Our initial boundary layer for this case study has 93% relative humidity and is only about 50 m thick. The boundary layer was obtained by integrating in time with a constant geostrophic wind equal to 5 m/sec and a constant sea surface temperature for a few days to allow the humidity to increase. It proved necessary to impose a significant subsidence velocity, 3 cm/sec at 1 km, to prevent the formation of a cloud layer; this is the reason for our relatively thin boundary layer.

Figure 2.1 shows that a temperature drop of at least  $6^{\circ}\text{C}$  is necessary to generate a purely advective fog in our initial boundary layer with its 93% relative humidity. In fact, we used  $\Delta T = 5^{\circ}\text{C}$ , which means that we rely on radiative cooling to assist in the fog production, so that the fog does not appear immediately after the surface temperature drop. The evolution following the surface temperature drop was carried out under nocturnal

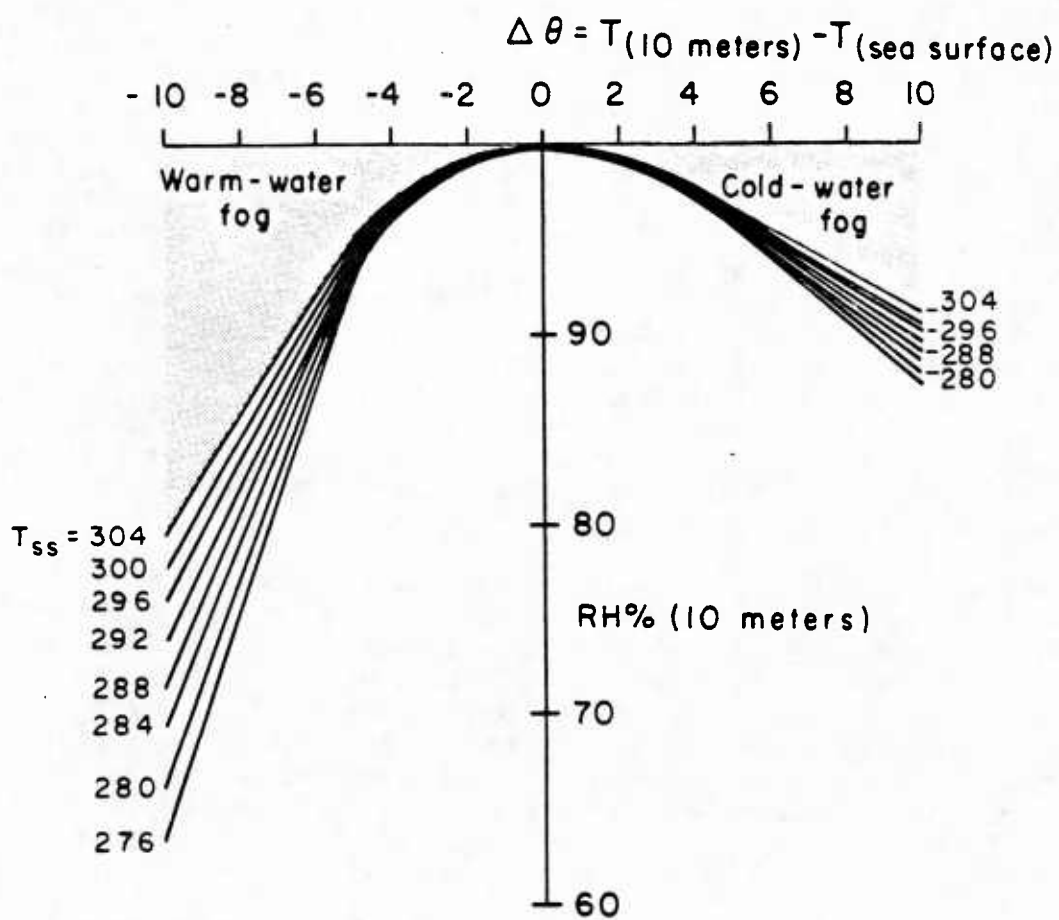


Figure 2.1. Schematic showing the air relative humidity and air-sea temperature differences required for pure advective fogs.



conditions.

Figures 2.1 through 2.5 show the profiles of temperature, heat flux, liquid water content, and radiative cooling at several times after the change in surface conditions. We see from Figures 2.1 and 3.1 that the initial boundary layer has a warm surface and a positive heat flux at the bottom; this is required to balance the radiative cooling which is evident at  $t = 0$  in Figure 2.5

After 20 minutes, the surface temperature shows the  $5^{\circ}\text{C}$  decrease from  $290^{\circ}\text{K}$  to  $285^{\circ}\text{K}$ , and that the heat flux has changed sign in the lowest 15 m. There is some cooling of the main part of the boundary layer, by about  $0.5^{\circ}\text{C}$ , due to the radiative cooling, and this occurs in the absence of a change in surface temperature. However, in the latter case, the temperature only drops by about  $1^{\circ}\text{C}$  over several hours and no fog is formed.

Figure 2.5 shows some radiative heating at the surface after 20 minutes; but this only extends about 2 m vertically, so that the bulk of the boundary layer is being cooled by both turbulent transfer and by radiation. This causes the temperature to drop more rapidly than the humidity (which is only reduced by turbulent transfer) so that the air eventually saturates and a fog forms around  $t = 45$  mins. At this stage the air has cooled, so that the surface heat flux is reduced in magnitude from its value at 20 minutes, but the air is still warmer than the surface. The fog extends about 12 m vertically at this stage (see Figure 2.4). Also at  $t = 45$  min, Figure 2.5 shows the beginning of the increased radiation from the top of the fog.

After  $t = 45$  min the fog develops in depth and intensity, and the air temperatures continue to fall due to radiative cooling from the fog top. The heat flux profiles show that the lower part of the fog is cooled by turbulent transfer. Shortly after  $t = 80$  m, the air temperatures drop below the surface temperature, and we have a warm surface fog thereafter. The development continues after this time with the depth of the fog layer increasing and both turbulent and radiative heat fluxes also increasing.

Thus, in this particular case, a cold water fog develops roughly 40 minutes after the change in surface temperature, and persists as a cold-water fog for a further 40 minutes; after this time it is converted to a warm-water fog and continues to deepen and intensify. One may expect that fogs initiated by smaller drops in surface temperature will transition to a warm water fog more quickly. For a cold-water fog to persist it appears necessary to have both relatively strong winds and a drop in surface temperature which is stronger than that indicated in Figure 2.1 for the particular ambient relative humidity.

Figure 2.4 shows that the liquid water content in the calculated fog increases rapidly up to an equilibrium level of about  $1\text{g/kg}$ . This value appears to be significantly higher than atmospheric measurements which typically give liquid water contents of  $0.1 - 0.2\text{ g/kg}$ . It seems likely that the reason for this discrepancy is the absence of any mechanism for removal of liquid water through gravitational settling in the model. In measurements



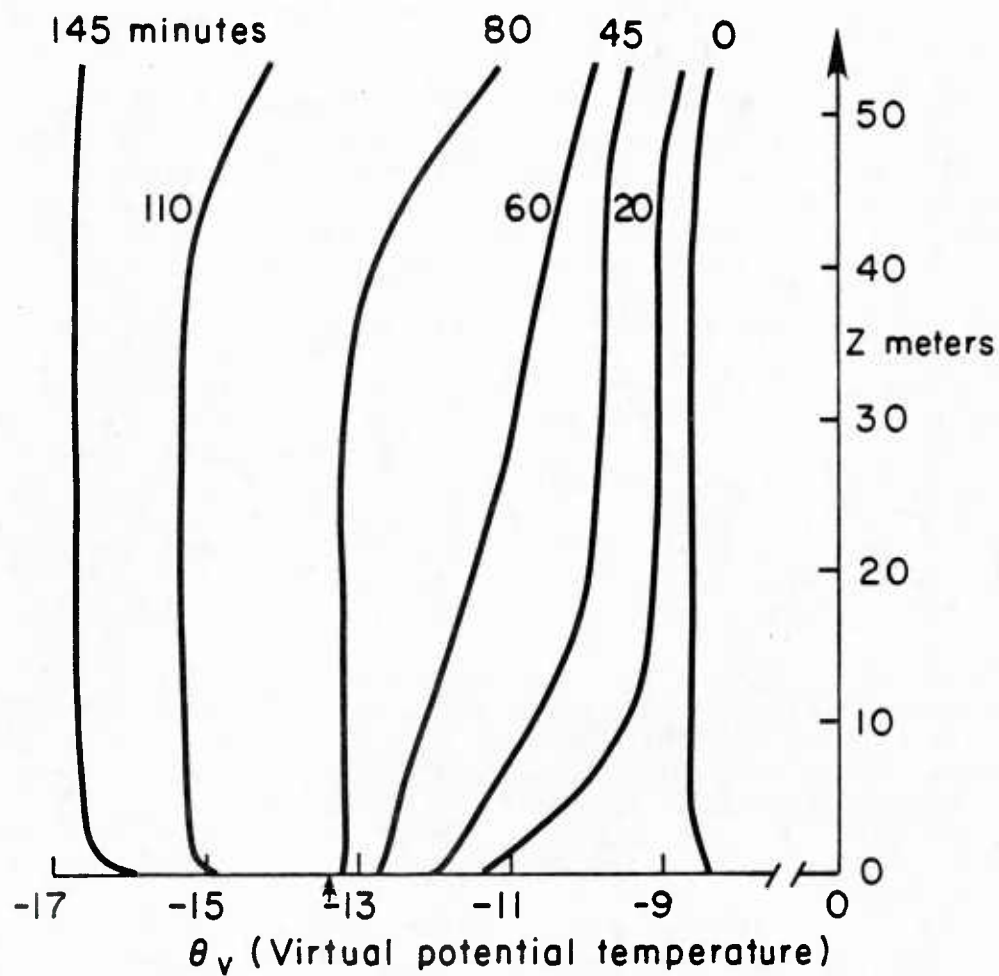


Figure 2.2. Evolution of air virtual potential temperature following a drop of 5°C in the sea surface temperature.

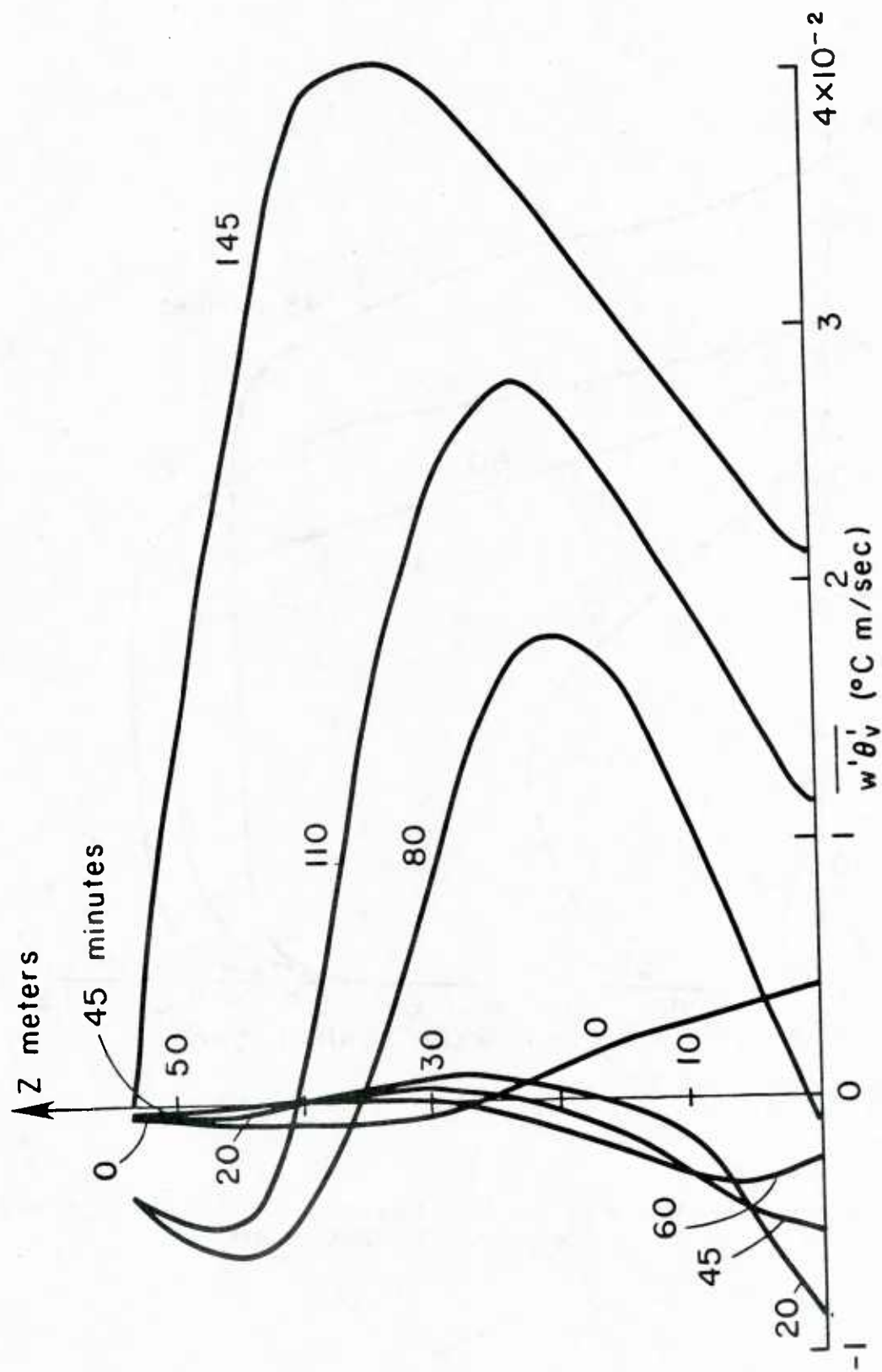


Figure 2.3. Evolution of the turbulent heat flux following a drop of 5°C in the sea surface temperature.

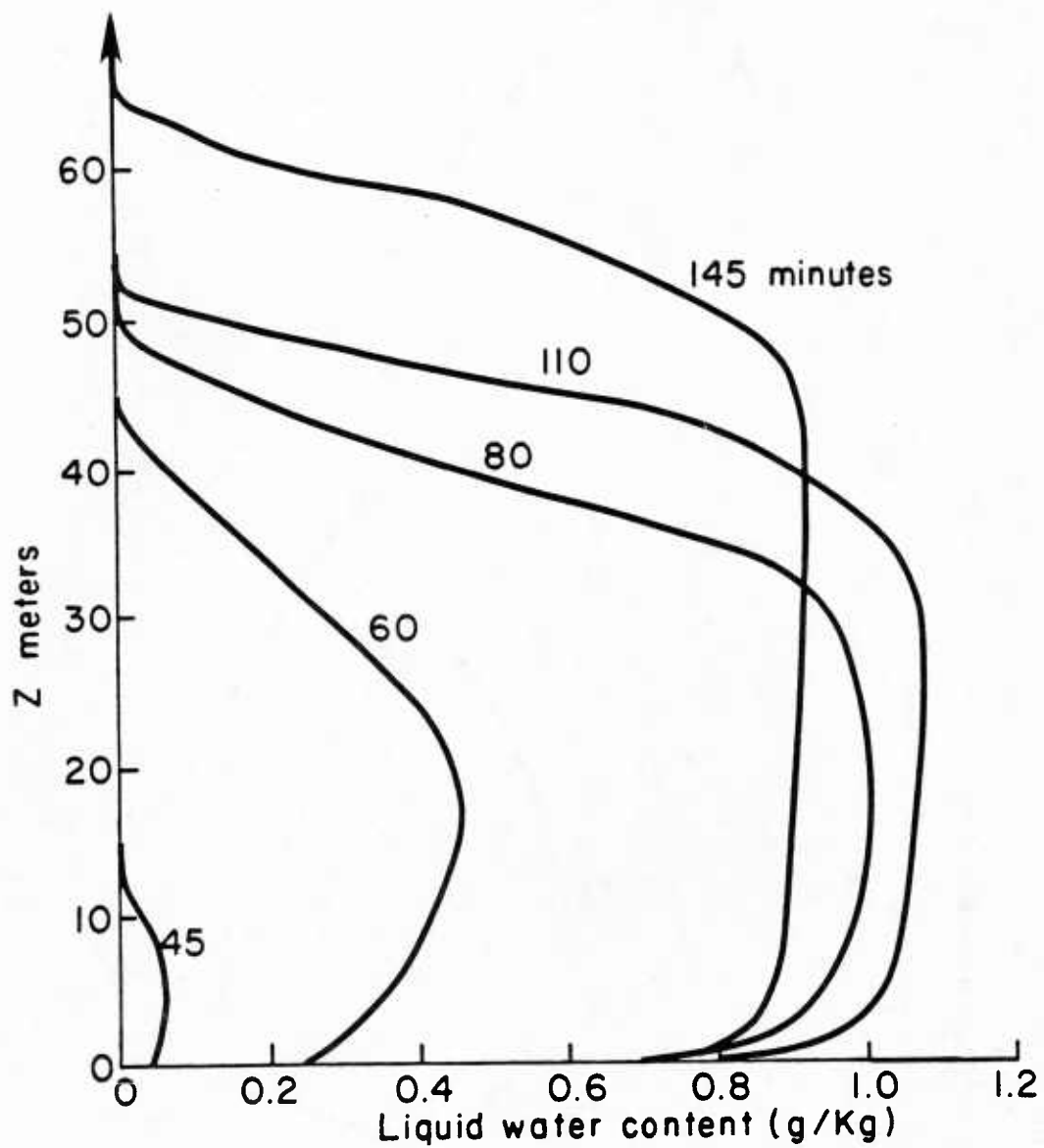


Figure 2.4. Evolution of the liquid water content following a drop of 5°C in the sea surface temperature.

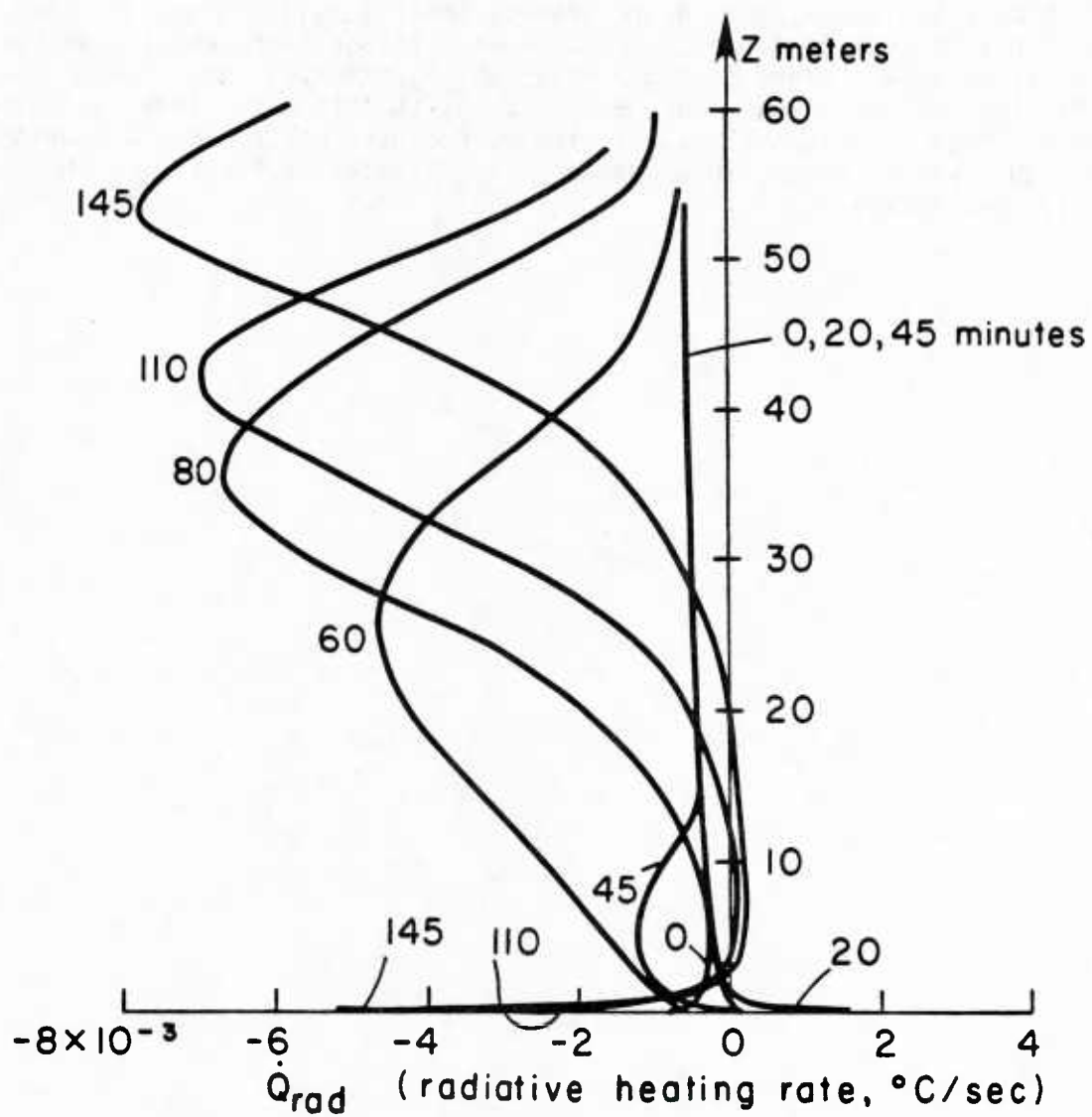


Figure 2.5 Evolution of the radiative cooling rate following a drop of  $5^{\circ}\text{C}$  in the sea surface temperature.

over land, (Reference 19) concluded that only a small fraction of the liquid water which condensed actually remained in the boundary layer. The balance was presumed to have been deposited on the ground by gravitational settling. In our model, we assume a fixed droplet size spectrum for the purposes of the radiation calculation, and ignore gravitational settling since this is negligible for our assumed spectrum. A significant improvement would probably be obtained from a cloud physics' model which accounted for droplet growth within the fog and allowed the heavier drops to fall out. These processes have not been unambiguously identified as dominant controlling mechanisms on the liquid water content in atmospheric fog studies, but they are the most likely candidates.

### 3. HYBRID INTEGRAL-DIFFERENTIAL DESCRIPTION OF THE PLANETARY BOUNDARY LAYER USING SECOND-ORDER CLOSURE TURBULENCE THEORY

#### 3.1. Introduction

In this work we describe a hybrid integral-differential procedure for the prediction of the dynamics of the horizontally homogeneous planetary boundary layer (PBL) according to a second-order closure theory of turbulence. This procedure is aimed at enhancing the quality of the usual finite difference solution of these equations by the incorporation of integral constraints. In particular, the intent is that a finite difference solution utilizing on the order of five grid cells should provide adequate accuracy with the hybrid method. The result would be a computationally efficient procedure which would be useful in operational applications. Such a method used as the basis for the inhomogeneous (three-dimensional) PBL would offer similar computational advantage and efficiency.

In Section 3.2 we present the basic concept of the method. In Section 3.3 we indicate the manner in which integral constraints are incorporated with the finite-difference solution. In Section 3.4, we illustrate the method.

#### 3.2. Concept of the Hybrid Method

The second-order closure theory of the PBL developed and in use at A.R.A.P. (References 2, 7, 10) has proved quite successful in describing the dynamics of the PBL under most general steady state and transient situations and from stable to unstable conditions, including the presence of a capping inversion layer. Even for the horizontally homogeneous layer, the computational volume for executing these descriptions is still considerable, requiring 30 to 50 vertical grid levels for adequate resolution, particularly if an inversion is present. Many of the principal quantities of interest in the PBL are global, or surface quantities, rather than detailed local interior quantities. These key quantities include the surface fluxes of momentum, heat, and species, as well as the total boundary layer depth and the cross isobaric wind angle. As such they are described by the integral forms of the equations of motion; however, these integral forms contain integrals over the profiles of the mean and turbulent field variables.

There are two regions of sharp gradients in the general PBL: the surface layer and the inversion layer. It is therefore useful to treat these regions as "integral" regions in which analytical or approximate forms of the profiles are utilized in integral forms of the equations of motion. The "outer layer" which exists between the surface layer and inversion layer may then be treated either in integral ("single layer") fashion or with a full finite difference treatment.



The hybrid integral-differential method combines integral constraint equations with the full finite difference equations which describe the outer layer. The method can thus be used either with a large number of finite difference levels or with a sparse number of levels with a "good" solution for the boundary layer parameters still achievable in the limit in which the finite difference levels consist of no points, i.e., the description is purely integral. In this limit, the method bears some resemblance to various "layer" parameterization procedures (References 20, 21, 22). However, there is an essential difference between these layer parameterization schemes and the hybrid procedure we describe here. Mathematical approximation for simplicity of solution and physical modelling interplay together in the formulation of the layer parameterization models cited above. The hybrid procedure described here including its integral constraints is rigorously based upon the second order closure theory of turbulence. Hence, turbulence modelling issues are confined to the validity of the general second order closure theory. The hybrid procedure is directed to the representation of this system of equations and the method of solution of the system. Thus, in the hybrid method described here, solution approximation issues are separated from turbulence modelling issues. The capability for continuous transition from a purely integral description to a fully differential description is one of the features we have attempted to incorporate in the hybrid procedure. Of major interest is the intent that the integral constraints which are part of the hybrid method will significantly improve the solution of the PBL for cases in which a sparse grid of only four to six finite difference levels is used over that which would be obtained in absence of these integral constraints.

A full second-order closure PBL model which could adequately perform with only four to six finite difference cells would be computationally efficient and would possess advantages for operational implementation in various applications as well as providing an economical basis for fully three-dimensional (horizontally inhomogeneous) PBL descriptions.

The full range of PBL behavior ranging from stable to unstable including those capped by an inversion layer may, in principle, be treated with the hybrid method. Large scale divergence, humidity effects, and radiative transport represent further key processes which require inclusion in the hybrid method. We have selected the following reasonable steps of development and evaluation of the hybrid method for the I-D homogeneous PBL.

1. Neutral PBL
2. General PBL (stratified)
3. General PBL including inversion layer and large scale divergence
4. General Moist PBL (including humidity and radiative transport)

In the present report steps 1 and 2 have been completed and sample results are presented. These results are worthy enough to encourage us to begin steps 3, 4. The major activities in these steps involve the development of the integral equations for the inversion layer as well as integral equations for the prediction of the humidity boundary layer thickness and fluxes and the cloud base and cloud top elevations.



### 3.3 Integral Constraints and Their Incorporation Into the Hybrid Method

#### 3.3.1 Governing Equations of the Horizontally Homogeneous PBL

We consider a horizontally homogeneous PBL in coordinates  $x, y, z$  aligned with  $z$  normal to the surface and  $x, y$  as coordinates in the plane perpendicular to  $z$ . Let  $\vec{U} = \vec{U}(U, V)$  be the velocity field in the plane and let  $(U_g, V_g)$  be the geostrophic wind velocity components defining the pressure gradients. The momentum equations in the  $(x, y)$  plane may be expressed as

$$\frac{\partial}{\partial t} (U_\infty - U) = \frac{\partial}{\partial z} (\overline{uw}) - f (V - V_g) + \dot{U}_\infty \quad (3.1)$$

$$\frac{\partial}{\partial t} (V_\infty - V) = \frac{\partial}{\partial z} (\overline{vw}) + f (U - U_g) + \dot{V}_\infty \quad (3.2)$$

In the above,  $f$  is the Coriolis parameter,  $\overline{uw}$ ,  $\overline{vw}$  are the stress components and  $\vec{U}_\infty = \vec{U}_\infty(U_\infty, V_\infty)$  is the velocity vector in the inviscid region above the boundary layer. The corresponding mean thermal energy equation for the virtual potential temperature  $\theta$  is

$$\frac{\partial}{\partial t} (\theta_\infty - \theta) = \frac{\partial}{\partial z} (\overline{w\theta}) - \dot{Q} + \dot{\theta}_\infty \quad (3.3)$$

where  $\overline{w\theta}$  is the vertical turbulent heat flux and  $\dot{Q}$  is the thermal energy source term. The inviscid region forms of Eqs. (3.1) through (3.3) are

$$\frac{\partial U_\infty}{\partial t} = -f (V_\infty - V_{g_\infty}) = \dot{U}_\infty \quad (3.4)$$

$$\frac{\partial V_\infty}{\partial t} = +f (U_\infty - U_{g_\infty}) = \dot{V}_\infty \quad (3.5)$$

$$\dot{\theta}_{\infty} = \dot{Q}_{\infty} \quad (3.6)$$

where  $U_{g\infty}, V_{g\infty}$  define the pressure gradients outside the boundary layer. In what follows we shall assume  $U_g = U_{g\infty}, V_g = V_{g\infty}$ . Thus Eqs. (3.1) through (3.3) may be expressed as

$$\frac{\partial}{\partial t} (U_{\infty} - U) = \frac{\partial}{\partial z} (\overline{uw}) + f (V_{\infty} - V) \quad (3.7)$$

$$\frac{\partial}{\partial t} (V_{\infty} - V) = \frac{\partial}{\partial z} (\overline{vw}) - f (U_{\infty} - U) \quad (3.8)$$

$$\frac{\partial}{\partial t} (\theta_{\infty} - \theta) = \frac{\partial}{\partial z} (\overline{w\theta}) - (\dot{Q}_{\infty} + \dot{Q}) \quad (3.9)$$

The turbulent moment equations at second-order closure level which we shall employ include those for the Reynolds stresses, heat flux, temperature variance, and the turbulent scale equation. We do not repeat the full set of turbulence equations here, but refer the reader to Reference 7. The two equations from the turbulence set which we will repeat here because of their use in the integral developments are the turbulent kinetic energy equation for the turbulent kinetic energy  $(1/2)q^2$  and the turbulent scale equation for the scale  $\Lambda$ . These are

$$\begin{aligned} \frac{\partial}{\partial t} \left( \frac{1}{2} q^2 \right) = & - \overline{uw} \frac{\partial U}{\partial z} - \overline{vw} \frac{\partial V}{\partial z} + \frac{g}{\theta_0} \overline{w\theta} \\ & + 0.3 \frac{\partial}{\partial z} q \Lambda \frac{\partial}{\partial z} \left( \frac{1}{2} q^2 \right) - \frac{1}{4} \left( \frac{q}{\Lambda} \right) \left( \frac{1}{2} q^2 \right) \end{aligned} \quad (3.10)$$

$$\begin{aligned} \frac{\partial \Lambda}{\partial t} = & 0.35 \frac{\Lambda}{qz} \left( \overline{uw} \frac{\partial \Lambda}{\partial z} + \overline{vw} \frac{\partial \Lambda}{\partial z} \right) + 0.075 q + 0.3 \frac{\partial}{\partial z} \left( q \Lambda \frac{\partial \Lambda}{\partial z} \right) \\ & - \frac{0.375}{q} \left( \frac{\partial q \Lambda}{\partial z} \right)^2 + 0.8 \frac{\Lambda}{q^2} \frac{g}{T_0} \overline{w\theta} \end{aligned} \quad (3.11)$$

Eqs. (3.7) through (3.10) along with the remaining second-order closure equations form the basis for the subsequent development.

The mean defect kinetic energy equation from Eqs. (3.7) and (3.8) is

$$\frac{\partial E^{(m)}}{\partial t} = (U_\infty - U) \frac{\partial}{\partial z} (\overline{uw}) + (V_\infty - V) \frac{\partial}{\partial z} (\overline{vw})$$

where

$$E^{(m)} = \frac{1}{2} |\vec{U}_\infty - \vec{U}|^2$$

The total energy equation derived from Eq. (3.10) and the above equation

$$\begin{aligned} \frac{\partial E}{\partial t} = & \frac{\partial}{\partial z} \left[ \overline{uw} (U_\infty - U) + \overline{vw} (V_\infty - V) \right] + 0.3 \frac{\partial}{\partial z} \left[ q \Lambda \frac{\partial}{\partial z} \left( \frac{1}{2} q^2 \right) \right] \\ & + \frac{g}{\theta_0} \overline{w\theta} - \frac{1}{4} \left( \frac{q}{\Lambda} \right) \left( \frac{1}{2} q^2 \right) \end{aligned} \quad (3.12)$$

where

$$E = E^{(m)} + \frac{1}{2} q^2$$

### 3.3.2 Integral Parameters and Integral Constraints

The important integral (global as opposed to local) parameters of the neutral PBL are readily cited as the surface shear stress or shearing velocity components ( $u_*^2, v_*^2$ ) and the overall boundary layer depth ( $\delta$ ). In addition to these, integral parameters may be generated by simply taking moments over the mean and turbulent fluid field variables. The first moments are the average velocity components:

$$\langle U \rangle = \delta_0^{-1} \int_{z_0}^{\delta} U(z) dz \quad \langle V \rangle = \delta_0^{-1} \int_{z_0}^{\delta} V(z) dz$$

In the above equations we have  $\delta_0 \equiv (\delta - z_0)$  where  $z_0$  is the effective roughness height. These average velocities are equally expressible in terms of the displacement thickness  $\delta_u, \delta_v$  defined as

$$\delta_u = |\vec{U}_\infty|^{-1} \int_{z_0}^{\delta} (U_\infty - U) dz \quad \delta_v = |\vec{U}_\infty|^{-1} \int_{z_0}^{\delta} (V_\infty - V) dz \quad (3.13)$$

where  $\vec{U} = \vec{U}(U, V)$  is the local velocity vector,  $\vec{U}_\infty$  is the velocity vector in the inviscid region above the boundary layer and  $(U_\infty, V_\infty)$  are the velocity components in this inviscid region.

In a stable PBL, the surface heat flux expressed in terms of  $\theta_*$  will enter the set of integral parameters as well as the average temperature  $\langle \theta \rangle$ , or equivalently, a thermal energy thickness  $\delta_\theta$  defined as

$$\delta_\theta = \theta_r^{-1} \int_{z_0}^{\delta} (\theta_\infty - \theta) dz \quad (3.14)$$

here  $\theta_r$  is a reference temperature and  $\theta_\infty$  is the virtual potential temperature in the inviscid zone at the boundary layer edge. If other energy

source terms appear in the thermal energy equation (such as radiative source terms) the temperature  $\theta_\infty$  requires more detailed definition appropriate to the particular source term in question. Note that  $\theta_\infty$  may be a function of  $Z$ .

In an unstable PBL, the above parameters also enter; however in addition a significant set of integral (over the inversion layer) parameters describing the inversion layer will also enter. We do not take up the additional integral parameters and constraint equations for the inversion layer in this report as described on page 20.

The integral constraint equations corresponding to the foregoing integral parameters are the first spatial moments of Eqs. (3.7) through (3.9). These are (assuming  $z_0$  independent of  $t$ ):

$$\frac{\partial}{\partial t} (|\vec{U}_\infty| \delta_u) = u_\star^2 + f \delta_v |\vec{U}_\infty| \quad (3.15)$$

$$\frac{\partial}{\partial t} (|\vec{U}_\infty| \delta_v) = v_\star^2 - f \delta_u |\vec{U}_\infty| \quad (3.16)$$

$$\frac{\partial}{\partial t} (\theta_r \delta_\theta) = |\vec{u}_\star| \theta_\star + s_\theta \quad (3.17)$$

The surface shear velocity vector is  $\vec{u}_\star^2 = \vec{u}_\star^2 (u_\star^2, v_\star^2)$  where  $u_\star^2 = -(\overline{uw})_0$ ,  $v_\star^2 = -(\overline{vw})_0$ ,  $|\vec{u}_\star| \theta_\star = -(\overline{w\theta})_0$  and  $(\quad)_0$  denotes a surface value. The thermal energy source term  $s_\theta$  is defined by

$$s_\theta = \int_{z_0}^{\delta} [\dot{Q}_\infty - \dot{Q}(z)] dz$$

The next moments involve products of the velocity. The defect mean kinetic energy thickness  $\delta_E^{(m)}$  is defined as

$$\delta_E^{(m)} = E_r^{-1} \int_{z_0}^{\delta} \frac{|\vec{U}_\infty - \vec{U}|^2}{2} dz \quad (3.18)$$

where  $E_r$  is a reference energy which requires specification to complete definition. The turbulent kinetic energy thickness may be defined as

$$\delta_E^{(t)} = E_r^{-1} \int_{z_0}^{\delta} \frac{1}{2} q^2 dz$$

where  $q$  is the RMS turbulence velocity. One can also consider the total energy thickness  $\delta_E$  defined as

$$\delta_E = \delta_E^{(m)} + \delta_E^{(t)} \quad (3.19)$$

Since it is the turbulent viscous field which underlies the defect mean kinetic energy as well as the turbulent kinetic energy, it is appropriate to select the reference energy  $E_r$  as the surface turbulent kinetic energy expressed in terms of the surface RMS turbulence velocity  $q_0$  for neutral or stable boundary layers:

$$E_r = \frac{1}{2} q_0^2 \quad (3.20)$$

We describe the method of selecting  $E_r$  in the case of unstable boundary layers in Section 3.6. The integral total energy equation has the form

$$\frac{\partial}{\partial t} (E_r \delta_E) = u_*^2 U_\infty + v_*^2 V_\infty + \frac{g}{\theta_0} \int_{z_0}^{\delta} \overline{w\theta} dz - \frac{1}{4} \int_{z_0}^{\delta} \frac{q}{\Lambda} \frac{1}{2} q^2 dz \quad (3.21)$$

The characteristic average scale in the boundary layer may be defined as

$$\ell = \delta_0^{-1} \int_{z_0}^{\delta} \Lambda dz \quad (3.22)$$

The integral equation governing  $\lambda$  is then the integrated form of the scale equation (3.11):

$$\begin{aligned} \frac{\partial}{\partial t} (\lambda \delta_0) = & 0.35 \int_{z_0}^{\delta} \frac{\Lambda}{q^2} (\overline{uw} \frac{\partial U}{\partial z} + \overline{vw} \frac{\partial V}{\partial z}) dz + 0.075 \int_{z_0}^{\delta} q dz \\ & - 0.375 \int_{z_0}^{\delta} \frac{1}{q} \left( \frac{\partial}{\partial z} q \Lambda \right)^2 dz - 0.8 \int_{z_0}^{\delta} \frac{\Lambda}{q^2} \frac{g}{T_0} \overline{w\theta} dz \end{aligned} \quad (3.23)$$

It can be seen that the Eqs. (3.15 - 3.17) and (3.21 - 3.23) form a closed system for the integral parameters  $\delta_u$ ,  $\delta_v$ ,  $\delta_\theta$ ,  $\delta_E$ ,  $\lambda$  provided the fluxes  $u_*$ ,  $v_*$ ,  $\theta_*$  and the integrals appearing in Eqs. (3.21) and (3.23) can be expressed in terms of these quantities.



### 3.3.3 Structure Function Approach to the Surface Flux Laws and the Integral Parameters

We now take up the method of closure of the hybrid procedure which unifies the integral constraints with the fully differential procedure. The unifying vehicle is a system of structure functions. We consider first the representation of the surface fluxes in terms of the integral parameters.

In the absence of stratification effects, the velocities and turbulent momentum fluxes in the surface layer in a right handed orthogonal coordinate system with the  $U$  component aligned parallel to the outer flow velocity  $\vec{U}_\infty$  may be represented as

$$\overline{uw} = - |\vec{u}_*^2| \cos\beta \quad (3.24)$$

$$\overline{vw} = - |\vec{u}_*^2| \sin\beta (1-\phi_1) \quad (3.25)$$

$$U = \frac{|\vec{u}_*|}{\kappa} \ln (z/z_0) \cos\beta \quad (3.26)$$

$$V = \frac{|\vec{u}_*|}{\kappa} \ln (z/z_0) \sin\beta (1-\phi_2) \quad (3.27)$$

where  $\vec{u}_*^2 = (u_*^2, v_*^2)$  is the vector of surface stress components lying in the plane of motion. Here  $\overline{uw}$ ,  $\overline{vw}$  are the turbulent momentum fluxes parallel and perpendicular to the outer flow velocity  $\vec{U}_\infty$  while  $U$ ,  $V$  are the corresponding velocity components. The angle between the local velocity  $\vec{U}$  and the outer flow  $\vec{U}_\infty$  is denoted as  $\beta$ . The absolute magnitude of the surface shear stress components lying in the plane of the flow is  $|\vec{u}_*|$ . The functions  $\phi_1(z)$ ,  $\phi_2(z)$  are representations of the effects of the Coriolis force-induced pressure gradient in forcing  $\overline{vw}$  and  $V$  to deviate from constant and logarithmic values respectively which is the first manifestation of the pressure gradient effect on the surface layer for  $z > z_0$ , (Reference 23):

$$\phi_1(z) = \frac{f|\vec{U}_\infty|}{|\vec{u}_*|^2 \sin\beta} \left[ z - z_0 - \frac{|\vec{u}_*|}{\kappa|\vec{U}_\infty|} \cos\beta z\gamma(z) \right] \quad (3.28)$$

$$\phi_2(z) = \frac{f|\vec{U}_\infty|}{|\vec{u}_*|^2 \sin\beta \ln(z/z_0)} \left\{ z - z_0 - z_0 \ln(z/z_0) - \frac{|\vec{u}_*|}{\kappa|\vec{U}_\infty|} \cos\beta \left[ z\gamma(z) - [z_0 \ln(z/z_0) - (z-z_0)] \right] \right\} \quad (3.29)$$

with

$$\gamma(z) \equiv \ln(z/z_0) - (1-z_0/z)$$

Now let  $\alpha_\infty$  denote the angle of the outer flow velocity  $\vec{U}_\infty$  with respect to the  $x$  axis of an arbitrary coordinate system fixed to the earth. Let  $\alpha$  denote the angle of the local velocity  $\vec{U}$  makes with the same coordinate system. The angle  $\beta$  is related to  $\alpha_\infty$ ,  $\alpha$  as

$$\beta = \alpha - \alpha_\infty$$

The surface layer momentum flux and velocity components in this general coordinate system in which we shall formulate the procedure are given by

$$\overline{uw} = - |\vec{u}_*|^2 [\cos\alpha + \sin\beta \sin\alpha_\infty \phi_1(z)] \quad (3.30)$$

$$\overline{vw} = - |u_*|^2 [\sin\alpha - \sin\beta \cos\alpha_\infty \phi_1(z)] \quad (3.31)$$

$$U = \frac{|\vec{u}_*|}{\kappa} \ln(z/z_0) [\cos\alpha + \sin\beta \sin\alpha_\infty \phi_2(z)] \quad (3.32)$$

$$V = \frac{|\vec{u}_*|}{\kappa} \ln(z/z_0) [\sin\alpha - \sin\beta \cos\alpha_\infty \phi_2(z)] \quad (3.33)$$

Consider  $z = \delta_s$  as the height of the surface layer. Then at this level we have from Eqs. (3.32) and (3.33)

$$|\vec{u}_*| = \frac{\kappa|\vec{U}_s|}{\Phi(\delta_s) \ln(\delta_s/z_0)} \quad (3.34)$$

where

$$\Phi(\delta_s) = \{1 + \sin^2 \beta \phi_2(\delta_s) [\phi_2(\delta_s) - 2]\}^{1/2}$$

Let us now compare this result with the Monin-Obukhov surface layer similarity theory for stratified flows which (neglecting Coriolis effects) has the form

$$|\vec{u}_*| = \frac{\kappa |\vec{u}_s|}{\ln(\delta_s/z_0) + \mu_u} \quad (3.35)$$

where  $\mu_u = \mu_u(\delta_s/L)$  is a Monin-Obukhov similarity function for momentum transfer and has different forms depending upon whether the Monin-Obukhov length  $L$  is greater or less than zero. The Monin-Obukhov length is defined as

$$L = \frac{T_0}{g\kappa} \frac{|\vec{u}_*|^2}{\theta_*}$$

We observe that the form Eq. (3.34) which includes first order corrections for the effects of the Coriolis forces in the surface layer was derived with the condition that  $u_*$  and the RMS turbulence velocity  $q_0$  were approximately constant in the surface layer. On the other hand, the Monin-Obukhov similarity form (3.35) is based on the condition that  $|\vec{u}_*|$  is constant in the surface layer. For flows in which the angle  $\beta$  is not too large, it may then be possible to obtain a general "extended" surface layer resulting in the form

$$|\vec{u}_*| = \frac{\kappa |\vec{u}_s|}{D_u} \quad (3.36)$$

where

$$D_u \equiv \Phi(\delta_s/z_0) \ln(\delta_s/z_0) + \mu_u \quad (3.37)$$

Although we have not proved it here, we conjecture that the form Eq. (3.37) is correct to first order in the surface layer expansion parameter

$$\delta_s/L_c = \frac{f |\vec{u}_\infty| \delta_s}{|\vec{u}_*|^2 |\sin \beta|} \quad (3.38)$$

where Eq. (3.38) defines the Coriolis surface length  $L_C$  which can be interpreted as the height at which Coriolis force induced pressure gradients disturb the uniformity of  $|\vec{u}_*|$  and the pure logarithmic form of the velocity variation in the surface layer.

We note that by choosing  $\delta_s \ll |L|$ ,  $\delta_s \ll L_C$  we may always render the form of  $D_u$  in Eq. (3.37) in the pure logarithmic form. There is a usefulness, however, in allowing the surface layer to be as thick as possible with consideration for the validity of Eqs. (3.30) - (3.33) in application of the hybrid procedure with a space-grid finite difference procedure. Incorporation of virtually the full logarithmic layer below  $z = \delta_s$  then allows the finite difference procedure a better resolution of the more linear region for  $z \geq \delta_s$ . In the absence of stratification, Eqs. (3.30) - (3.33) are quite accurate even for  $\delta_s > L_C$  yielding results that are within 10% of the exact solution for the steady state PBL at  $\delta_s = 10 L_C$ .

The counterparts to Eqs. (3.30) - (3.33) for heat flux and temperature distribution in the surface layer are

$$\overline{w\theta} = - |\vec{u}_*| \theta_* \quad (3.39)$$

$$\theta - \theta_0 = \theta_* P_R D_\theta / \kappa \quad (3.40)$$

from which we may write

$$\theta_* = \frac{\kappa}{P_R D_\theta} (\theta_s - \theta_0) \quad (3.41)$$

where  $\theta_s$  is the virtual potential temperature at  $z = \delta_s$ ,  $\theta_0$  is the surface temperature,  $\theta_r$  is a reference temperature, and  $P_R$  is the turbulent Prandtl number. The function  $D_\theta$  like  $D_u$  consists of a logarithmic portion and a stratification portion embedded in the Monin-Obukhov similarity function  $\mu_\theta$ :

$$D_\theta = \ln(\delta_s/z_0) + \mu_\theta(\delta_s/L) \quad (3.42)$$

To relate the fluxes  $|\vec{u}_*|$ ,  $\theta_*$ , and the surface layer angle  $\alpha$  (or  $\beta$ ) to the integral parameters  $\delta_u$ ,  $\delta_v$ ,  $\delta_\theta$  we express  $U_s$ ,  $V_s$ , and  $\theta_s - \theta_0$  in terms of the structure functions  $S(U)$ ,  $S(V)$ ,  $S(\theta)$  as follows:

$$U'_s = S^{(U)} \langle U' \rangle_0 \quad (3.43)$$

$$V'_s = S^{(V)} \langle V' \rangle_0 \quad (3.44)$$

$$\theta_s - \theta_0 = S^{(\theta)} \langle \theta - \theta_0 \rangle_0 \quad (3.45)$$

where the  $( )'$  indicates representation in the coordinate system aligned with  $\vec{U}_\infty$  and the  $\langle \rangle_0$  indicate a spatial average over the outer part of the boundary layer:

$$\langle ( ) \rangle_0 = (\delta - \delta_s)^{-1} \int_{\delta_s}^{\delta} ( ) dz$$

These averages may in turn be related to the displacement thicknesses  $\delta_u^{(0)}$ ,  $\delta_v^{(0)}$ ,  $\delta_\theta^{(0)}$  as

$$\langle U' \rangle_0 = |\vec{U}_\infty| (1 - \cos \alpha_\infty \delta_u^{(0)} / \delta_{s0} - \sin \alpha_\infty \delta_v^{(0)} / \delta_{s0}) \quad (3.46)$$

$$\langle V' \rangle_0 = |\vec{U}_\infty| (\sin \alpha_\infty \delta_u^{(0)} / \delta_{s0} - \cos \alpha_\infty \delta_v^{(0)} / \delta_{s0}) \quad (3.47)$$

$$\langle \theta - \theta_0 \rangle_0 = \theta_r [(\theta_\infty - \theta_0) / \theta_r - \delta_\theta^{(0)} / \delta_{s0}] \quad (3.48)$$

where  $\delta_{s0} \equiv \delta - \delta_s$ . Thus, given the structure functions  $S^{(U)}$ ,  $S^{(V)}$ ,  $S^{(\theta)}$  we obtain the flux laws which relate  $|\vec{u}_*|$ ,  $\alpha$  (or  $\beta$ ),  $\theta_*$  to the integral parameters  $\delta_u^{(0)}$ ,  $\delta_v^{(0)}$ ,  $\delta_\theta^{(0)}$  as

$$|\vec{u}_*| = \frac{\kappa |\vec{U}_s|}{D_u} \quad (3.49)$$

$$\theta_* = \frac{\kappa}{P_R D_\theta} (\theta_\infty - \theta_s) \quad (3.50)$$

$$\beta = \alpha - \alpha_\infty = \tan^{-1}(V'_S/U'_S) \quad (3.51)$$

with  $U'_S$ ,  $V'_S$  and  $\theta_\infty - \theta_S$  given as

$$U'_S = |\vec{U}_\infty| S^{(U)} (1 - \cos \alpha_\infty \delta_u^{(o)}/\delta_{s0} - \sin \alpha_\infty \delta_v^{(o)}/\delta_{s0}) \quad (3.52)$$

$$V'_S = |\vec{U}_\infty| S^{(V)} (\sin \alpha_\infty \delta_u^{(o)}/\delta_{s0} - \cos \alpha_\infty \delta_v^{(o)}/\delta_{s0}) \quad (3.53)$$

$$|\vec{U}_S| = \sqrt{(U'_S)^2 + (V'_S)^2} \quad (3.54)$$

$$(\theta_\infty - \theta_S) = \theta_r S^{(\theta)} \left( \frac{\theta_\infty - \theta_0}{\theta_r} - \delta_\theta^{(o)}/\delta_{s0} \right) \quad (3.55)$$

The "outer" thicknesses  $\delta_u^{(o)}$ ,  $\delta_v^{(o)}$ ,  $\delta_\theta^{(o)}$  are related to the total thicknesses  $\delta_u$ ,  $\delta_v$ ,  $\delta_\theta$  as

$$\delta_j^{(o)} = \delta_j - \delta_j^{(i)}$$

where the inner thicknesses  $\delta_j^{(i)}$  are related to  $|\vec{u}_*|$ ,  $\beta$ ,  $\theta_*$  through

$$\delta_u^{(i)} = (\delta_{s0}/\delta_0) |\vec{U}_\infty|^{-1} \int_{z_0}^{\delta_s} (U_\infty - U) dz \quad (3.56)$$

$$\delta_v^{(i)} = (\delta_{s0}/\delta_0) |\vec{U}_\infty|^{-1} \int_{z_0}^{\delta_s} (V_\infty - V) dz \quad (3.57)$$

$$\delta_{\theta}^{(i)} = (\delta_{s0}/\delta_0)\theta_r \int_{z_1}^{\delta_s} (\theta_{\infty}-\theta)dz \quad (3.58)$$

where  $U$ ,  $V$ ,  $\theta$  in Eqs. (3.56) - (3.58) are given in terms of the surface layer expressions (3.32), (3.33), and (3.40).

Equations (3.49) - (3.55) are the key results of this section. They provide the surface flux laws which relate  $u_*$  and  $\theta_*$  to the integral parameters  $\delta_u$ ,  $\delta_v$ ,  $\delta_{\theta}$  and in so doing naturally introduce the structure functions  $S(U)$ ,  $S(V)$ ,  $S(\theta)$  which are obtained from detailed solution of the differential equations. Equations (3.36) and (3.41) are exact statements provided the structure functions  $S(U)$ ,  $S(V)$ ,  $S(\theta)$  are known. These equations relate the surface fluxes  $u_*$ ,  $v_*$ ,  $\theta_*$  to the integral thickness  $\delta_u$ ,  $\delta_v$ ,  $\delta_{\theta}$ . As such, they may be considered friction and heat flux laws for integral PBL description. We now observe that if the detailed profiles  $U(z)$ ,  $V(z)$ ,  $\theta(z)$  are known, the structure functions  $S(U)$ ,  $S(V)$ ,  $S(\theta)$  may be directly calculated (with specification of the thickness  $\delta_s$ ). Hence, these structure functions may be calculated in terms of the profiles generated by the finite difference solution. It may be further observed that the integral constraints furnish  $u_*$ ,  $v_*$ ,  $\theta_*$  in terms of the integral thickness  $\delta_u$ ,  $\delta_v$ ,  $\delta_{\theta}$ . Hence, these surface fluxes together with the surface layer functions Eqs. (3.52, 3.33, and 3.40), determine the boundary data at  $z = \delta_s$  for the finite difference description of the domain  $\delta_s < z < \delta$ . As such, the derivative boundary condition normally required at the top of the surface layer  $z = \delta_s$  for the finite-difference equations is dispensed with. The derivative boundary conditions are thus replaced by the integral constraints. The interest is that this procedure for treating the surface conditions should significantly improve the quality of the overall finite difference description when a sparse set of grid levels is utilized consisting of perhaps only four to six grid cells.



### 3.3.4 Transfer Coefficients

We may define transfer coefficients  $c_f$ ,  $c_\theta$  for momentum and heat transfer to the surface as

$$c_f = \frac{|\vec{u}_*|^2}{|\vec{U}_\infty|^2} \quad (3.59)$$

$$c_\theta = \frac{|\vec{u}_*|_{\theta_*}}{|\vec{U}_\infty|_{\theta_r}} \quad (3.60)$$

The momentum and heat fluxes are then expressed as

$$u_*^2 = c_f |\vec{U}_\infty|^2 \cos\alpha \quad (3.61)$$

$$v_*^2 = c_f |\vec{U}_\infty|^2 \sin\alpha \quad (3.62)$$

$$|\vec{u}_*|_{\theta_*} = c_\theta |\vec{U}_\infty|_{\theta_r} \quad (3.63)$$

It is also useful to define differential momentum and heat transfer coefficients which characterize the rates of change of  $u_*^2$ ,  $v_*^2$ ,  $|\vec{u}_*|_{\theta_*}$  with respect to the integral parameters  $\delta_u$ ,  $\delta_v$ ,  $\delta_\theta$  (with all other quantities held fixed). Let  $\delta_\alpha$  represent the vector of thicknesses  $\delta_u$ ,  $\delta_v$ ,  $\delta_\theta$  and  $c_\alpha$  the vector of fluxes  $c_f \cos\alpha$ ,  $c_f \sin\alpha$ ,  $c_\theta$ :

$$\delta_\alpha = \begin{pmatrix} \delta_u \\ \delta_v \\ \delta_\theta \end{pmatrix} \quad c_\alpha = \begin{pmatrix} c_f \cos\alpha \\ c_f \sin\alpha \\ c_\theta \end{pmatrix} \quad (3.64)$$

The differential exchange coefficients  $\bar{c}_{\alpha\beta}$  are then defined as

$$c_{\alpha\beta} = \delta_{\alpha\beta} \partial c / \partial \delta_{\beta} \quad (3.65)$$

For the case in which  $\alpha_{\infty} \equiv 0$  these exchange coefficients have the form

$$\begin{Bmatrix} c_{11} \\ c_{12} \\ c_{21} \\ c_{22} \end{Bmatrix} = c_f \frac{|\vec{U}_{\infty}|}{|\vec{U}_s|} \begin{Bmatrix} S^{(U)} \left[ 2 \left( \frac{1+3\Delta_u}{\Delta} \right) \cos^2 \beta + \sin^2 \beta \right] \\ S^{(U)} \left[ \left( 2 \frac{1+3\Delta_u}{\Delta} - 1 \right) \sin \beta \cos \beta \right] \\ S^{(V)} \left[ \left( 2 \frac{1+3\Delta_v}{\Delta} - 1 \right) \cos \beta \sin \beta \right] \\ S^{(V)} \left[ 2 \left( \frac{1+3\Delta_v}{\Delta} \right) \sin^2 \beta + \cos^2 \beta \right] \end{Bmatrix} \quad (3.66)$$

$$\begin{Bmatrix} c_{13} \\ c_{23} \end{Bmatrix} = c_f \left( \frac{\theta_s}{\theta_s - \theta_0} \right) S^{(\theta)} \quad 2 \frac{\Delta_u}{\Delta} \begin{Bmatrix} \cos \beta \\ \sin \beta \end{Bmatrix} \quad (3.67)$$

$$\begin{Bmatrix} c_{31} \\ c_{32} \end{Bmatrix} = c_{\theta} \frac{|\vec{U}_{\infty}|}{|\vec{U}_s|} \left( \frac{1-3\Delta_{\theta}}{\Delta} \right) \begin{Bmatrix} S^{(U)} \cos \beta \\ S^{(V)} \sin \beta \end{Bmatrix} \quad (3.68)$$

$$c_{33} = c_{\theta} \left( \frac{\theta_r}{\theta_s - \theta_0} \right) S^{(\theta)} \left( \frac{1-\Delta_{\theta}}{\Delta} \right) \quad (3.69)$$

In the foregoing

$$\Delta_u = \frac{L}{D_u} \frac{\partial \mu_u}{\partial L}$$

$$\Delta_{\theta} = \frac{L}{D_{\theta}} \frac{\partial \mu_{\theta}}{\partial L}$$

$$\Delta = 1 + 2\Delta_u - \Delta_\theta$$

In the stable limit where  $\mu_u \sim \frac{1}{L}$ ,  $\mu_\theta \sim \frac{1}{L}$  the functions  $\Delta_u$ ,  $\Delta_\theta$  become

$$\Delta_u = -\frac{\mu_u}{D_u} \quad \Delta_\theta = -\frac{\mu_\theta}{D_\theta}$$

and obey

$$-1 \leq \Delta_u \leq 0 \quad -1 \leq \Delta_\theta \leq 0$$

with

$$\Delta_u, \Delta_\theta \rightarrow 0 \quad \text{as } L \rightarrow \infty$$

$$\Delta_u, \Delta_\theta \rightarrow -1 \quad \text{as } L \rightarrow 0$$

We may note that as  $L \rightarrow \infty$ ,  $\Delta_u \rightarrow 0$  and the coefficients  $C_{13}$ ,  $C_{23} \rightarrow 0$ . The momentum flux then becomes decoupled from the heat flux. On the other hand, for finite  $L$ , the heat flux and momentum flux are coupled. In the case where  $\alpha = 0$ , the Brunt Väisälä frequency in the surface layer is given by

$$\omega_{BV}^{(S)} = \sqrt{C_{13}C_{31}} |\vec{U}_\infty| / \delta_0 \quad (3.70)$$

When  $L < 0$ , the product  $C_{13}C_{31}$  is less than zero and the Brunt Väisälä frequency is imaginary.

### 3.3.5 Surface Layer Depth

Let us now consider the surface layer depth  $\delta_s$ . This depth is rigorously determined by the strength of the terms in Eqs. (3.7 - 3.9) which disturb the condition

$$\frac{\partial}{\partial z} (\overline{uw}, \overline{vw}, \overline{w\theta}) \approx 0$$

and the validity of the surface layer solutions Eqs. (3.24 - 3.27). There are three general effects: (1) the Coriolis effect, (2) unsteady effects, and (3) thermal source terms. From the work of Reference 23 it can be shown that the Coriolis effect leads to  $\delta_s$  determined by

$$\delta_s \lesssim L_c = |\sin\beta| |\vec{u}_*|^2 / (|f| |\vec{U}_\infty|) \quad (3.71)$$

Let us now consider the unsteady effects characterized by unsteady forcing frequencies  $f_u^{(\infty)}$ ,  $f_\theta^{(\infty)}$ . Such effects lead to conditions of the form

$$\delta_s \lesssim |\vec{u}_*|^2 / (|f_u^{(\infty)}| |\vec{U}_\infty|) \quad \delta_s \lesssim |\vec{u}_*| |\theta_*| / (|f_\theta^{(\infty)}| |\theta_r|) \quad (3.72)$$

Under all conditions the surface layer depth  $\delta_s$  should be limited by

$$\delta_s \lesssim |L| \quad (3.73)$$

We remark that although the expedient of setting

$$\delta_s = \epsilon \delta_0 \quad (3.74)$$

(where  $\epsilon$  is some small fraction) is simple and attractive, such a procedure is not necessarily consistent with the definition of the surface layer as that region in which the solutions Eqs. (3.24 - 3.27) are valid. Although Eq. (3.74) would likely lead to a determination of  $\delta_s$  consistent with Eqs. (3.24 - 3.27), the conditions (3.71), (3.72), and (3.73) are the more rigorous conditions for the determination of  $\delta_s$ .

### 3.3.6 Energy Thickness and the Dynamic Equation for the PBL Thickness

We now consider the development of the integral energy equation in terms of integral structure functions. We consider the choice of a characteristic energy  $E_r$  and characteristic RMS turbulence velocity  $q_r$ . In a stable PBL ( $L > 0$ ) we select  $q_r$  as the surface value  $q_0$ . In the case of an unstable PBL ( $L < 0$ ) the surface turbulence level does not characterize the average turbulence levels within the PBL because of the buoyant production of turbulence. In this case, we select  $q_r$  as

$$q_r = q_0 \left( 1 - \frac{8\ell}{\kappa L} \frac{|\vec{u}_*|^3}{q_0^3} \right)^{1/3}$$

Hence, the reference turbulence and energy levels are given by

$$q_r = \begin{cases} q_0 & L > 0 \\ q_0 \left( 1 - \frac{8\ell}{\kappa L} \frac{|\vec{u}_*|^3}{q_0^3} \right)^{1/3} & L < 0 \end{cases} \quad (3.75)$$

$$E_r = \frac{1}{2} q_r^2 \quad (3.76)$$

We now represent the integrals appearing in the total energy equation as

$$\int_{z_0}^{\delta} \left( \frac{q}{\Lambda} \right) \left( \frac{1}{2} q^2 \right) dz = S_E^{(d)} \frac{q_r}{\ell} \delta_E E_r \quad (3.77)$$

$$\int_{z_0}^{\delta} \frac{g}{\theta_0} \overline{w\theta} dz = - S_E^{(b)} \frac{|\vec{u}_*|^3}{\kappa L} \delta_E \quad (3.78)$$

The above equations are the defining equations for the structure functions  $S_E^{(d)}$ ,  $S_E^{(b)}$  which are the structure functions for turbulent decay and buoyant production/destruction of the total energy. The quantity  $\ell$  is the characteristic turbulent scale size with the boundary layer. This quantity is governed by the integral form of the turbulent scale equation which is described in Section 3.7.

In the usual fashion we define  $\delta_0$  as that elevation at which the viscous turbulent levels have fallen to an arbitrarily small fraction of the maximum values within the boundary layer. We choose to relate this thickness  $\delta_0$  directly to the total energy thickness  $\delta_E$ . Thus, we relate  $\delta_E$  through a parameter  $r$  as

$$\delta_0 = r\delta_E \quad (3.79)$$

$$\delta = r\delta_E + z_0$$

The total energy integral equation now becomes an equation for  $\delta_0$  by eliminating  $\delta_E$  through Eq. (3.79):

$$\frac{\partial}{\partial t} (E_r \delta_0) = \omega_E^{(d)} E_r (\delta_0^* - \delta_0) - \omega_E^{(b)} E_r \delta_0 \quad (3.80)$$

In Eq. (3.80), the energy decay rate  $\omega_E^{(d)}$  is given by

$$\omega_E^{(d)} = S_E^{(d)} q_r / (4\ell) \quad (3.81)$$

while the buoyant production/decay rate is given by

$$\omega_E^{(b)} = S_E^{(b)} |\vec{u}_*|^3 / (\kappa L E_r) \quad (3.82)$$

The equilibrium boundary layer thickness  $\delta_0^*$  is given by

$$\delta_0^* = \frac{4r\ell(u_*^2 U_\infty + v_*^2 V_\infty)}{S_E^{(d)} q_r E_r} \quad (3.83)$$

We see that in the neutral case ( $L \rightarrow \infty$ ), the total boundary layer thickness relaxes to the equilibrium thickness  $\delta_0^*$  on a time scale given by  $\omega_E^{(d)-1}$ .



### 3.3.7 Average Scale and Integral Scale Equation

It will be noted that in the expression of the various integrals of the total energy equation in terms of non-dimensional structure functions, it was necessary to utilize the average scale  $\ell$ . We now take up the structure function transformation of the integrated scale equation (3.23) which governs  $\ell$ . We define the structure functions  $S_\ell^{(d)}$  for the turbulent destruction of scale as

$$\int_{z_0}^{\delta} \left[ 0.35 \frac{\Lambda}{q^2} (\overline{uw} \frac{\partial U}{\partial z} + \overline{vw} \frac{\partial V}{\partial z}) - \frac{0.375}{q} \left( \frac{\partial q \Lambda}{\partial z} \right)^2 \right] dz$$

$$= - S_\ell^{(d)} \ell \left( \frac{u_*^2 U_\infty + v_*^2 V_\infty}{q_r |\vec{U}_\infty|} \right) \quad (3.84)$$

The structure function for turbulent production of scale  $S_\ell^{(p)}$  is defined by the statement

$$\int_{z_0}^{\delta} 0.075 q dz = S_\ell^{(p)} q_r \delta_0 \quad (3.85)$$

The structure function for buoyant production/destruction of scale is defined by

$$\int_{z_0}^{\delta} \frac{\Lambda}{q^2} \frac{g}{T_0} \overline{w\theta} dz = S_\ell^{(b)} \frac{|\vec{u}_*|^3}{\kappa q_r^2} \frac{\delta_0}{L} \ell \quad (3.86)$$

The integral form of the scale equation may then be expressed as

$$\begin{aligned} \frac{1}{\delta_0} \frac{\partial}{\partial t} (\ell \delta_0) = & - S_\ell^{(d)} \frac{(u_\infty^2 + v_\infty^2)}{q_r |\vec{U}_\infty|} \frac{\ell}{\delta_0} + S_\ell^{(p)} q_r \\ & - 0.8 S_\ell^{(b)} \frac{|\vec{u}_*|^3}{\kappa q_r L} \frac{\ell}{L} \end{aligned} \quad (3.87)$$

We may express the above result as

$$\frac{1}{\delta_0} \frac{\partial}{\partial t} (\ell \delta_0) \equiv \omega_\ell^{(d)} (\ell^* - \ell) - \omega_\ell^{(b)} \ell \quad (3.88)$$

where  $\omega_\ell^{(d)}$  is the scale decay rate given by

$$\omega_\ell^{(d)} = S_\ell^{(d)} \frac{(u_\infty^2 + v_\infty^2)}{q_r \delta_0 |\vec{U}_\infty|} \quad (3.89)$$

and  $\omega_\ell^{(b)}$  is the buoyant production/decay rate for scale:

$$\omega_\ell^{(b)} = 0.8 S_\ell^{(b)} \frac{|\vec{u}_*|^3}{\kappa q_r L} \quad (3.90)$$

The equilibrium scale  $\ell^*$  is given by

$$\ell^* = \frac{S_\ell^{(p)} q_r^2 |\vec{U}_\infty|}{S_\ell^{(d)} (u_\infty^2 + v_\infty^2)} \delta_0 \quad (3.91)$$

Nominal values for these structure functions are  $S_\ell^{(d)} = 0.2$ ,  $S_\ell^{(p)} = 0.0125$ ,  $S_\ell^{(b)} = 0.5$ . The behavior of the scale in the neutral and stable limits is of particular interest. In the neutral limit the scale will take the equilibrium value indicated by Eq. (3.91). For the above nominal values of the structure functions we find for a steady state, neutral PBL (with  $V_\infty \equiv 0$ )

$$\ell_* = 0.06 \delta_0 \quad (3.92)$$

in good agreement with the characteristic scale predicted in Reference 24. In the strongly stable limit ( $0 < L \ll \delta_0$ ) the scale will tend to an equilibrium value given by the balance between the last two terms of eq. (3.87)

$$\ell = \frac{s_\ell^{(p)} \kappa q_r^3}{s_\ell^{(b)} (0.8) |\vec{u}_*|^3} L \quad (3.93)$$

which yields  $\ell = 0.16 L$  for the nominal structure function values. This result is in agreement with the appropriate limit on  $\ell$  of  $\approx 0.2 L$  for strongly stable boundary layers.

### 3.3.8 Linearized Forms of the Integral Equations

We may express the integral equations for the mean flow, Eqs. (3.20 - 3.22) in terms of the thickness and flux vectors  $\delta_\alpha$ ,  $c_\alpha$  defined in Section 3.4 as

$$\frac{d\delta_\alpha}{dt} = |\vec{U}_\infty| c_\alpha + f \Sigma_{\alpha\beta} \delta_\beta - B_{\alpha\beta} \delta_\beta \quad (3.94)$$

where  $\Sigma_{\alpha\beta}$  is the partial anti-symmetric matrix:

$$\Sigma_{\alpha\beta} = \begin{pmatrix} 0 & 1 & 0 \\ -1 & 0 & 0 \\ 0 & 0 & 0 \end{pmatrix} \quad (3.95)$$

and  $B_{\alpha\beta}$  is the matrix of forcing functions:

$$B_{\alpha\beta} = \begin{pmatrix} f_U^{(\infty)} & 0 & 0 \\ 0 & f_V^{(\infty)} & 0 \\ 0 & 0 & f_\theta^{(\infty)} \end{pmatrix} \quad (3.96)$$

where

$$f_U^{(\infty)} = f_V^{(\infty)} = \frac{1}{|\vec{U}_\infty|} \frac{d|\vec{U}_\infty|}{dt} \quad (3.97)$$

$$f_\theta^{(\infty)} = \frac{1}{\theta_r} \frac{d\theta_r}{dt} \quad (3.98)$$

The linear expansion of  $c_\alpha$  about some state  $c_\alpha(0)$ ,  $\delta_\alpha(0)$  is

$$c_{\alpha} = c_{\alpha}(0) - \delta_0^{-1} c_{\alpha\beta}(\delta_{\beta} - \delta_{\beta}(0))$$

where  $C_{\alpha\beta}$  is the differential transfer matrix defined by Eq. (3.65). Substituting this form into Eq. (3.94) we obtain

$$\frac{d\delta_{\alpha}}{dt} = |\vec{U}_{\infty}| c_{\alpha}(0) + A_{\alpha\beta} \delta_{\beta} + \delta_0^{-1} |\vec{U}_{\infty}| c_{\alpha\beta} \delta_{\beta}(0) \quad (3.99)$$

where  $A_{\alpha\beta}$  is the fundamental matrix of the system:

$$A_{\alpha\beta} = f\Sigma_{\alpha\beta} - \delta_0^{-1} |\vec{U}_{\infty}| c_{\alpha\beta} - B_{\alpha\beta} \quad (3.100)$$

If the state  $\delta_{\alpha}(0)$  is an equilibrium state, then the equation governing perturbations  $\delta'_{\alpha} \equiv \delta_{\alpha} - \delta_{\alpha}(0)$  about this state is

$$\frac{d\delta'_{\alpha}}{dt} = A_{\alpha\beta} \delta'_{\beta} \quad (3.101)$$

We thus see that the matrix  $A_{\alpha\beta}$  contains all the fundamental linear response modes of the system including the rotational (Coriolis) modes and the Brunt Väisälä modes. Two of the eigenvalues of  $A_{\alpha\beta}$  may be identified with the rotational modes while the third eigenvalue may be identified with the Brunt Väisälä mode.

The integral equations for the boundary layer thickness  $\delta_0$  and the scale  $\ell$ , Eqs. (3.80) and (3.89) are similarly in a form in which linearization is readily applied. We point out the linear forms of these equations because they form the basis of the computational solution technique. We do not finite difference the equations for  $\delta_{\alpha}$ ,  $\delta_0$ ,  $\ell$ . Rather we utilize the linearized, constant coefficient forms of these equations, assuming their validity over a small time interval  $\Delta t$  connecting the two states at  $t_1$ ,  $t_2$  in terms of analytical solutions to the linear forms with the coefficients held fixed at their values at the time  $t_1$ . After the solution is obtained at time  $t_2$ , the coefficients are re-evaluated and the process is repeated for the next level  $t_3 = t_2 + \Delta t$ , etc.

### 3.3.9 Coupling of the Integral and Differential Systems

As noted previously, the integral equations for the variables  $\delta_u, \delta_y, \delta_\theta, \delta, \ell$  and the fluxes  $u_\star^2, v_\star^2, \theta_\star$  form a closed dynamical system if the structure functions  $S^{(U)}, S^{(V)}, S^{(\theta)}, S_E^{(b)}, S_\ell^{(d)}, S_\ell^{(p)}, S_\ell^{(b)}$  are known. Because of the manner in which these structure functions are defined, they are only sensitive to the integrals over detailed profile shape and are not sensitive to the characteristic magnitudes of the variables. Thus, one can specify the structure functions as pure non-dimensional numbers and obtain reasonably good solutions for the integral and surface parameters. For example, for a neutral PBL with unsteady forcing which is not too rapid compared to the rotation rate  $f$ , the values  $S^{(U)} = 0.8, S^{(V)} = 3.0, S_E^{(d)} = 0.15, S_\ell^{(b)} = 0.0125, S_\ell^{(d)} = 0.2, r = 0.35$  will yield satisfactory results with  $\delta_s = 5L_c$ .

For flows with strong forcing, more accurate results are to be obtained by introducing a finite difference system in the "outer" domain  $\delta_s < z < \delta$  wherein the general, second order closure system of equations is solved.

This finite difference system requires boundary data at the surface  $z = \delta_s$  as well as the free stream conditions at  $z = \delta$ . Finite difference derivative boundary conditions which would otherwise be required at the surface layer "edge"  $z = \delta_s$  are dispensed with; instead, the boundary data for  $\bar{U}(\delta_s, t), \theta(\delta_s, t), \dots, \overline{uw}(\delta_s, t), \dots$  are taken from the integrally determined surface layer conditions and flux laws. Hence, the surface boundary condition for the differential equation set are fixed by the integral parameters.

The coupling back upon the integral constraint equations from the finite difference generated profiles is through the non-dimensional structure functions which involve integrals over the profiles of the velocity, temperature, and turbulence fields. In the limit in which no finite difference points are used, i.e., the method is purely integral, these structure functions may be specified as pure numbers. Hence, at appropriate time levels in the course of evolution of the integral equations, the structure functions are up-dated by explicit calculation of the integrals over the profiles generated by the evolution of the differential equation set.

The finite difference system is set up on a dynamically moving grid whose first point is located at  $z = \delta_s(t)$  and whose uppermost (top) point is located at  $z = \delta(t)$ . The motion of the grid is thus fixed by  $\delta(t)$  which is in turn determined by the integral equation of the total kinetic energy. The basic flow of information is shown schematically in Figure 3.1.

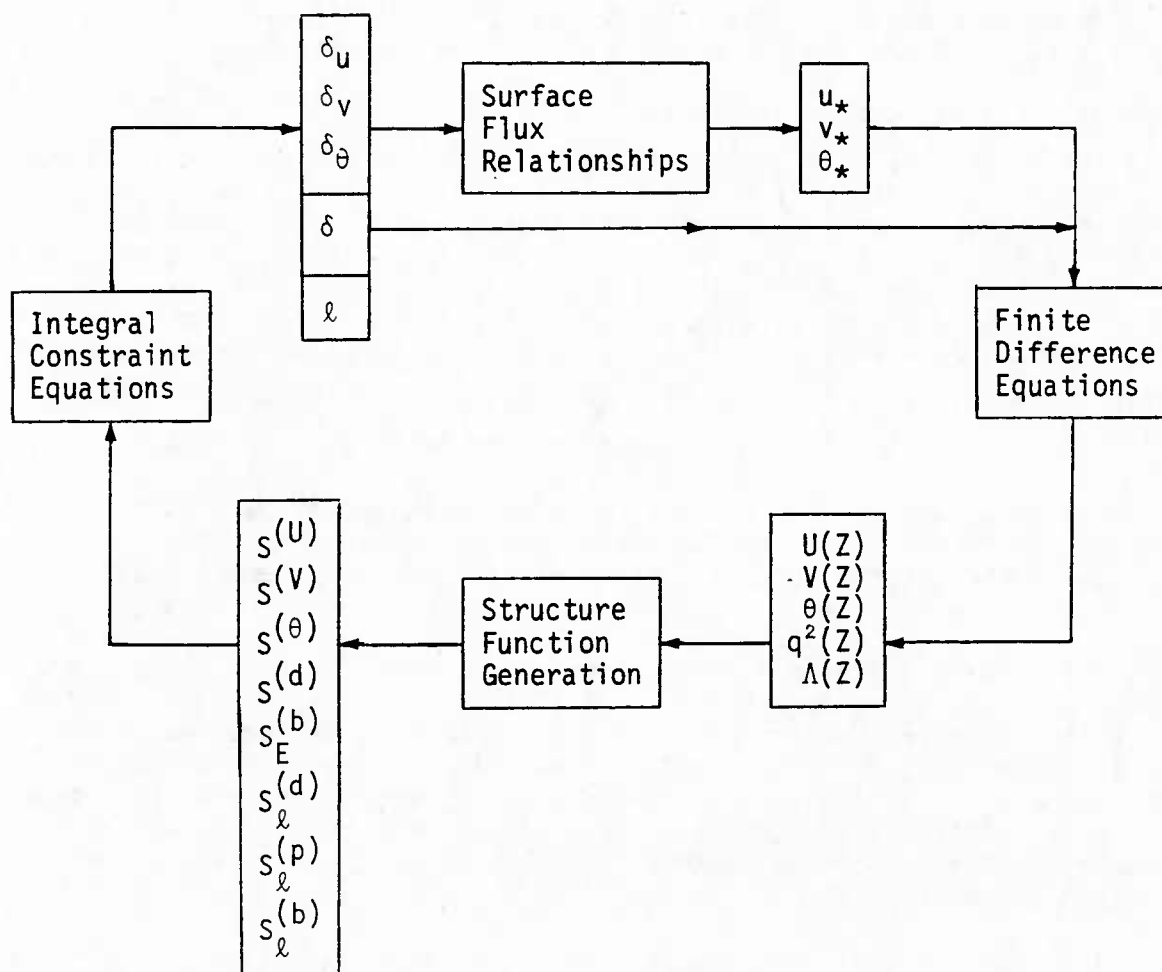


Figure 3.1 - Information flow in hybrid integral-differentiation description of the PBL.



### 3.4 Illustrations

#### 3.4.1 PBL Subjected to Unsteady Forcing

As a basis for illustration we consider a particular unsteady problem for the neutral PBL. These problems will involve ramp transitions of the inviscid region velocity from one steady state level to another. If  $U_{\infty}(0)$  is the initial steady state and  $U_{\infty}(1)$  is the final steady state, the ramp transition is defined by

$$U_{\infty}(t) = \begin{cases} U_{\infty}(0) & t < t_0 \\ U_{\infty}(0) + \frac{U_{\infty}(1) - U_{\infty}(0)}{\tau} f(t - t_0) & t_0 < t < t_0 + \tau f^{-1} \\ U_{\infty}(1) & \tau f^{-1} < t \end{cases} \quad (3.102)$$

The transient is specified by the parameters  $U_{\infty}(0)$ ,  $U_{\infty}(1)$ ,  $\tau$ . The general problem is: A boundary layer in steady state corresponding to an inviscid velocity  $U_{\infty}(0)$  is subjected to a linearly increasing inviscid velocity over a time period  $\tau f$  until it reaches a value  $U_{\infty}(1)$  at which point the velocity remains fixed at the new steady state value  $U_{\infty}(1)$ . Determine the motion within the PBL. As such, this problem allows us to study the neutral PBL subject to both Coriolis effects and unsteady forcing.

The geostrophic conditions ( $U_g$ ,  $V_g$ ) are established so that for all time,

$$U_{\infty} = U_{\infty}(t) \quad V_{\infty} = 0 \quad (3.103)$$

We select conditions exhibited in Table 3.4.1. It should be observed that these conditions describe a very severe transient in that the forcing frequency  $f(u)$  [Eq. (3.97)] is initially ten times greater than the Coriolis frequency  $f$ .

Table 3.4.1

Conditions for Neutral PBL Subjected to Ramp Transition

$$U_{\infty}(0) = 1 \text{ m/sec}$$

$$U_{\infty}(1) = 10 \text{ m/sec}$$

$$\tau = 1$$

$$f = 10^{-4} \text{ sec}^{-1}$$

The solutions for this problem are determined in three different ways. In the first, we utilize the standard A.R.A.P. second-order closure theory implemented in a fully finite-difference procedure utilizing of the order of 40 grid levels. The PBL response (as reflected in surface RMS turbulence and cross-isobaric angle) computed in this manner is shown in Figure 3.2. In the coordinates utilized, the Coriolis period is equal to  $2\pi$ . It can be seen that  $q_0$  makes an initially rapid transition (including an overshoot and undershoot) during the period of acceleration of the outer flow and then oscillates about its new level with the oscillation slowly damping. The angle particularly evidences higher harmonics of  $f$ . These result from the nonequilibrium rotational wave modes which are present in the turbulence equations.

In Figure 3.3 we show the response to the same problem as computed in the second manner: the hybrid procedure with no finite difference levels, i.e., the procedure in pure integral form. The integral model accurately exhibits the initial overshoot in  $q_0$  (but fails to give an undershoot), and then yields a similar decline over the period of acceleration. Because it does not contain dynamic equations for the full Reynolds stresses, the pure integral form of the hybrid model does not yield the higher harmonics of  $f$ , but only oscillates at the fundamental. The average angle response follows the full finite difference solution well but climbs more rapidly to the peak value following the period of outer flow acceleration.

In Figure 3.4 we show the response to the same problem as computed in the third manner: the hybrid procedure with 5 finite difference levels. The response is equally well predicted with a tendency for the first harmonic (but not a second) to appear in the angle response. We remark that the hybrid procedure with only 5 grid levels is somewhat sensitive to numerical instabilities in the following sense. If the profile computation over 5 points develops any significant errors, the degrading influence on the structure functions can feed back through the surface conditions and further degrade the profile structure near the surface.

Nonetheless, the hybrid procedure executes at least 8 times faster than the full finite difference procedure and as much as 40 times faster for the purely integral version. The good quality of these results, given the vast decrease in computer resources spent, seems highly worthwhile.

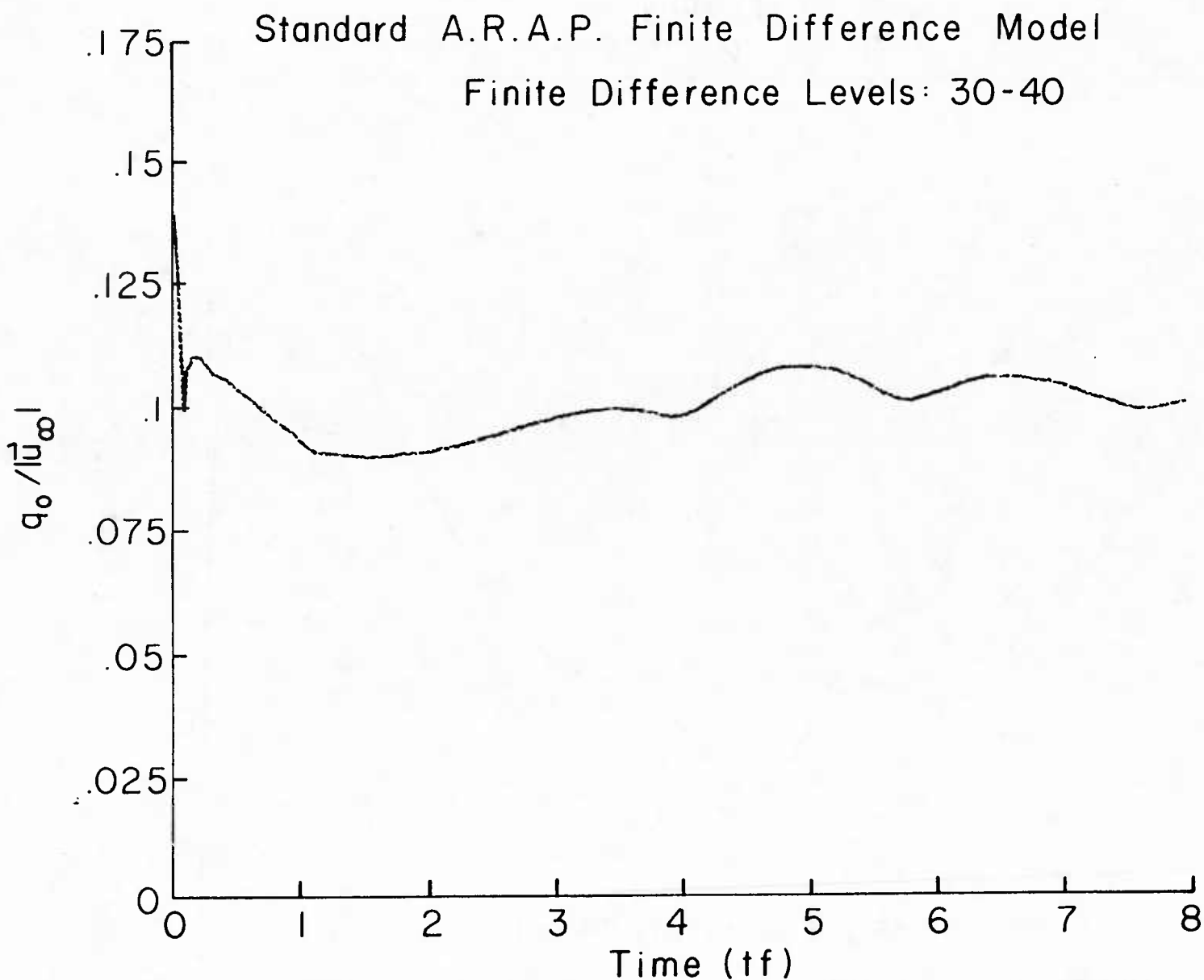


Figure 3.2(a). Surface RMS turbulence response to unsteady forcing of the PBL. Period of outerflow acceleration is from  $tf = 0$  to  $tf = 1$ . Standard ARAP finite difference model.

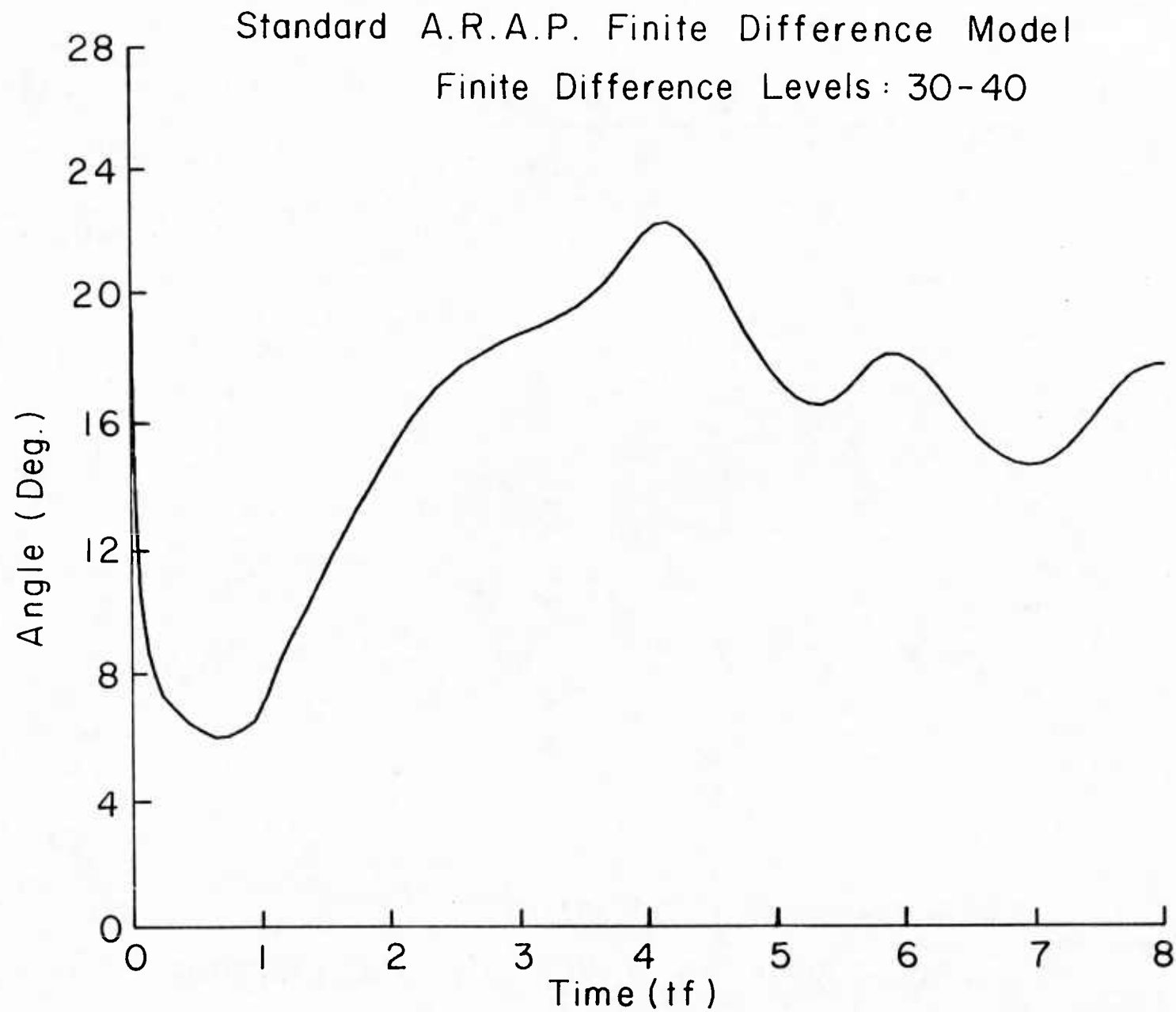


Figure 3.2(b). Cross isobaric angle for conditions of Figure 3.1(a).

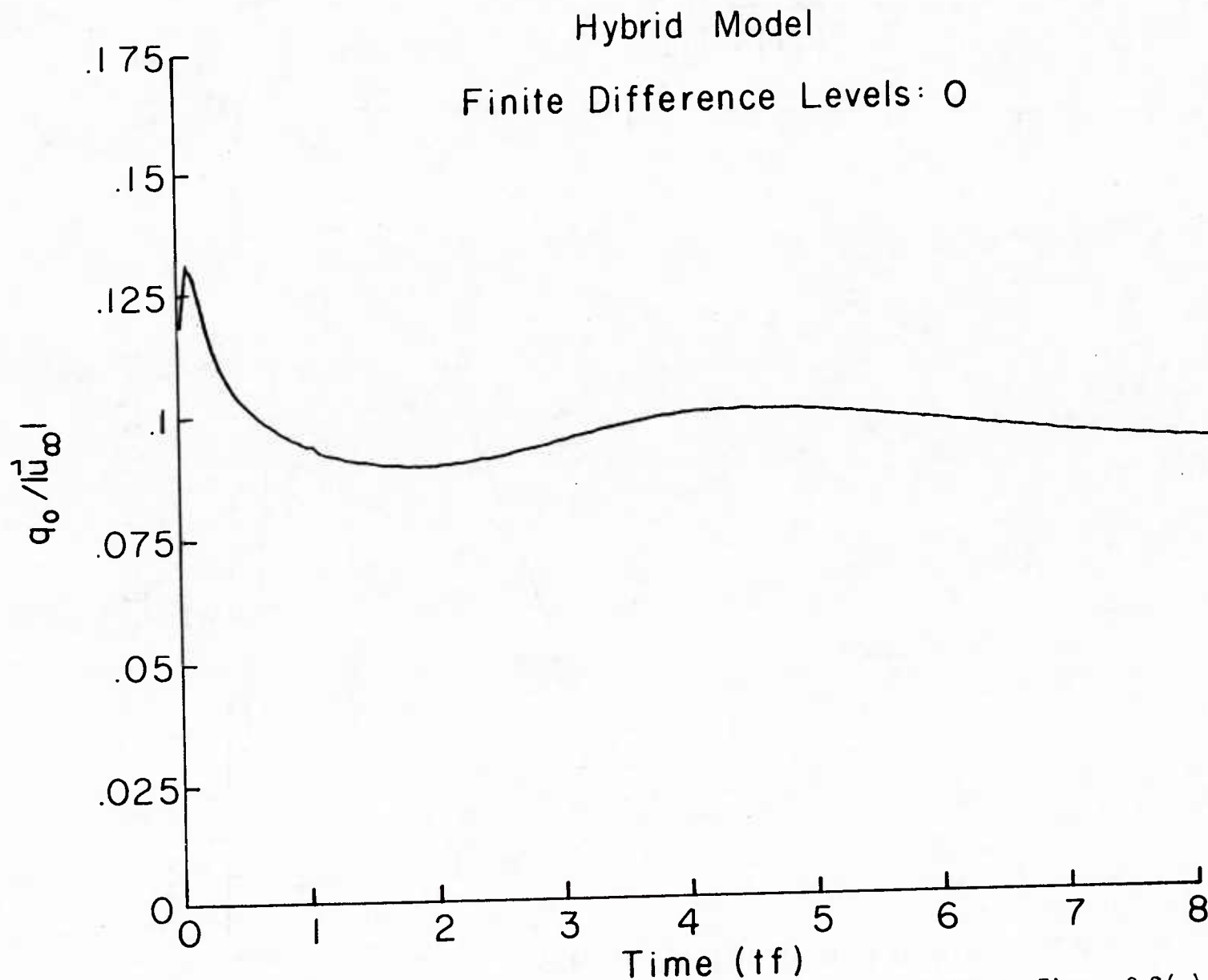


Figure 3.3(a). Surface RMS turbulence response corresponding to Figure 3.2(a) but with purely integral form of hybrid procedure.

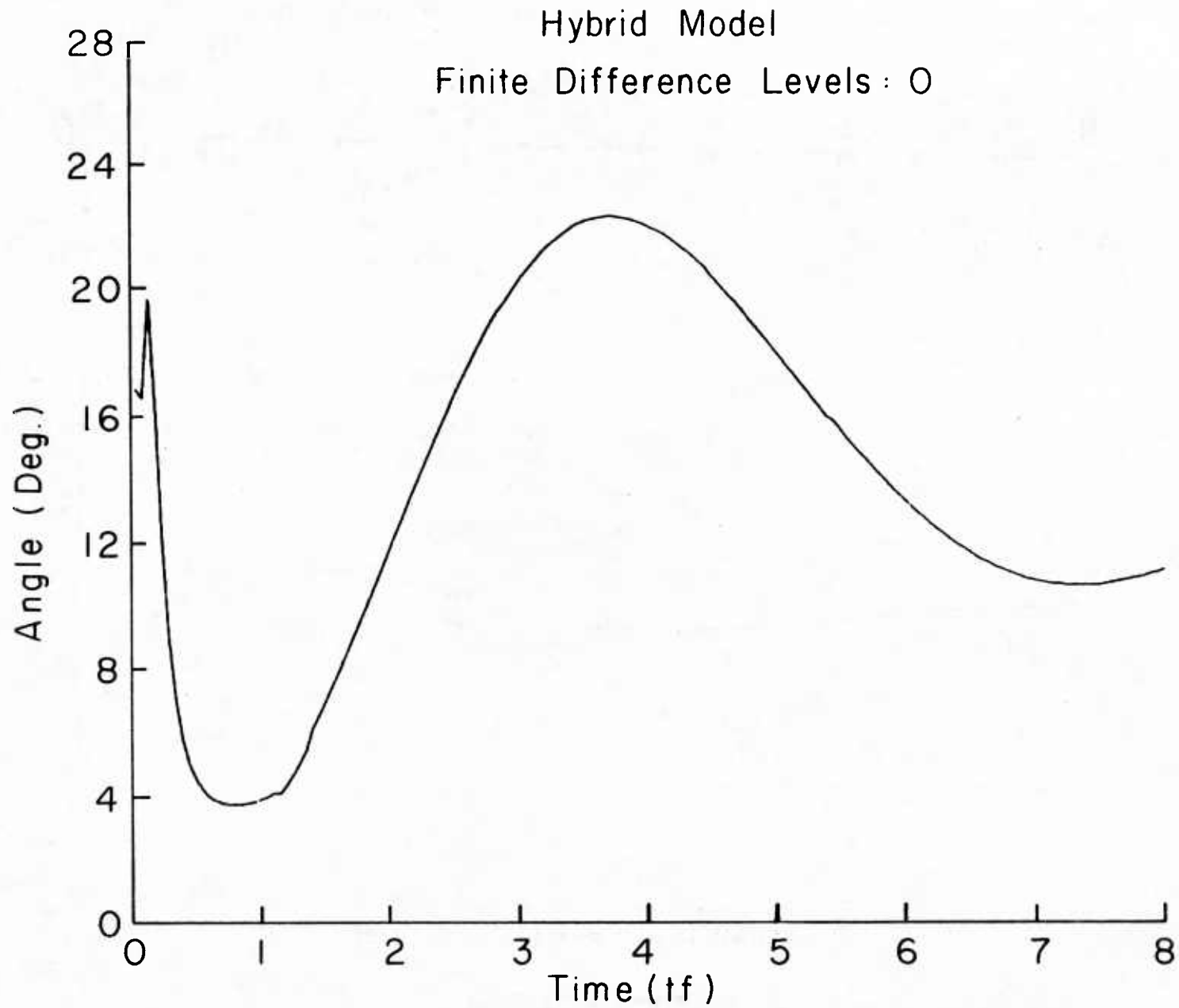


Figure 3.3(b). Cross isobaric angle for conditions of Figure 3.3(a).

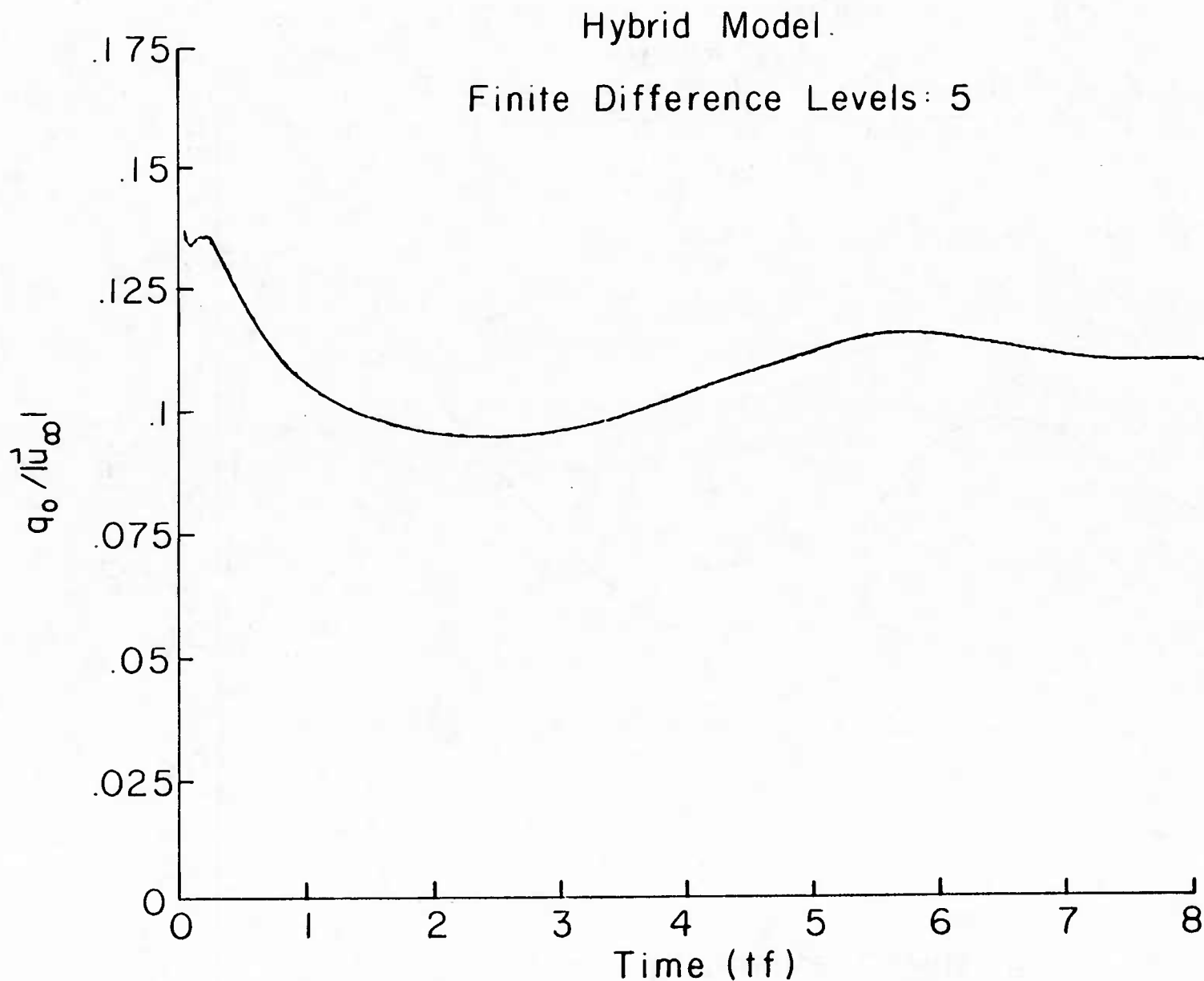


Figure 3.4(a). Surface RMS turbulence response corresponding to Figure 3.2(a) but with 5 grid level hybrid procedure.



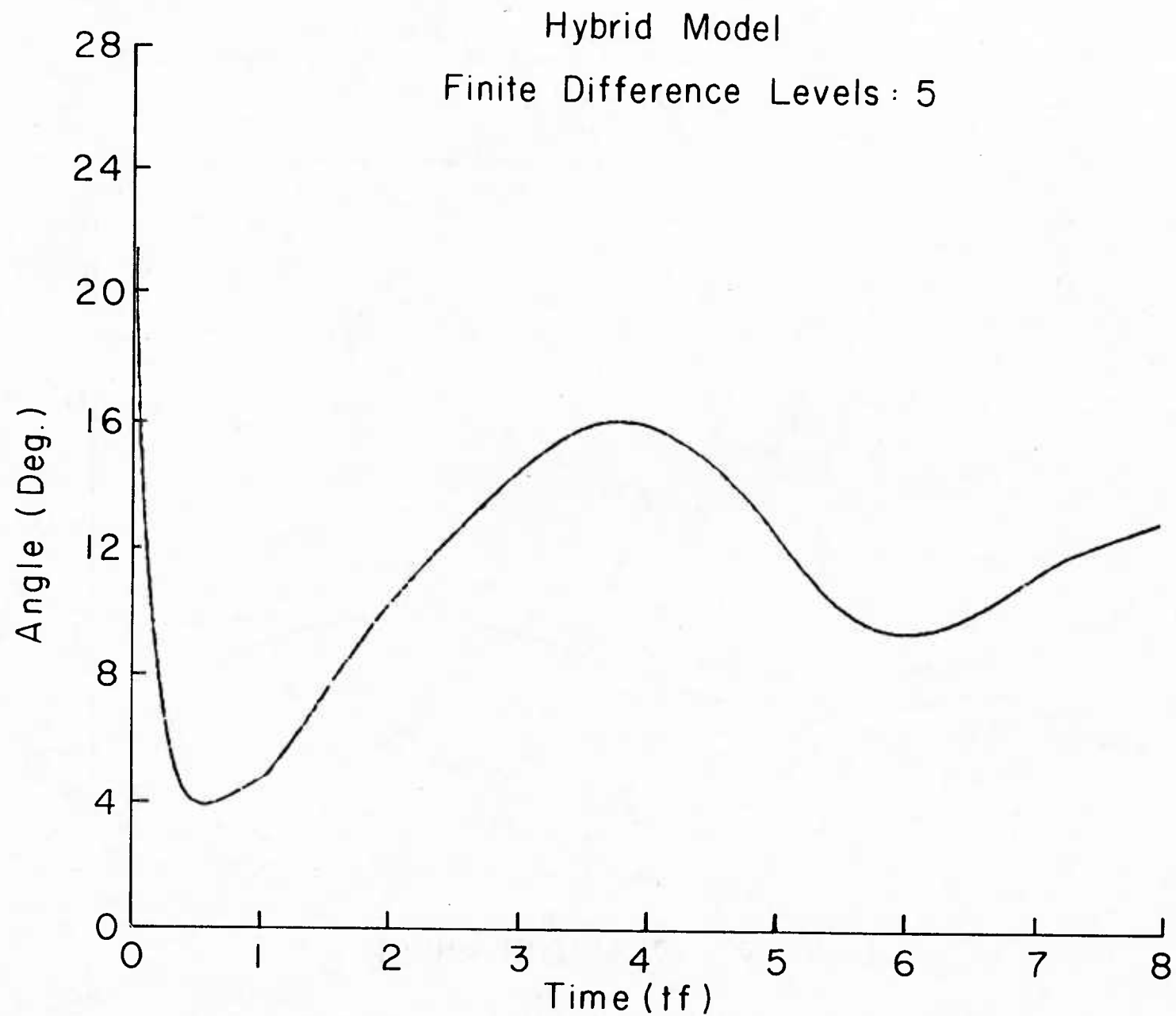


Figure 3.4(b). Cross isobaric angle for conditions of Figure 3.4(a).

### 3.4.2 Stable PBL Illustrations

As a second illustration, we consider the computation of stable PBL response. Our illustration for this case will be the archetypal problem of a constant surface cooling rate in which a quasi-steady boundary layer is established (References 25-27). We begin with an equilibrium neutral PBL at time  $t = 0$  at which time a constant surface cooling rate is applied. After a period of several Coriolis periods, the quasi-steady state is established. The computation illustrated here is for the purely integral version of the hybrid procedure. The conditions for the illustration are presented in Table 3.4.2.

Table 3.4.2  
Conditions for Constant Surface Cooling  
Rate Stable PBL Illustration

$ \vec{U}_\infty $	10 m/sec
$z_0$	$10^{-2}$ m
$f$	$10^{-4}$ sec $^{-1}$
$\frac{d\theta_0}{dt}$	1 K/hr
$S^{(U)}$	0.8
$S^{(V)}$	3.0
$S^{(\theta)}$	0.6
$S_E^{(d)}$	0.15
$S_E^{(b)}$	0.5
$S_\ell^{(d)}$	0.20
$S_\ell^{(p)}$	0.0125
$S_\ell^{(b)}$	0.4
$r$	0.35

The evolution of the boundary layer for these conditions is shown in Figure 3.5. After a transient of approximately 2 Coriolis periods the characteristic boundary layer parameters approach quasi-steady values. These quasi-steady values are consistent with those predicted in Reference 25. The hybrid model indicates an initial undershoot in cross-isobaric angle of  $-15^\circ$  before evolving to a steady state values of approximately  $50^\circ$ . This steady state value is about  $10^\circ$  larger than that predicted in Reference 25; no attempt has been made to fine-tune the values of the structure functions in these illustrations to effect more exact comparisons. The value of the

Zilitinkevich parameter  $d = \delta \sqrt{f / |\vec{u}_*|} L$  is shown in Figure 3.5(e) and its value of 0.44 at quasi-steady state is closely consistent with that of Reference 24 and 25.

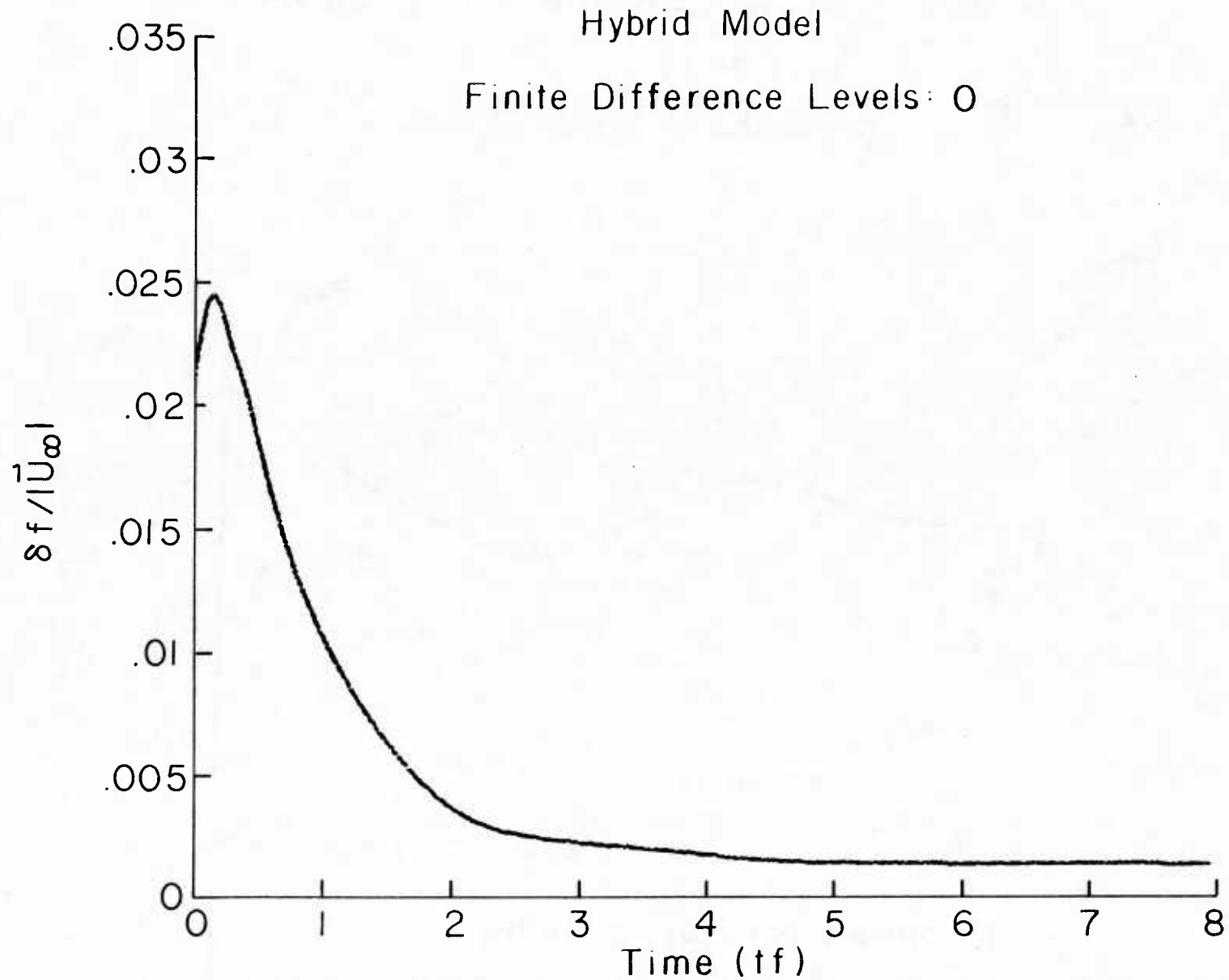


Figure 3.5(a). Boundary layer thickness of response following onset of a constant surface cooling rate corresponding to the condition of Table 3.4.2.

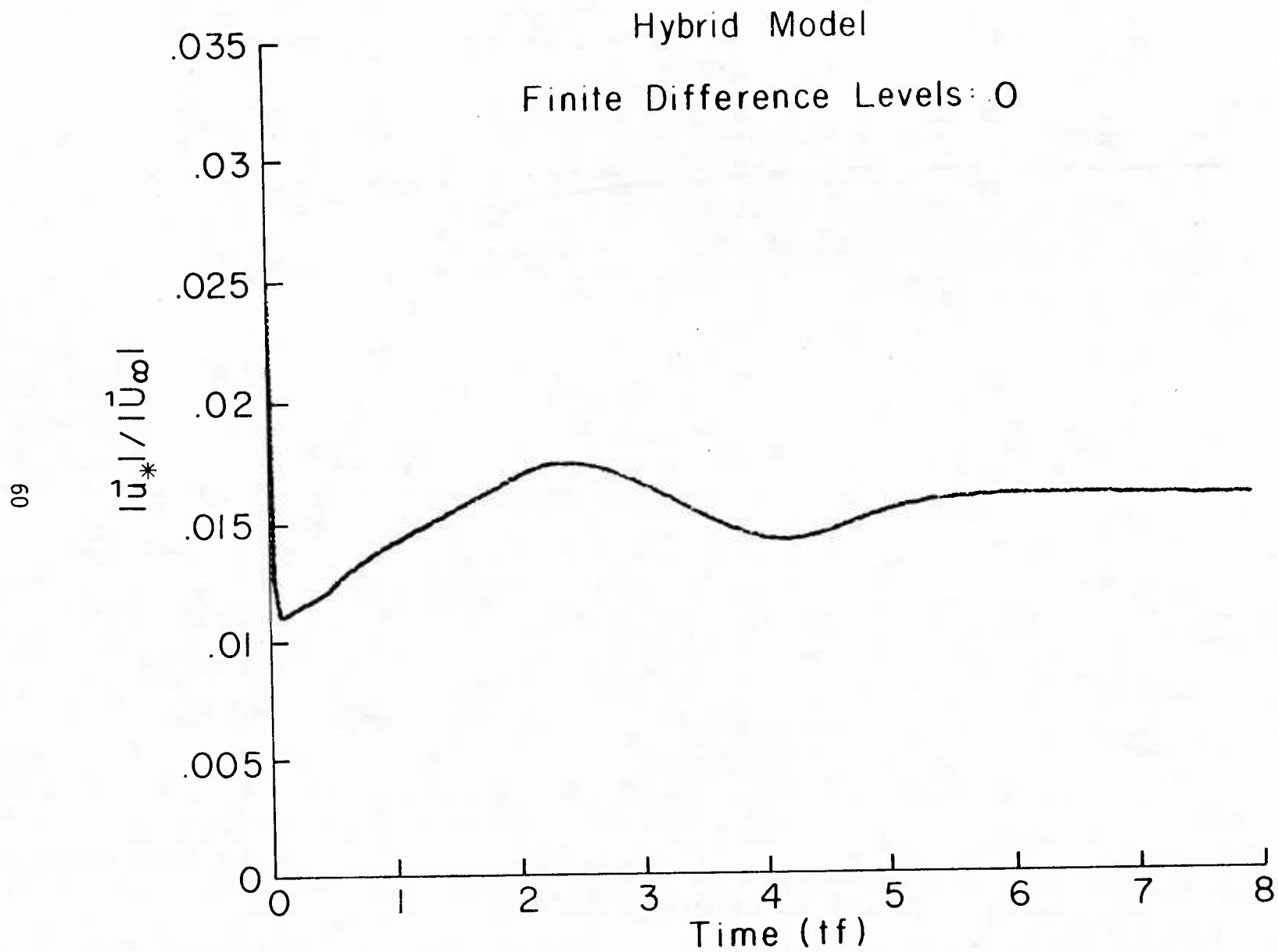


Figure 3.5(b). Surface shear velocity corresponding to Figure 3.5(a).

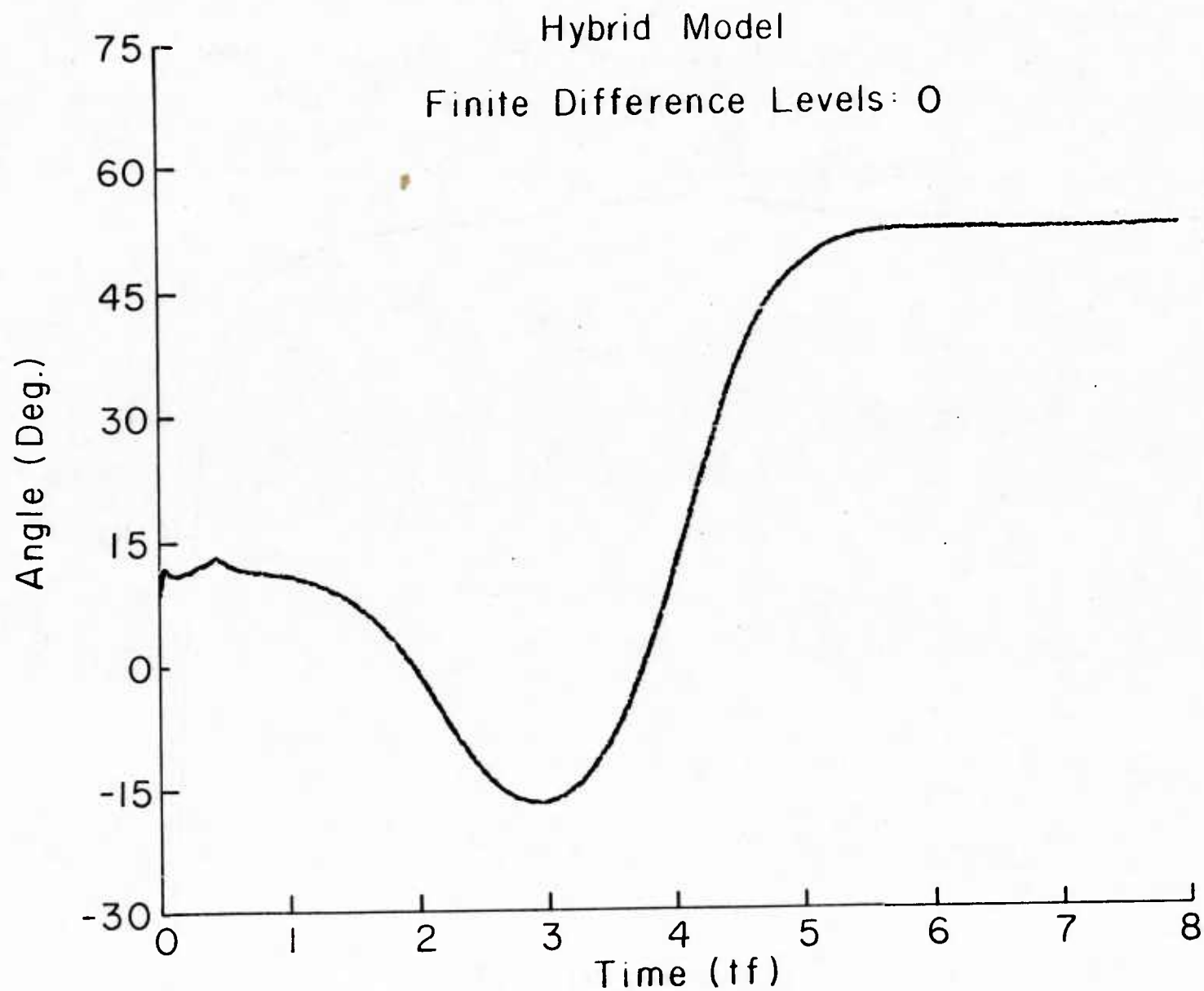


Figure 3.5(c). Cross-isobaric angle response corresponding to Figure 3.5(a).

Hybrid Model

Finite Difference Levels: 0

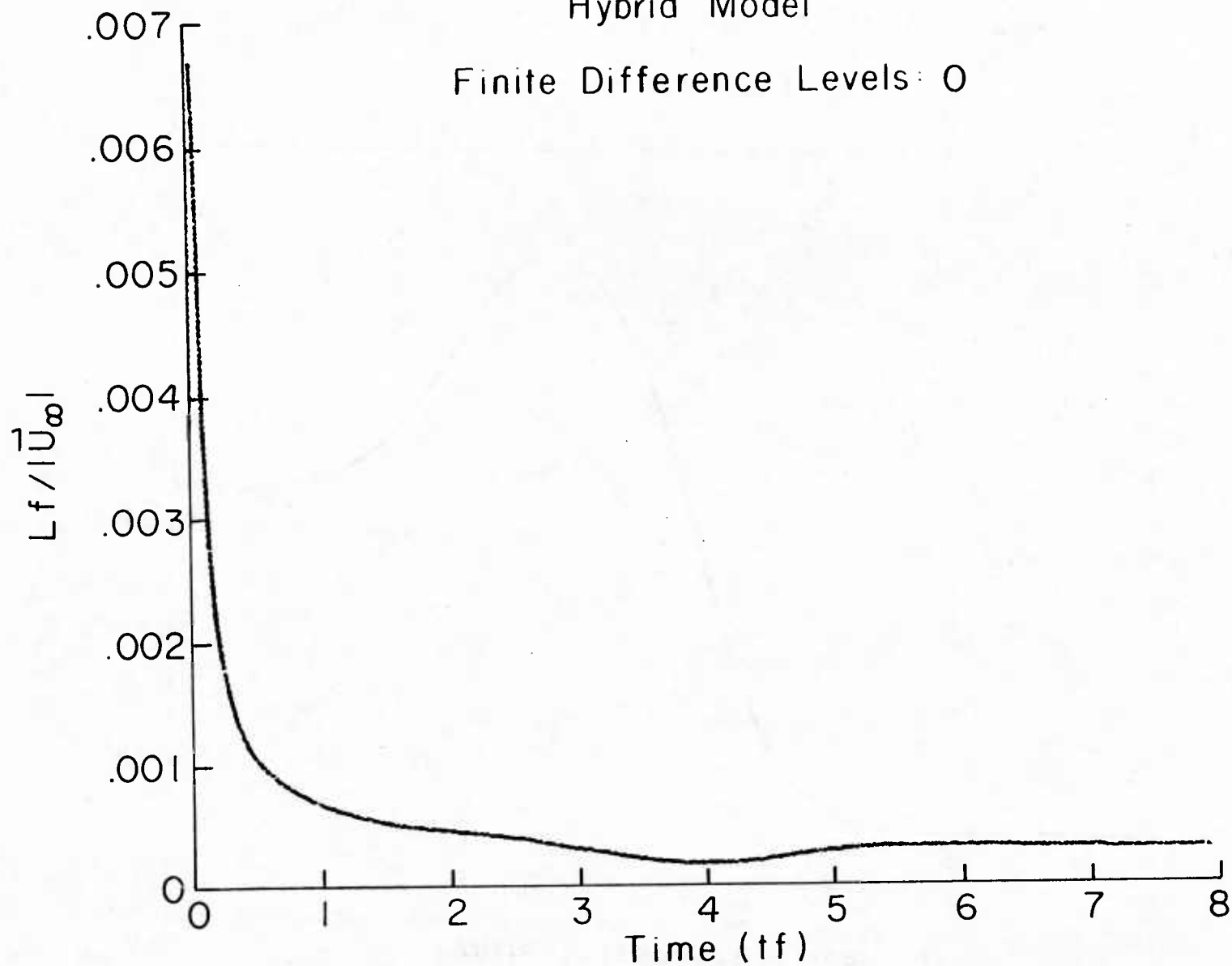


Figure 3.5(d). Monin-Obukhov length corresponding to Figure 3.5(a).



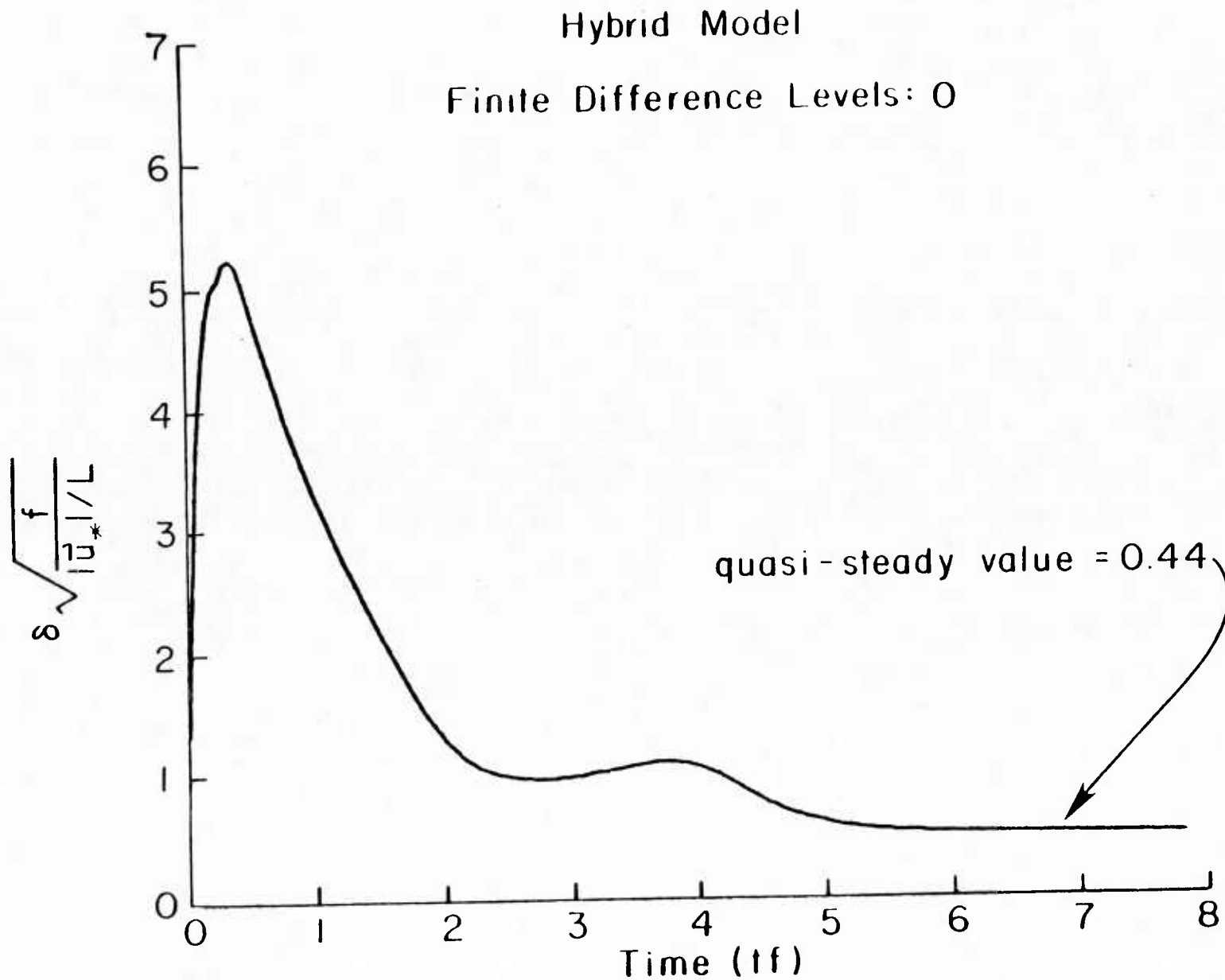


Figure 3.5(e). Zilitinkevich scaling parameter  $d$  corresponding to Figure 3.5(a).

#### 4. THE INTERACTION OF TURBULENCE WITH PRECIPITATION: FORMULATION OF A PRECIPITATION MODEL FOR THE PLANETARY BOUNDARY LAYER

##### 4.1 Introduction

Many of the atmospheric Planetary boundary layer (PBL) processes and episodes which are successfully describable in terms of a second order closure theory of turbulence such as that in use at ARAP (Reference 10) involve the transport, condensation, and evaporation of water. It is important that such models correctly describe the overall balance of water by the various evaporation, condensation, diffusion, and advection mechanisms. In some cases of interest, precipitation of cloud water in the form of rain or drizzle to the surface is an important process controlling the balance of water. In addition, precipitation is of interest in its own right; for it is desirable to predict the likelihood and magnitude of precipitation drizzle or rain events. In the present work we therefore present a discussion and model of precipitation for use in atmospheric PBL models. Because we restrict attention to the PBL, we consider only warm (non-freezing) precipitation and cloud droplet growth processes.

Following the stage of condensation growth in the early period of cloud formation (droplet radii  $r \lesssim 10 \mu\text{m}$ ), further growth of the cloud droplets to reach precipitation size is generally believed to occur by collisional coalescence of droplets. Gravitational sedimentation has received virtually the exclusive attention of theorists as the collisional coalescence mechanism of atmospheric clouds (References 28-30). There seems little doubt that the collisional coalescence of drops of different size is an important droplet growth mechanism at some stages of cloud evolution. On the other hand, in the early stages of growth ( $1 \lesssim r \lesssim 50 \mu\text{m}$ ) this mechanism possesses certain limitations. Two of these limitations are (1) the inherent requirement of differential size for a non-zero collision rate, and (2) the sharply diminished collision efficiencies which result for the vanishing relative Reynolds numbers of differential sedimentation when both collision partners approach the same size. These two limitations when viewed in the light of a further result from classical condensation theory - namely the narrowing of the droplet spectrum into a single size during condensation growth - suggest that collisional growth mechanisms other than gravitational sedimentation may play an important role in the initial growth stage of clouds into precipitation size drops. In particular, atmospheric turbulence may play an important and direct role in the evolution of the cloud drop spectrum.

We propose, therefore, to include in the collision mechanism of our precipitation model the effects of atmospheric turbulence in addition to classical gravitational sedimentation. There appear to be at least two unique ways in which turbulence affects the evolution of the cloud drop spectrum. The first is in the dynamics of condensation. Although classical condensation theory predicts a narrowing spectrum, (forcing a single size

cloud droplet) it appears that when condensation is considered in a turbulent environment, the spectrum may be broadened (References 31, 32). The second role is in the collisional growth stage in which the turbulent velocity field provides not one but several mechanisms for the collisions of drops.

In Section 4.2 we review the stages of condensation and growth processes for clouds pointing out the regimes in which turbulence can be of importance. In Section 4.3 we discuss in detail the turbulence collision mechanisms and develop the collision kernel for the processes of both turbulence induced collisions and gravitational sedimentation. In section 4 we present a two-group precipitation model based upon the growth mechanisms discussed in Section 4.3 which we term the Cloud-Precipitation (CP) model. In Section 4.5 we present some illustration calculations of the CP model for the infinite, homogenous cloud.

#### 4.2 Condensation, Evolution of the Cloud Droplet Spectrum, and Precipitation

To set the stage for the model we propose, we first review the various processes which take place from the onset of a water mixing ratio in excess of the saturation value to the final stage (if it occurs in the time scale of a particular problem) in which drops precipitate to the surface. We point out the role of turbulence in certain of these stages of development. The stages of drop evolution may be defined in the following scheme:

- |                                   |   |
|-----------------------------------|---|
| (1) The Nuclei Activation Stage   |   |
| drop (particle) size              | = $10^{-2} \mu\text{m} \lesssim r \lesssim 1 \mu\text{m}$ |
| time scale                        | = 1 sec. or less  |
| (2) The Condensation Growth Stage |   |
| drop size                         | = $1 \mu\text{m} \lesssim r \lesssim 10 \mu\text{m}$      |
| time scale                        | = 1-100 sec.  |
| (3) The Collisional Growth Stage  |   |
| drop size                         | = $10 \mu\text{m} \lesssim r \lesssim 10^3 \mu\text{m}$   |
| time scale                        | = $\gtrsim 100 \text{ sec. but highly variable}$          |
| (4) The Sedimentation Stage       |   |
| drop size                         | = $100 \mu\text{m} \lesssim r \lesssim 10^3 \mu\text{m}$  |
| time scale                        | = $10^{-3}$ -10 hours                                     |

Once the water mixing ratio exceeds the local saturation value, nuclei must be activated before water may condense in realistic time scales. Following nuclei activation, drops grow by the direct condensation of vapor and interact negligibly via collisions. In most atmospheric situations, the liquid water formed by the overall amount of excess saturation and the number of nuclei available and activated results in a cloud with drop number densities ranging from  $10^8$ - $10^9 \text{ m}^{-3}$  and radii ranging from 1 to  $10 \mu\text{m}$ . It should be noted that classical condensation theory predicts a spectrum evolution through the stages of nuclei activation and condensation growth which is progressively

narrowing (Reference 33) ultimately yielding a cloud in which all particles are the same size. Thus, in classical condensation theory, size differential in the cloud spectrum can only result from the residue of size differential of nuclei. A limited amount of work has been devoted to the examination of droplet evolution in the nuclei activation and condensation growth stages in a turbulent environment (References 31,32). Although the "turbulence" models used in these investigations are seriously over simplified, it does appear that turbulent condensation theory provides significant broadening of the droplet spectrum which can dominate over the "natural narrowing" of classical condensation theory. We have made some preliminary investigations of more rigorous turbulent, second order closure versions of the droplet kinetic equations and find both broadening and narrowing effects which can result from the turbulent correlations  $\overline{w'w'}, \overline{w'\theta'}$  where  $w$  is the vertical velocity,  $\theta$  the potential temperature, and an overbar denotes a turbulent ensemble average. We shall report on these investigations in subsequent publications.

For cloud droplets to grow significantly beyond the range of radii  $r \gtrsim 10 \mu\text{m}$  up to precipitation sizes, collisional coalescence processes must be operative. The time scale for these collisional processes are highly variable when turbulence induced collisions are included in addition to the gravitational sedimentation collisions of classical coalescence theory. We find this result (which will be discussed in Section 3) consistent with the highly variable nature of natural clouds to grow to rain or drizzle size drops. A critical feature of the collisional growth process is the creation of a small number of drops much larger than the average. This long tail effect in the distribution function is the result of the increasing collision cross-section of large drops.

The final stages of drop evolution occur when drops have grown significantly large enough to develop a significant precipitation velocity. These precipitable drops then leave the cloud and progress to the surface where they then leave the atmosphere.

The precipitation model we shall describe in section 4 in the present work treats the first two stages of cloud evolution described above in very simple parametric fashion. The collisional growth and sedimentation processes, however, will be treated in some mechanistic detail that includes the effects of turbulence upon collisional growth.

#### 4.3 Turbulence and the Collisional/Coalescence Process

We first consider the conceptual picture of atmospheric turbulence and its influence on the collisions of liquid drops embedded in such an environment. Atmospheric turbulence consists of the random motion of eddy structures ranging from the largest energy containing scales to the dissipation scales where molecular viscosity comes into play. The largest scale is of the order of the largest characteristic macro-length  $L$  (e.g. the PBL depth, terrain dimension, etc.) while the smallest scale is of the order of the Taylor micro-scale  $\lambda_0$ , defined in terms of the turbulence energy dissipation  $\epsilon = q^3/\Lambda$  as  $\lambda_0 = (\eta^3/\epsilon)^{1/4}$  where  $\eta$  is the molecular kinematic viscosity. Similarly, a micro-time characterizing the time scale of fluctuations of the dissipation can

be defined as  $\tau_0 = (\eta/\epsilon)^{1/2}$  and a micro-acceleration characterizing the acceleration of the flow field within the eddy as  $a_0 = \lambda_0/\tau_0^2$ . The magnitudes of these quantities for the range of turbulence dissipation rates encountered in the atmosphere are present in table 4.1.

Table 4.1  
Turbulence Length, Time, and Acceleration Scales in the Atmosphere  
for Dissipation Scale Eddies

$\epsilon$ ( $\text{m}^2/\text{sec.}^3$ )	$\lambda_0$ ( $\mu\text{m}$ )	$\tau_0$ ( $\text{ms}$ )	$a_0/g$ -
0.001	1510	130	0.009
0.01	846	42	0.05
0.10	476	13	0.28
1.0	268	4.2	1.58
10.0	151	1.3	8.9

Since drops of radius  $r$  will generally satisfy the condition  $r \ll L$ , the nature of turbulence induced collisions will turn first on the question of whether  $r > \lambda_0$  or  $r \leq \lambda_0$ .

It can be seen that even for the highest dissipation rates, only drops greater than about  $150 \mu\text{m}$  would be larger than the dissipation scale eddies. We conclude, therefore, that under most circumstances (and particularly for drop sizes in the critical range  $1 \leq r \leq 50 \mu\text{m}$ ) a cloud droplet will execute its collisional dynamics within a dissipation scale eddy. The precise nature of the flow field within a dissipation scale eddy is not clearly understood at present; however, such flow fields must, of necessity, be characterized by a high shear rate.

The average shear rates in the dissipation scale eddy can be related to the turbulence dissipation as (Reference 34)

$$S \approx (\epsilon/\eta)^{1/2} = 1/\tau_0$$

The first effect of turbulence upon the collision rate of cloud drops is thus to place them in a shear flow of average shearing rate  $S$ . Thus, two drops of radii  $r_1, r_2$  lying within a collision cylinder will possess a relative velocity with respect to one another of magnitude

$$\Delta V^{(s)} \approx (r_1 + r_2) S$$

This collisional relative velocity mechanism, in contrast to that of gravitational sedimentation, does not require a size difference between the collisional partners.

The second effect of turbulence is to create an acceleration field  $a_0$  for the flow field of the drops in addition to that of gravity. Hence, differential size relative motion will be enhanced by the presence of the turbulent field.



The third effect of turbulence upon collisional encounter is for the drops with  $r \gtrsim \lambda_0$ . This regime is the most complex involving the complication of the flow field of eddy scales larger than the Taylor scale. A simulation of the collision dynamics which may in some respects model this regime with an arbitrarily varying background velocity field but with turbulence induced shearing neglected Almeida (Reference 35) indicates, as one would expect, the enhancement of collisional efficiencies of such drops due to the agitation of the background field. However, the collision efficiencies of such large drops are already much larger than the minimal levels characteristic of drops in the 1-50  $\mu\text{m}$  range even in the absence of turbulence. In addition, the critical range for growth of 1-50  $\mu\text{m}$  will be such that drops turbulently collide primarily by the shearing mechanism. We thus disregard the turbulence effects on drops with  $r > \lambda_0$  and include the effects of turbulence on the shearing rate and acceleration of the flow field surrounding drops within dissipation scale eddies.

Let us now consider the formulation of the collision kernel for the collisional encounters of such drops. The total collision rate per unit volume between two populations of drops of radius  $r_1$  and number density  $n_1$  and radius  $r_2$  and number density  $n_2$  may be expressed as

$$N = n_1 n_2 v_0(r_1, r_2)$$

where  $v_0(r_1, r_2)$  is the collision kernel. Five basic processes contribute to the collision kernel in the atmosphere. These are

1. Turbulent Shearing
2. Turbulent Accelerations
3. Gravitational Sedimentation
4. Brownian Motion
5. Electrostatic Attraction

In what follows, we restrict attention to the first three processes. Brownian motion is only expected to be important for particle sizes much smaller than the average cloud drop. No attempt is made to estimate the influence of electrostatic attraction.

The collision kernel  $v_0$  may be expressed as (Reference 36)

$$v_0^2 = v_1^2 + v_2^2 + v_3^2$$

Where  $v_1$ ,  $v_2$ ,  $v_3$  and the contributions of turbulence induced shearing, turbulence induced accelerations, and gravitational sedimentation respectively. These are expressed as

$$v_1 = \Delta V_{12}^{(s)} E_1(r_1, r_2) \pi r_{12}^2$$

$$v_2 = \sqrt{1.3} \frac{a_0}{g} \Delta V_{12}^{(g)} E_2(r_1, r_2) \pi r_{12}^2$$

$$v_3 = \Delta V_{12}^{(g)} E_3(r_1, r_2) \pi r_{12}^2$$

In the above  $\Delta V_{12}^{(s)}$  is the effective relative velocity of the drops due to the shearing motion of the fluid expressed in terms of the shearing rate  $S$ :

$$\Delta V_{12}^{(s)} = r_{12} S \frac{1.3}{\pi}$$

where  $S$  is given in terms of the turbulent dissipation rate. The collision cylinder radius is  $r_{12} = (r_1 + r_2)$ . The relative velocity  $\Delta V_{12}^{(g)}$  is the difference between the terminal gravitational sedimentation velocities of the two particles:

$$\Delta V_{12}^{(g)} = |V_1 - V_2|$$

The form of  $V_i(r_i)$  depends upon the flow regime of the particles. In the Stokes range

$$V_i(r_i) = \left( \frac{\rho_0}{\rho_\infty} - 1 \right) \frac{2}{9} \frac{g}{\eta} r_i^2$$

where  $\rho_0, \rho_\infty$  are the densities of drop liquid and surrounding fluid respectively and  $\eta$  is the kinematic viscosity of the surrounding fluid. The quantities  $E_1, E_2, E_3$  are the collision efficiencies for each of the processes respectively. These are defined in terms of the cross-sectional area  $Q$  perpendicular to the relative velocity vector  $\Delta V_{12}$  within which the centers of the drops must lie if they are to collide compared to the geometrical hard sphere collision cross-section of the two drops:

$$E_i = \frac{Q_i}{\pi r_{12}^2}$$

Although it is not indicated functionally, the collision efficiencies  $E_i$  are functions of the radius ratio of the colliding drops and the relative Reynolds number. For gravitational sedimentation, this number depends purely upon the radii  $r_1, r_2$ . For shearing motion, however, the efficiency depends upon the shearing rate as well as the radii  $r_1, r_2$ . The collision efficiency  $E_3$  in the absence of turbulence is summarized in Reference 37. There are, as yet, no reliable calculations or measurements of the efficiencies  $E_1, E_2$  (or correspondingly an overall efficiency which depends upon shearing rate) although the work in Reference 38 is noteworthy.

We thus may summarize the three collisional processes of interest here by noting that of the three, shearing collisions are the only ones which are operative among drops of equal size; hence turbulence provides a mechanism (outside of the Brownian range) of coagulating drops of equal size which is otherwise not available in the more conventional gravitational sedimentation picture of collisional coagulation.

#### 4.4 The Cloud Precipitation (CP) Model

##### 4.4.1 The Division of Liquid Water Into Cloud and Precipitation Groups

As described in section 2, the collisional evolution of the droplet spectrum of the cloud is such that a small number of larger droplets are created and characterized as the tail of the cloud distribution. Because the droplet sedimentation velocity is a strong function of particle size, it is not useful to characterize the precipitation flux as an average over the entire liquid water distribution. This is because the bulk of the droplets have negligible sedimentation velocities. Rather, it is useful to define a precipitation group as those particles with sedimentation velocities greater than a certain minimum value. This minimum value cannot be given by the cloud micro physical process, but is determined by the overall macro-dynamics of the problem at hand. This sedimentation velocity is selected so that a drop will fall over a characteristic macro-length in some characteristic macro-time. We thus select (as a model parameter for the precipitation process) a sedimentation velocity (or corresponding particle size) which separates cloud droplets (whose contribution to the sedimentation flux we neglect) from drizzle or rain drops (which constitute the full precipitation flux.) Let us designate this velocity as  $V_*$  and the corresponding particle radius as  $r_*$ . Since most dynamical events within the PBL take place on a length scale of the order of  $10^3\text{m}$  or less and on a time scale of the order of 1 hr. we find the minimum precipitation velocity should be greater than or equal to about  $1\text{km/hr}$  which corresponds to the sedimentation velocity of a particle of  $r_* \approx 50\text{ }\mu\text{m}$  in still air. The total liquid water is thus divided into two groups: a cloud group consisting of all droplets with sizes  $r < r_*$  and a precipitation group with sizes  $r > r_*$ . Let us now specify the various collisional and condensation processes which take place between these two groups.

We choose not to describe the details of nuclei activation and the dynamics of cloud spectrum formation. These processes may be summarized in terms of two model parameters: the average cloud droplet radius  $R_C$  and the non dimensional dispersion of the cloud spectrum  $\sigma_C$ . For the present model, we choose to consider the limit  $\sigma_C = 0$  and to specify  $R_C$  as the single cloud-type parameter which for virtually the full range of cloud types lies in the range  $5\text{ }\mu\text{m} < R_C < 20\text{ }\mu\text{m}$ . Thus, given the total liquid water present as cloud, the cloud droplet number density  $n_C$  is implied in terms of the cloud droplet average radius  $R_C$ . It also becomes clear that in addition to the usual conservation equations for total liquid water, two additional conservation equations are required to determine the precipitation water content and the number density (or average size) of precipitation drops.

With the cloud droplet variables  $n_C, R_C$ , so determined, three collisional interaction processes and an evaporation process, then emerge which define the precipitation drop group characteristics. These three collisional processes are the cloud-cloud collisions, cloud-precipitation collisions, and precipitation-precipitation collisions. Cloud-cloud collisions whose



coalescences result in drops with radii greater than  $r_*$  constitute the cloud - to - cloud precipitation conversion process. Cloud-precipitation-precipitation collisions constitute the precipitation aggregation process. This latter process is only important in situations when the precipitation drop number density is very large. When precipitation drops exist in otherwise unsaturated air, evaporation of the precipitation drops takes place, and we term this process the precipitation evaporation process.

#### 4.4.2 Cloud and Precipitation Variables and Conservation Equations

The usual mixing ratios are given in terms of the average droplet sizes  $R_C$ ,  $R_p$  and number densities  $n_C$ ,  $n_p$  for cloud and precipitation groups respectively as

$$\begin{aligned} H_V &= \rho_V / \rho_\infty \\ H_C &= 4/3 \pi R_C^3 \rho_0 / \rho_\infty n_C \\ H_p &= 4/3 \pi R_p^3 \rho_0 / \rho_\infty n_p \\ H_\ell &= H_C + H_p \\ H &= H_V + H_\ell \end{aligned} \quad (4.1)$$

In Eqs. (4.1)  $\rho_V$  is the mass density of water in the vapor phase, while  $\rho_0$  is the mass density of the liquid water, and  $\rho_\infty$  is the mass density of the mixture. The mixing ratio for vapor is  $H_V$ , that of cloud water  $H_C$ , and that of precipitation water  $H_p$ . The total liquid mixing ratio is  $H_\ell$  and the total water mixing ratio is  $H$ .

The relationship between the constituents is as follows. If the mixture is unsaturated ( $H < H_S$ ), then

$$\begin{aligned} H_C &= 0 \\ H_\ell &= H_p \\ H_V &= H - H_\ell \end{aligned} \quad (4.2)$$

In these statements it is assumed that the cloud droplets are in equilibrium with the vapor; the precipitation drops need not be in equilibrium. If the mixture is saturated ( $H > H_S$ ) then

$$\begin{aligned} H_V &= H_S \\ H_C &= H - H_S - H_p \\ H_\ell &= H_C + H_p \end{aligned} \quad (4.3)$$

For the general case, we may thus write

$$\begin{aligned}
H_c &= (H - H_s - H_p) \mathcal{H}(H - H_s) \\
H_\ell &= H_c + H_p \\
H_v &= H - H_\ell
\end{aligned} \tag{4.4}$$

Where  $\mathcal{H}(x)$  is the Heaviside function.

It will be noted that in addition to the saturation mixing ratio  $H_s$ , the water-air mixture system possesses two degrees of freedom as we have constructed it consisting of cloud drops and rain drops. If  $H$  and  $H_p$  are specified, all the water species variables are determined. In general we shall utilize  $H$  and  $H_p$  as the two independent variables which determine the various water species variables. It can be readily seen that these variables are sufficient to fix the values of  $H_v$ ,  $H_c$ , and  $H_\ell$ .

The precipitation drop number density conservation statement is

$$\frac{Dn_p}{Dt} + \frac{\partial}{\partial x_i} (n_p v_{pi}) = N_{cp} - N_{pa} \tag{4.5}$$

In the above  $v_{pi}$  is the average sedimentation velocity of the precipitation drops. The production of precipitation drops from cloud droplets by the cloud to precipitation conversion process is  $N_{cp}$ . The loss of precipitation drops by self-collisions among the precipitation drops is  $N_{pa}$ .

The conservation equation of precipitation water is

$$\frac{DH_p}{Dt} + \frac{\partial}{\partial x_i} (H_p v_{pi}) = \dot{H}_{cp} + \dot{H}_{cc} - \dot{H}_{pe} \tag{4.6}$$

The production rate of precipitation water by the cloud to precipitation conversion process is  $\dot{H}_{cp}$ . The production of precipitation water by the cloud collection process is  $\dot{H}_{cc}$ . The loss of precipitation water by evaporation of precipitation drops in unsaturated air is  $\dot{H}_{pe}$ . The various rates  $N_{cp}$ ,  $N_{pa}$ ,  $\dot{H}_{cp}$ ,  $\dot{H}_{cc}$ ,  $\dot{H}_{pe}$  are described in subsequent sections. Equations (4.5) and (4.6) provide the additional dynamical equations which fix the properties of the precipitation group, since these equations determine  $n_p$  and  $H_p$ , the average precipitation drop radius  $R_p$  is determined the third of Eqs. (4.1). The conservation equation of total water mixing ratio is modified by the presence of a precipitation flux and becomes

$$\frac{DH}{Dt} + \frac{\partial}{\partial x_i} (H v_{pi}) = 0 \tag{4.7}$$

#### 4.4.3 The Cloud Conversion to Precipitation (CP) Process

We now describe the CP process and develop expressions for the CP rates  $N_{cp}$ ,  $\dot{H}_{cp}$ . Let  $v$  be the volume of any given drop and let  $v_1$  be the volume of the smallest cloud drop under consideration. Then  $m = v/v_1 = (r/r_1)^3$  is a size specification parameter. The number density of drops of size

$m$  we denote as  $n_m$ . The total number of cloud droplets  $n_c$  and precipitation drops  $n_p$  are then given by

$$n_c = \sum_{m=1}^{m_*} n_m \quad n_p = \sum_{m=m_*+1}^{\infty} n_m \quad (4.8)$$

The distribution function of cloud droplets we denote as  $f_m = n_m/n_c$ . We may express the rate  $N_{cp}$  as

$$N_{cp} = n_c^2/2 \sum_{k=1}^{m_*} f_k f_{m_*-k} v(r_k, r_{m_*-k}) \quad (4.9)$$

where  $v(r_1, r_2)$  is the collision kernel discribed in section 4.3. The corresponding rate  $\dot{H}_{cp}$  is

$$\dot{H}_{cp} = (\rho_0/\rho_{\infty})(n_c^2/2) \sum_{k=1}^{m_*} (k+m_*-k) f_k f_{m_*-k} v(r_k, r_{m_*-k}) \quad (4.10)$$

which may be expressed as

$$\dot{H}_{cp} = (\bar{\rho}_0/\rho_{\infty}) m_* N_{cp} \quad (4.11)$$

A realistic calculation of the cloud to precipitation rate does require some information about the cloud droplet distribution function  $f_m$  since the size  $m_*$  lies in the tail region of the distribution.

There is one of the very few exact solutions to the collisional coalescence problem which provides a frame work for parameterization of the CP process. The solution for  $f_m(t)$  beginning with a single size of cloud droplets  $r_1$  at time  $t=t_0$  subject to a constant collision kernel  $v_0$  is (Reference 39)

$$f_m(t) = (1-T) T^{m-1} \quad (4.12)$$

where  $T$  is determined by the solution of

$$\frac{dT}{dt} = \omega_0 (1-T)^2 \quad (4.13)$$

with  $\omega_0 \equiv v_0 n_{co}/2$  where  $n_{co}$  is the number density of cloud droplets at time  $t=t_0$  when collisions become to be more important than condensation growth in determining cloud droplet size. Substituting the form (4.12) into the CP rate expression (4.9) we find

$$N_{cp} = n_c^2 m_* v_0 (1-T)^2 T^{m_*-2} \quad (4.14)$$

we shall use this result as the basis for this simplified two group model by adopting the forms for  $N_{cp}$  and  $\dot{H}_{cp}$  given by Eqs. (4.11) and (4.14) with the following provisions:

- (1) The choice of  $v_0$  becomes an effective parameter of the model. Loosely speaking, it should be selected as an "average" collision kernel over the range  $1 \leq m \leq m_*$
- (2) For purposes of describing the conversion to precipitation rate, the cloud droplet spectrum is approximated as originating as a single size at the radius  $r_1 = R_c$

#### 4.4.4 The Cloud Collection (CC) Process

The collisional interaction of precipitation drops with cloud droplets, we assume, results only in coalescences which enter the precipitation group. The cloud collection rate  $N_{cc}$  is then formally defined as

$$N_{cc} = n_c n_p \sum_{m=1}^{m_*} \sum_{k=m_*+1}^{\infty} f_m f_k v(r_k, r_m)$$

We approximate this result as

$$N_{cc} = n_c n_p v(R_c, R_p) \quad (4.15)$$

#### 4.4.5. The Precipitation Evaporation Process

The evaporation of precipitation drops in unsaturated cloud-free air has to be considered to complete the processes that balance the liquid water existing as cloud droplets and as precipitation drops. The process is represented by the precipitation evaporation rate  $\dot{H}_{pe}$ . We assume that all precipitation drops evaporate at a rate given by that of a droplet at the average precipitation size  $R_p$ .

Let us now determine the rate  $\dot{H}_{pe}$ . The evaporation rate from a droplet of radius  $R_p$  in stagnant air may be expressed as

$$\left( \dot{H}_{pe} \right)_{\text{stag}} = 4\pi R_p D n_p (\rho_{v1} - \rho_{v\infty}) / \rho_{\infty} \quad (4.16)$$

where  $D$  is the diffusion coefficient,  $\rho_{v1}$  is the saturation vapor density at the surface of the particle and  $\rho_{v\infty}$  is the vapor density of the environment.

For a droplet in a convective flow, the evaporation rate is enhanced. Various correlations have been developed to model the increased evaporation and they are generally of the form

$$\left(\dot{H}_{pe}\right)_{\text{conv}} = \left(\dot{H}_{pe}\right)_{\text{stag}} (1 + C R_e^{\frac{1}{2}} S_c^{\frac{1}{3}}) \quad (4.17)$$

where the Reynolds number  $R_e$  is based upon the droplet diameter and sedimentation velocity relative to the air, and the Schmidt number,  $S_c$ , is for the vapor diffusion into the ambient. The coefficient  $C$  has the value  $C = 0.276$  recommended in Reference 40. The precipitation evaporation rate is then expressed as

$$\dot{H}_{pe} = 4\pi n_p \eta_p / S_c \left[ 1 + 0.276 \left( \frac{2VR_p}{\eta} \right)^{\frac{1}{2}} S_c^{\frac{1}{3}} \right] [H_s - (H - H_p)] \quad (4.18)$$

when

$$H < H_s \quad \text{and} \quad H_p > 0. \quad \text{When} \quad H > H_s, \quad \dot{H}_{pe} = 0.$$

#### 4.5 Illustration of the CP Model for the Homogeneous Cloud

Vertical inhomogeneity is an important aspect of any cloud and precipitation process. However, preliminary to incorporation with the general, turbulent, vertically inhomogeneous PBL model we may examine some of the characteristics of the CP model for a homogeneous cloud with given turbulence and liquid water inputs.

We thus consider a homogeneous cloud which at time  $t=0$  consists of a given amount of liquid water  $H_l$  existing completely as cloud water [ $H_p(t=0) \equiv 0$ ] with droplets of radius  $R_c$ . We consider the presence of a uniform precipitation flux divergence term which we represent as

$$\frac{\partial}{\partial x_i} (H_p V_{pi}) = H_p V_{pz} / \ell_c \quad (4.19)$$

where  $\ell_c$  is a modeling parameter for this homogeneous illustration only representing an equivalent characteristic vertical gradient. We further assume that the liquid water total  $H_l$  existing initially is not replenished by further decreases in saturation mixing ratio as water precipitates from the cloud.

To carry out specific calculations we must specify the values of the collision efficiency functions  $E_1, E_2, E_3$  and the average collision kernel  $v_0$  in the cloud-precipitation conversion rate, Eq. 4.14. We represent  $v_0$



as the geometric mean of the extreme kernels over the collision range of partners from  $r_1$  to  $r_*$ :

$$v_0 = \sqrt{v(r_1, r_1)v(r_1, r_*)} \quad (4.20)$$

This representation has the property  $v_0 \rightarrow 0$  as  $v(r_1, r_1) \rightarrow 0$  as indeed it should for the model in which the original cloud is considered to consist of single size droplets. For the collision frequencies, we assume  $E_2 \approx E_3$  since both involve differential settling velocities. We utilize the summary formulae that in Reference 41 for these collision efficiencies. A fundamental gap is the absence of data for collision efficiency  $E_1$  of drops colliding in the presence of shear. Although this efficiency should depend upon the relative Reynolds number of the colliding partners (and the shear rate), there seems to be a reasonable validation of data over a wide range of shear with a constant value  $E_1 = 0.36$  (Reference 41). We adopt this value for these illustrations.

The evaluations of the cloud and precipitation variables for a range of turbulence dissipation rates and for a nominal liquid water level for the conditions of Table 4.2 are shown in Figures 4.1 through 4.4. The general trends as well as detailed structure exhibited are consistent with model conditions of this illustration. We must emphasize, however, that these results must be viewed against the two fundamental conditions of the illustration: (1) Cloud water  $H_c$  and precipitation water  $H_p$  originate from a fixed total liquid water content  $H_L$  and (2) The cloud is homogenous with a precipitation flux divergence uniformly distributed over the cloud given by Eq. (4.19). All cases are terminated when the liquid water is reduced to 5% of the original cloud water.

The most basic and general trend in these illustrations is in the decrease of the time to reach a maximum precipitation drop number density as well as the time for onset of significant precipitation flux as the turbulence levels rise. This result is simply a manifestation of the increased conversion to precipitation rate  $N_{cp}$  as the turbulence collision rate increases. The second general trend is in the magnitude of the precipitation flux ranging from 0.08 cm/hr at the lowest turbulence level to 0.35 cm/hr at the highest turbulence level.

It should be noted that at the highest levels of turbulence ( $\epsilon = 10 \text{ m}^2 \text{ sec}^{-3}$ ) (Fig 4.5), a significant precipitation flux is established on the order of several tens of minutes. Such turbulence levels may be characteristic of the dynamics within cumulus clouds and it is of interest to examine the evolutions predicted here with those of a "standard" (albeit unverified) precipitation model for the cumulus cases (Reference 42). Kessler model results are shown in Fig 4.6 for the same illustration conditions of Figs 4.1-4.5: The time scales and general evolution seem comparable to the present model for turbulence levels  $\epsilon > 1 \text{ m}^2 \text{ sec}^{-3}$ . It should be noted, however, that the Kessler model inherently utilizes the Marshall-Palmer distribution function for rain drops as an empirical input characteristic of rain from cumulus clouds. The CP model has no such

empirical input restricting it to such cumulus parameterizations. Thus, in the absence of updraft, the high turbulence levels of the CP model generate precipitation of high number density and moderate size ( $R_p \approx 130\mu\text{m}$ ). We believe this is physically consistent with strong turbulence in the absence of updraft. With updraft present, the drops generated by the CP process would be maintained in contact with the cloud droplets for a longer duration before raining out and hence grow to larger size. Thus, while the Kessler model by virtue of its parameterization is incapable of describing the stratus case in absence of updraft, we believe the CP model when integrated with fluid dynamic mean motion including an updraft, would predict rain drop sizes consistent with the Kessler model and the Marshall-Palmer parameterization.

These illustrations indicate that the model and its parameters exhibit results in terms of time scales and magnitudes of precipitation sizes and fluxes which are consistent with those occurring naturally in the atmosphere. The turbulence levels which effect these results are typical of naturally occurring turbulence levels in the atmosphere.

Table 4.2

Conditions For Illustration of the CP Model For a Homogeneous Cloud

$r_*$	50 $\mu\text{m}$
$R_c$	10 $\mu\text{m}$
$H_l$	0.001 kg/kg
$l_c$	1 km

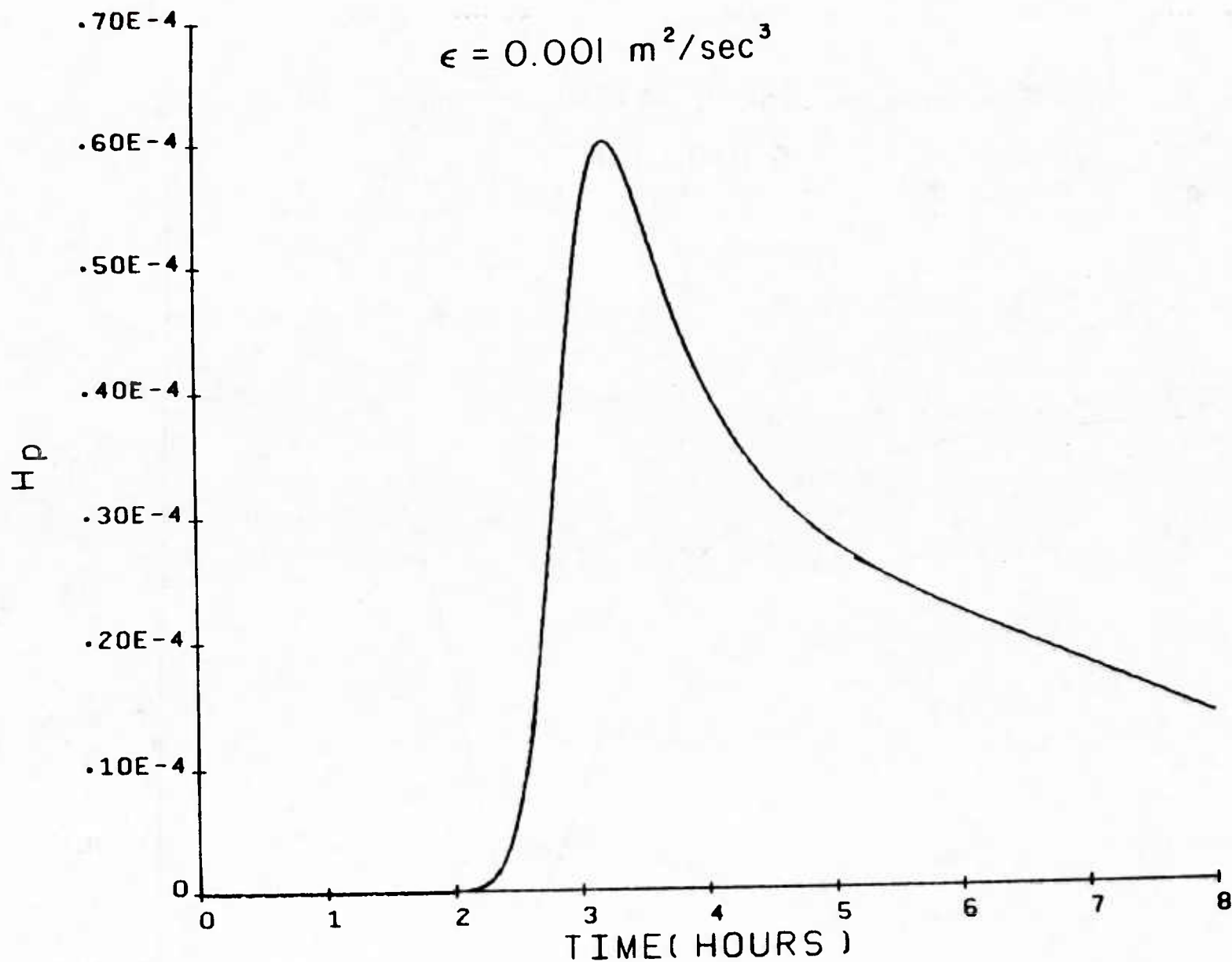


Figure 4.1(a). Evolution of precipitation water mixing ratio  $H_p$  for a homogeneous cloud with all water existing as cloud water  $H_c$  at time  $t = 0$ . Lowest turbulence level of these illustrations,  $\epsilon = .001 \text{ m}^2/\text{sec}^3$ .



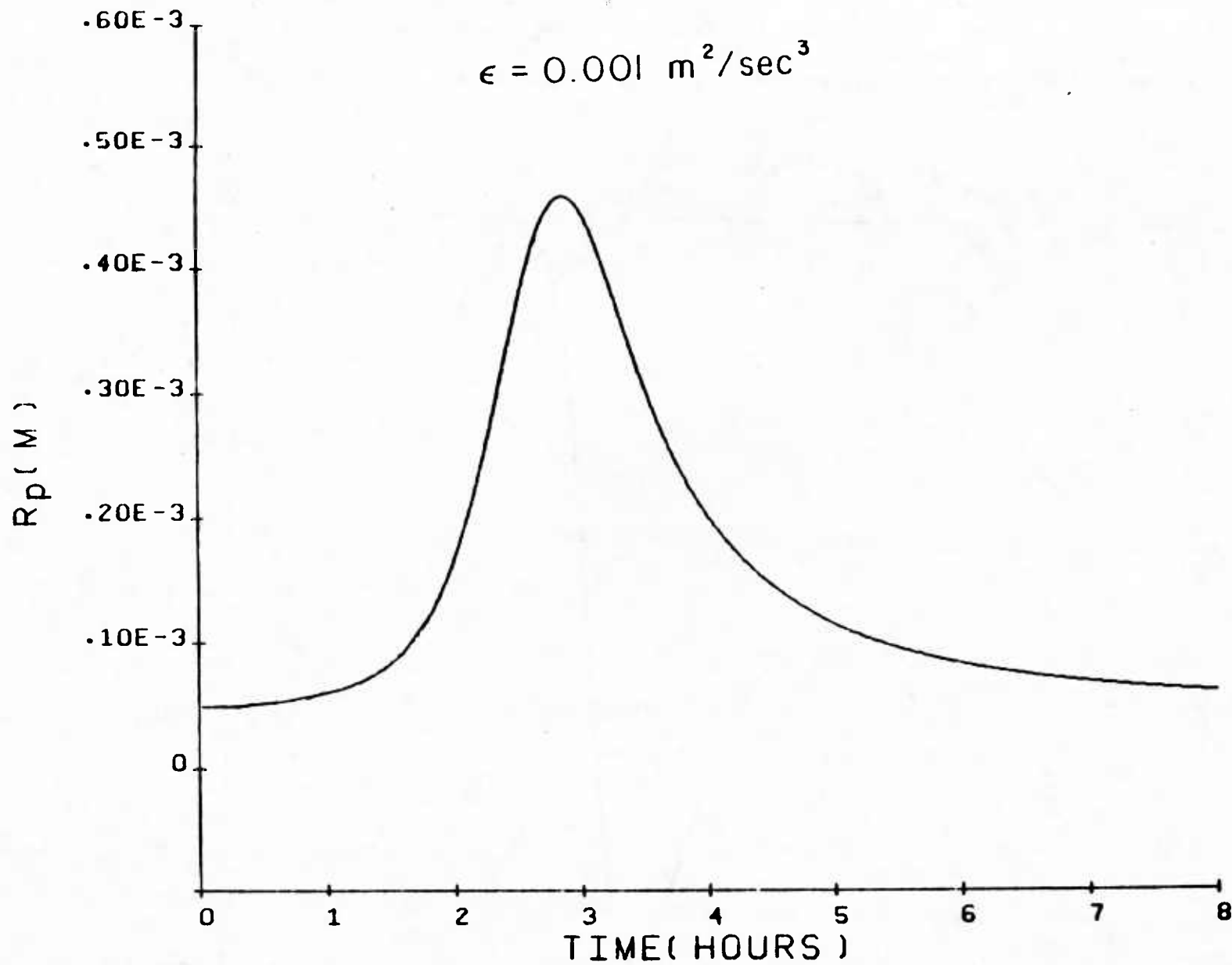


Figure 4.1(b). Evolution of average precipitation drop radius corresponding to Figure 4.1(a).

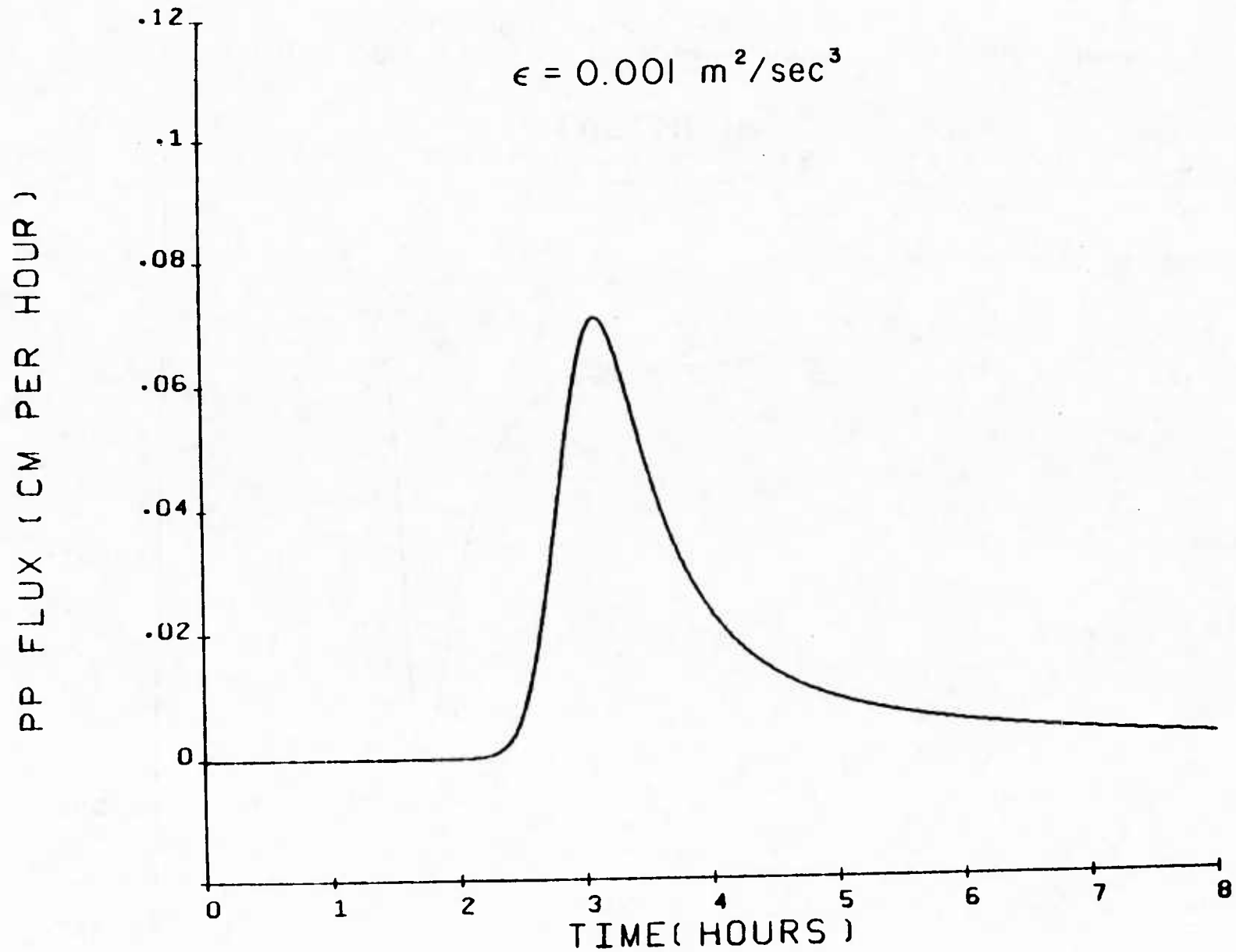


Figure 4.1(c). Evolution of precipitation flux corresponding to Figure 4.1(a).

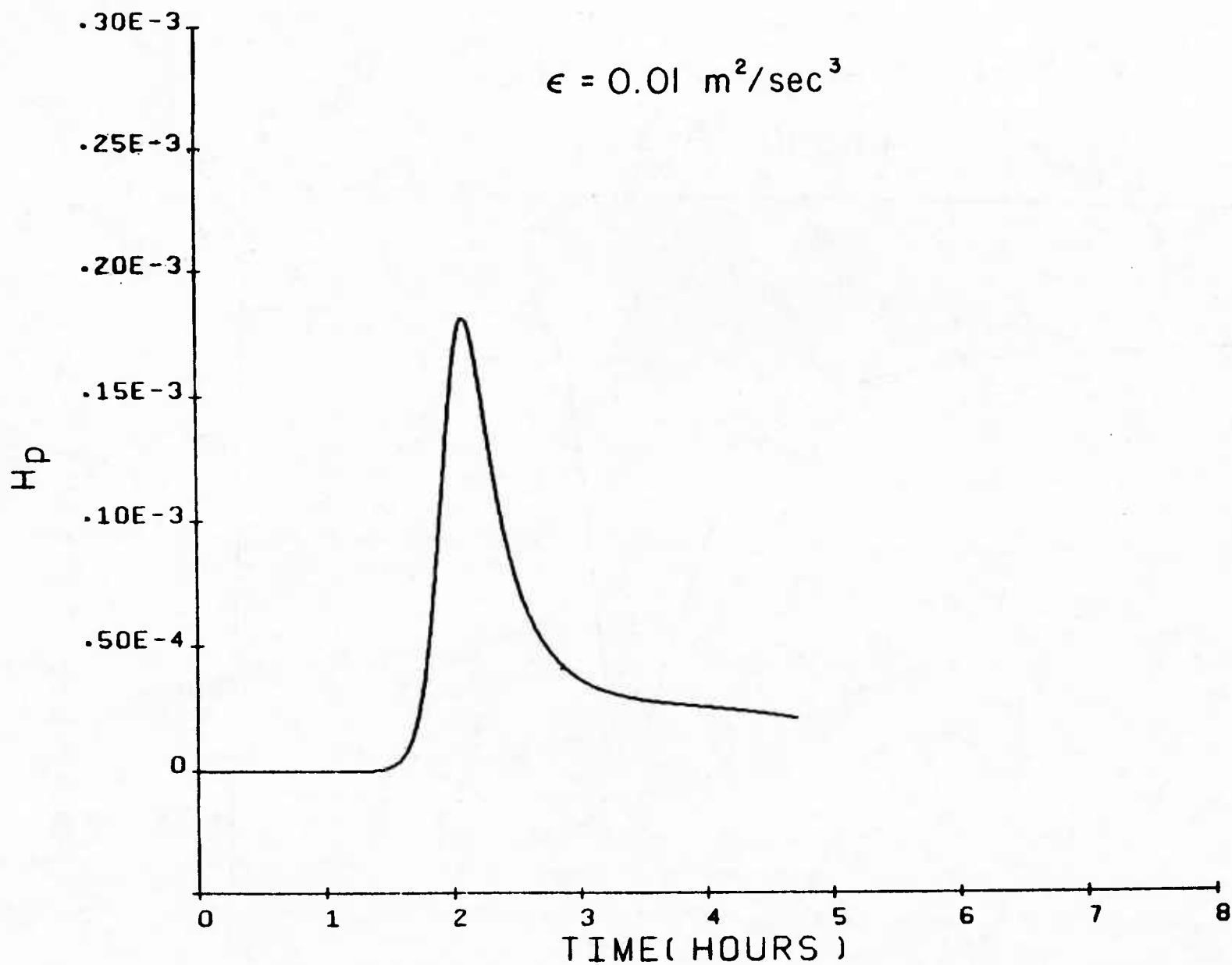


Figure 4.2(a). Evolution of precipitation water mixing ratio  $H_p$ . Turbulence level  $\epsilon = 0.01 \text{ m}^2/\text{sec}^3$ .

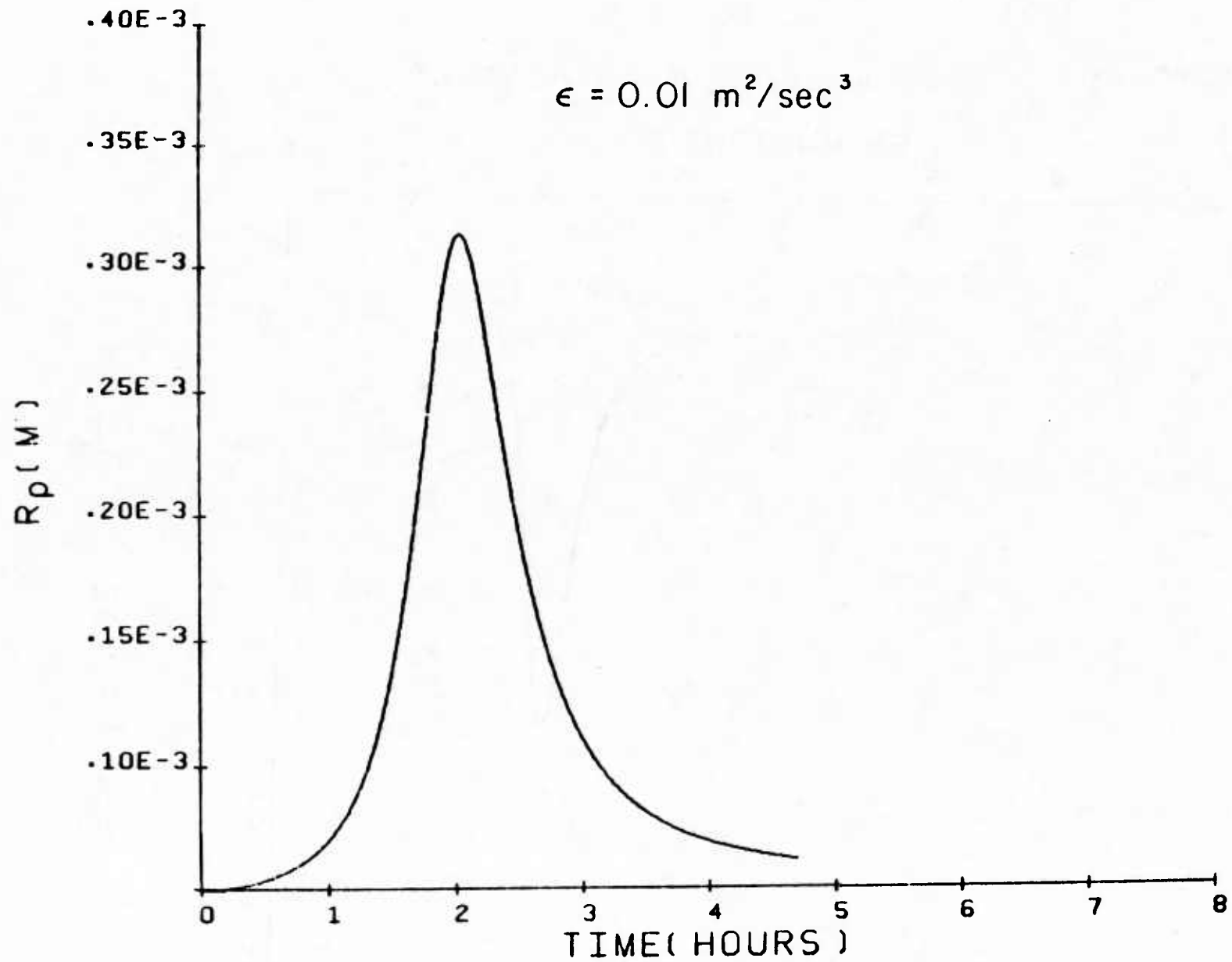


Figure 4.2(b). Evolution of average precipitation drop radius corresponding to Figure 4.2(a).

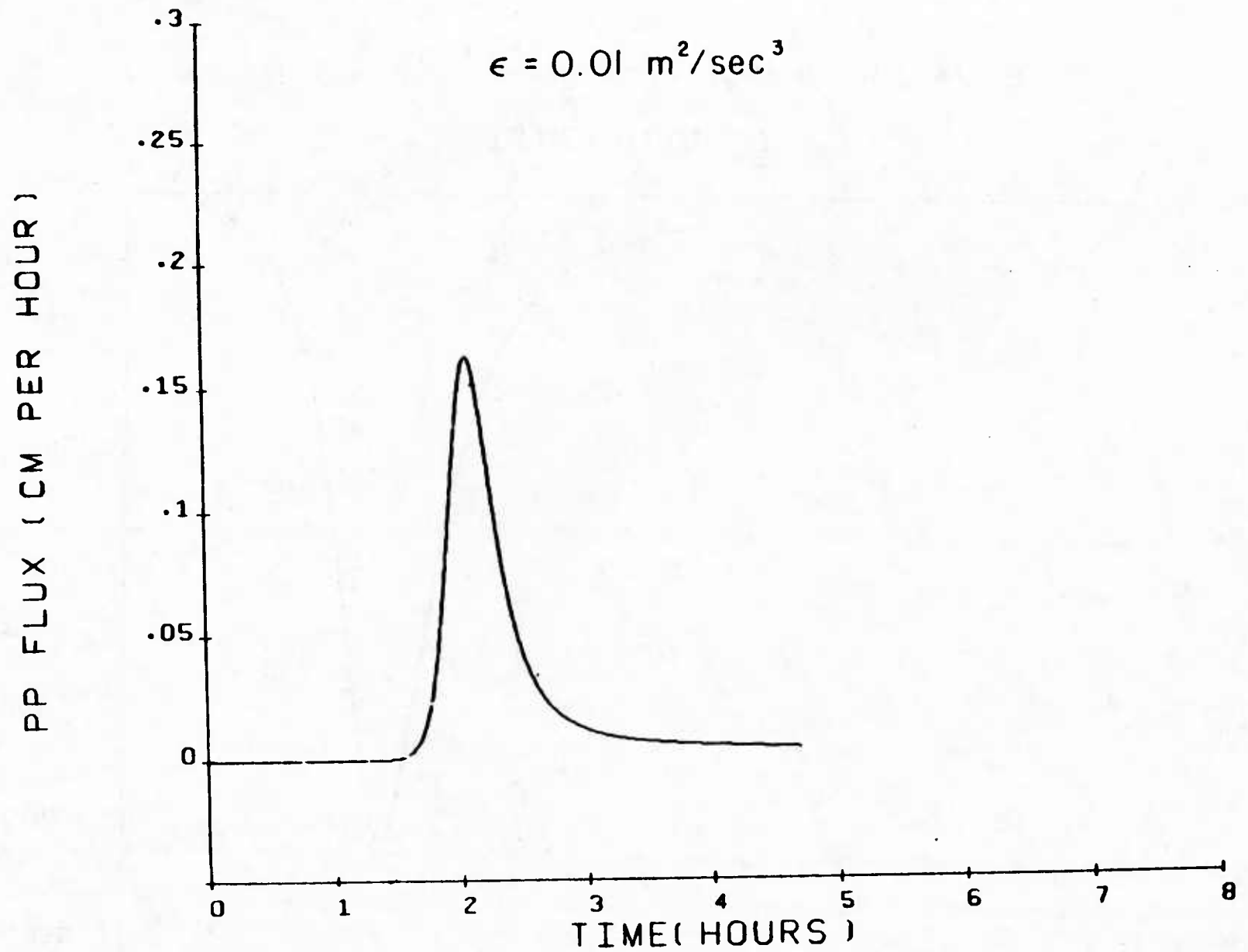


Figure 4.2(c). Evolution of precipitation flux corresponding to Figure 4.2(a).

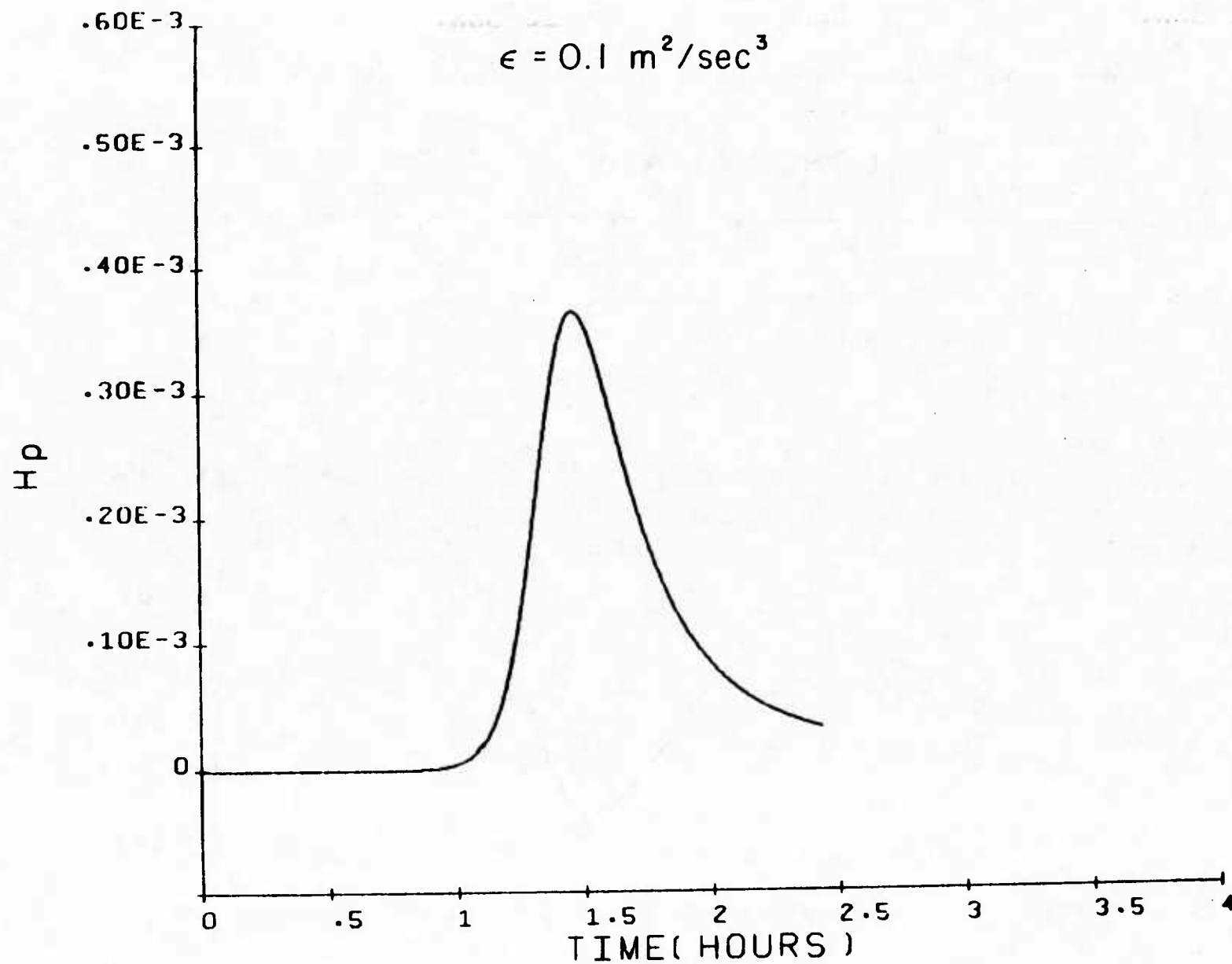


Figure 4.3(a). Evolution of precipitation mixing ratio  $H_p$  for turbulence level  $\epsilon = 0.1 \text{ m}^2/\text{sec}^3$ .

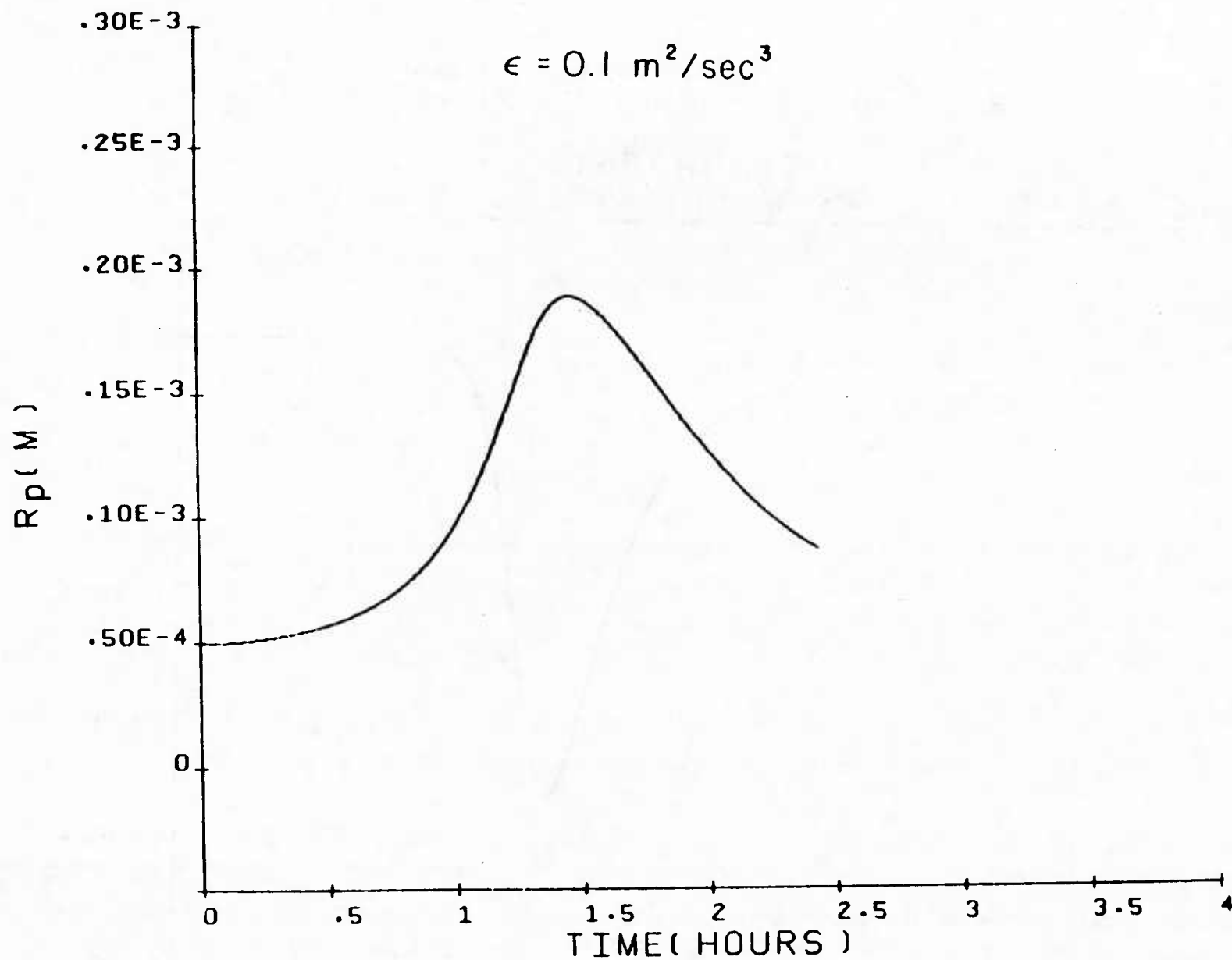


Figure 4.3(b). Evolution of precipitation drop average radius corresponding to Figure 4.3(a).

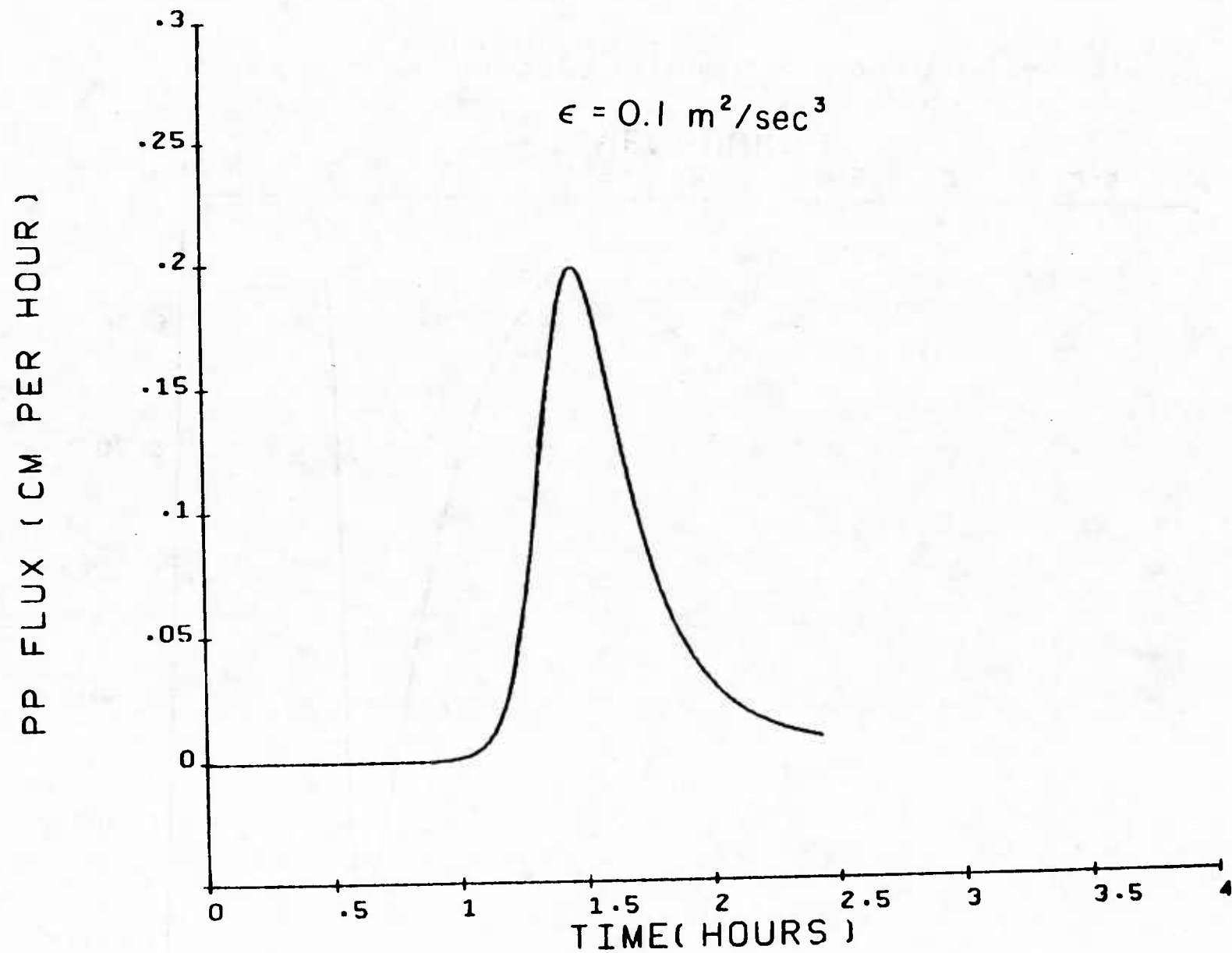


Figure 4.3(c). Evolution of precipitation flux corresponding to Figure 4.3(a).



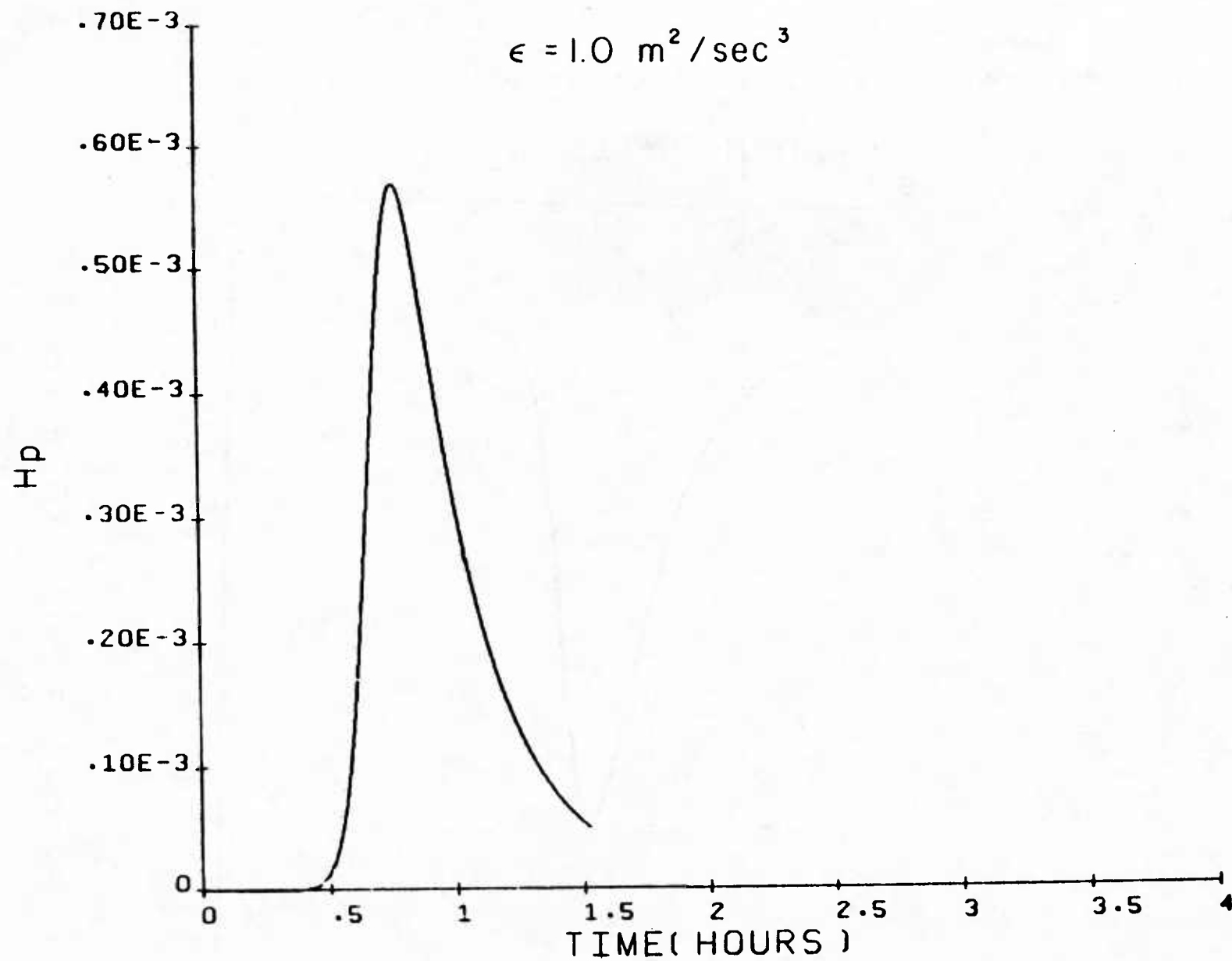


Figure 4.4(a). Evolution of precipitation water mixing ratio  $H_p$  for turbulence level  $\epsilon = 1.0 \text{ m}^2/\text{sec}^3$ .

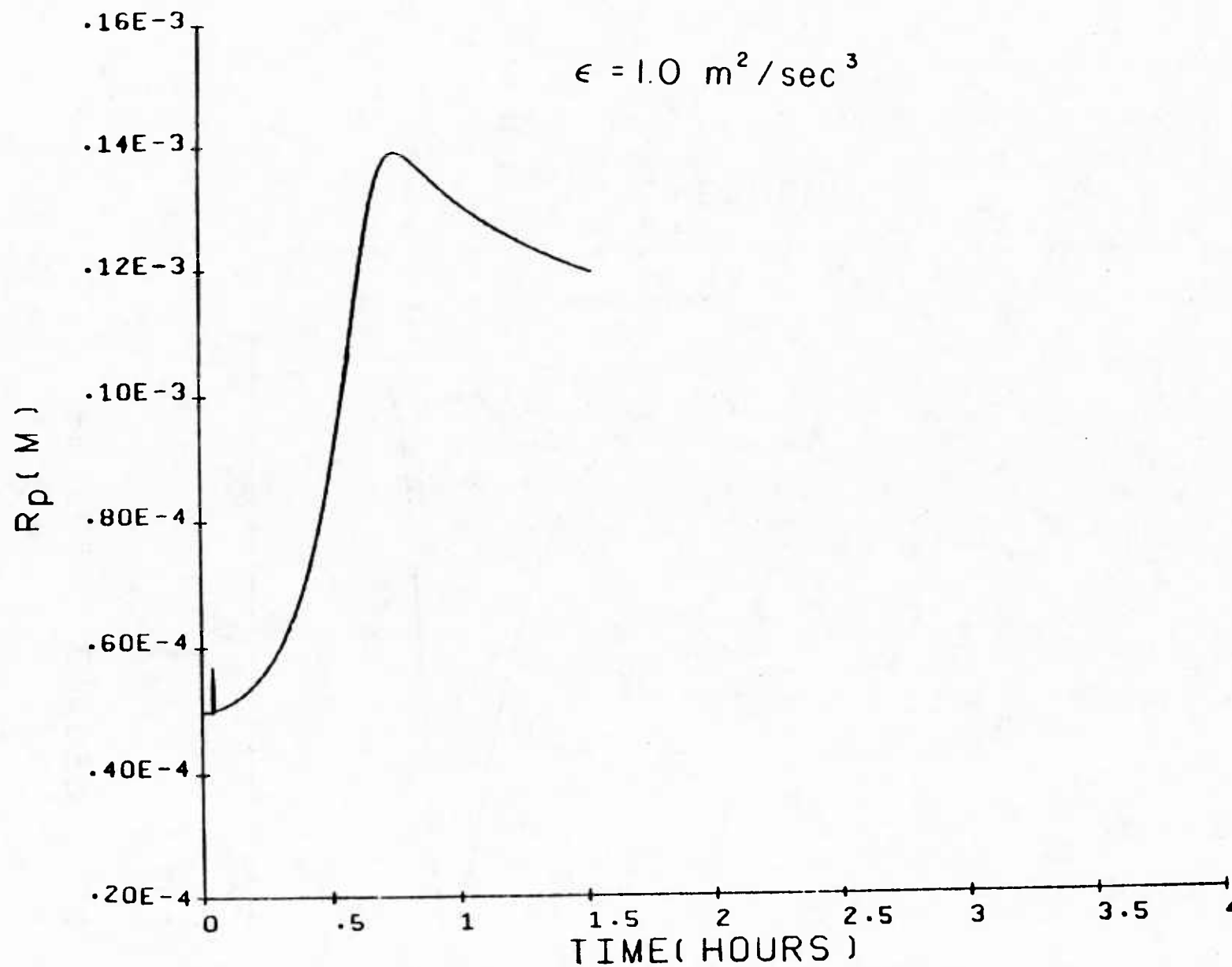


Figure 4.4(b). Evolution of precipitation drop average radius corresponding to Figure 4.4(a).

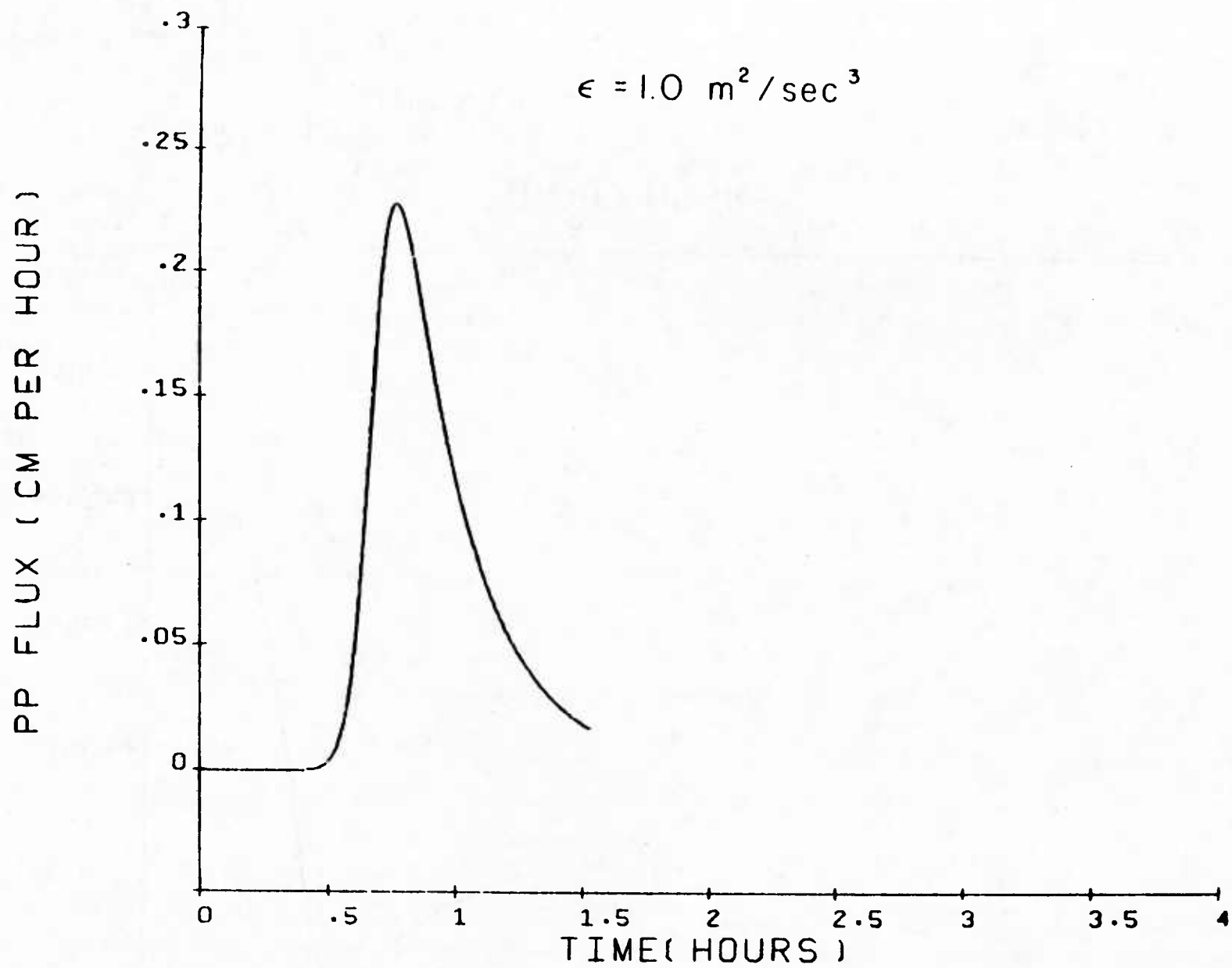


Figure 4.4(c). Evolution of precipitation flux corresponding to Figure 4.4(a).

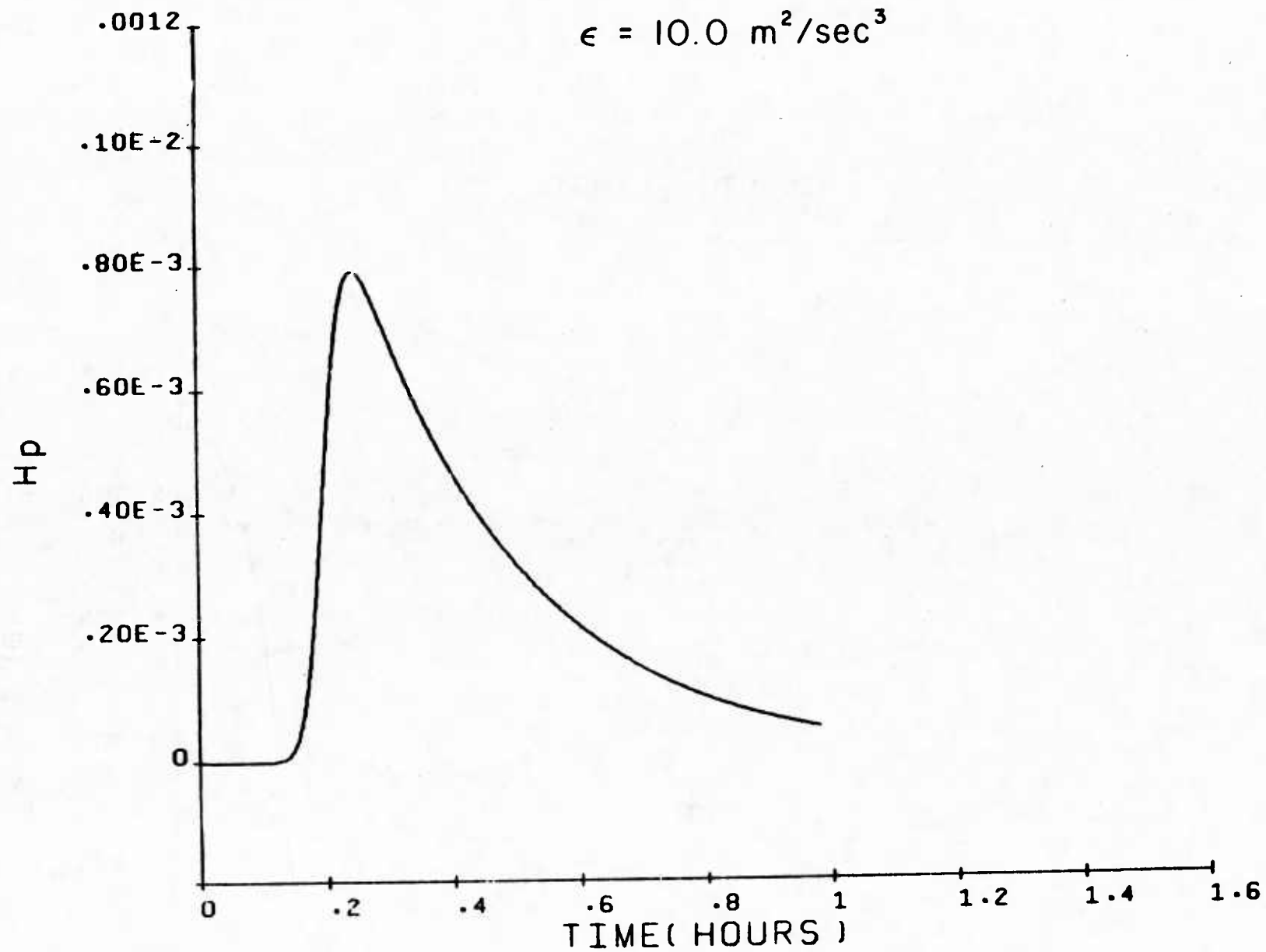


Figure 4.5(a). Evolution of precipitation water mixing ratio  $H_p$  for turbulence level  $\epsilon = 10 \text{ m}^2/\text{sec}^3$ .

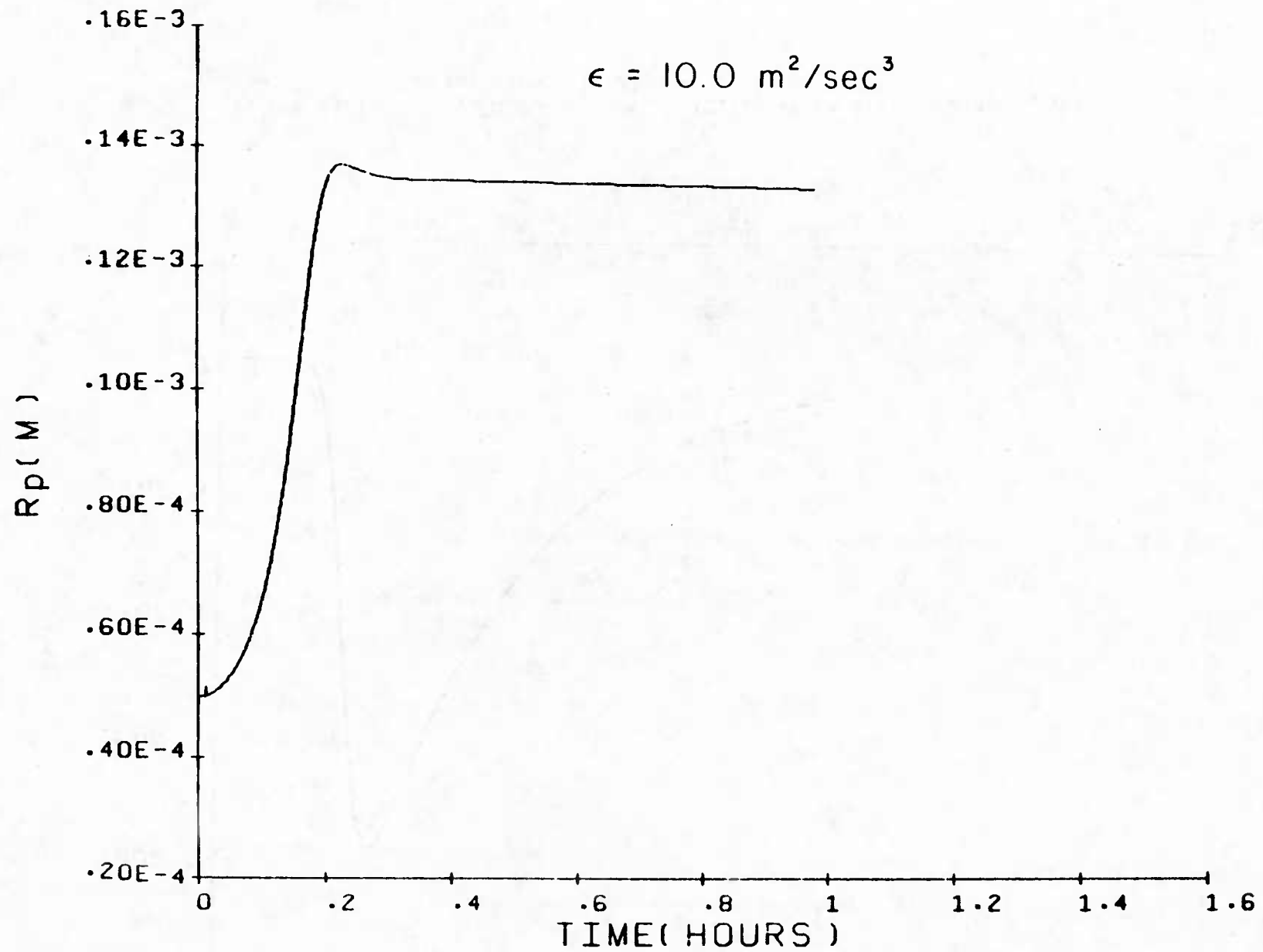


Figure 4.5(b). Evolution of precipitation drop average radius corresponding to Figure 4.5(a).

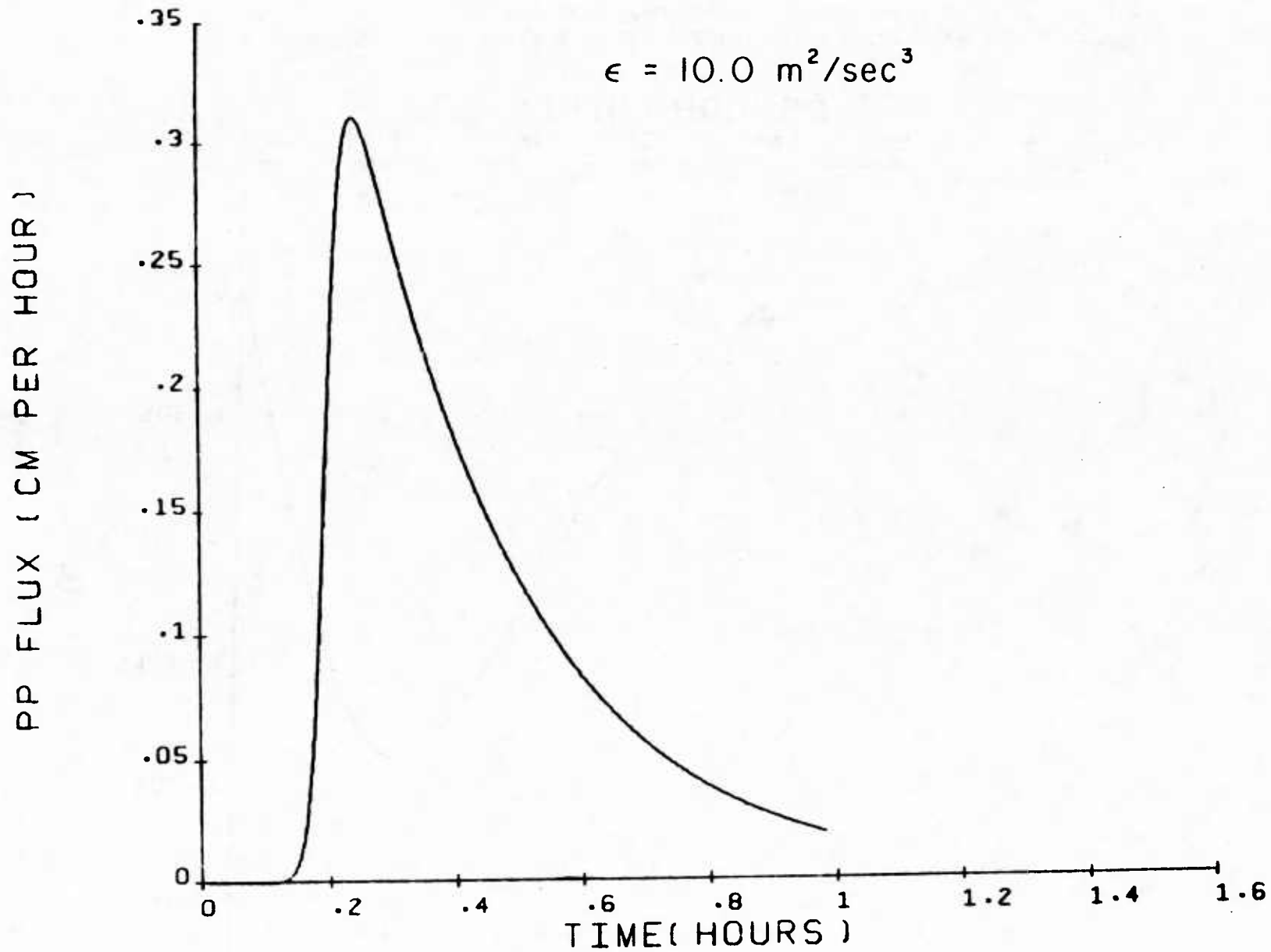


Figure 4.5(c). Evolution of precipitation flux corresponding to Figure 4.5(a).

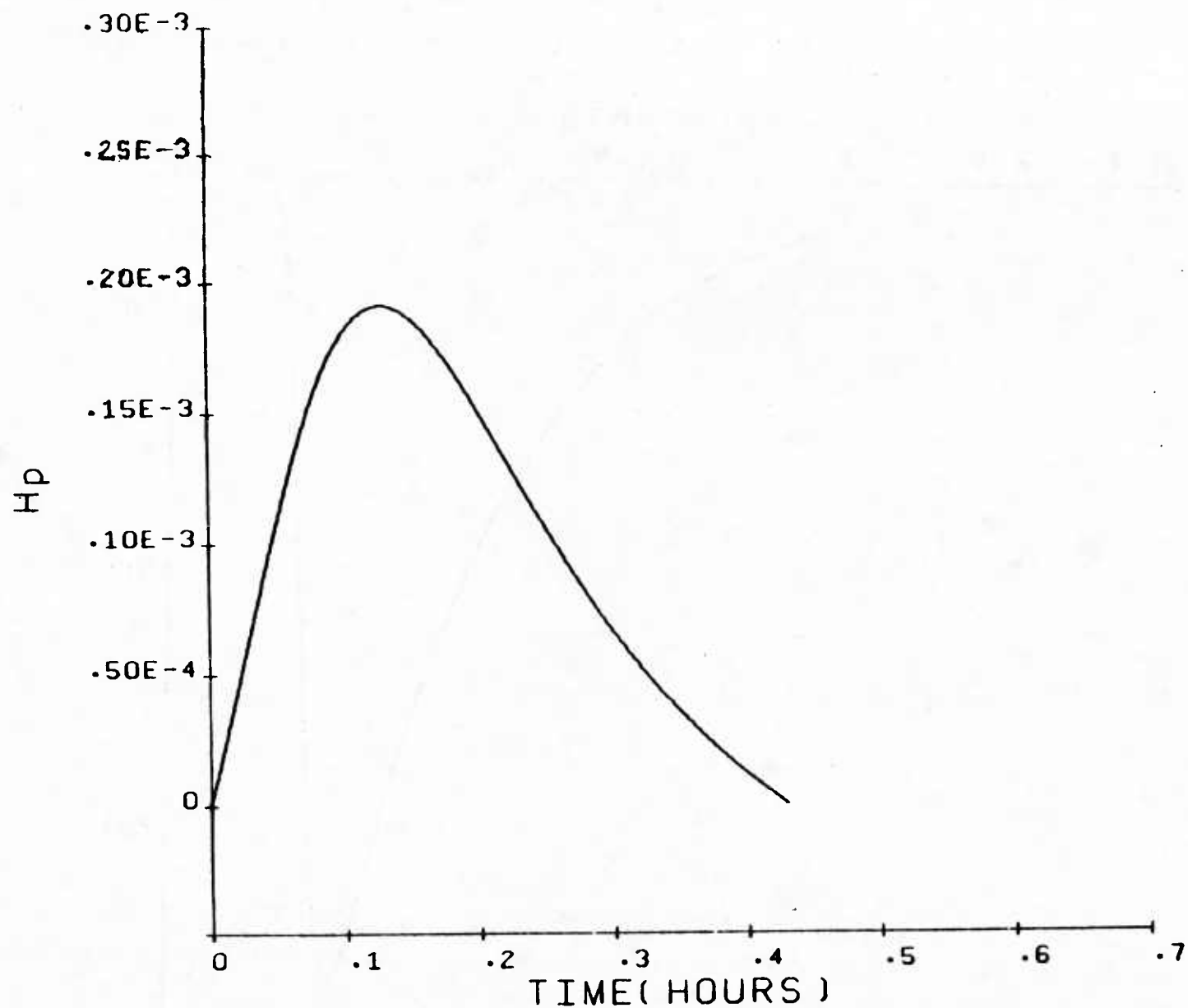


Figure 4.6(a). Evolution of the precipitation water mixing ratio for the homogeneous cloud evolution conditions of Figures 1-4 as predicted by the Kessler model (Reference 42). There is no dependence upon turbulence in the Kessler model.

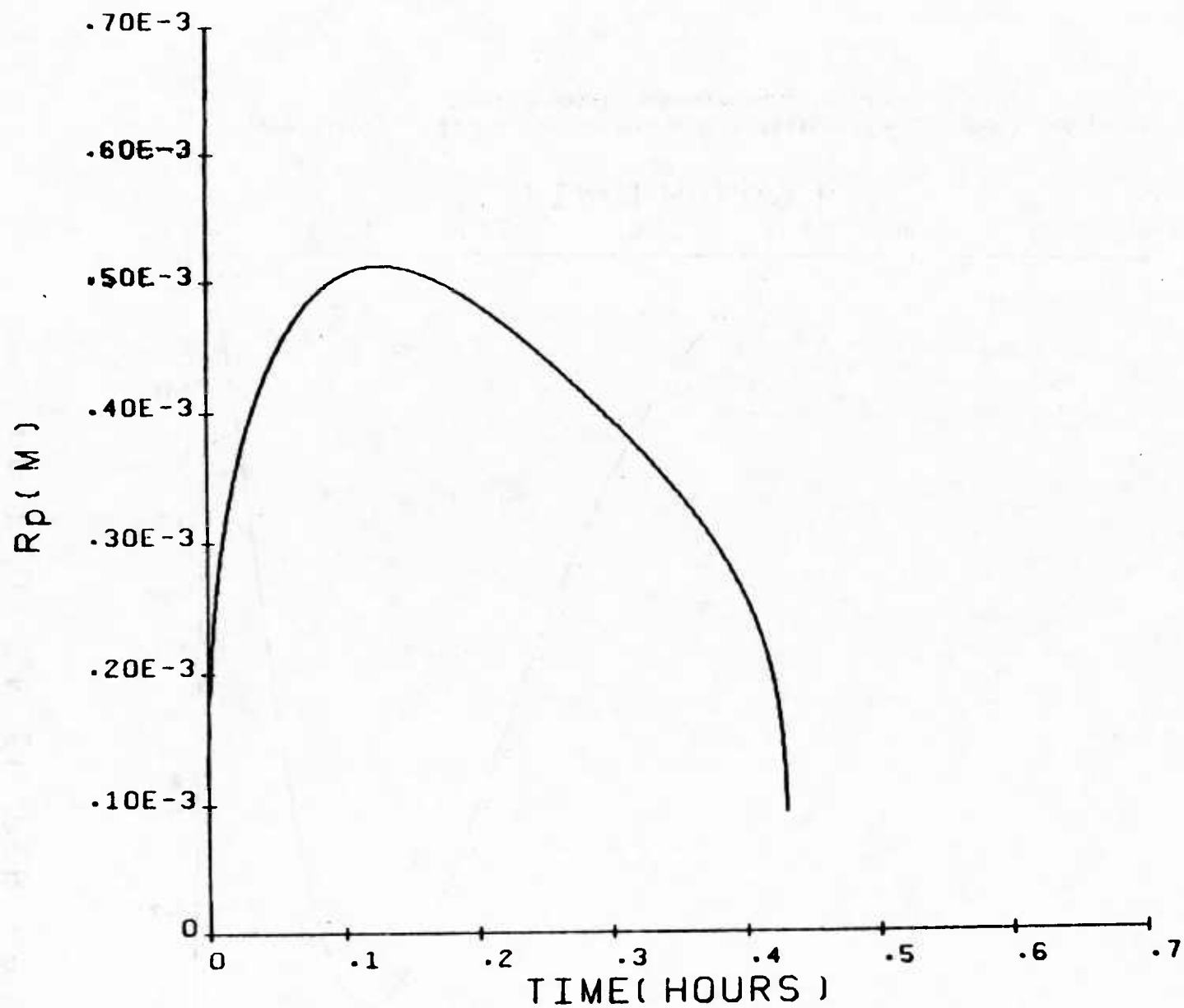


Figure 4.6(b). Evolution of the average precipitation drop radius as predicted by the Kessler model corresponding to Figure 4.6(a).



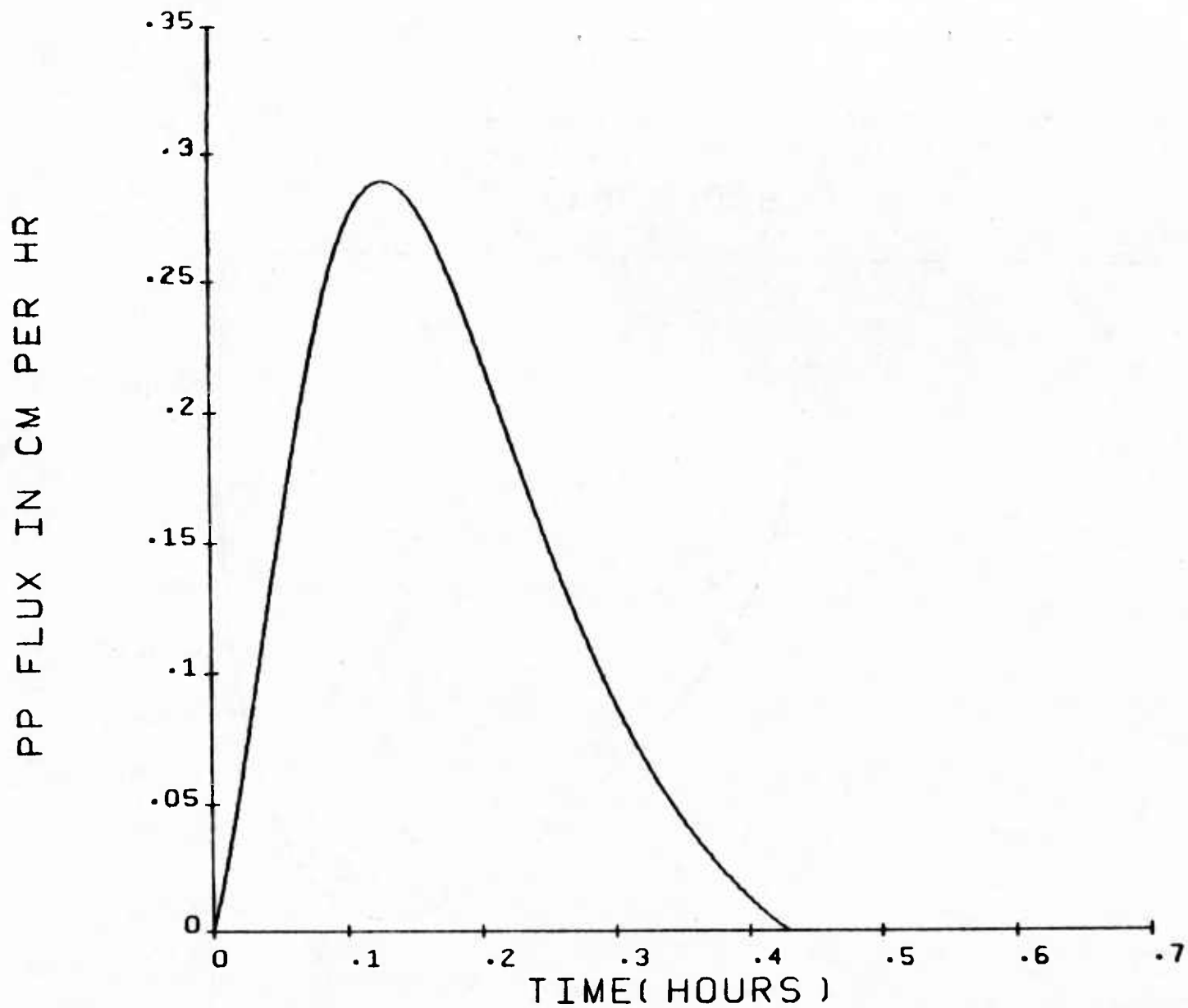


Figure 4.6(c). Evolution of the precipitation flux as predicted by the Kessler model corresponding to Figure 4.6(a).

## 5. A.R.A.P. MODEL PROBLEMS

Model difficulties may be divided into four areas: those involving the basic turbulent transport model, those involving additional physical mechanisms not incorporated within the model, those involving the numerical complexities of faithfully following the modeled equations, and those involved in obtaining adequate field data to rigorously test the accuracy of the model and to drive it under cases of practical interest. We are actively involved in all but the last experimental area. We believe we can best contribute to this last area by exercising the model to determine which parameters have the strongest influence on the model behavior and in this way help to give some guidance to observers as to which parameters most critically need to be measured. A discussion of the first three areas are given in the following sections.

### 5.1 Turbulent Transport Model

An important problem area of the turbulent transport model is its inability to correctly predict the horizontal variance under conditions which lead to a strong disparity between the horizontal and vertical velocity variance. As pointed out in Section 3.1 in Reference 18, the model provides for a Monin-Obukhov similarity for the horizontal velocity which does not exist in the data. Similarly the horizontal velocity variance predicted by the model for free convection departs significantly from the data near the top and the bottom of the layer as shown in Figure 3.3.2 of Reference 18. Perhaps even more important the model cannot represent the transition to strongly stratified conditions where the flow becomes essentially two-dimensional. As explained in Reference 18, we believe the principal difficulty is the anisotropic nature of the turbulence scales. In all of these example problem areas the vertical scale becomes much less than the horizontal scale in regions of the flow. Lewellen and Sandri (Reference 16) attempted a modification to our basic single scale model which permitted the horizontal macro-length scale to be different from the vertical macro-length scale. The vertical scale was identified with the single scale as previously modeled and the horizontal scale was allowed to vary with the mixed-layer height. This preliminary attempt at a 2-scale model did successfully eliminate the Monin-Obukhov scaling of the horizontal velocity variance and replace it with a dependence on the mixed-layer thickness which is consistent with data.

However, further tests of the 2-scale model as formulated by Lewellen and Sandri (Reference 16) have shown that it lacks the generality desired for adaptation into the basic model. The most noticeable failure was that in strongly stratified flow it did not force the ratio of the vertical velocity variance to the horizontal velocity variance to approach zero to permit a transition to two-dimensional turbulence. The coupling between the two time scales given in the Lewellen and Sandri (Reference 16) formulation did not allow this decoupling. We are currently reformulating the two scale model to remove this problem.

If the basic Rotta term for return to isotropy is reinterpreted as a tendency for axial symmetry about the 3 coordinate axes, then this part of the pressure strain term may be written as

$$\pi_{ij} = -\frac{1}{\tau} (\overline{u_i u_j} - \frac{q^2}{3} \delta_{ij}) \quad (5.1)$$

$$\begin{aligned} &= -\frac{1}{3\tau} [\overline{u_i u_j} - \frac{q^2}{2} (\delta_{ij} - \delta_{1i} \delta_{1j})] \\ &\quad - \frac{1}{3\tau} [\overline{u_i u_j} - \frac{q^2}{2} (\delta_{ij} - \delta_{2i} \delta_{2j})] \\ &\quad - \frac{1}{3\tau} [\overline{u_i u_j} - \frac{q^2}{2} (\delta_{ij} - \delta_{3i} \delta_{3j})] \end{aligned} \quad (5.2)$$

As long as there is the single time scale for the three return-to-axial symmetry terms, Eqs. (5.1) and (5.2) are identical. However, when one of the time scales is assumed to be unequal to the other two, then Eq. (5.2) provides the basis for a correction to the Rotta terms, namely,

$$\begin{aligned} \pi_{ij} &= -\frac{1}{\tau} (\overline{u_i u_j} - \frac{q^2}{3} \delta_{ij}) \\ &\quad - \frac{1}{3} \left( \frac{1}{\tau_1} - \frac{1}{\tau} \right) [\overline{u_i u_j} - \frac{q^2}{2} (\delta_{ij} - \delta_{1i} \delta_{1j})] \end{aligned} \quad (5.3)$$

The subscript (1) represents the single coordinate direction about which the flow is assumed to be biased. The time scale  $\tau$  is generally taken to be the eddy turnover time  $\Lambda/q$ . The analogous turnover time in the biased direction would appear to be  $\Lambda_1/(u_1 u_1)^{1/2}$ . When  $\tau_1 \ll \tau$ , Eq. (5.3) suggests that energy will be taken out of the  $u_1 u_1$  components on a time scale of  $\Lambda_1/(u_1 u_1)^{1/2}$ . This will provide a tendency towards equalibrating the two time scales even when the length scales are quite unequal. We are currently proceeding to rework the analysis of Lewellen and Sandri (Reference 16) following the formulation suggested by Eq. (5.3). This approach appears to have the potential for duplicating those results and providing the transition to nearly two-dimensional turbulence under conditions of strong stratification.

## 5.2 Uncertain Physical Processes

We have attempted to incorporate into the model those processes which appeared most pertinent, but a number of unmodeled phenomena may play a role under some conditions. Certainly the micro-scale cloud physics addressed in Chapter 4 plays an important role in determining the rate of precipitation to the surface under conditions conducive to rain or drizzle. We believe the formulation described in Chapter 4 forms the basis for incorporating this phenomena into the basic model, but at the present time the interaction of turbulence and cloud microphysics remains an area of considerable uncertainty.

Surface breaking along the air-sea interface is a process not included within the model which is important in determining aerosol concentrations in the surface layers and may also be important in determining the effective  $z_0$  of the surface of the ocean.

The role of internal waves within the atmospheric marine boundary layer is another uncertain phenomenon. They almost certainly exist a significant fraction of the time. How important their interaction with the turbulent transport within the layer is, remains to be determined, although the sample calculation of Appendix A demonstrates that there can be a strong interaction under some conditions.

A more speculative possibility is for a double diffusive instability to exist along the top of the boundary layer when the air in it is both cooler and more moist than the air above it. The boost that radiation provides for the transport of heat provides a difference in effective diffusivities for heat and moisture which might drive a double diffusive instability. That is, a finger of warm dry air protruding into the boundary layer from above has the potential for cooling faster than the moisture mixes into it and, thus, continuing to fall because it becomes heavier than the surrounding boundary layer air.

Under some unstable conditions the boundary layer turbulence penetrates well into the troposphere in the form of cumulus clouds. These cumulus clouds play an important role in the coupling of a global atmospheric model to the surface. This penetrative turbulence is beyond the capability of the current model.

## 5.3 Numerical Difficulties

The entire spectrum of turbulent flow phenomena might be interpreted as a numerical problem since the Navier-Stokes equations provide a rigorous formulation. The difficulty is that, although these equations may be solved rather straightforwardly with today's computing resources for simple boundary conditions, the large range of scales involved in the motions of the atmospheric boundary layer prohibits a complete detailed solution. Since these motions range from the small dissipative eddies, as small as  $10^{-3}$  meters, it is essential that some averaging and approximating is required for any practical model.

The present model requires at least an averaging over one spatial coordinate to form a 2-D unsteady model. Most of our calculations have used the 1-D unsteady model, which goes even further and averages over both horizontal directions. This program which assumes horizontal homogeneity is appropriate for many, if not most conditions over the open ocean, provided the role of 2 and 3-D motions are adequately parameterized within the turbulence model. But other conditions such as that occurring along irregular coast lines cannot be represented by either the 1-D or 2-D models.

Chapter 3 details our current attempt at providing increased averaging in the vertical direction so that we can gain the potential for resolving some completely 3-D features with the model.



## 6. FUTURE PLANS

The dynamics of the temperature inversion at the top of the boundary layer represents one of the regions involving the most uncertainties in current planetary boundary layer models. Below this altitude, dynamics are dominated by turbulence, while above it, internal gravity waves dominate. The mutual feedback between turbulence and waves in this transition region provides a complex interaction which controls such important phenomena as peak values of  $C_N^2$ . We plan to continue the type computations given in Appendix A which allow the large essentially 2-D features, either internal waves or turbulent eddies, to be resolved as part of the ensemble mean motion while the smaller scale turbulence is treated by the turbulence closure model. By allowing the computation to resolve a significant part of the interaction, dependency on uncertainties in the closure model are reduced. The results can then be time averaged to compare with simpler 1-D models or scaling relationships. Principal effort, will be expended on the 2-D calculations but we expect to complete sufficient analysis of these results to suggest means for improving the simpler representation.

We plan to continue our effort described in Section 4 to incorporate more cloud physics into our model. The current model is based on quite simple physics. Thermodynamic equilibrium is assumed to exist between liquid and gas phase water at all times. The liquid which exists is assumed to be in the form of small droplets of specified size. The droplet size is constant in space and time. Only the number density varies as the liquid water content varies. In actuality, we would expect the droplet size distribution to be controlled by a complex interaction between the turbulent fluctuations in relative humidity and the ambient concentration of condensation nuclei. Since the droplet size distribution is such an important variable in determining visibility within a fog of given liquid water content, we are attempting to make use of the analytical and experimental studies performed by other NASC contractors on fog droplet dynamics to incorporate, at least, some droplet growth dynamics within our model. The important interaction between thermal radiation and droplet size will also be included.

A third task for the future calls for us to exercise the model to investigate conditions which lead to the initiation of fog or low-level stratus. Concurrently, with extending the model's capability, we wish to utilize it to exemplify phenomena of interest to the Navy. At least some of these calculations will be in support of the fog model evaluation study being carried out by Calspan.

We also plan to explore the feasibility of 2 major extensions of the model. We would not expect to complete these extensions within the next year, but do expect to determine the relative attractiveness of proceeding with these extensions. The first of these calls for exploring the use of second-order closure techniques to improve the parameterization of the effects of cumulus clouds in global atmospheric models. The intent would be to view the occurrence of cumulus as a penetration of boundary layer turbulence well into the troposphere. A first step in this exploration would be to become more familiar with how the effects of cumulus are parameterized in current models. The final task calls for exploring the extension of our model to 3

dimensions. This should be an attractive alternative if the 1-D integral model described in Chapter 3 works sufficiently accurately to allow the vertical distributions of the primary variables to be represented by just a few grid points. A code which is no larger than our present 2-D, unsteady model could then be constructed to examine completely 3-D, unsteady events which happen in real coastal environments.

The development and testing of such a 3-D Code based upon a general hybrid treatment of the full 3-D problem described by second order closure turbulence theory is a task of major proportion. We feel that validation of the hybrid method for the general 1-D homogeneous case including the presence of an inversion, stratus cloud, and radiative transport should be demonstrated before commitment is made to develop such a 3-D hybrid/integral code. The development and validation of the inversion layer and moisture transport including the presence of stratus cloud for the 1-D homogeneous case as noted on page 20 is our immediate near term goal for the hybrid procedure.

We expect to pursue this research in close cooperation with NEPRF personnel in order to be responsive to particular questions which may arise during the course of this investigation.

## REFERENCES

1. Donaldson, Coleman duP., 1973: "Construction of a Dynamic Model of the Production of Atmospheric Turbulence and the Dispersal of Atmospheric Pollutants," In Workshop on Micro-meteorology, pp. 313-392.
2. Lewellen, W.S., 1977: "Use of Invariant Modeling," In Handbook of Turbulence, edited by W. Frost, Plenum Press, pp. 237-290.
3. Lewellen, W.S. and Teske, M.E., 1973: "Predictions of the Monin-Obukhov Similarity Functions from an Invariant Model of Turbulence," J. Atmos. Sciences 30, 1340-1345.
4. Lewellen, W.S., Teske, M.E. and Donaldson, Coleman duP., 1974: "Turbulence Model of Diurnal Variations in the Planetary Boundary Layer," Proc. 1974 Heat Transfer and Fluid Mechanics Institute (L.R. Davis & R.E. Wilson, Eds.), Stanford University Press, pp. 301-319.
5. Lewellen, W.S., Teske, M.E., and Donaldson, Coleman duP., 1976: "Examples of Variable Density Flows Computed by a Second-Order Closure Description of Turbulence," AIAA J. 14, 3, 382-387.
6. Lewellen, W.S. and Teske, M.E., 1976: "Second-Order Closure Modeling of Diffusion in the Atmospheric Boundary Layer," Boundary Layer Meteor. J. 10, 69-90.
7. Lewellen, W.S. and Teske, M.E., 1975: "Development of a Low-Level Atmospheric Turbulence Model for Marine Environments," Aeronautical Research Associates of Princeton, Inc., A.R.A.P. Report No. 255.
8. Lewellen, W.S., Oliver, D.A., Teske, M.E., and Williamson, G.G., 1976: "Status Report on a Low-Level Atmospheric Turbulence Model for Marine Environment," Aeronautical Research Associates of Princeton, Inc., A.R.A.P. Report No. 289.
9. Lewellen, W.S. and Teske, M.E., 1976: "A Second-Order Closure Model of Turbulent Transport in the Coastal Planetary Boundary Layer," Presented at Conference on Coastal Meteorology, Virginia Beach, Virginia.
10. Oliver, D.A., Lewellen, W.S. and Williamson, G.G., 1978: "The Interaction Between Turbulent and Radiative Transport in the Development of Fog and Low-Level Stratus," J. Atmos. Sci. 35, 301-316.
11. Lewellen, W.S., Oliver, D.A., Teske, M.E., Segur, H. and Cote, O., 1977: "1977 Status Report on Low-Level, Atmospheric Turbulence Model for Marine Environments," Aeronautical Research Associates of Princeton, Inc., A.R.A.P. Report No. 320.



12. Lewellen, W.S., M.E. Teske, D.A. Oliver, Y.P. Sheng, and Segur, H., 1979: "1979 Status Report on Low-Level, Atmospheric Turbulence Model for Marine Environments," Aeronautical Research Associates of Princeton, Inc., A.R.A.P. Report No. 385.
13. Teske, M.E. and Lewellen, W.S., 1979: "Horizontal Roll Vortices in the Planetary Boundary Layer," Presented at the AMS Fourth Symposium on Turbulence, Diffusion, and Air Pollution, Reno, Nev.
14. Lewellen, W.S., Teske, M.E. and Sheng, Y.P., 1980: "Micrometeorological Applications of a Second-Order Closure Model of Turbulent Transport, Turbulent Shear Flows 2 (Selected papers from the Second International Symposium on Turbulent Shear Flows, Imperial College, London, July 2-4, 1979), Springer-Verlag, pp. 366-378.
15. Lewellen, W.S., Oliver, D.A., Sullivan, R.D. and Sandri, G., 1980: "1980 Status Report on Low-level, Atmospheric Turbulence Model for Marine Environments," Aeronautical Research Associates of Princeton, Inc., A.R.A.P. Report No. 420.
16. Lewellen, W.S. and Sandri, G., 1980: "Incorporation of an Anisotropic Scale into Second-Order Closure Modeling of the Reynolds Stress Equation," Aeronautical Research Associates of Princeton, Inc., A.R.A.P. T.M. No. 80-11
17. Lewellen, W.S., 1980: "Transport of Water Vapor Through the Atmospheric Boundary Layer," In Atmospheric Water Vapor, Edited by Deepak, A, et. al., Academic Press, pp. 527-550.
18. Lewellen, W.S., 1981: "Modeling the Lowest 1 km of the Atmosphere," AGARDograph.
19. Roach, W.T., Brown, R., Caughey, S.J., Garland, J.A. and Readings, C.J., 1976: "The Physics Radiation Fog: I - a Field Study," Quart. J. Roy. Met. Soc. 102, 313-333.
20. Zeman, O., 1979: "Parameterization of the Dynamics of Stable Boundary Layers and Nocturnal Jets," J. Atmos. Sci. 36, 792-804.
21. Mahrt, L., and Lenschow, D.H., 1976: "Growth Dynamics of the Convectively Mixed Layer," J. Atmos. Sci. 33, 41-51.
22. Zeman, O. and Tennekes, H., 1977: "Parameterization of the Turbulent Energy Budget at the Top of the Daytime Atmospheric Boundary Layer," J. Atmos. Sci. 34, 111- 123.
23. Lewellen, W.S., 1977a: "Influence of Body Forces on Turbulent Transport Near a Surface," J. App. Math. and Phys. (ZAMP) 28, 825-834.

24. Lewellen, W.S. and Williamson, G., 1976: "Wind Shear and Turbulence Around Airports," NASA CR-2752, prepared by A.R.A.P. for Marshall Space Center.
25. Brost, R.A. and Wyngaard, N.C., 1978: "A Model Study of the Stably Stratified Planetary Boundary Layer," J. Atmos. Sci. 35, 1427-1440.
26. Wyngaard, J.C., 1975: "Modelling the Planetary Boundary Layer-Extension to the Stable Case," Boundary Layer Meteor. 9, 441-460.
27. Delage, Y., 1974: "A Numerical Study of the Nocturnal Atmospheric Boundary Layer," Quart. J. Roy. Meteor. Soc. 100, 351-354.
28. Berry, E.X., 1967: "Cloud Droplet Growth by Collection," J. Atmos. Sci. 24, 688-701.
29. Warshaw, M., 1967: "Cloud Droplet Coalescence: Statistical Foundations and a One-dimensional Sedimentation Model," J. Atmos. Sci. 24, 278-86.
30. Twomey, S., 1966: "Computations of Rain Formation by Coalescence," J. Atmos. Sci. 23, 404-41.
31. Levin, L. and Sedunov, Yu. S., 1966: "The Theoretical Model of the Drop Spectrum Formation Process in Clouds," PAGEOPH 69, 320-335.
32. Jeou-Jang, J., 1966: "Statistical Theory of Precipitation Process," Tellus XVIII 4, 722-729.
33. Sedunov, Y.S., 1967: "Kinetika Nach al' noi Stadii Kondensatzii v Oblakakh, Izv. Akad. Nauk S.S.S.R., Ser. Fizika Atmosfery i Okenna. No. 1
34. Taylor, G.I., 1935: Proc. Roy. Soc. A. 151, 429.
35. Almeida, F.C., 1979: "The Collisional Problem of Cloud Droplets Moving in a Turbulent Environment - Part II: Turbulent Collision Efficiencies," J. Atmos. Sci. 36, 1564-1576.
36. Saffman, P.G. and Turner, J.S., 1956: "On the Collision of Drops in Turbulent Clouds," J. Fluid Mech. 1, 16-30.
37. Mason, B.J., 1971: The Physics of Clouds, 671 pp.
38. Jonas, P.R. and Goldsmith, P., 1972: "The Collection Efficiencies of Small Droplets Falling Through a Sheared Air Flow", J. Fluid. Mech. 52, Part 3, 593-608.

39. Smoluchowski, M., 1917: Z. Phys. Chem, 92, p.129
40. Williams, F., 1965: Combustion Theory, Addison-Wesley, Boston
41. Swift, D.L. and Friedlander, D.K., 1964: "The Coagulation of hydrosols by Brownian motion and Laminar Shear Flow," J. Colloid Sci. 19, 621-647.
42. Kessler, E., 1969: "On the Distribution and Continuity of Water Substance in Atmospheric Circulations," Meteorological Monographs 10, AMS, Boston.

## DISTRIBUTION

CHIEF OF NAVAL RESEARCH  
LIBRARY SERVICES (CODE 734)  
RM. 633, BALLSTON TOWER #1  
800 QUINCY ST.  
ARLINGTON, VA 22217

OFFICE OF NAVAL RESEARCH  
CODE 420  
ARLINGTON, VA 22217

CHIEF OF NAVAL OPERATIONS  
(OP-952)  
U.S. NAVAL OBSERVATORY  
WASHINGTON, DC 20390

CHIEF OF NAVAL OPERATIONS  
ATTN: DR. R. W. JAMES, OP-952D1  
U.S. NAVAL OBSERVATORY  
34TH & MASS. AVE., NW  
WASHINGTON, DC 20390

NAVAL DEPUTY TO THE  
ADMINISTRATOR, NOAA  
RM. 200, PAGE BLDG. #1  
3300 WHITEHAVEN ST., NW  
WASHINGTON, DC 20235

OFFICE OF NAVAL RESEARCH  
EASTERN/CENTRAL REGIONAL OFFICE  
BLDG 114 SECT. D  
459 SUMMER ST.  
BOSTON, MA 02210

COMMANDING OFFICER  
OFFICE OF NAVAL RESEARCH  
1030 E. GREEN STREET  
PASADENA, CA 91101

OFFICE OF NAVAL RESEARCH  
SCRIPPS INSTITUTE OF OCEANO.  
LA JOLLA, CA 92037

COMMANDING OFFICER  
NORDA, CODE 101  
NSTL STATION  
BAY ST. LOUIS, MS 39529

COMMANDING OFFICER  
FLENUMOECANEN  
MONTEREY, CA 93940

SUPERINTENDENT  
LIBRARY REPORTS  
U.S. NAVAL ACADEMY  
ANNAPOLIS, MD 21402

COMMANDER (2)  
NAVAIRSYSCOM  
ATTN: LIBRARY (AIR-0004)  
WASHINGTON, DC 20361

COMMANDER  
NAVAIRSYSCOM (AIR-370)  
WASHINGTON, DC 20361

COMMANDER  
NAVAIRSYSCOM  
METEORO. SYS. DIV. (AIR-553)  
WASHINGTON, DC 20360

COMMANDER  
NAVAIRSYSCOM (AIR-03)  
DEPT. OF THE NAVY  
WASHINGTON, DC 20361

COMMANDER  
NAVAL SEA SYSTEMS COMMAND  
ATTN: LCDR S. GRIGSBY  
PMS-405/PM-22  
WASHINGTON, DC 20362

COMMANDER  
NAVAL OCEAN SYSTEMS CENTER  
ATTN: CODE 4473  
SAN DIEGO, CA 92152

COMMANDER  
NAVAL OCEAN SYSTEMS CENTER  
CODE 532, DR. J. RICHTER  
SAN DIEGO, CA 92152

COMMANDER  
ATTN: DR. B. KATZ  
WHITE OAKS LABORATORY  
NAVAL SURFACE WEAPONS CENTER  
SILVER SPRING, MD 20910

COMMANDER  
PACMISTESTCEN  
GEOPHYS. OFFICER (CODE 3250)  
PT. MUGU, CA 93042

DEPT. OF METEOROLOGY  
NAVAL POSTGRADUATE SCHOOL  
MONTEREY, CA 93940

DEPT. OF OCEANOGRAPHY  
NAVAL POSTGRADUATE SCHOOL  
MONTEREY, CA 93940

DEPT. OF PHYSICS & CHEMISTRY  
NAVAL POSTGRADUATE SCHOOL  
MONTEREY, CA 93940

LIBRARY  
NAVAL POSTGRADUATE SCHOOL  
MONTEREY, CA 93940

USAFETAC/TS  
SCOTT AFB, IL 62225

AFGL/LY  
HANSCOM AFB, MA 01731

AFOSR/NC  
BOLLING AFB  
WASHINGTON, DC 20312

COMMANDER & DIRECTOR  
ATTN: DELAS-DM-A  
U.S. ARMY ATMOS. SCIENCES LAB  
WHITE SANDS MISSILE RANGE,  
WHITE SANDS, NM 88002

COMMANDING OFFICER  
U.S. ARMY RESEARCH OFFICE  
ATTN: GEOPHYSICS DIV.  
P.O. BOX 12211  
RESEARCH TRIANGLE PARK, NC 27709

DIRECTOR (12)  
DEFENSE TECH. INFORMATION CENTER  
CAMERON STATION  
ALEXANDRIA, VA 22314

DIRECTOR  
OFFICE OF ENV. & LIFE SCI.  
OFFICE OF UNDERSEC. OF DEFENSE  
FOR RSCH & ENGINEERING (E&LS)  
ROOM 3D129, THE PENTAGON  
WASHINGTON, DC 20301

DIRECTOR  
NATIONAL METEOROLOGICAL CENTER  
NWS/NOAA  
WORLD WEATHER BLDG. W32, RM 204  
WASHINGTON, DC 20233

ACQUISITIONS SECTION IRDB-D823  
LIBRARY & INFO. SERV. DIV. NOAA  
6009 EXECUTIVE BLVD.  
ROCKVILLE, MD 20852

DIRECTOR GEO. FLUID DYN. LAB.  
NOAA, PRINCETON UNIVERSITY  
P.O. BOX 303  
PRINCETON, NJ 08540

DIRECTOR  
TECHNIQUES DEVELOPMENT LAB  
GRAMAX BLDG. 8060 13TH ST.  
SILVER SPRING, MD 20910

DR. E. W. FRIDAY, DEP. DIR.  
NATIONAL WEATHER SERVICE  
GRAMAX BLDG.  
8060 13TH ST.  
SILVER SPRING, MD 20910

HEAD, ATMOSPHERIC SCIENCES DIV.  
NATIONAL SCIENCE FOUNDATION  
1800 G. STREET, NW  
WASHINGTON, DC 20550

LABORATORY FOR ATMOS. SCIENCES  
NASA GODDARD SPACE FLIGHT CENTER  
GREENBELT, MD 20771

PROFESSOR Y. SASAKI  
UNIV. OF OKLAHOMA  
ROOM 219  
200 FELGAR ST.  
NORMAN, OK 73069

NATIONAL CENTER FOR ATMOS. RSCH.  
LIBRARY ACQUISITIONS  
P.O. BOX 1470  
BOULDER, CO 80302

DEPT. OF ATMOS. SCIENCES  
ATTN: LIBRARIAN  
COLORADO STATE UNIVERSITY  
FT. COLLINS, CO 80521

CHAIRMAN  
DEPT. OF METEOROLOGY  
PENN STATE UNIVERSITY  
503 DEIKE BLDG.  
UNIVERSITY PARK, PA 16802

CHAIRMAN  
DEPT. OF METEOROLOGY  
MASSACHUSETTS INSTITUTE OF TECH.  
CAMBRIDGE, MA 02139

ATMOSPHERIC SCIENCES DEPT.  
UNIV. OF CHICAGO  
1100E. 57TH ST.  
CHICAGO, IL 60637

ATMOSPHERIC SCIENCES DEPT.  
UNIV. OF WASHINGTON  
SEATTLE, WA 98195

CHAIRMAN  
DEPT. OF METEOROLOGY  
UNIV. OF WISCONSIN  
METEORO. & SPACE SCI. BLDG.  
1225 W. DAYTON STREET  
MADISON, WI 53706

DIRECTOR OF METEOROLOGY  
DEPT. OF EARTH & ATMOS. SCI.  
ST. LOUIS UNIV.  
P.O. BOX 8099  
ST. LOUIS, MO 63156

ATMOSPHERIC SCIENCES DEPT.  
OREGON STATE UNIVERSITY  
CORVALLIS, OR 97331

DIRECTOR  
OFFICE OF PROGRAMS RX3  
NOAA RESEARCH LAB  
BOULDER, CO 80302

CHAIRMAN  
INSTITUTE OF ATMOS. PHYSICS  
UNIV. OF ARIZONA  
TUSCON, AZ 85721

TEXAS A&M UNIVERSITY  
DEPT. OF METEOROLOGY  
COLLEGE STATION, TX 77843

CHAIRMAN  
DEPT. OF METEOROLOGY  
UNIV. OF OKLAHOMA  
NORMAN, OK 73069

CHAIRMAN  
DEPT. OF METEOROLOGY  
CALIFORNIA STATE UNIV.  
SAN JOSE, CA 95192

DOCUMENT LIBRARY LO-206  
WOODS HOLE OCEANOGRAPHIC INST.  
WOODS HOLE, MA 02543

DOCUMENTS/REPORTS SECTION  
LIBRARY  
SCRIPPS INST. OF OCEANOGRAPHY  
LA JOLLA, CA 92037

DIRECTOR  
OCEANOGRAPHIC INSTITUTE  
OLD DOMINION UNIV.  
NORFOLK, VA 23508

DR. W. D. NEFF  
WAVE PROPAGATION LABORATORY  
BOULDER, CO 80303

DR. ROGER PIELKE  
DEPT. OF ATMOS. SCIENCES  
COLORADO STATE UNIVERSITY  
FT. COLLINS, CO 80523

DR. JOOST BUSINGER  
DEPT. OF ATMOS. SCIENCES  
UNIV. OF WASHINGTON  
SEATTLE, WA 98195

DR. RAY NOONKEOTER  
NAVAL OCEAN SYSTEMS CENTER  
SAN DIEGO, CA 92152

DR. S. A. PIACSEK  
NORDA, CODE 322  
NSTL STATION, MS 39529

MR. WILLIAM ROGERS  
CALSPAN CORP.  
BUFFALO, NY 14225

DR. JEROME WEINSTOCK  
NOAA  
AERONOMY LABORATORY  
BOULDER, CO 80303

DR. JAMES DEARDORFF  
DEPT. OF ATMOS. SCIENCES  
OREGON STATE UNIV.  
CORVALLIS, OREGON 97331

DR. R. A. ANTONIA  
DEPT. OF MECHANICAL ENG.  
UNIV. OF NEWCASTLE, N.S.W. 2308  
AUSTRALIA

DR. J. C. ANDRE  
DIRECTION DE LA METEOROLOGIE  
EERM/GMD  
92100 BOULOGNE, FRANCE

DR. R. A. BROST  
NCAR  
P.O. BOX 3000  
BOULDER, CO 80307

JOHNS HOPKINS UNIV.  
APPLIED PHYSICS LAB  
R.E. GIBSON LIBRARY  
JOHNS HOPKINS ROAD  
LAUREL, MD 20810

DIRECTOR  
COASTAL STUDIES INSTITUTE  
LOUISIANA STATE UNIV.  
ATTN: O. HUH  
BATON ROUGE, LA 70803

ATMOSPHERIC SCIENCES DEPT.  
UCLA  
405 HILGARD AVE.  
LOS ANGELES, CA 90024

COLORADO STATE UNIV.  
DEPT. OF ATMOS. SCI. LIBRARY  
FOOTHILLS CAMPUS  
FT. COLLINS, CO 80523

UNIV. OF MARYLAND  
DEPT. OF METEOROLOGY  
COLLEGE PARK, MD 20742

LIBRARY  
THE RAND CORP.  
1700 MAIN STREET  
SANTA MONICA, CA 90406

LIBRARY  
CSIRO DIV.  
ATMOSPHERIC PHYSICS  
STATION STREET  
ASPENDALE, 3195  
VICTORIA, AUSTRALIA

DR. EARL E. GOSSARD  
WAVE PROPAGATION LAB., R45X6  
ENVIRONMENTAL RESEARCH LABS  
BOULDER, CO 80303

DR. GEORGE L. MELLOR  
GEOPHYSICAL FLUID DYNAMICS LAB  
PRINCETON, NJ 08540

DR. TETSUJI YAMADA  
LOS ALAMOS NATIONAL LAB  
P.O. BOX 1663, MS 466  
LOS ALAMOS, NM 87545

DR. HANS PANOFSKY  
METEOROLOGY DEPT.  
PENN STATE UNIV.  
UNIVERSITY PARK, PA 16802

DR. MARVIN WESELY  
ARGONNE NATIONAL LAB  
ARGONNE, IL 60439

DR. CARL FRIEHE  
NCAR  
P.O. BOX 3000  
BOULDER, CO 80307

DR. DOUGLAS LILLY  
NCAR  
P.O. BOX 3000  
BOULDER, CO 80307

DR. JOHN LUMLEY  
SIBLEY SCHOOL OF MECHANICAL &  
AEROSPACE ENGINEERING  
CORNELL UNIVERSITY  
ITHACA, NY 14853

DR. F.T.M. NIEUWSTADT  
ROYAL NETHERLANDS  
METEOROLOGICAL INSTITUTE  
DE BILT, THE NETHERLANDS

DR. W. R. COTTON  
DEPT. OF ATMOS. SCIENCES  
COLORADO STATE UNIVERSITY  
T. COLLINS, CO 80523

BUREAU OF METEOROLOGY  
ATTN: LIBRARY  
BOX 1289K, GPO  
MELBOURNE, VIC, 3001  
AUSTRALIA

AUSTRALIAN NUMERICAL  
METEOROLOGY RSCH. CENTER  
ATTN: DR. R. L. HUGHES  
P.O. BOX 5089A  
MELBOURNE, VICTORIA  
3001 AUSTRALIA

MONASH UNIVERSITY  
MECHANICAL ENGINEERING DEPT.  
CLAYTON, VICTORIA 3168  
AUSTRALIA

METEOROLOGICAL OFFICE LIBRARY  
LONDON ROAD  
BRACKNELL, BERKSHIRE  
RG 12 2SZ ENGLAND

EUROPEAN CENTRE FOR MEDIUM  
RANGE WEATHER FORECASTS  
SHINFIELD PARK, READING  
BERKSHIRE RG29AX, ENGLAND

INSTITUT FUR METEOROLOGIE  
JOHANNES GUTENBERG UNIVERSITAT  
ATTN: DR. R. JAENICKE  
D-65 MAINZ  
FEDERAL REPUBLIC OF GERMANY

KONINKLIJK NEDERLANDS  
METEOROLOGISCH INSTITUUT  
POSTBUS 201  
3730 AE DEBILT  
NETHERLANDS

DR. JOHN WYNGAARD  
NCAR  
P.O. BOX 3000  
BOULDER, CO 80307

DR. MICHAEL CLANCY  
NORDA  
NSTL STATION, MS 39529

DR. ROBERT BORNSTEIN  
DEPT. OF METEOROLOGY  
SAN JOSE STATE UNIV.  
SAN JOSE, CA

DR. BRIAN LAUNDER  
DEPT. OF MECHANICAL ENG.  
UNIV. OF MANCHESTER  
INSTITUTE OF SCI. & TECH.  
P.O. BOX 88  
MANCHESTER M60 1QD  
ENGLAND

DR. W. C. REYNOLDS  
DEPT. OF MECHANICAL ENG.  
STANFORD UNIVERSITY  
STANFORD, CA

DR. GILLES SOMMERIA  
LABORATOIRE DE METEOROLOGIE  
DYNAMIQUE  
E.N.S. 24 RUE L'HOMOND  
75005 PARIS, FRANCE

DR. PH. BOUGEAULT  
DIRECTION DE LA METEOROLOGIE  
EERM/GMD  
92100 BOULOGNE, FRANCE



## APPENDIX A

### A Numerical Study of Breaking Kelvin-Helmholtz Billows Using a Reynolds-Stress Turbulence Closure Model\*

by

R. I. Sykes and W. S. Lewellen

Aeronautical Research Associates of Princeton, Inc.

50 Washington Road, P.O. Box 2229

Princeton, New Jersey 08540

#### ABSTRACT

A two-dimensional numerical study of breaking Kelvin-Helmholtz billows is presented. The turbulent breaking process is modeled using second-order closure methods to describe the small-scale turbulence, whilst the large scale billow itself is calculated explicitly as a two-dimensional flow. The numerical results give detailed predictions of turbulence levels and time scales, and are consistent with laboratory and atmospheric observations. Two general predictions of the model are that the structure of turbulent temperature fluctuations is very different from that of the velocity fluctuations, the former being much more striated, and secondly that the timescale of the growth and breaking process is virtually completely determined by the initial velocity shear.

---

\*Submitted for publication in J. Atmos. Sci., September 1981.

## 1. Introduction

Shear instabilities are now widely recognized as a significant mechanism for producing turbulence and mixing in stably-stratified fluids. There are numerous observations of "billow turbulence" in the atmosphere and oceans (see Maxworthy and Browand, 1975) and these events have been associated with Kelvin-Helmholtz instabilities of the wind profile. Laboratory studies by Thorpe (1973) show similar vortex roll-up features and the generation of a turbulent layer of fluid which mixes and spreads the initial shear layer before decaying back to a quiescent flow.

The initial stages of the instability are now well understood. Finite amplitude numerical computations by Patnaik, et al. (1976), Peltier, et al. (1978) have confirmed the linear stability predictions of growth rates and mode structure of the growing waves, and have gone on to calculate the roll-up of the vortex layer. However, these laminar calculations at moderate Reynolds numbers have been unable to identify the secondary instability which results in the breakdown of the vortex into a turbulent layer. Davis and Peltier (1980) made calculations up to a Reynolds number of 500 based on shear layer thickness but failed to produce a secondary instability. In the latter paper, the authors calculated local Rayleigh numbers in the flow, and showed that with a Reynolds number of 500, a region of very high Rayleigh number was produced in the rolled-up vortex. They speculate that this region is in fact convectively unstable, but that the most unstable modes will be longitudinal rolls since the flow is strongly sheared. This hypothesis accounts for the fact that the instabilities have not been triggered in the two-dimensional numerical models.

The aim of the present study is to model the breakdown of the rolled-up vortex layer and the subsequent spread and decay of the turbulence using a second-order closure scheme to describe the three-dimensional, small scale turbulence field. Second-order closure models have been used extensively to study horizontally-homogeneous atmospheric boundary layer flows, and in particular are capable of representing the major dynamical processes involved in turbulent convection (see Wyngaard and Coté, 1974; Lewellen and Teske, 1975; Yamada and Mellor, 1975). [There are difficulties associated with the turbulent transport of turbulent kinetic energy (see Zeman and Lumley, 1976; Andre, et al., 1976), but this is not a serious problem for the prediction of the mean profiles of the major second-order quantities.] Since the model calculates the growth of turbulent correlations in an unstable environment moderately accurately (because the growth is driven directly by production terms in the equations without recourse to empirical closure), we may reasonably expect the results of the calculation to have some validity. One would not have the same expectation of, say, a mixing-length closure model, since the timescale of the growth of the turbulence is the same as the mean flow timescale, while the mixing-length model implicitly assumes that the turbulence is in local equilibrium. Thus turbulent stresses and heat fluxes would be generated as soon as the density profile became unstable if the mixing-length were related to the stability as in the model of Orlanski and Ross (1973).

As we shall demonstrate, the second-order closure model produces results which are certainly qualitatively correct. Quantitative data on turbulence quantities is not sufficiently detailed to make any meaningful assessment of model accuracy, but there are more general quantities associated with the breakdown which can be used for comparison. There are estimates of the



timescale of the turbulence decay and measurements of the final states from the experiments by Thorpe (1973), for example. The final state of the shear layer is an important quantity in deciding the importance of Kelvin-Helmholtz instability as a mixing process in stratified fluids, since this is a measure of the total amount of mixing produced by the event. Another source of data is high-resolution radar probing of the atmosphere, where vortex roll-up events have been reported by many investigators, as discussed in Chapter III of the main report. However, although it is possible to estimate the intensity of the turbulent fluctuations from the intensity of the radar echo, the measurements of the initial wind and temperature profiles immediately prior to the instability are generally inadequate for a crucial test.

In spite of the lack of detailed information, there is certainly sufficient data to determine whether the turbulence model is reasonably accurate, and hopefully some of the numerical results will prompt more detailed measurements.

## 2. Model Equations and Numerical Solution

The second-order closure scheme employed in this study has been described in detail by Lewellen (1977) and we therefore present only the final equations. We consider incompressible, Boussinesq flow, and write the Reynolds-averaged equations with turbulent correlations denoted by an overbar. For two-dimensional motion in the (x,z)-plane, with z in the upward vertical direction we define a stream-function  $\psi$ , such that  $u = \partial\psi/\partial z$ ,  $w = -\partial\psi/\partial x$ . Then the vorticity  $\zeta = \nabla^2\psi$ , and the equations of motion are

$$\frac{\partial \zeta}{\partial t} + u \frac{\partial \zeta}{\partial x} + w \frac{\partial \zeta}{\partial z} = - \frac{g}{T_0} \frac{\partial T}{\partial x} - \frac{\partial^2}{\partial z^2} \overline{uw} - \frac{\partial^2}{\partial x \partial z} (\overline{uu} - \overline{ww}) + \frac{\partial^2}{\partial x^2} \overline{uw}$$

(1)

$$\frac{\partial T}{\partial t} + U \frac{\partial T}{\partial x} + W \frac{\partial T}{\partial z} = - \frac{\partial}{\partial x} \overline{u\theta} - \frac{\partial}{\partial z} \overline{w\theta} \quad (2)$$

$$\begin{aligned} \frac{D}{Dt} \overline{u^2} = & - 2\overline{uu} \frac{\partial U}{\partial x} - 2\overline{uw} \frac{\partial U}{\partial z} + v_c \frac{\partial}{\partial x} \left( q\Lambda \frac{\partial \overline{u^2}}{\partial x} \right) \\ & + v_c \frac{\partial}{\partial z} \left( q\Lambda \frac{\partial \overline{u^2}}{\partial z} \right) - \frac{g}{\Lambda} \left( \overline{uu} - \frac{q^2}{3} \right) - \frac{2bq^3}{3\Lambda} \end{aligned} \quad (3)$$

$$\frac{D}{Dt} \overline{v^2} = v_c \frac{\partial}{\partial x} \left( q\Lambda \frac{\partial \overline{v^2}}{\partial x} \right) + v_c \frac{\partial}{\partial z} \left( q\Lambda \frac{\partial \overline{v^2}}{\partial z} \right) - \frac{g}{\Lambda} \left( \overline{v^2} - \frac{q^2}{3} \right) - \frac{2bq^3}{3\Lambda} \quad (4)$$

$$\begin{aligned} \frac{D}{Dt} \overline{w^2} = & - 2\overline{uw} \frac{\partial W}{\partial x} - 2\overline{ww} \frac{\partial W}{\partial z} + \frac{2g}{T_0} \overline{w\theta} + v_c \frac{\partial}{\partial x} \left( q\Lambda \frac{\partial \overline{w^2}}{\partial x} \right) \\ & + v_c \frac{\partial}{\partial z} \left( q\Lambda \frac{\partial \overline{w^2}}{\partial z} \right) - \frac{g}{\Lambda} \left( \overline{w^2} - \frac{q^2}{3} \right) - \frac{2bq^3}{3\Lambda} \end{aligned} \quad (5)$$

$$\begin{aligned} \frac{D}{Dt} \overline{uw} = & - \overline{uu} \frac{\partial W}{\partial x} - \overline{ww} \frac{\partial U}{\partial z} + \frac{g}{T_0} \overline{u\theta} + v_c \frac{\partial}{\partial x} \left( q\Lambda \frac{\partial \overline{uw}}{\partial x} \right) \\ & + v_c \frac{\partial}{\partial z} \left( q\Lambda \frac{\partial \overline{uw}}{\partial z} \right) - \frac{g}{\Lambda} \overline{uw} \end{aligned} \quad (6)$$

$$\begin{aligned}
\frac{D}{Dt} \overline{u\theta} &= - \overline{uu} \frac{\partial T}{\partial x} - \overline{uw} \frac{\partial T}{\partial z} - \overline{u\theta} \frac{\partial U}{\partial x} - \overline{w\theta} \frac{\partial U}{\partial z} + v_c \frac{\partial}{\partial x} \left( q\Lambda \frac{\partial \overline{u\theta}}{\partial x} \right) \\
&\quad + v_c \frac{\partial}{\partial z} \left( q\Lambda \frac{\partial \overline{u\theta}}{\partial z} \right) - \frac{Aq}{\Lambda} \overline{u\theta}
\end{aligned} \tag{7}$$

$$\begin{aligned}
\frac{D}{Dt} \overline{w\theta} &= - \overline{ww} \frac{\partial T}{\partial x} - \overline{ww} \frac{\partial T}{\partial z} - \overline{u\theta} \frac{\partial W}{\partial x} - \overline{w\theta} \frac{\partial W}{\partial z} + v_c \frac{\partial}{\partial x} \left( q\Lambda \frac{\partial \overline{w\theta}}{\partial x} \right) \\
&\quad + v_c \frac{\partial}{\partial z} \left( q\Lambda \frac{\partial \overline{w\theta}}{\partial z} \right) - \frac{Aq}{\Lambda} \overline{w\theta} + \frac{g}{T_0} \overline{\theta^2}
\end{aligned} \tag{8}$$

$$\begin{aligned}
\frac{D}{Dt} \overline{\theta^2} &= - 2\overline{u\theta} \frac{\partial T}{\partial x} - 2\overline{w\theta} \frac{\partial T}{\partial z} + v_c \frac{\partial}{\partial x} \left( q\Lambda \frac{\partial \overline{\theta^2}}{\partial x} \right) \\
&\quad + v_c \frac{\partial}{\partial z} \left( q\Lambda \frac{\partial \overline{\theta^2}}{\partial z} \right) - \frac{2bsq}{\Lambda} \overline{\theta^2}
\end{aligned} \tag{9}$$

$$\begin{aligned}
\frac{D}{Dt} \Lambda = & 0.35 \frac{\Lambda}{q^2} \left( \overline{uu} \frac{\partial U}{\partial x} + \overline{uw} \frac{\partial U}{\partial z} + \overline{uw} \frac{\partial W}{\partial x} + \overline{ww} \frac{\partial W}{\partial z} \right) \\
& + 0.6bq + v_c \frac{\partial}{\partial x} \left( q\Lambda \frac{\partial \Lambda}{\partial x} \right) + v_c \frac{\partial}{\partial z} \left( q\Lambda \frac{\partial \Lambda}{\partial z} \right) \\
& - \frac{0.375}{q} \left[ \left( \frac{\partial q\Lambda}{\partial x} \right)^2 + \left( \frac{\partial q\Lambda}{\partial z} \right)^2 \right] + \frac{0.8\Lambda}{q^2} \frac{g}{T_0} \overline{w\theta}
\end{aligned} \tag{10}$$

In the above,  $(U, W)$  is the mean velocity,  $T$  is the mean temperature,  $(u, v, w)$  is the turbulent velocity fluctuation,  $\theta$  is the temperature fluctuation, and  $q = [\overline{u^2} + \overline{v^2} + \overline{w^2}]^{1/2}$ .  $\Lambda$  is a length scale, and appears in the modelled terms in the Reynolds-averaged turbulent correlation equations. The values of the empirical constants are as follows:  $b = 1/8$ ,  $A = 0.75$ ,  $v_c = 0.3$ , and  $s = 1.8$ . These values were previously chosen to match model results with a set of experiments with simple geometries as described by Lewellen (1977).

For the Kelvin-Helmholtz instability calculation, we begin with a profile of temperature and velocity, viz,

$$T = T_0 + \Delta T \tanh \frac{z}{\delta} \tag{11}$$

$$U = \Delta U \tanh \frac{z}{\delta} \tag{12}$$

Note that velocity and temperature both have the same profile shape. The initial conditions define a Richardson number  $Ri = (g/T_0)(\Delta T \delta / \Delta U^2)$ , which will be the basic dimensionless number in our experiments. The problem also contains a Reynolds number, but since we have omitted explicit laminar diffusive terms from the equations of motion, we are effectively studying the high Reynolds number limit.

In order to begin the integration, we have to specify initial values for the turbulence energy,  $q^2$ , and the length scale  $\Lambda$ ; in the calculations reported here, all other turbulence quantities were initially set to zero. A perturbation vorticity was also added so that the instability would amplify this disturbance and produce the vortex roll-up. The specification of these initial conditions will be discussed in the next section.

Periodic boundary conditions were employed in the x-direction, and the length of the domain was chosen somewhat larger than the wavelength of the fastest growing linear mode. This choice is suggested by the nonlinear calculations of Patnaik, et al. (1976), which show that the longer waves grow to larger amplitude, and may therefore dominate the finite amplitude development of the wave. For most of our integrations, a domain length of  $15\delta$  was used, although some runs were made with different lengths to investigate the sensitivity.

The boundaries in the z-direction were placed sufficiently far from the shear layer for them to have negligible effect on the flow development. A zero normal gradient condition was specified on all flow quantities on the upper and lower boundaries.

The equations of motion are discretized on a finite-difference grid which is uniformly spaced in the horizontal but has finer vertical resolution in the vicinity of the shear layer. The equations are solved using centered spatial

derivatives, and an ADI scheme for the temporal derivative. The advection operator conserves first and second moments apart from time-dependence errors arising from the use of explicit advective velocity components in the ADI scheme. The time-stepping is made more stable by the introduction of a coupling between the mean variables and the turbulent fluxes by the artifice of an additional implicit eddy diffusive flux which is explicitly subtracted when the correct turbulent flux is added (Lewellen and Sheng, 1980). Provided the time-step is sufficiently small, the errors introduced by this procedure will be negligible.

Finally, the Poisson equation for the streamfunction is solved directly using the decomposition method of Swarztrauber and Sweet (1975).

### 3. Results

We consider an initial state, as described in the Section 2, given by

$$T = T_0 + \Delta T \tanh \frac{Z}{\delta} \quad (13a)$$

$$U = \Delta U \tanh \frac{Z}{\delta} \quad (13b)$$

which defines a Richardson number  $Ri = (g\delta\Delta T/T_0\Delta U^2)$ . This is in fact the minimum gradient Richardson number, defined by  $Ri_G = [(g/T_0)(\partial T/\partial z)]/(\partial U/\partial z)^2$ , which occurs at  $z = 0$ . Linear inviscid theory (Miles, 1961) shows that the flow is stable to small perturbations provided  $Ri > 0.25$ .

We first present detailed results from a calculation with  $Ri = 0.1$ . In this example, we applied a sinusoidal (in  $x$ ) variation to the vorticity in order to initiate the instability. The perturbation vorticity amplitude of

$0.1\Delta U/\delta$  is quite large; this is because we are mainly interested in the finite-amplitude breaking of the billow and the subsequent turbulent development, so that we do not wish to spend time computing the initial growth from a very small perturbation. Checks were made to ensure that the initial perturbation was sufficiently small that it did not influence the finite-amplitude development.

The turbulence energy  $q^2$  was initially set at  $10^{-3}\Delta U^2$  throughout the domain, with the turbulence length scale,  $\Lambda$ , set equal to  $0.4\delta$ . The turbulence energy is initially small enough to be effectively zero, but the initial length scale does have some effect on the results. Variations in these initial values will be discussed in more detail in Section 6 below.

The integration was performed using a domain of length  $15\delta$  and a height of  $12\delta$  centered on the mid-point of the shear layer. The computational mesh consisted of  $41 \times 61$  points, with 41 points spaced uniformly in the horizontal, and a non-uniform vertical mesh giving a grid spacing of  $0.1\delta$  in the central region and expanding out to roughly  $0.2\delta$ .

Figure 1 shows a sequence of contour plots of the dimensionless temperature field,  $(T - T_0)/\Delta T$ , at dimensionless time  $\tau = 1.5, 2.8, 4.3, 5.8, 7.3$ , and  $11.8$ , where  $\tau = t(g\Delta T/T_0\Delta U)$ . Corresponding plots of the small-scale turbulent energy  $q^2/\Delta U^2$  are presented in Figure 2. The billow develops initially as an effectively laminar flow with a growing vortex core in the center, and thin braids forming between the cores. The initial turbulent perturbation in  $q^2$  is amplified slowly in the braids where the shear is highest, and the local Richardson number is lowest. At  $\tau = 2.8$  the instability has vertically reached its maximum amplitude, with temperature contours quite convoluted in the vortex core, and the braids have become very thin. At this stage the temperature field is statically unstable in the core,

and the  $q^2$  contours show growth of turbulence associated with the buoyant instability, although the turbulence is still relatively small everywhere with the buoyantly produced turbulence in the core comparable with the turbulence levels in the braids.

At the next time,  $\tau = 4.3$ , most of the temperature structure in the core has been mixed by the turbulence which has reached a relatively high level around the outer part of the core; the maximum value of  $q^2$  is  $0.18\Delta U^2$ . The core has already begun to spread horizontally, although the braids are still quite distinct. At  $\tau = 5.8$ , the braids have been mixed, and the turbulence has spread throughout the layer in the horizontal. There is evidence of smaller scale disturbances in the temperature field, and a movie of the time evolution shows them to be travelling wave-like disturbances moving along the top and bottom of the layer, and also weakly rolling up in a manner similar to the original instability. However, they are also being mixed by the high background turbulence so that they do not persist long. There is also some remnant of the original large scale vortex which continues to slowly turn the isotherms. We can still identify the regions of production of the turbulent energy, since the level of  $q^2$  in the center is about twice the level at the edges of the domain.

The trend toward flattening the isotherms, and spreading the turbulence horizontally continues until at the latest time,  $\tau = 11.8$ , there is virtually no further mean motion, and the turbulence is almost homogeneous in the horizontal. The turbulence level has dropped to  $0.022\Delta U^2$  at this stage, i.e., almost a factor of 10 below its maximum amplitude which occurred around  $\tau = 4.3$ .



The evolution described above is qualitatively similar to the turbulent breakdown of Kelvin-Helmholtz billows generated in the laboratory as described by Thorpe (1973). In the tank experiments, the small-scale turbulence is generated in the vortex cores, and spreads horizontally to amalgamate the billows at dimensionless time of roughly  $\tau = \tau_0 + 2$ , where  $\tau_0$  is the time at which the fine-scale turbulence first appears. Since  $\tau_0 \approx 3$  in the numerical integration, the observation that the turbulence merges horizontally at some time between  $\tau = 4.3$  and  $\tau = 5.8$  is quite consistent with the experimental data. Furthermore, the thickness of the region of turbulent fluid increases slowly after merging in the horizontal and seems to reach an equilibrium level near the end of the integration. This is again consistent with the experimental observations of Thorpe (1973), which show the layer increasing in thickness up to  $\tau = \tau_0 + 7$ , i.e.,  $\tau = 10$  in our case. Also the non-dimensional height,  $R_L = g(\Delta T.h)/(2\Delta U^2)$  where  $h$  is the thickness of the turbulent layer, reaches a value of about 0.4 in accordance with the experiments.

Some insight into the dynamics is obtainable from examination of the energy budgets. In Figure 3, we plot the roll energy,  $EK$ , and the small-scale turbulence energy,  $EQ$ , defined by

$$EK = \frac{1}{\Delta U^2 \delta^2} \iint \{ [u - \bar{u}(z)]^2 + w^2 \} dx dz \quad (14)$$

$$EQ = \frac{1}{\Delta U^2 \delta^2} \iint q^2 dx dz \quad (15)$$

where

$$\overline{u}(z) = \frac{1}{L} \int_0^L U \, dx \quad (16)$$

We can see the rapid initial build-up of roll energy as the growing billow extracts kinetic energy from the mean shear, whilst the turbulence energy  $E_T$  remains virtually constant at its initial perturbation level. At roughly  $\tau = 2.5$ ,  $E_T$  begins to increase as the billow starts to break, and  $E_K$  levels off at its maximum value. The kinetic energy is effectively transferred via potential energy to the small-scale turbulence which reaches a peak at  $\tau = 5$ . The large scale motion loses its energy very rapidly after breaking, while the small-scale turbulence persists throughout the integration, and exhibits a relatively slow rate of decay. Thorpe (1973) shows that the turbulence persists until roughly  $\tau = \tau_0 + 12 = 15$ , at which point there appears to be a collapse of the turbulent eddies into striated structures. The present second-order closure model of the small-scale eddies provides a poor representation of this final stage of the decay of turbulence in a stably-stratified medium, and we have therefore not attempted to integrate beyond  $\tau = 13$ .

Profiles of the initial and final ( $\tau = 11.8$ ) local gradient Richardson number,

$$Ri_G = \frac{g}{T_0} \frac{\partial T / \partial z}{(\partial U / \partial z)^2} \quad (17)$$

are shown in Figure 4. The final value of  $Ri_G$  in the layer is not quite

constant, but lies between 0.3 and 0.35. This is again consistent with Thorpe's estimate of the final Richardson number. This value is significantly larger than the critical value of 0.25, so that the mixing-process apparently extracts sufficient energy from the initially unstable flow to mix the mean profiles further than the point at which no more energy can be extracted. The agreement between the calculation and the experiment on this number is some confirmation that the model describes the energy transfers in the initial stages reasonably accurately. The basic energy source is kinetic energy produced by the billow acting on the mean shear, and it seems likely that the final amount of mixing will be determined by the amount of energy that the billow can extract before it breaks. If the turbulence model predicted the wrong time-scales for the breaking process, we would be unlikely to obtain the correct final state.

The evolution from an initial Richardson number of 0.2 is illustrated in Figures 5 and 6. A mesh of  $41 \times 61$  grid points was used, as in the previous case, with a domain size of 158 in the horizontal again, but only 88 in the vertical. Contours of temperature and small-scale turbulent kinetic energy at  $\tau = 3.0, 6.0, 9.0, 14.6,$  and  $20.6$ . Clearly, the billow is much more restricted in the vertical due to the fact that there is relatively less kinetic energy available in the mean shear to drive the instability against the restoring buoyancy forces. The higher initial Richardson number also makes the turbulent kinetic energy production in the braids less important, so that at  $\tau = 3$  when the isotherms are only just being overturned, the maximum energy is already in the vortex core. Furthermore, the restricted size of the vortex core appears to result in the turbulence being spread throughout the region rather than being confined to the outer half of the vortex as in the  $Ri = 0.1$  case. The velocity in the core is also smaller in the  $Ri = 0.2$  case,

so there is less tendency for the turbulence to be swept around the outer part of the vortex.

As in the  $Ri = 0.1$  case, the turbulent vortex core spreads horizontally, with small scale waves running along the top and bottom of the layer producing local turbulence maxima. Finally, the mean motion is totally suppressed, and the isotherms become horizontal, and we have a homogeneous layer of turbulence.

The evolution of the large- and small-scale kinetic energies is shown in Figure 7. Comparing this with Figure 3, we see that the large-scale roll-up extracts much less energy than the  $Ri = 0.1$  case, but the maximum in small-scale energy is almost as large as the large-scale. Since the small-scale energy arises from the potential energy created by the roll-up process, this demonstrates that there is more potential energy per unit kinetic energy in the  $Ri = 0.2$  case. This should not be a surprise, since the Richardson number is a measure of the ratio of potential to kinetic energy in the initial profile, and a linearized disturbance will contain energy in the same proportion.

We may also note that if the time scale for the  $Ri = 0.2$  case is divided by two, then a number of features match up with the  $Ri = 0.1$  case. Defining  $\tau' = \tau/Ri$ , then the large scale energy maximizes at  $\tau' \approx 50$  in both cases. Furthermore, the small-scale energy is down to about half its maximum value at  $\tau' = 100$ . It seems that the timescale is determined by the shear velocity and the layer thickness, while the buoyancy timescale determines the details of the roll-up such as core size and energy partitioning.

The profile of gradient Richardson number at the final time,  $\tau = 20.6$ , is shown in Figure 8 for the case with initial  $Ri = 0.2$ . The final state is a region of virtually constant Richardson number at a value of roughly 0.45,

slightly larger than the case with  $Ri = 0.1$ . The laboratory experiments of Thorpe (1973) indicate that the final Richardson number is independent of the initial value, the final value being between 0.26 and 0.385, but this result is for initial Richardson number less than 0.14.

In considering atmospheric observations, we must recognize the fact that the high-resolution radars are measuring small-scale refractive index changes. The latter are very closely related to humidity and temperature fluctuations rather than the turbulence energy itself. Since humidity is a scalar, it satisfies the same equation as temperature, and it can be shown that the mean square humidity fluctuations are identical to the mean square temperature fluctuation provided the initial profiles are identical. It is therefore instructive to look at the behavior of temperature fluctuations, remembering that asymmetries can be introduced by having an asymmetric humidity profile. In fact, the length scale of the energy-containing turbulent eddies also affects the refractive index fluctuations at the short wavelengths visible to the radar, but variations in the length scale do not produce any significant changes in the pattern.

Contours of the mean square temperature fluctuation,  $\overline{\theta^2}/\Delta T^2$ , for the case with initial  $Ri = 0.1$  are shown in Figure 9 at  $\tau = 1.5, 2.8, 4.3$ , and  $8.8$ . The most obvious feature is the highly localized nature of  $\overline{\theta^2}$ . Initially,  $\overline{\theta^2}$  is concentrated in the developing braids, where the temperature gradient is very large. As the billow begins to break, there are local patches of high temperature variance in the mixing regions around the edges of the core, but these patches do not spread throughout the vortex core as it breaks. Rather, as the vortex breaks down, the temperature variance vanishes, and only remains in the braids at  $\tau = 4.3$ . As the braids are eroded by the turbulent mixing, the temperature variance decays, but remains in narrow bands which are drawn

out horizontally until they are almost flat. This qualitative description also applies to the  $Ri = 0.2$  case.

The difference between the temperature variance and velocity variance is also evident by comparing Figure 10 with Figures 3 and 7. The integrated value of the temperature variance tends to both grow and decay more rapidly than the integrated velocity variance.

The contrast in behavior between the temperature variance and turbulent kinetic energy may be somewhat better understood by examining the production terms in the second-order turbulence correlations. We have

$$P(q^2) = -2 \overline{u_i u_k} \frac{\partial U_i}{\partial x_k} + \frac{2g}{T_0} \overline{w\theta} \quad (18)$$

$$P(\overline{w\theta}) = -\overline{w^2} \frac{\partial T}{\partial z} - \overline{uw} \frac{\partial T}{\partial x} - \overline{w\theta} \frac{\partial W}{\partial z} - \overline{u\theta} \frac{\partial W}{\partial x} + \frac{g}{T_0} \overline{\theta^2} \quad (19)$$

$$P(\overline{\theta^2}) = -\overline{w\theta} \frac{\partial T}{\partial z} - \overline{u\theta} \frac{\partial T}{\partial x} \quad (20)$$

where  $P( )$  denotes production terms. The only other terms in the relevant equations are diffusion and dissipation terms. Now, as the vortex core rolls up, large gradients of mean quantities are generated, and consequently the production terms are also large.

Once the vortex breaks the mean gradients are rapidly mixed away, and therefore there is only diffusion and dissipation of  $\overline{\theta^2}$  which must begin to decay immediately. However, there is still production of  $\overline{w\theta}$  due to the term involving the temperature variance. Thus heat flux does not decay as quickly



as  $\overline{\theta^2}$ . Furthermore,  $\overline{w\theta}$  is the main production term in the  $q^2$  equation within the core, so the turbulent kinetic energy continues being produced while  $\overline{\theta^2}$  is decaying. Thus  $q^2$  grows in the core, and eventually spreads outward horizontally, whilst  $\overline{\theta^2}$  vanishes in the core, and only remains significant in the braids, where there is gradient production. When the braids are eroded, the temperature variance is slowly diffused and dissipated, while the mean shear stretches the regions of high  $\overline{\theta^2}$  into nearly horizontal stratifications.

The differences between the  $q^2$  and  $\overline{\theta^2}$  patterns are thus quite plausible. We note that this dynamical effect could not be reproduced by an effective viscosity model which has no equivalent interaction between second-order quantities. We should also note the implication that high resolution radar returns from atmospheric billow events of this type should always show highly-structured patterns with narrow bands of high intensity, rather than a homogeneous layer of turbulence. This is quite consistent with the observations reported in the literature. Figure 11 showing the evolution of K-H wave breaking as received by radar (Browning and Watkins, 1970) shows the same features as exhibited in Figure 9.

#### 4. Sensitivity Studies

There are a number of parameters in the numerical integrations presented in the previous section which must be chosen independently from the physical constants of the problem. These parameters include numerical discretization quantities such as the grid size and initial conditions for the dynamic variables. We do not include the empirical constants in the second-order turbulence closure model, since these are taken to be fixed from comparison with other experimental data. It is important to obtain some indication of the dependence of the results on these external parameters if we are to gain a

useful understanding from the numerical integrations. The few main quantities which need to be chosen are:

- 4.1 numerical resolution
- 4.2 initial turbulence level
- 4.3 initial turbulence length scale
- 4.4 length of the integration domain

We shall investigate variations in each of these quantities independently for the case with  $Ri = 0.2$ .

4.1 Numerical resolution. The integration presented in the previous section was carried out with a mesh of  $41 \times 61$  points; this was chosen to provide adequate resolution of the small scale flow features. This fact is demonstrated by comparing the results with those from an integration using  $32 \times 40$  grid-points. The kinetic energy evolution from both integrations is shown in Figure 12. Unfortunately, the low resolution integration had a slightly smaller initial vorticity perturbation which is responsible for some of the differences, but notwithstanding this initial discrepancy, the overall budgets are within about 10%.

Contour plots from the two runs show that the low resolution integration has much more numerical noise around the point where the vortex is breaking and gradients are highest. However, this does not adversely affect the evolution, as can be seen from the kinetic energy plots, and the two integrations do remain very close together throughout the period.



4.2 Initial turbulence level. The remaining sensitivity tests are all carried out using the low resolution model, so we are comparing with the run in Figure 12(b). Figure 13 shows the kinetic energy evolution using an initial value for  $q^2$  of  $3 \times 10^{-3} \Delta U^2$ , which is three times that of the previous run. The main effect here is a reduction in the large scale energy by about 12%, and an increase of about 10% in the small scale energy maximum. Thus a higher background turbulence level retards the development of the instability slightly, and also allows the vortex to break a little more quickly, extracting more of the potential energy from the roll-up. However, the effect is not large, and it can be reasonably assumed that the results are representative of small background turbulence levels. In fact, the initial value for  $q^2$  was chosen as large as reasonably possible in order to provide some turbulent mixing to prevent the braids from becoming too thin to be resolved by the numerical grid. Since the growth of  $q^2$  in the breaking is via the buoyancy term, it is virtually independent of the initial value for  $q^2$ , due to the rapid exponential growth in the initial stages. We therefore feel justified in choosing  $q^2$  large enough to control the braid thickness, as long as it is not large enough to influence the dynamics of the breaking.

Although the higher value of initial  $q^2$ ,  $3 \times 10^{-3} \Delta U^2$ , appears to have a small effect on the energy budgets, there was much less energy in the short numerical grid modes, so this run was chosen as the base integration for comparison of turbulence length scale and domain length variations.

4.3 Initial turbulence length scale. This is probably the most difficult and unfortunately one of the most sensitive parameters to choose. The choice of initial  $\Lambda$  is not entirely arbitrary, since it must bear some relation to the thickness of the shear layer,  $\delta$ , if we are studying turbulence generated

by the instability mechanism itself. We chose the value  $0.4\delta$  for the runs presented in the previous section; this is a reasonable value for a turbulence length scale, but cannot be justified too strongly. In order to test the sensitivity, we carried out integrations with initial  $\Lambda = 0.2\delta$  and  $0.8\delta$ , and the energy evolutions from all three runs are shown in Figure 14.

Firstly, the large scale kinetic energy is largely unaffected by the choice of  $\Lambda$ . The only difference is in the oscillation in the decaying phase of EK, which is accentuated by small values of  $\Lambda$ . However, the small scale energy does depend quite strongly on the initial value of  $\Lambda$ . Changing  $\Lambda$  by a factor of 2 in either direction from  $0.4\delta$  changes the maximum turbulence energy by almost a factor of 2 in the same direction. The source of the problem is the length scale equation, which does not allow the length scale to grow sufficiently quickly during the breaking stage, so that the turbulence does remember its initial condition for a long time. The length scale does grow as the billow breaks, but not so fast as  $q^2$  which is virtually independent of its initial condition.

On this point, all we are able to say is that  $0.4\delta$  is a reasonable initial value for  $\Lambda$ , and the results of this section illustrate the effect of varying  $\Lambda$ . We should emphasize that the qualitative results, both in the energy plots and the details of the contour fields, are not significantly changed by this variation in  $\Lambda$ . Apparently the initial value for  $\Lambda$  ought to be fixed by comparison of turbulence levels with experimental observation, or an improved dynamical equation for  $\Lambda$  is needed.

4.4 Integration domain length. We choose the wavelength of the unstable mode we are studying by fixing the length of our periodic domain. The runs in the previous section used a length of  $15\delta$ , which was suggested by the laminar

numerical integrations of Patnaik, et al. (1976) as giving the mode which grew to largest amplitude.

Figure 15 shows the energies from three runs with domain lengths of  $10\delta$ ,  $15\delta$ , and  $20\delta$ . Allowing for the length of the domain, the short domain clearly restricts the growth of the billow significantly; the large scale energy maximum is nearly a quarter of the  $15\delta$  domain case (i.e., the energy density is about 35%), and the turbulence energy is about half (i.e., energy density is 75%). It is therefore unlikely that this mode would be the dominant finite amplitude mode, since the longer modes would continue to grow. The long domain,  $20\delta$ , has a significantly larger energy in the vortex, but allowing for the length of the domain, the energy density per unit horizontal length is only a little longer. The turbulence energy per unit length is actually smaller.

Thus the case with a domain length of  $15\delta$  seems to represent the most efficient mode for producing kinetic energy, although there is not a great deal of difference with a length of  $20\delta$ .

## 5. Conclusions

This two-dimensional numerical study of breaking Kelvin-Helmholtz waves using a second-order turbulence closure model to describe the small-scale turbulence has shown agreement with experimental observations on several points. More importantly, given the lack of precise quantitative experimental data, the numerical integrations have suggested several general features of the dynamics of the fine-scale turbulence in addition to the specific quantitative predictions of the particular cases studied. These general points await further experimental evidence to provide confirmation or refutation.

The results demonstrate the utility of the closure model in studying this problem; the closure model contains most of the important dynamical effects necessary for a description of the flow. Furthermore, it is probably the minimum sophistication capable of describing the fine-scale turbulence, since it has shown that the turbulence develops on the same time scale as the mean flow, so that equilibrium assumptions would not be correct.

The numerical results indicate the correct qualitative behavior, namely the billow breaks to produce turbulence in the vortex core, which then spreads horizontally to form a homogeneous layer. The layer also spreads vertically to a small extent. The time-scale and extents of the spreading are in broad agreement with the visual observations of Thorpe (1973). The final value of the Richardson number for an initial  $Ri$  of 0.1 is consistent with Thorpe's measured value of  $0.32 \pm 0.06$ . However, Thorpe notes no dependence on initial  $Ri$  for  $Ri < 0.14$ , whilst our final value for  $Ri = 0.2$  is significantly higher. It remains to be clarified whether the experiments would show such a trend at higher values of  $Ri$ .

The integrations at different initial Richardson numbers suggests that the advective timescale  $\lambda/\Delta u$ , where  $\lambda$  is the wavelength of the billow and  $\Delta u$  the velocity difference across the shear layer, is the important timescale for the growth, breaking, and subsequent decay of the turbulence. The buoyancy timescale affects the type of flow since the ratio of the timescales is proportional to the square root of the Richardson number. It is quite possible that the buoyancy timescale is also important in the late stages of the decay, when the turbulent eddies collapse as the mean density gradient is re-established. We have not attempted to seriously study this part of the evolution, since the closure model has deficiencies in the limit of strongly-stratified turbulence.

The breaking of the billow itself is seen to be generated by a convective instability of the overturned fluid at the top and bottom of the vortex core. This turbulence is swept around the vortex, and actually remains largely in the outer part of the vortex for a significant length of time in the small Richardson number case. The turbulence eventually spreads throughout the layer, and amalgamates to form a horizontally homogeneous layer.

Finally, the results indicate that the temperature variance,  $\overline{\theta^2}$ , evolves quite differently from the turbulent-kinetic energy. Different buoyancy production terms in the second-order turbulence correlation equations imply the rapid decay of  $\overline{\theta^2}$  in the breaking vortex core, so that the regions of high  $\overline{\theta^2}$  remain highly localized in space. Effectively,  $\overline{\theta^2}$  is generated initially in the braids of the developing billow, and these long thin patches are then stretched out by the mean shear as they diffuse and decay after the braids have been moved away. The evolution of the Kelvin-Helmholtz wave breaking as observed by radar in the atmosphere is quite consistent with the evolution of the variance of humidity or temperature predicted by the model calculation.

#### Acknowledgements

This research was supported by the Office of Naval Research under contract number N00014-80-C-0873, and also by the Naval Air Systems Command under contract number N00019-80-C-0617.

## REFERENCES

- André, J. C., Moor, G., de LaCarrère, P., and Vachat, R. du, (1976);  
"Turbulence Approximation for Inhomogeneous Flows", J. Atmos. Sci. 33,  
476-491.
- Browning, K. A., and Watkins, C. D., (1970); "Observations of Clear Air  
Turbulence by High Power Radar", Nature 227, 260-263.
- Davis, P. A., and Peltier, W. R., (1979); "Some Characteristics of the  
Kelvin-Helmholtz and Resonant Overreflection Modes of Shear Flow  
Instability and of Their Interaction through Vortex Pairing", J. Atmos.  
Sci. 36, 2394-2412.
- Lewellen, W. S., (1977); "Use of Invariant Modeling", in Handbook of  
Turbulence, (edited by Walter Frost and Trevor H. Moulden), Plenum  
Publishing Corporation, Vol. 1, pp. 237-280.
- Lewellen, W. S., and Sheng, Y. P., (1980); "Modeling Tornado Dynamics",  
Nuclear Regulatory Commission, NUREG/CR-1585, 227 pp.
- Lewellen, W. S., Teske, M. E., and Donaldson, C. duP., (1975); "Variable  
Density Flows Computed by a Second-Order Closure Description of  
Turbulence", AIAA J. 14, 382-387.
- Maxworthy, T, and Browand, F. K., (1975); "Experiments in Rotating and  
Stratified Flows with Oceanographic Application", Ann. Rev. Fluid Mech. 7,  
273-305.
- Miles, J. W., (1961); "On the Stability of Heterogeneous Shear Flows", J.  
Fluid Mech. 10, 496-508.
- Orlanski, I., and Ross, B. B., (1973); "Numerical Simulation of the Generation  
and Breaking of Internal Gravity Waves", J. Geophys. Res. 78, 8808-8826.

- Patnaik, P. C., Sherman, F. S., and Corcos, G. M., (1976); "A Numerical Simulation of Kelvin-Helmholtz Waves of Finite Amplitude", J. Fluid Mech. 73, 215-140.
- Swartztrauber and Sweet (1975); "Efficient FORTRAN Subprograms for the Solution of Elliptic Partial Differential Equations", NCAR-TN/1A-109.
- Thorpe, S. A., (1973); "Experiments on Instability and Turbulence in a Stratified Sear Flow", J. Fluid Mech. 61, 731-751.
- Wyngaard, J. C., and Coté, O. R., (1974); "The Evolution of the Convective Planetary Boundary Layer - A Higher Order Closure Model Study", Boundary Layer Meteorology 7, 289-308.
- Yamada, T., and Mellor, G. L., (1975); "A Simulation of the Wangara Atmospheric Boundary Layer Data", J. Atmos. Sci. 32, 2309-2329.
- Zeman, O., and Lumley, J. L., (1976); "Modeling Buoyancy Driven Mixed Layers", J. Atmos. Sci. 33, 1974-1988.



## LIST OF FIGURES

- Figure 1 - Isopleths of dimensionless temperature  $(T - T_0)/\Delta T_h$  for the case with  $Ri = 0.1$ . The contour interval is 0.2, and positive contours (i.e., lighter fluid) are denoted by a dashed line. (a)  $\tau = 1.5$ , (b)  $\tau = 2.8$ , (c)  $\tau = 4.3$ , (d)  $\tau = 5.8$ , (e)  $\tau = 7.3$ , and (f)  $\tau = 11.8$ .
- Figure 2 - Isopleths of dimensionless turbulence kinetic energy,  $q^2/\Delta U^2$  at the same times as Figure 1, i.e., (a)  $\tau = 1.5$ , (b)  $\tau = 2.8$ , (c)  $\tau = 4.3$ , (d)  $\tau = 5.8$ , (e)  $\tau = 7.3$ , and (f)  $\tau = 11.8$ . Contour intervals are as follows: (a) 0.001, (b) 0.005, (c) 0.01, (d) 0.01, (e) 0.007, and (f) 0.002.
- Figure 3 - Evolution of total kinetic energies,  $E_K$  and  $E_Q$ , for the large eddy and the small-scale turbulence in the  $Ri = 0.1$  case.
- Figure 4 - Profiles of gradient Richardson number,  $Ri_G$ , for the  $Ri = 0.1$  case. Solid line is the initial profile at  $\tau = 0$ , dashed line is the profile at  $\tau = 11.8$ .
- Figure 5 - Isopleths of dimensionless temperature  $(T - T_0)/\Delta T$  for the case with  $Ri = 0.2$  at (a)  $\tau = 3$ , (b)  $\tau = 6$ , (c)  $\tau = 9$ , (d)  $\tau = 14.6$ , (e)  $\tau = 20.6$ . Contour interval is 0.2.
- Figure 6 - Isopleths of dimensionless turbulence kinetic energy,  $q^2/\Delta U^2$ , for  $Ri = 0.2$  at (a)  $\tau = 3$ , (b)  $\tau = 6$ , (c)  $\tau = 9$ , (d)  $\tau = 14.6$ , (e)  $\tau = 20.6$ . Contour intervals are (a) 0.0003, (b) 0.006, (c) 0.007, (d) 0.003, (e) 0.001.
- Figure 7 - Evolution of large scale and small scale eddy kinetic energies for the case with  $Ri = 0.2$ .



Figure 8 - Profile of gradient Richardson number,  $Ri_G$ , for the  $Ri = 0.2$  case, at  $\tau = 23$ .

Figure 9 - Isopleths of dimensionless temperature variance,  $\overline{\theta^2}/\Delta T^2$ , for the case with  $Ri = 0.1$ . (a)  $\tau = 1.5$ , (b)  $\tau = 2.8$ , (c)  $\tau = 4.3$ , (d)  $\tau = 8.8$ . Contour intervals are (a) 0.004, (b) 0.02, (c) 0.02, (d) 0.002.

Figure 10 - Evolution of the total volume-integrated temperature variance,  $ET$ , for the case with (a)  $Ri = 0.1$ , (b)  $Ri = 0.2$ .

Figure 11 - Schematic representation of the life cycle of an individual Kelvin-Helmholtz billow based on the data in the earlier figures. Time progresses from right to left. Thick lines correspond to the detectable clear air radar echo, which started as a single layer at 1243 and finished as a double layer at 1258 GMT. Schematic vertical profiles of  $(\Delta\theta/\Delta z)$  are indicated before and after the occurrence of Kelvin-Helmholtz instability. (From Browning and Watkins, 1970).

Figure 12 - Evolution of eddy kinetic energies for  $Ri = 0.2$  with (a) high resolution  $41 \times 61$ , (b) low resolution  $32 \times 40$ .

Figure 13 - Evolution of eddy kinetic energies for  $Ri = 0.2$  with different initial values of  $q^2/\Delta U^2$ , (a)  $10^{-3}$ , (b)  $3 \times 10^{-3}$ .

Figure 14 - Evolution of eddy kinetic energies for  $Ri = 0.2$  with different initial values of  $\Lambda/\delta$ , (a) 0.2, (b) 0.4, (c) 0.8.

Figure 15 - Evolution of eddy kinetic energies for  $Ri = 0.2$  with different domain lengths, (a)  $10\delta$ , (b)  $15\delta$ , (c)  $20\delta$ .

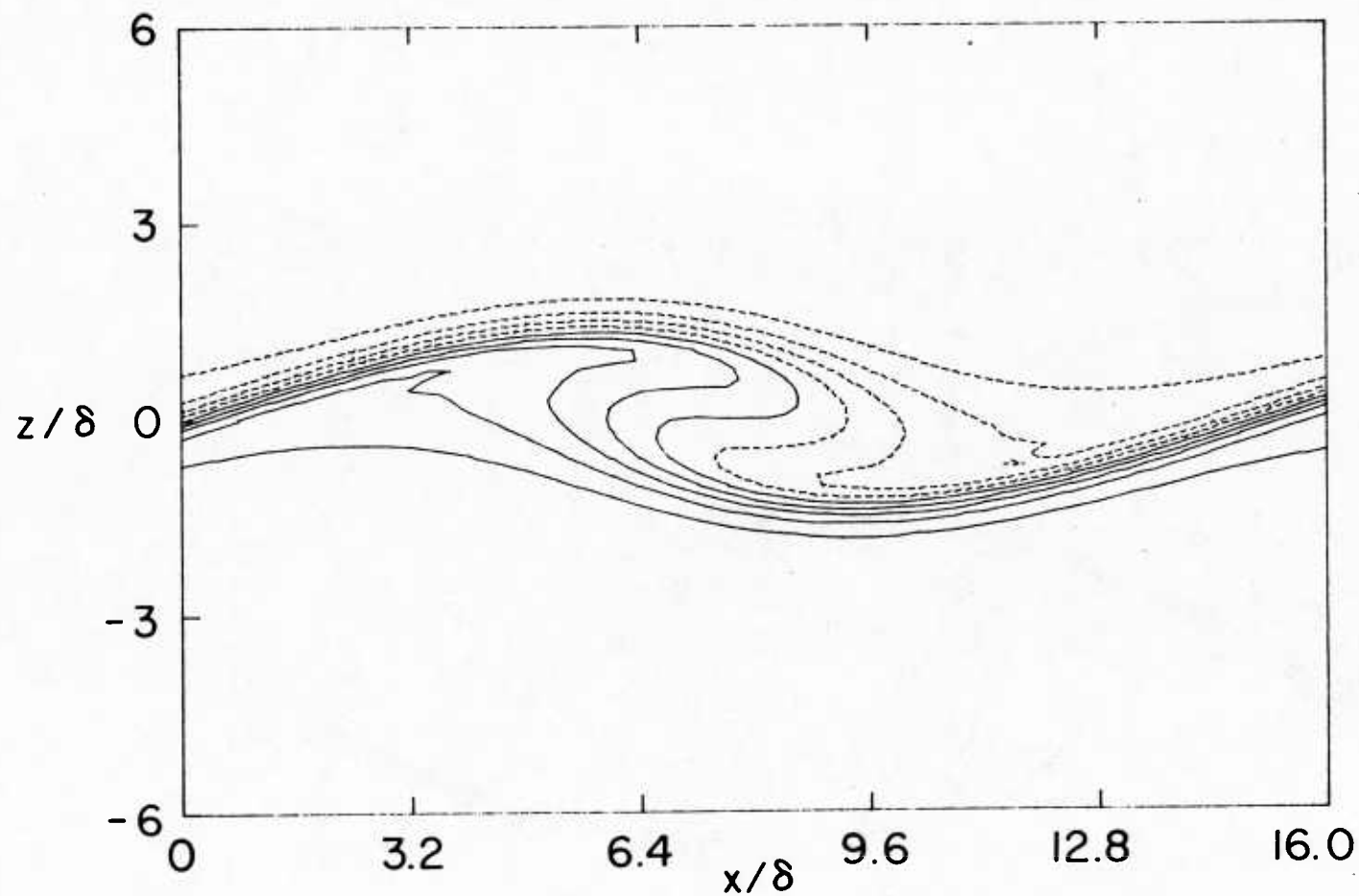


Figure 1 - Isopleths of dimensionless temperature  $(T - T_0)/\Delta T_h$  for the case with  $Ri = 0.1$ . The contour interval is 0.2, and positive contours (i.e., lighter fluid) are denoted by a dashed line. (a)  $\tau = 1.5$ .

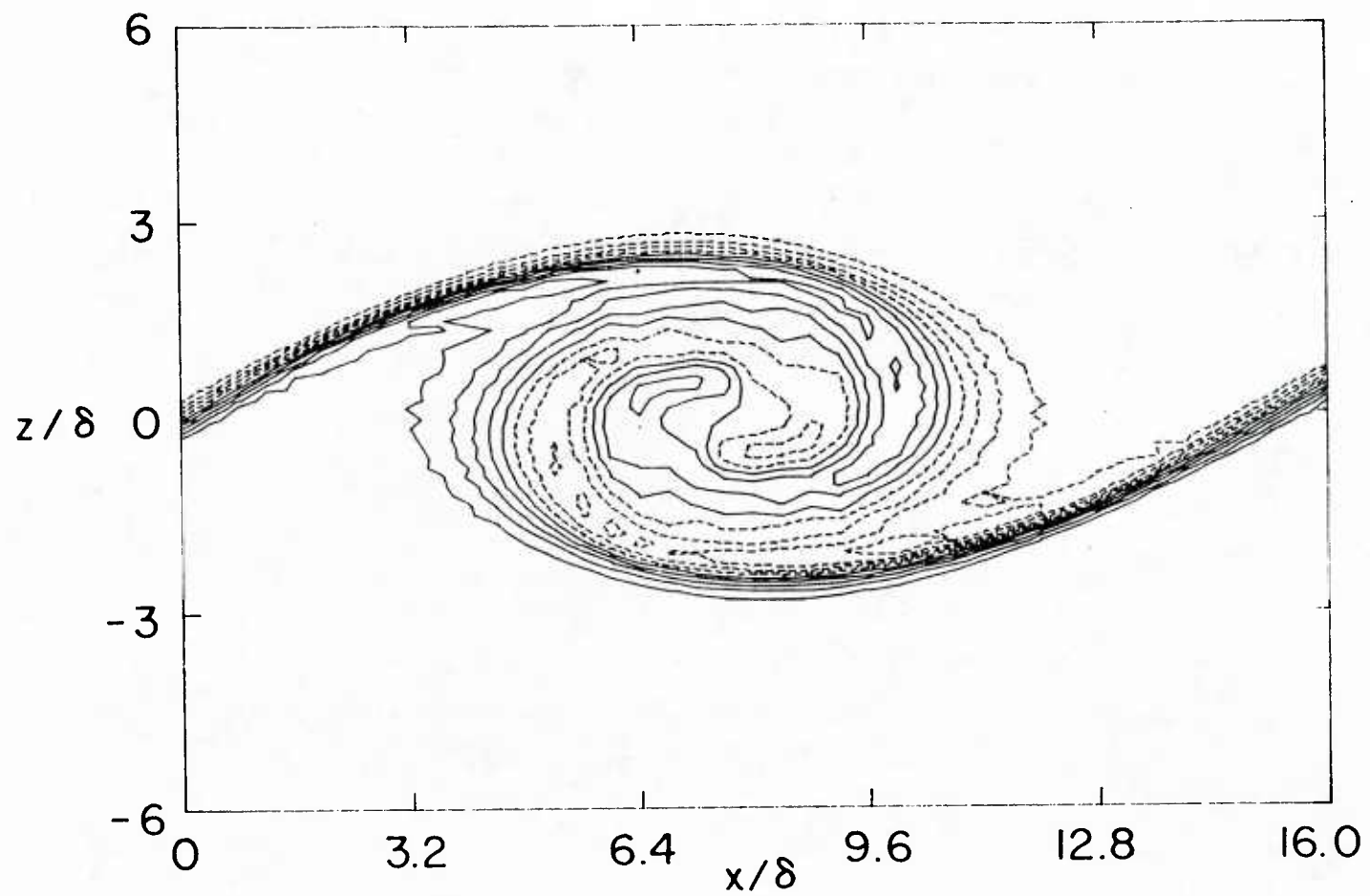


Figure 1(b) -  $\tau = 2.8$

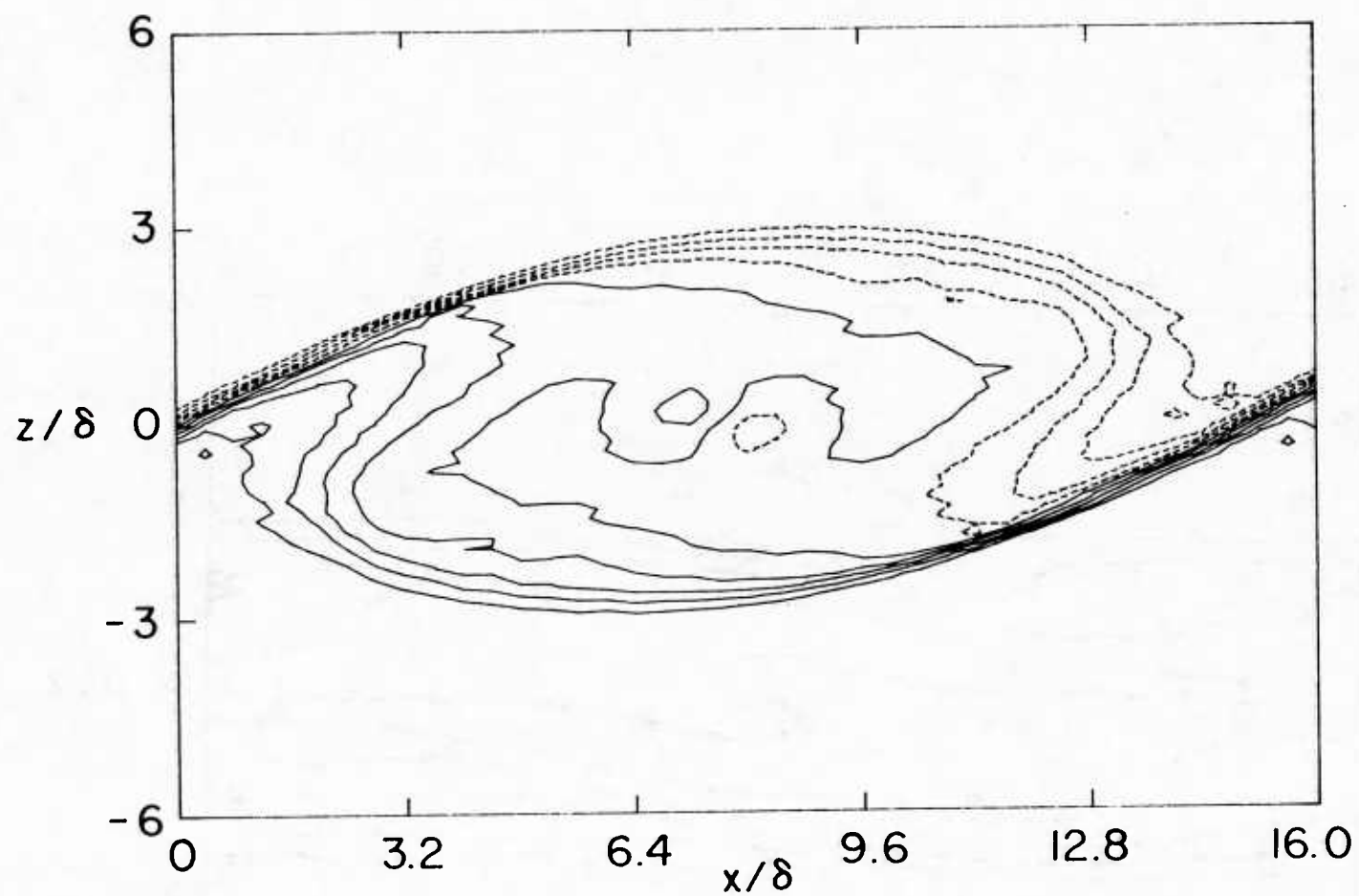
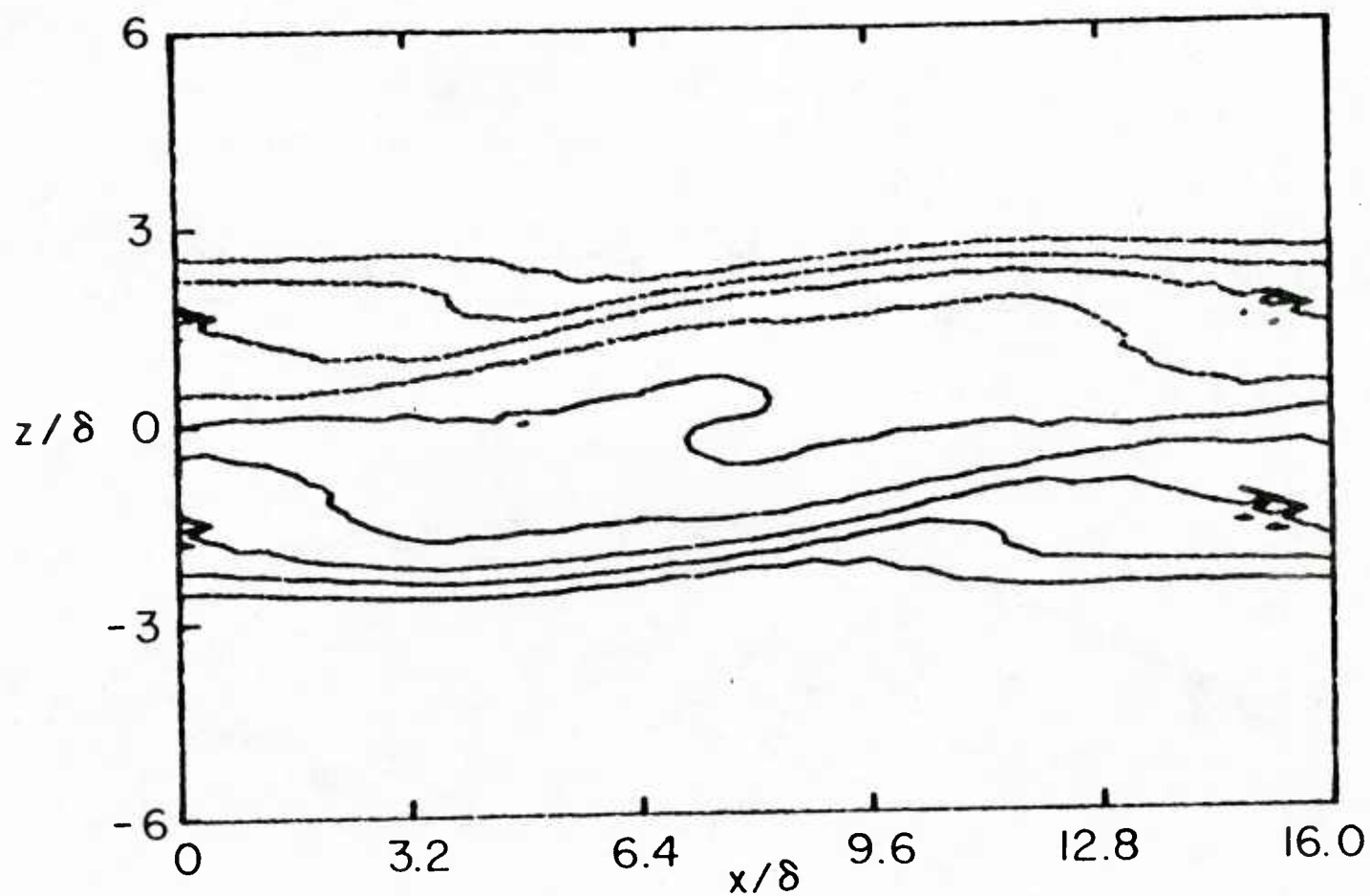
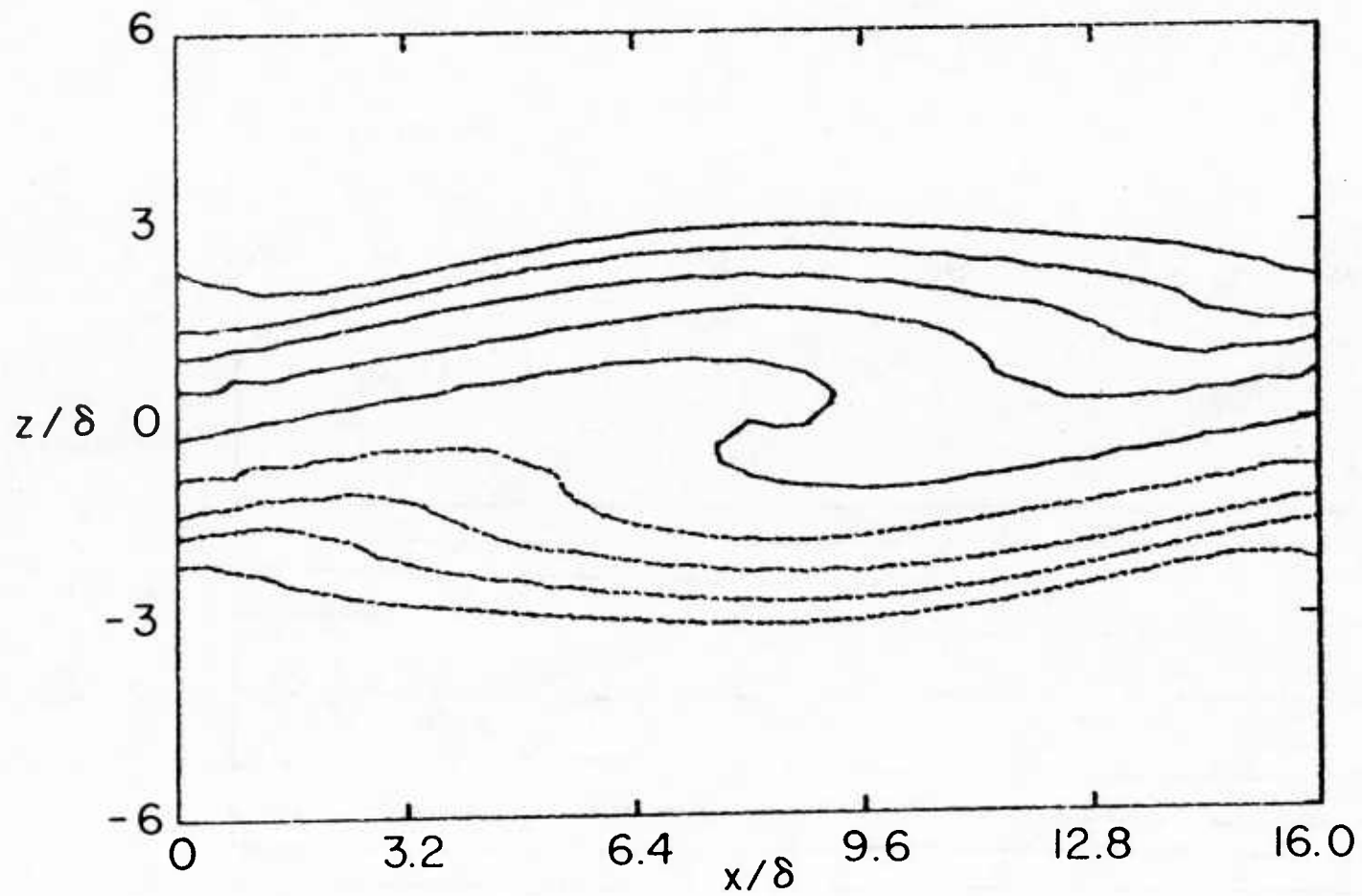
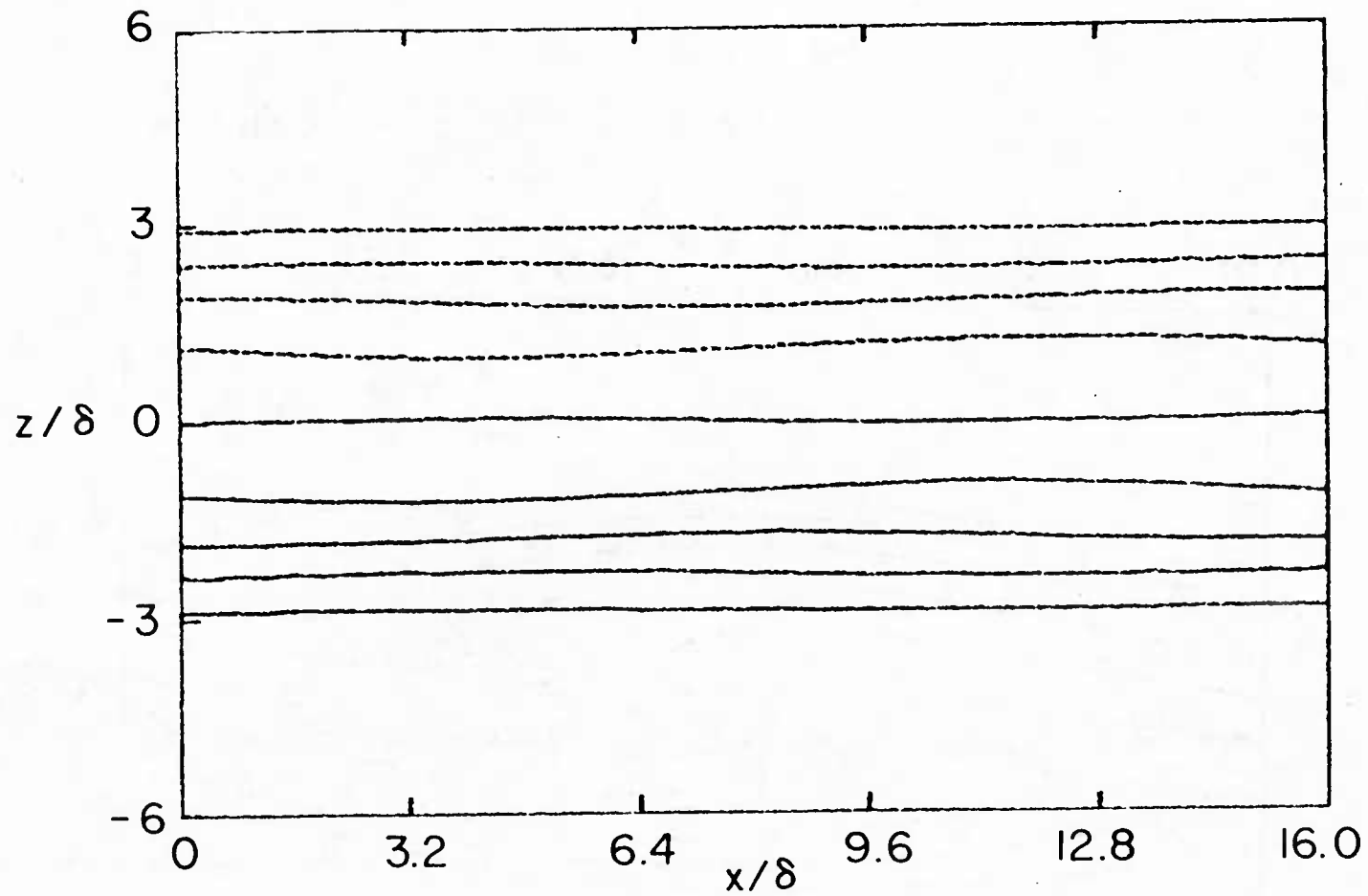


Figure 1(c) -  $\tau = 4.3$

Figure 1(d) -  $\tau = 5.8$

Figure 1(e) -  $\tau = 7.3$

Figure 1(f) -  $\tau = 11.8$

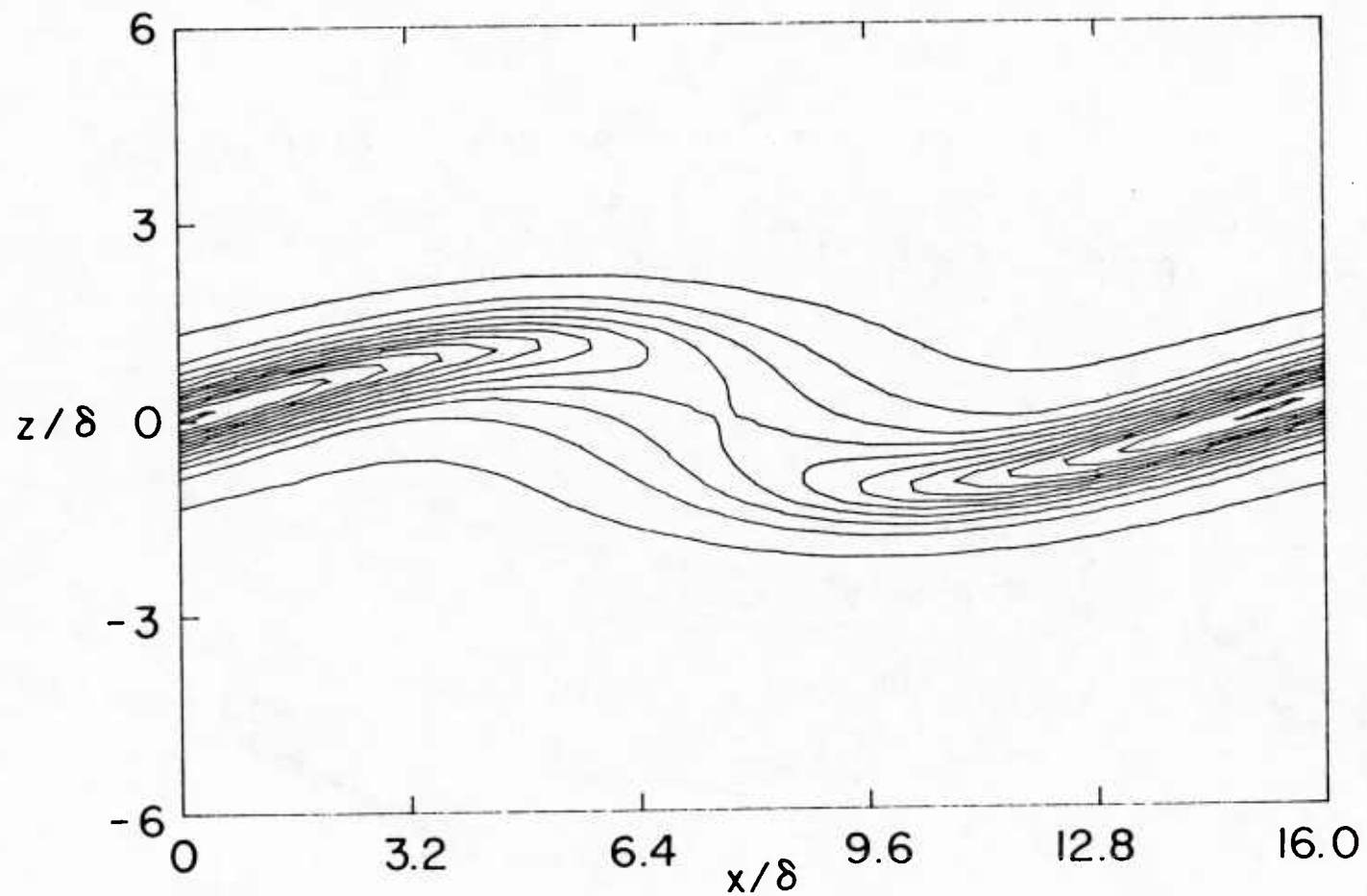


Figure 2 - Isopleths of dimensionless turbulence kinetic energy,  $q^2/\Delta U^2$  at the same times as Figure 1, i.e., (a)  $\tau = 1.5$ , contour intervals is 0.001.



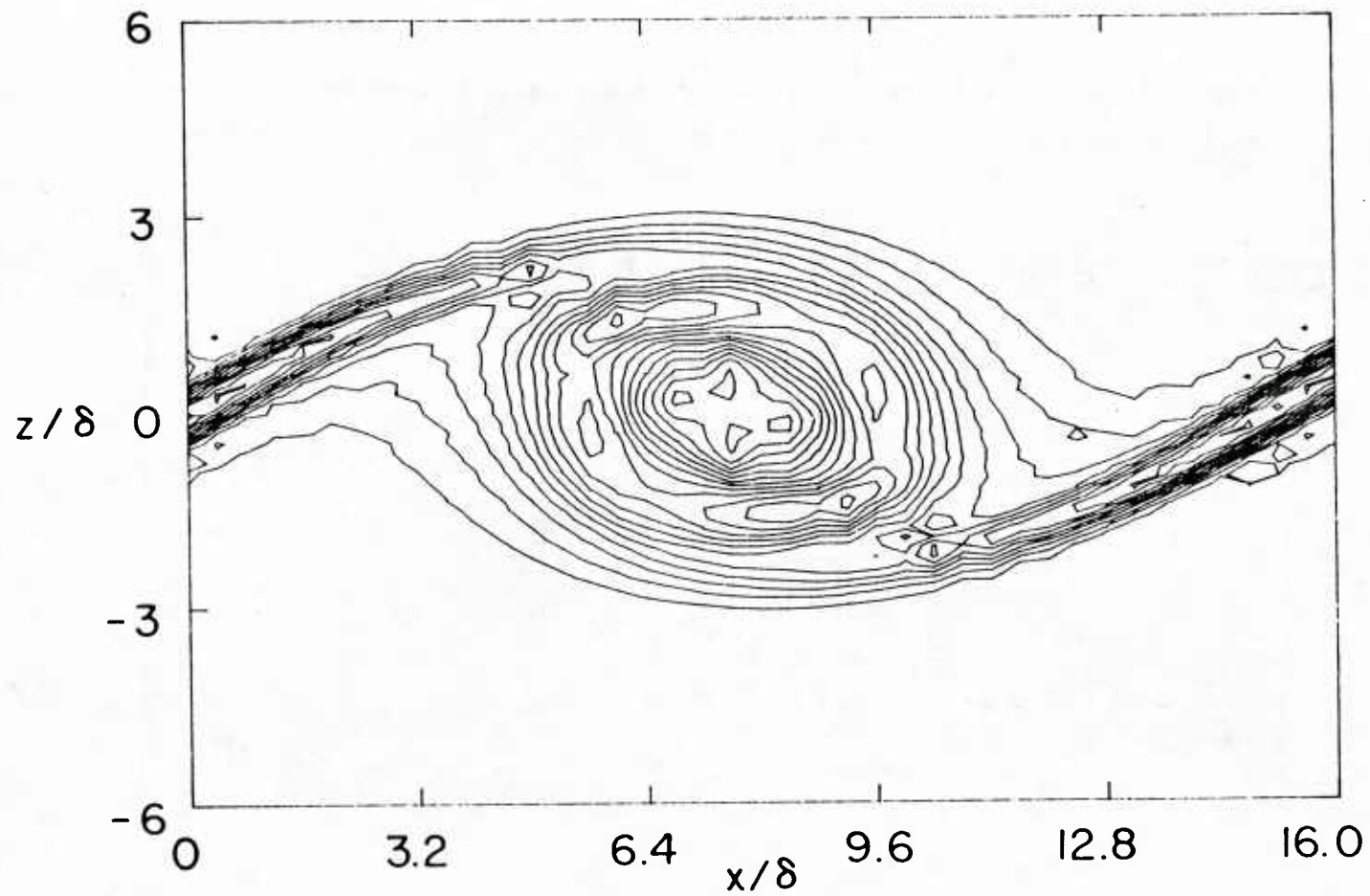


Figure 2(b) -  $\tau = 2.8$ , contour interval is 0.005.

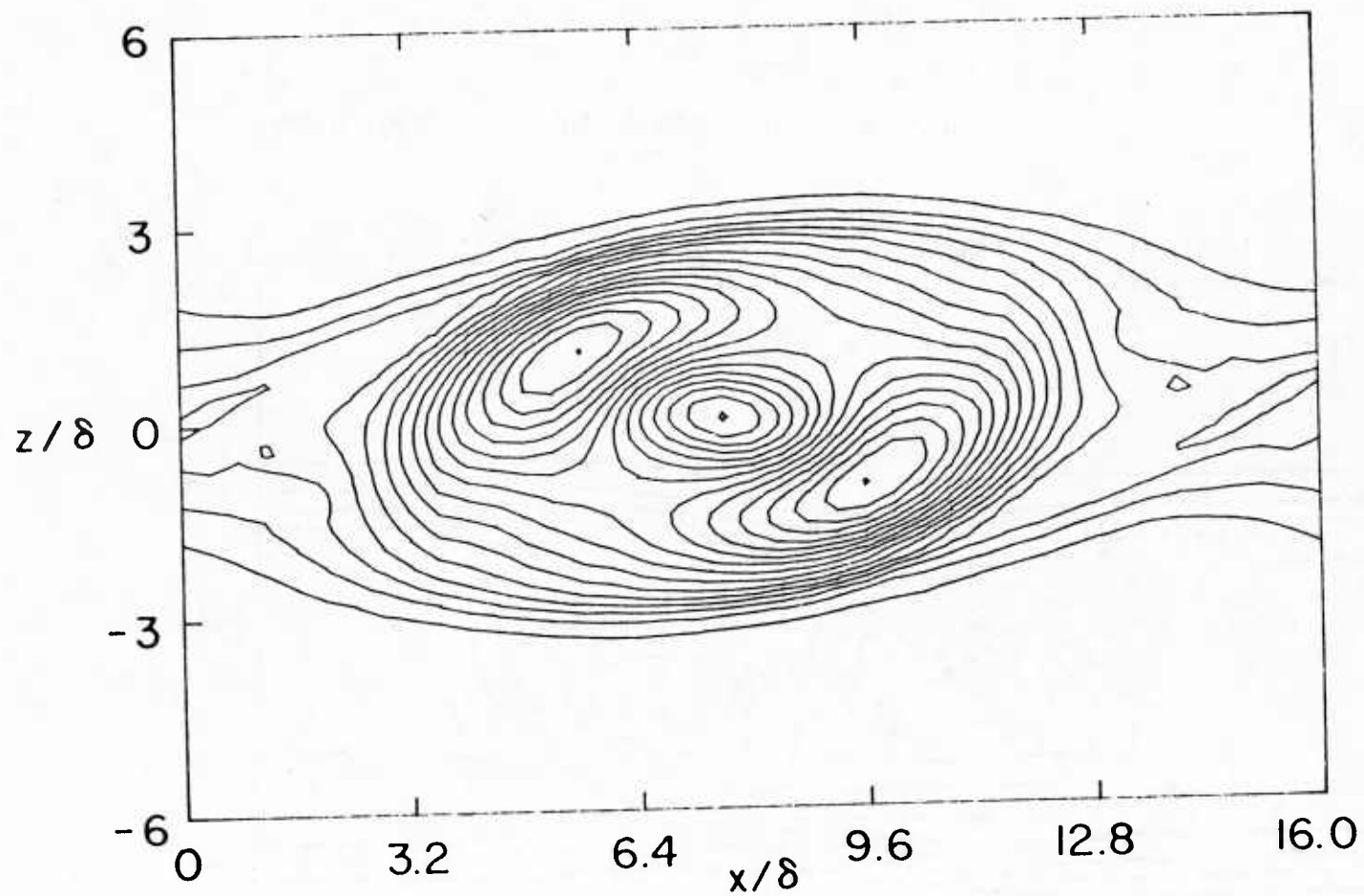


Figure 2(c) -  $\tau = 4.3$ , contour interval is 0.01.

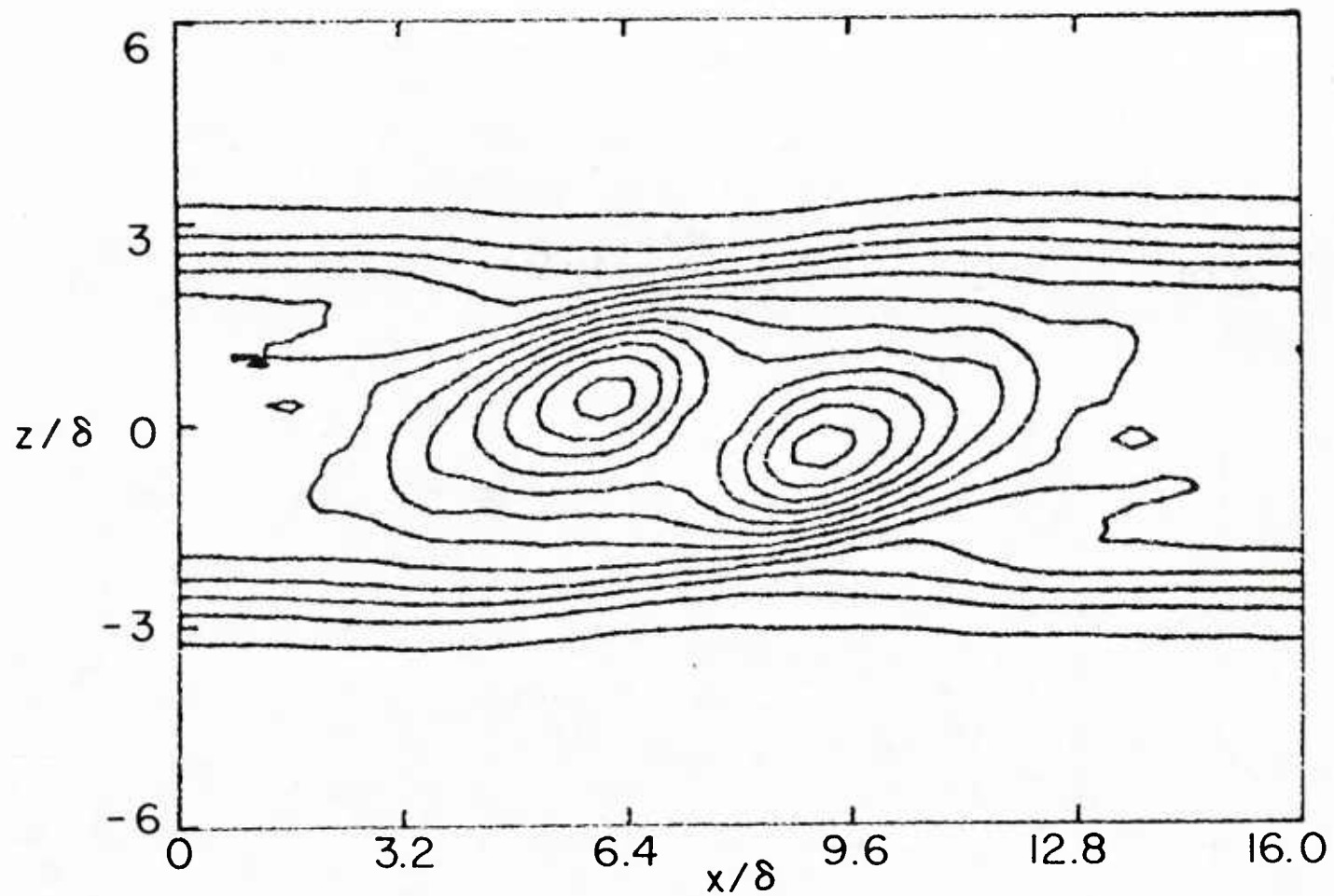


Figure 2(d) -  $\tau = 5.8$ , contour interval in 0.01.

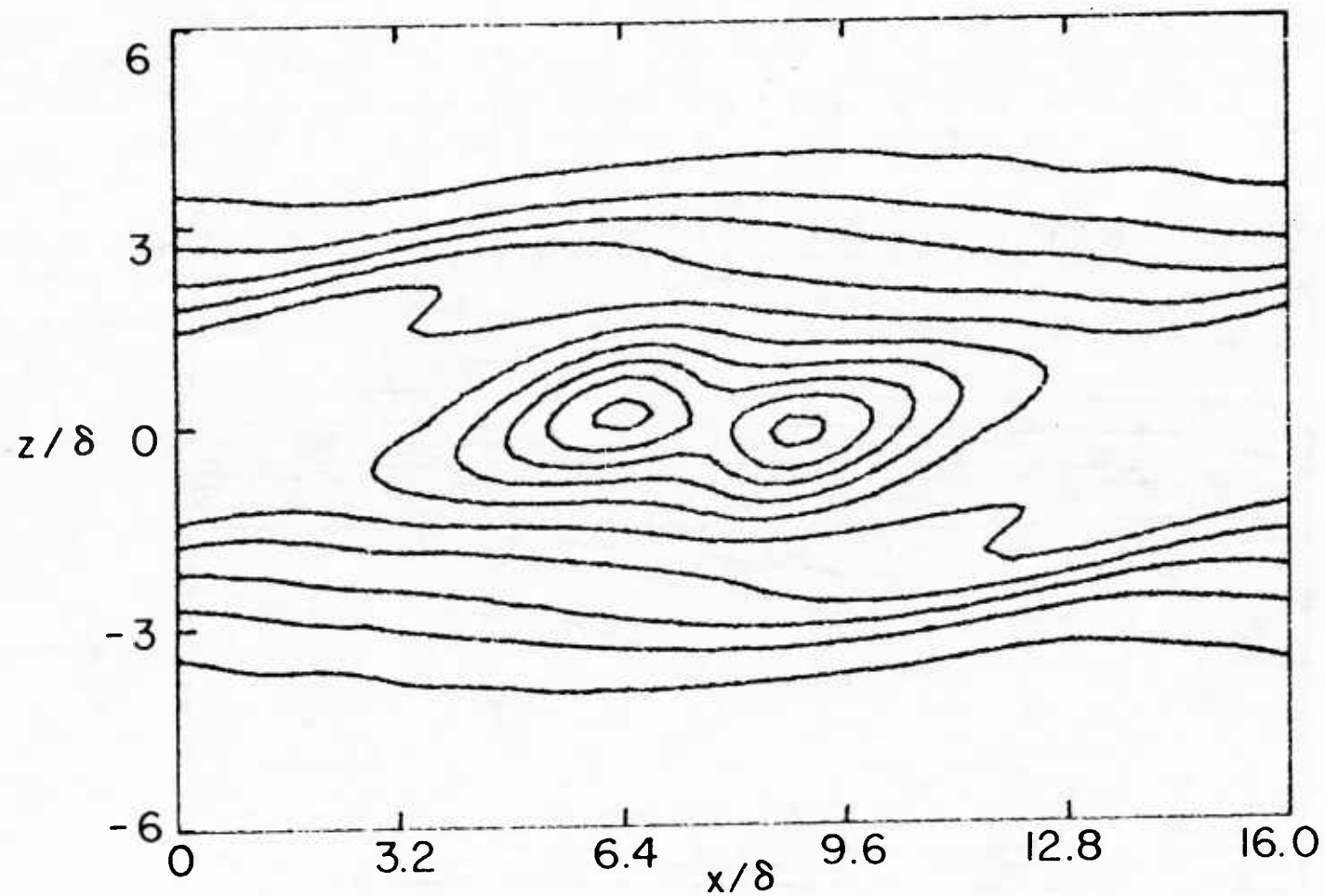


Figure 2(e) -  $\tau = 7.3$ , contour interval is 0.007.

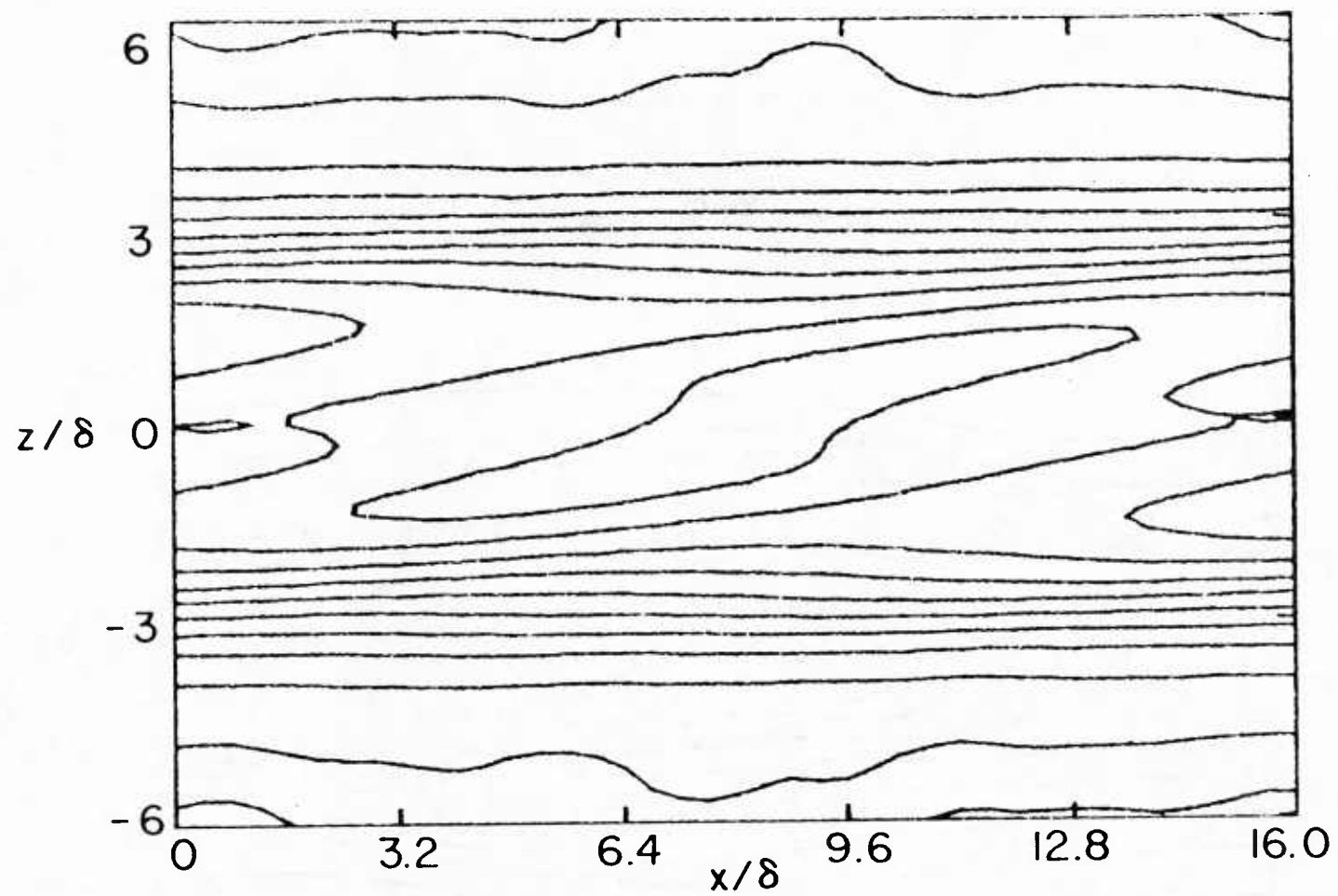


Figure 2(f) -  $\tau = 11.8$ , contour interval is 0.002.

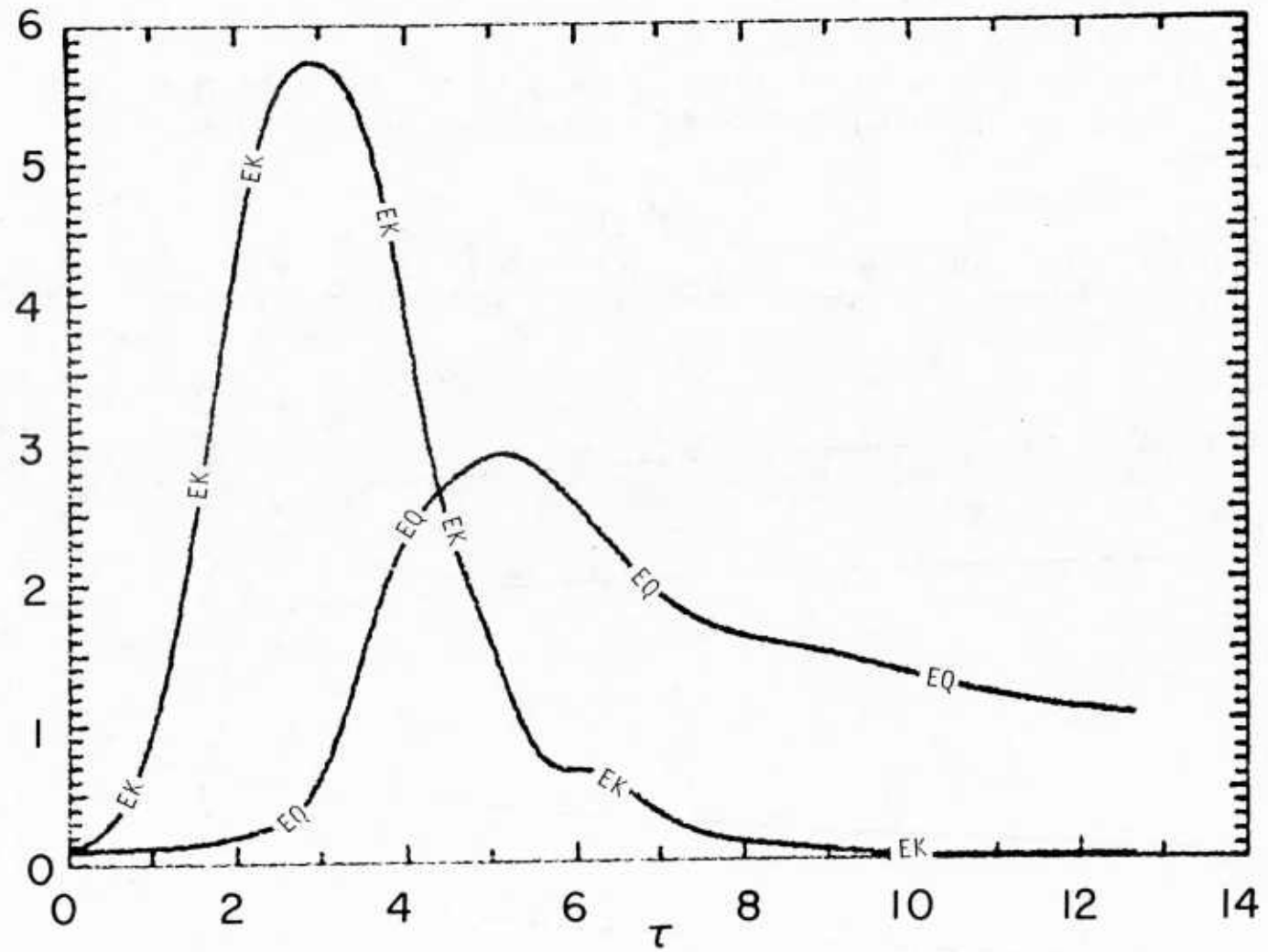


Figure 3 - Evolution of total kinetic energies,  $EK$  and  $EQ$ , for the large eddy and the small-scale turbulence in the  $Ri = 0.1$  case.



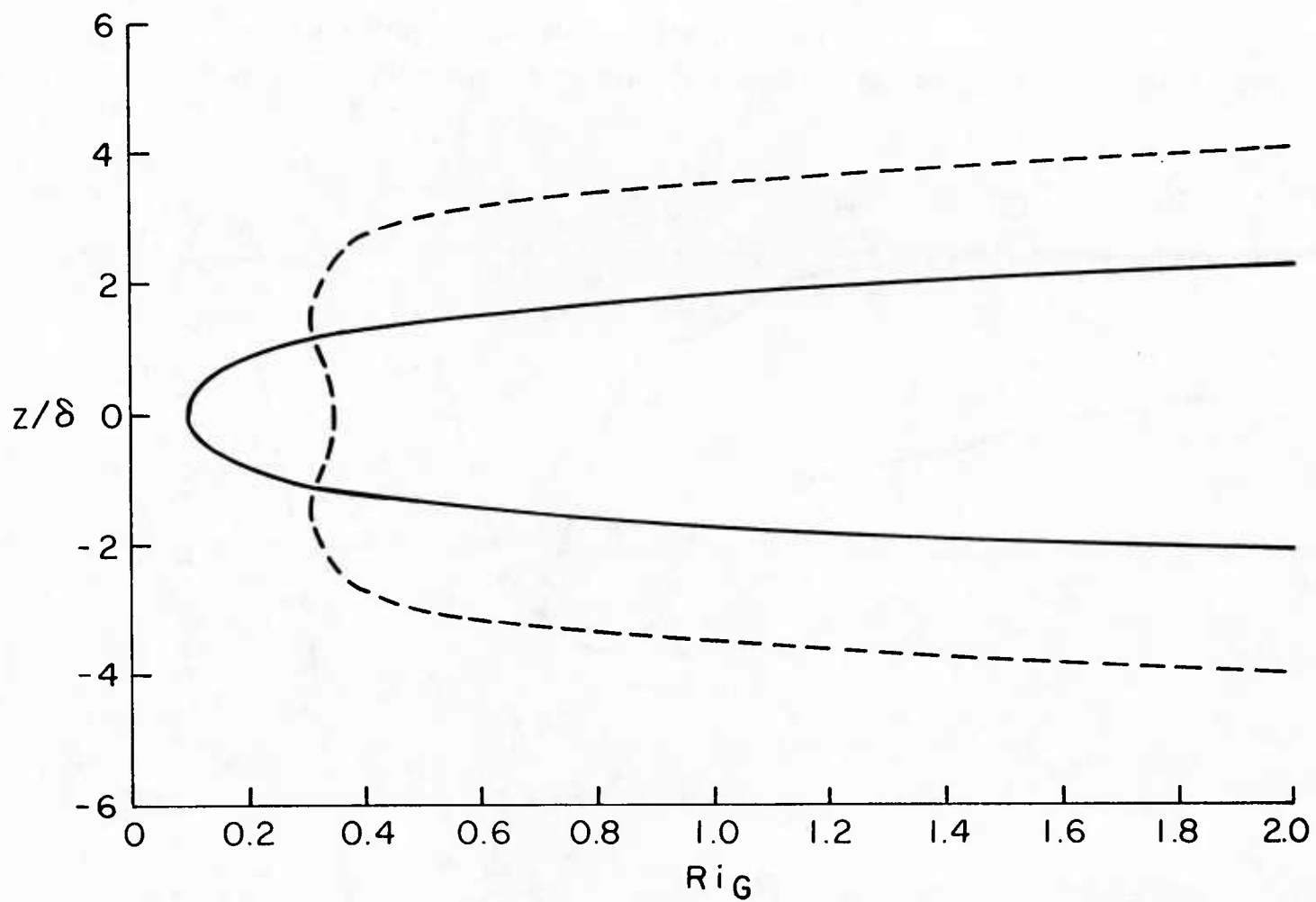


Figure 4 - Profiles of gradient Richardson number,  $Ri_G$ , for the  $Ri = 0.1$  case. Solid line is the initial profile at  $\tau = 0$ , dashed line is the profile at  $\tau = 11.8$ .

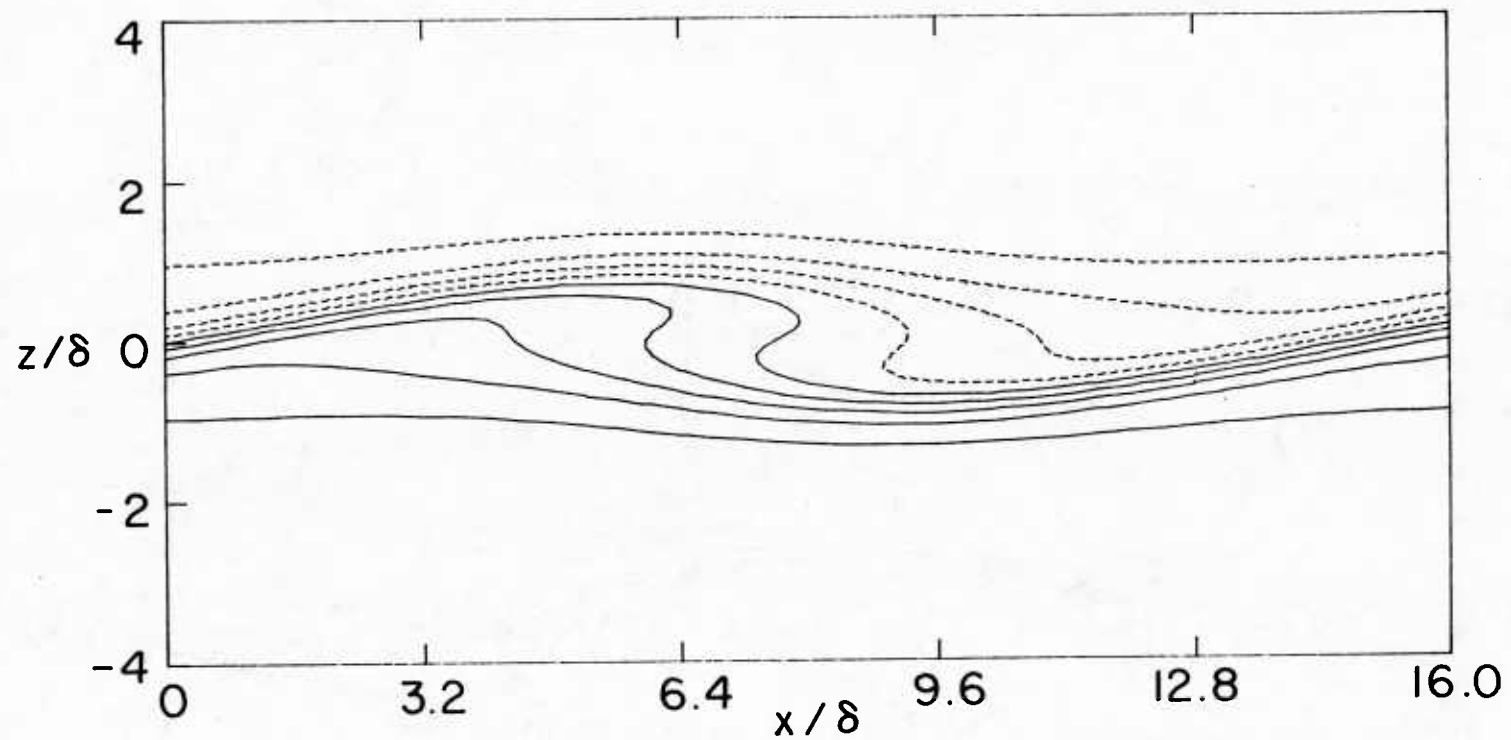


Figure 5 - Isolplets of dimensionless temperature  $(T - T_0)/\Delta T$  for the case with  $Ri = 0.2$  at (a)  $\tau = 3$ . Contour interval is 0.2.



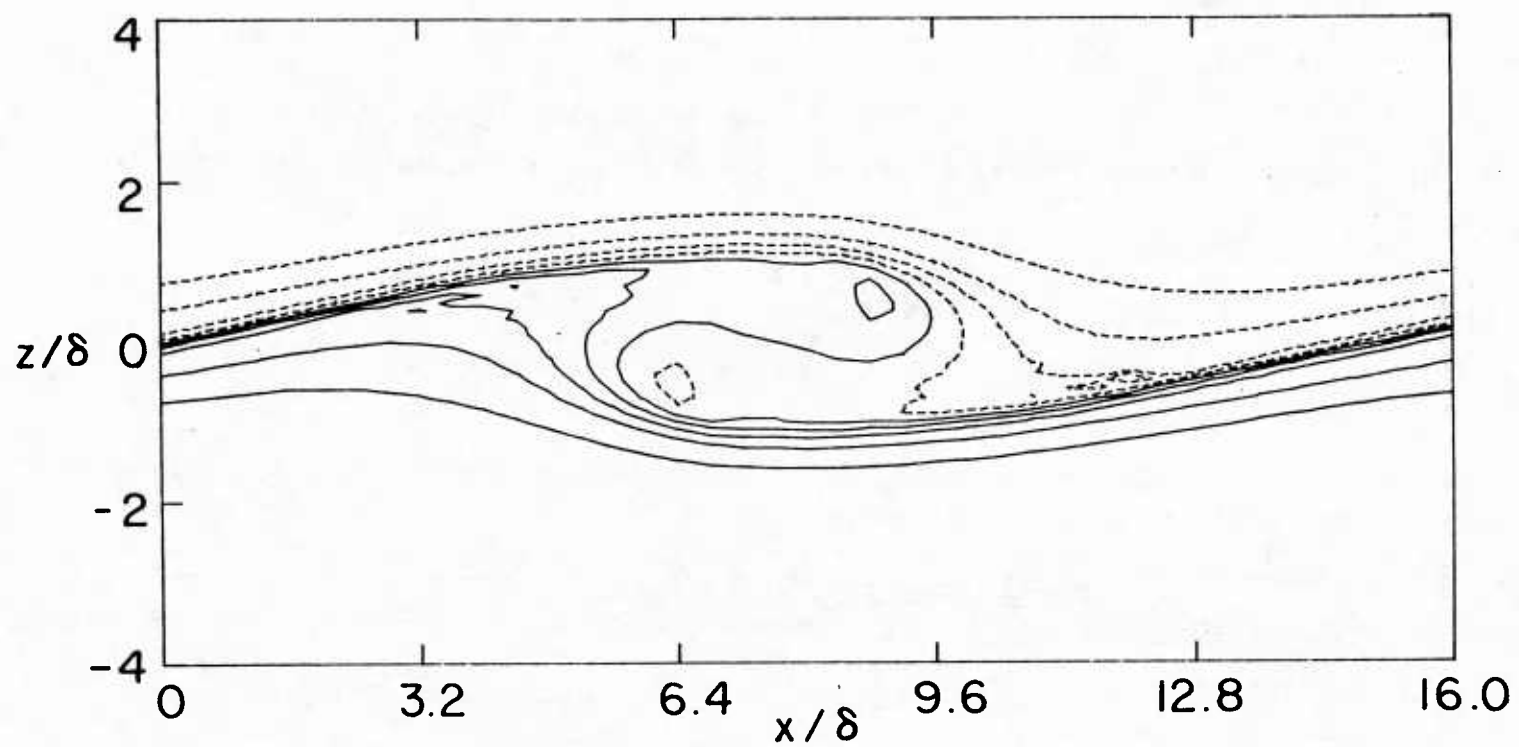
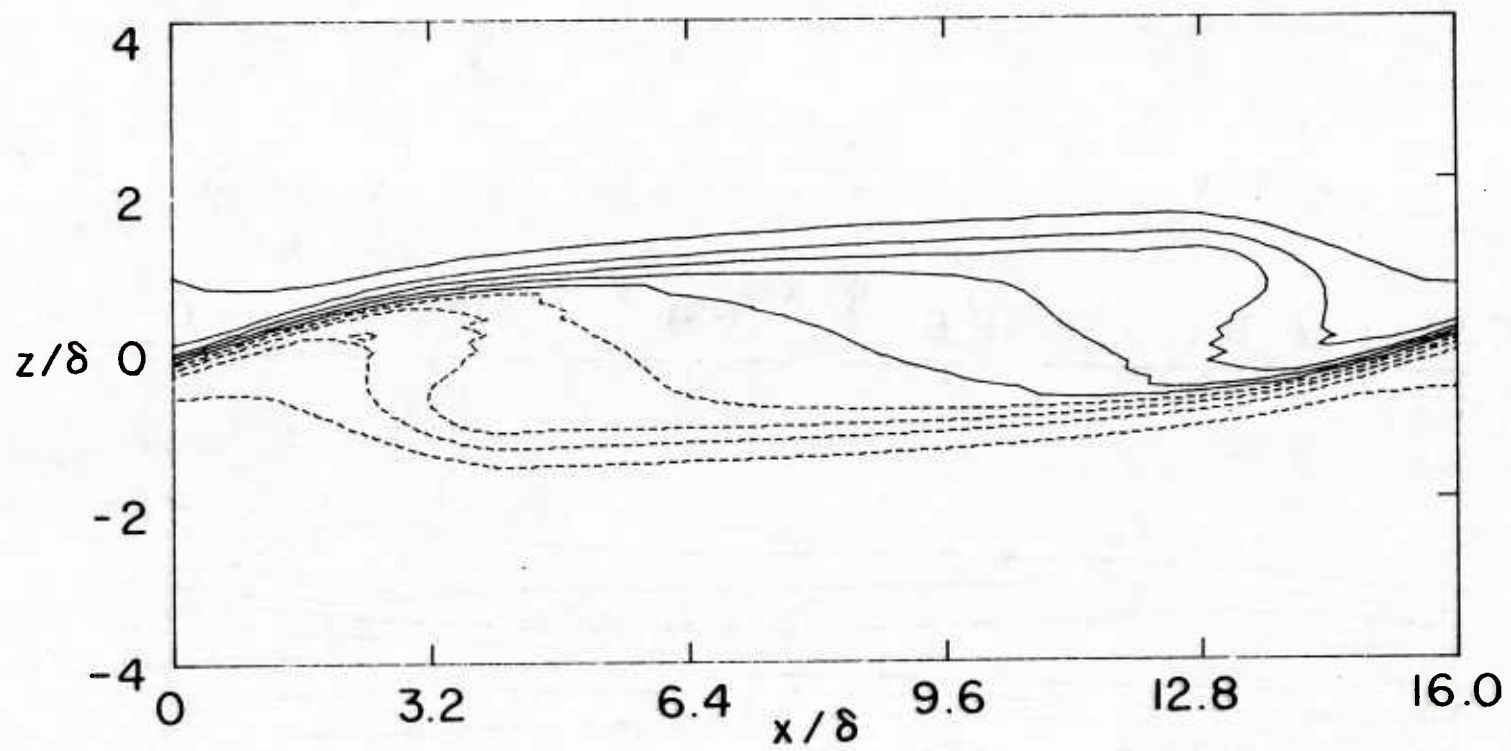


Figure 5(b) -  $\tau = 6$ .

Figure 5(c) -  $\tau = 9$ .

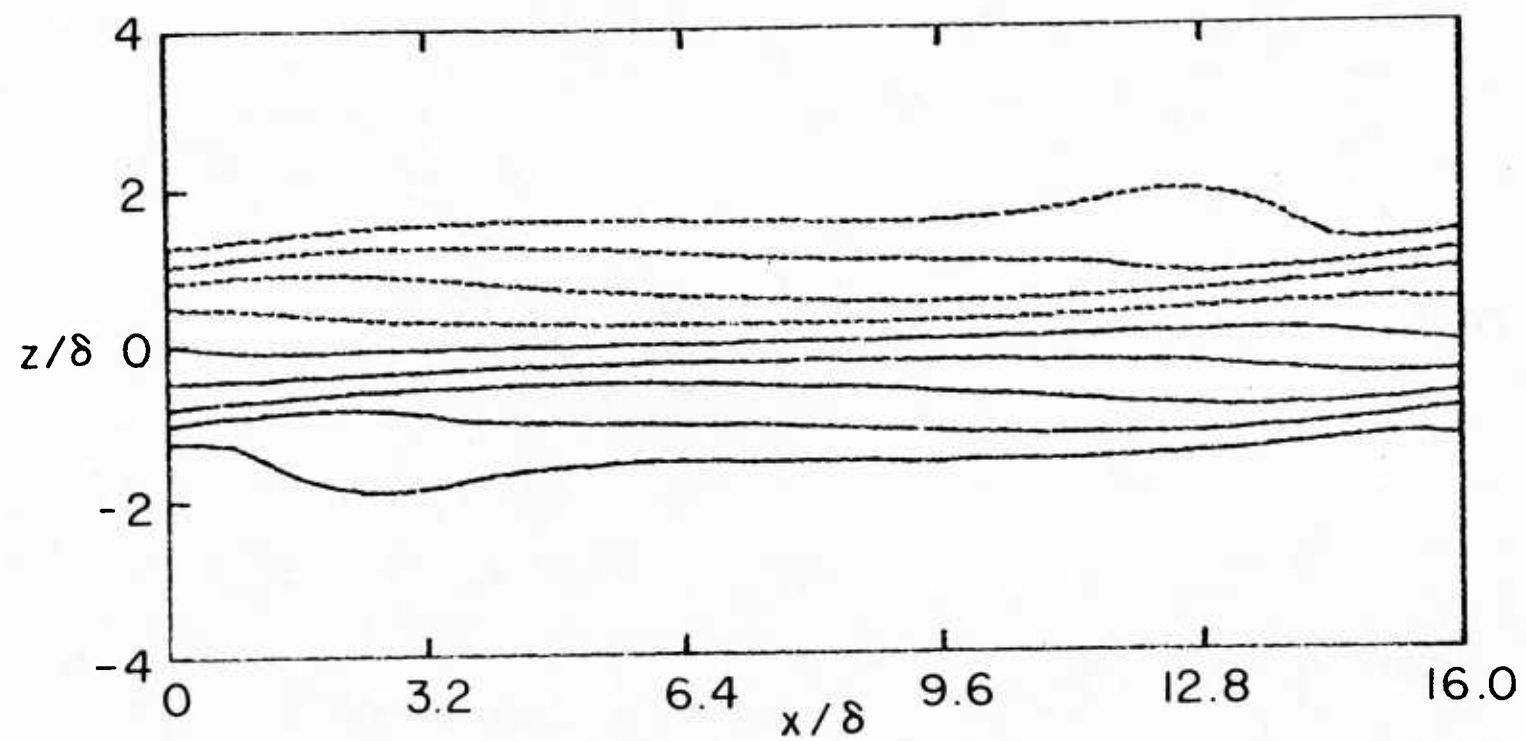


Figure 5(d) -  $\tau = 14.6$ .

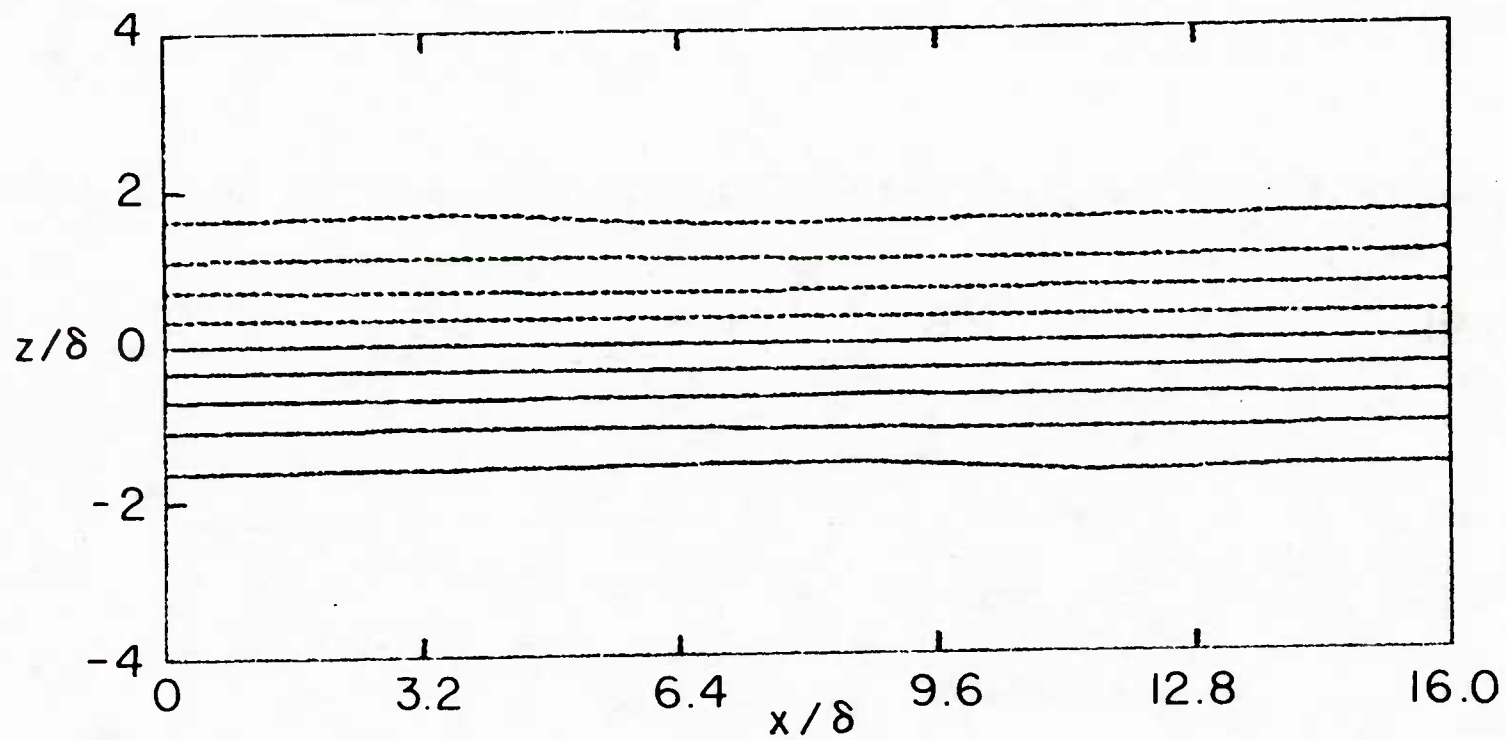


Figure 5(e) -  $\tau = 20.6$ .

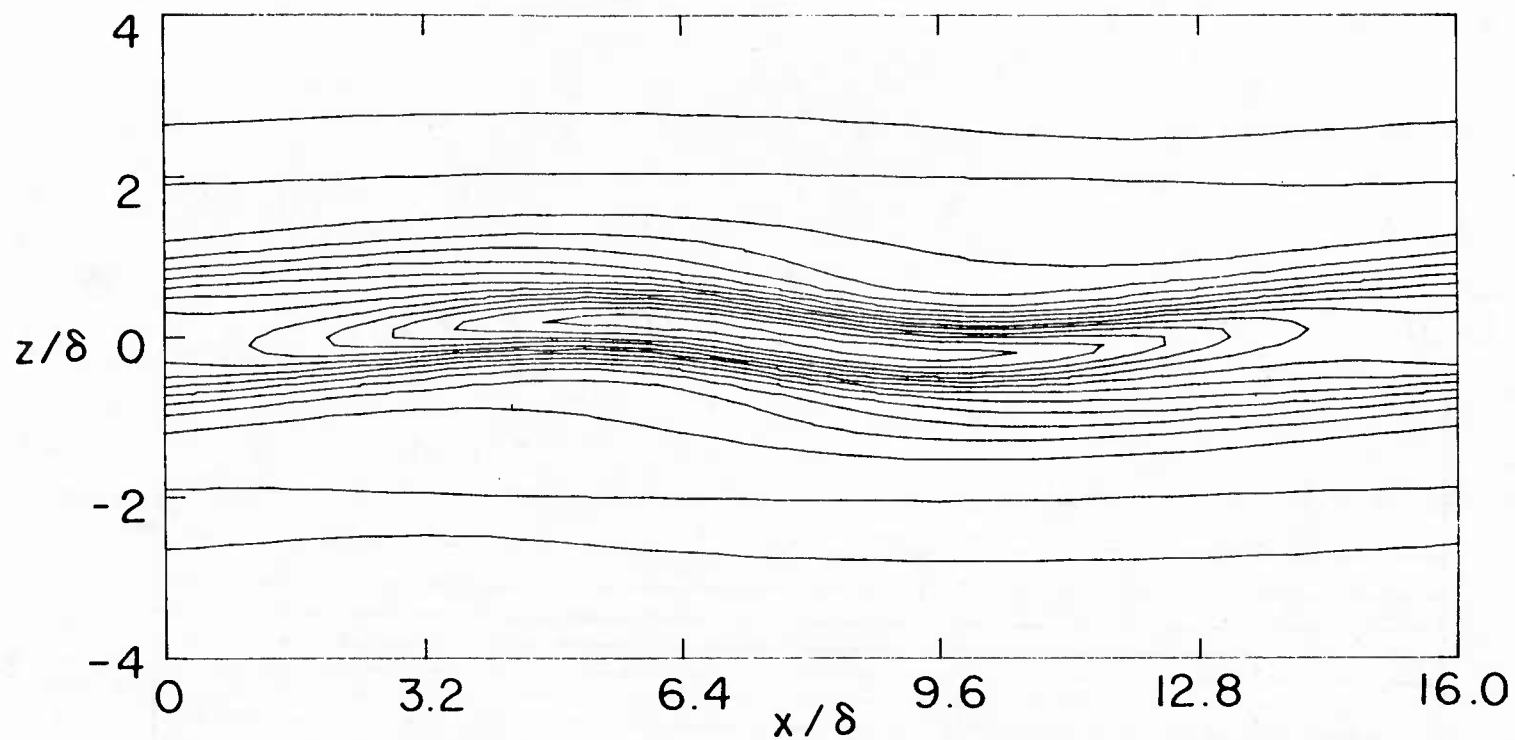


Figure 6 - Isopleths of dimensionless turbulence kinetic energy  $q^2/\Delta U^2$   $Ri = 0.2$  at (a)  $\tau = 3$ , contour interval is 0.0003.

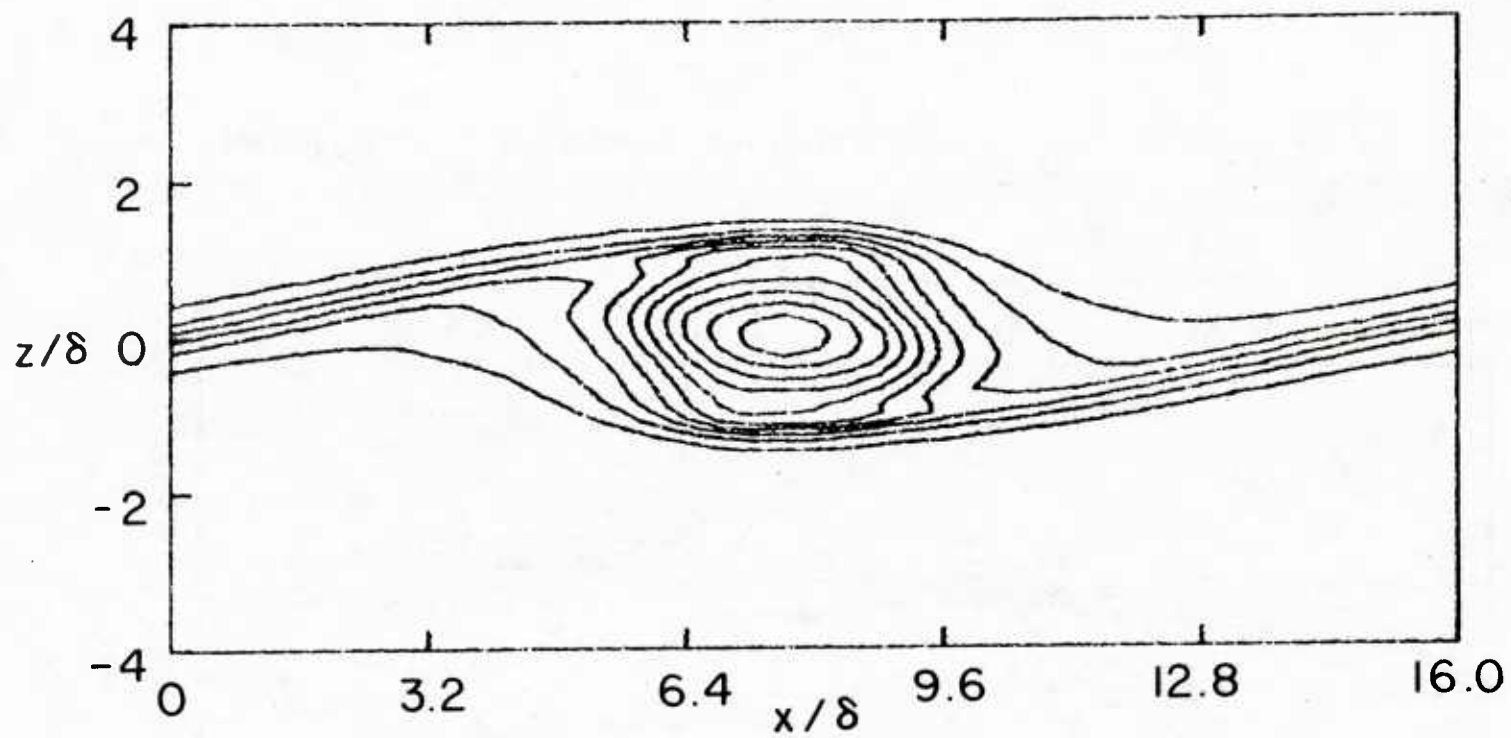


Figure 6(b) -  $\tau = 6$ , contour interval is 0.006.

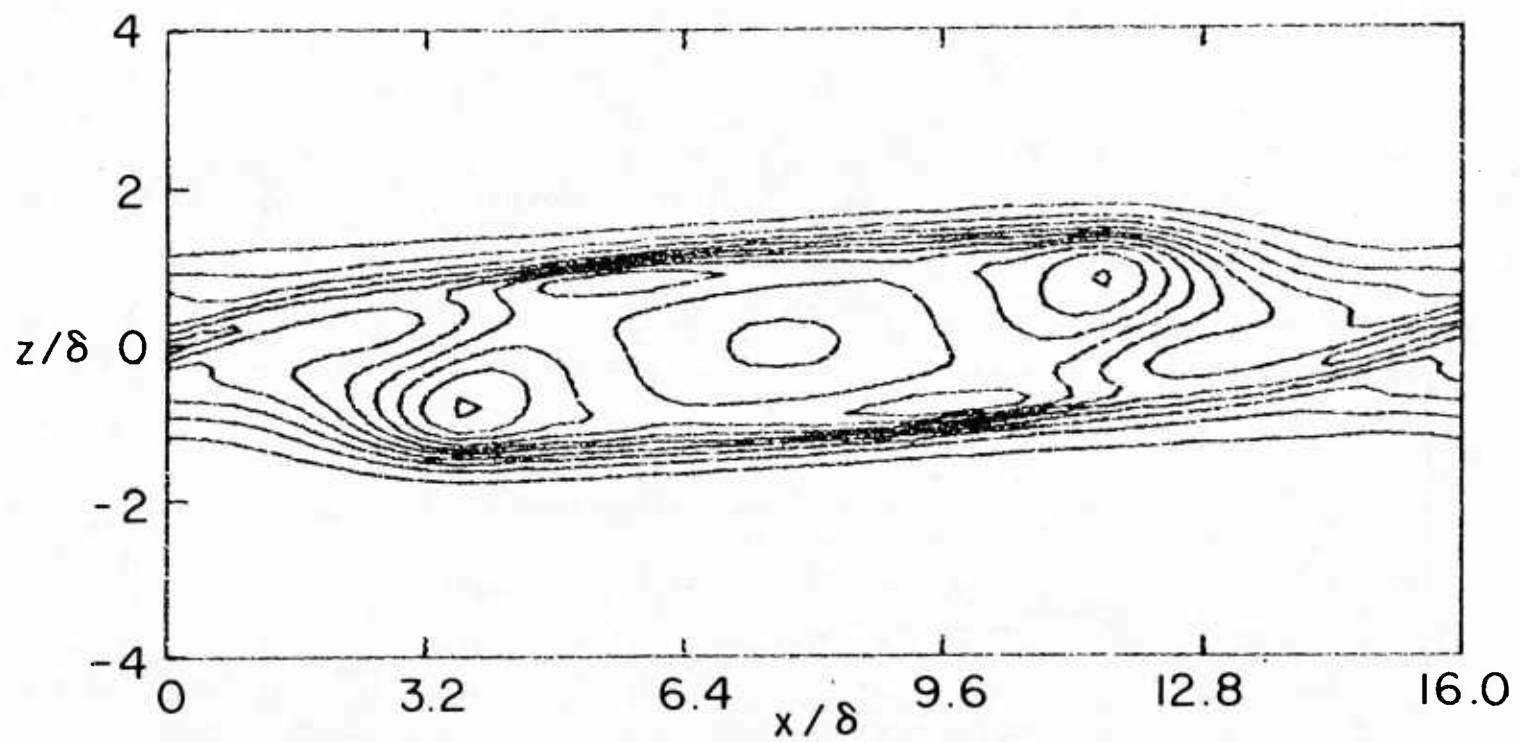


Figure 6(c) -  $\tau = 9$ , contour interval is 0.007

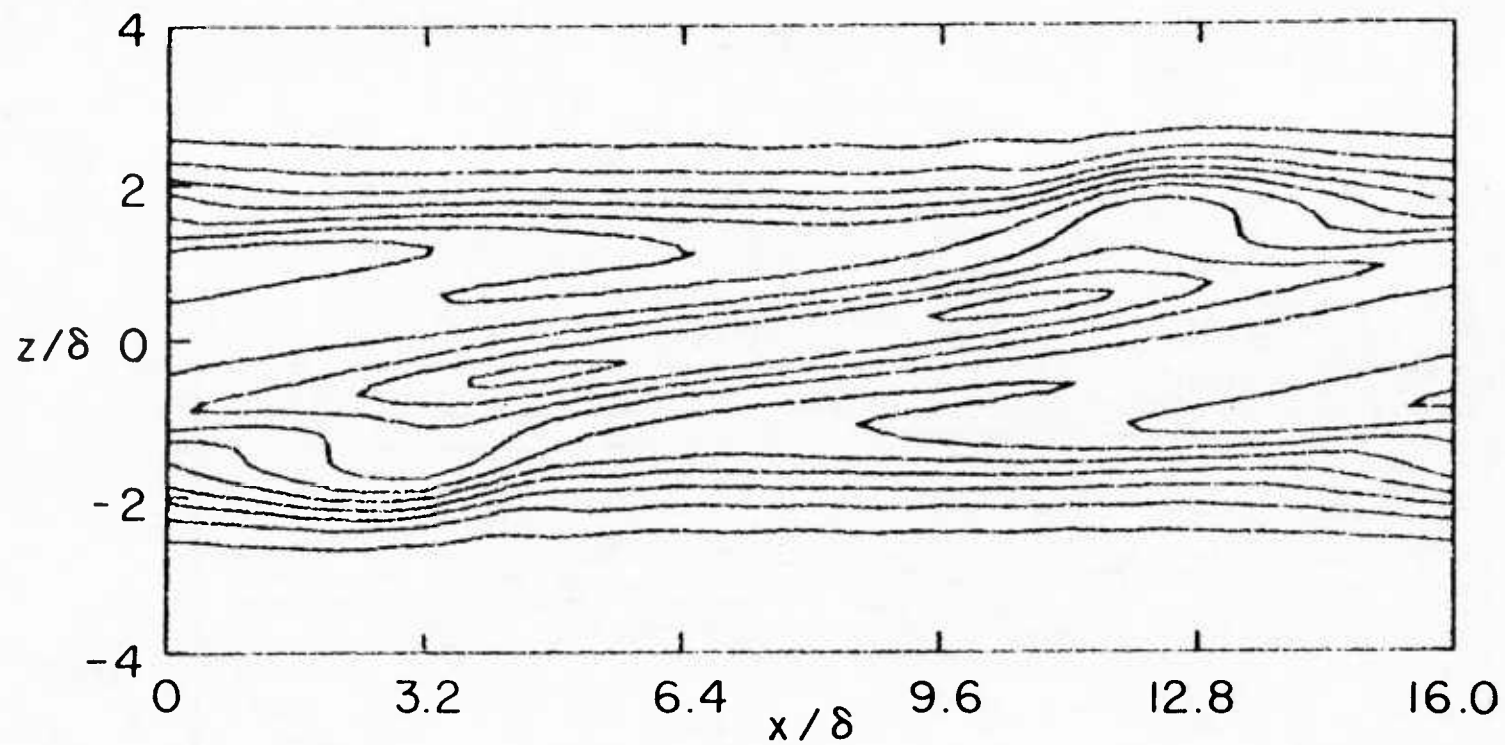


Figure 6(d) -  $\tau = 14.6$ , contour interval is 0.003.



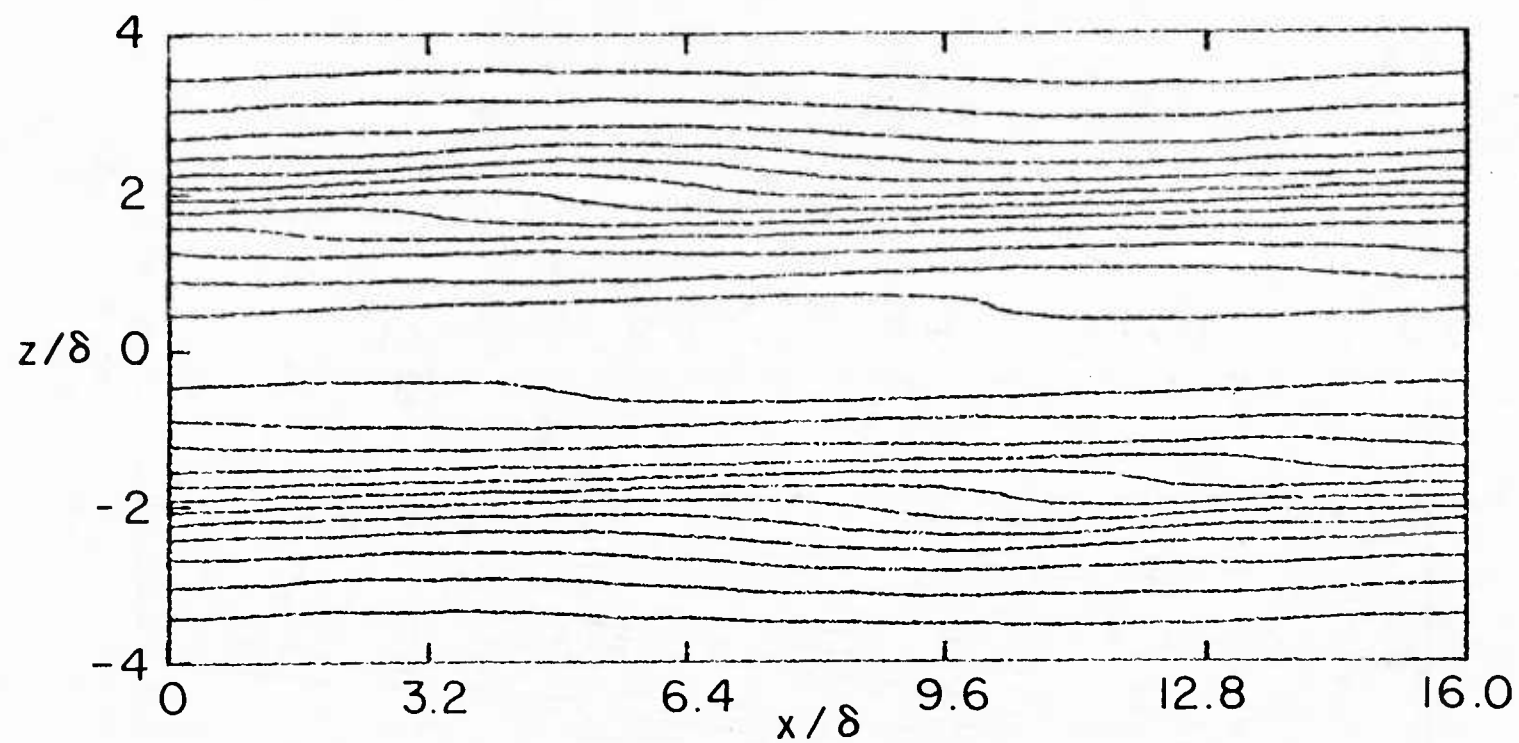


Figure 6(e) -  $\tau = 20.6$ , contour interval is 0.001.

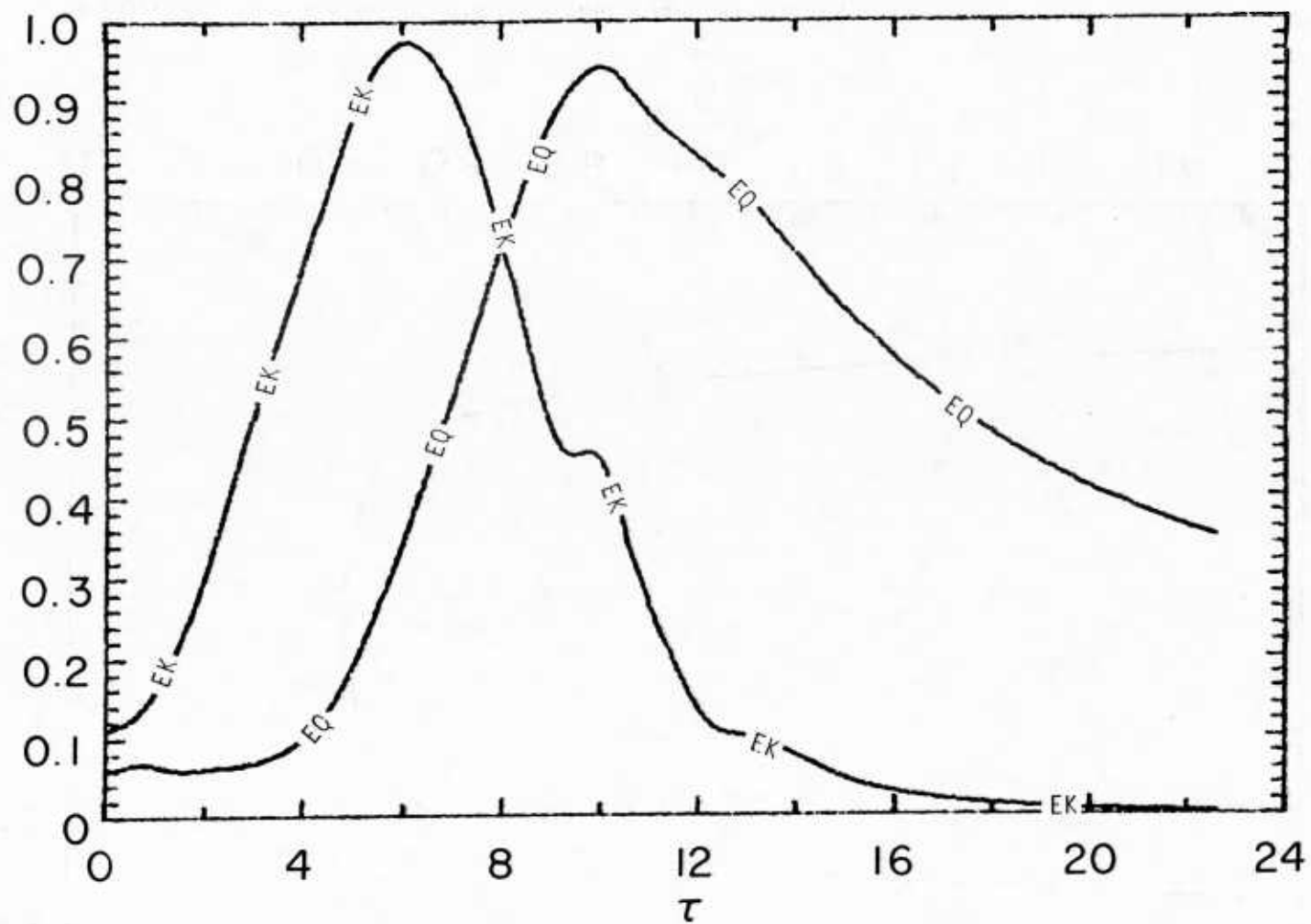


Figure 7 - Evolution of large scale and small scale eddy kinetic energies for the case with  $Ri = 0.2$ .

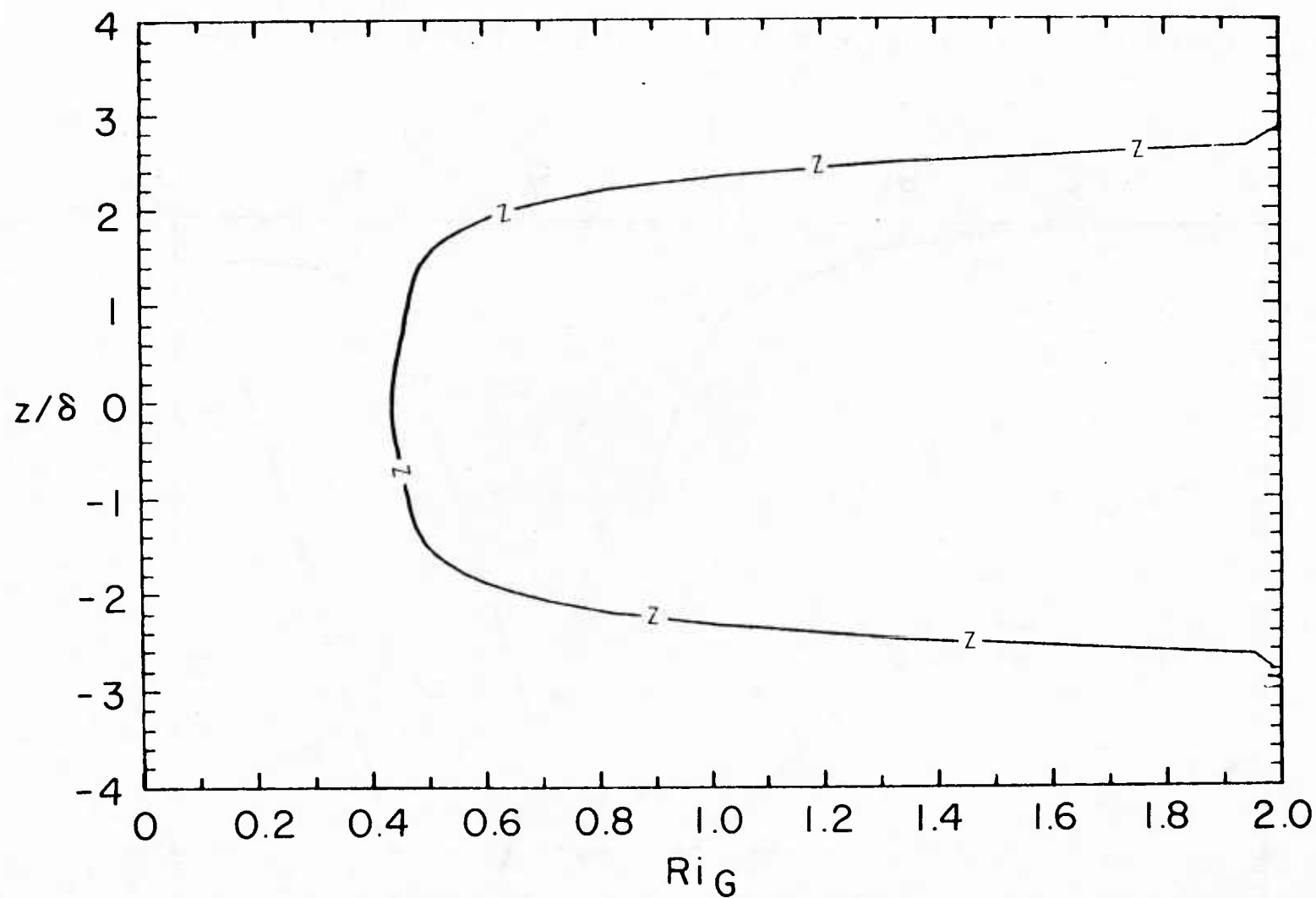


Figure 8 - Profile of gradient Richardson number,  $Ri_G$ , for the  $Ri = 0.2$  case, at  $\tau = 20.6$ .

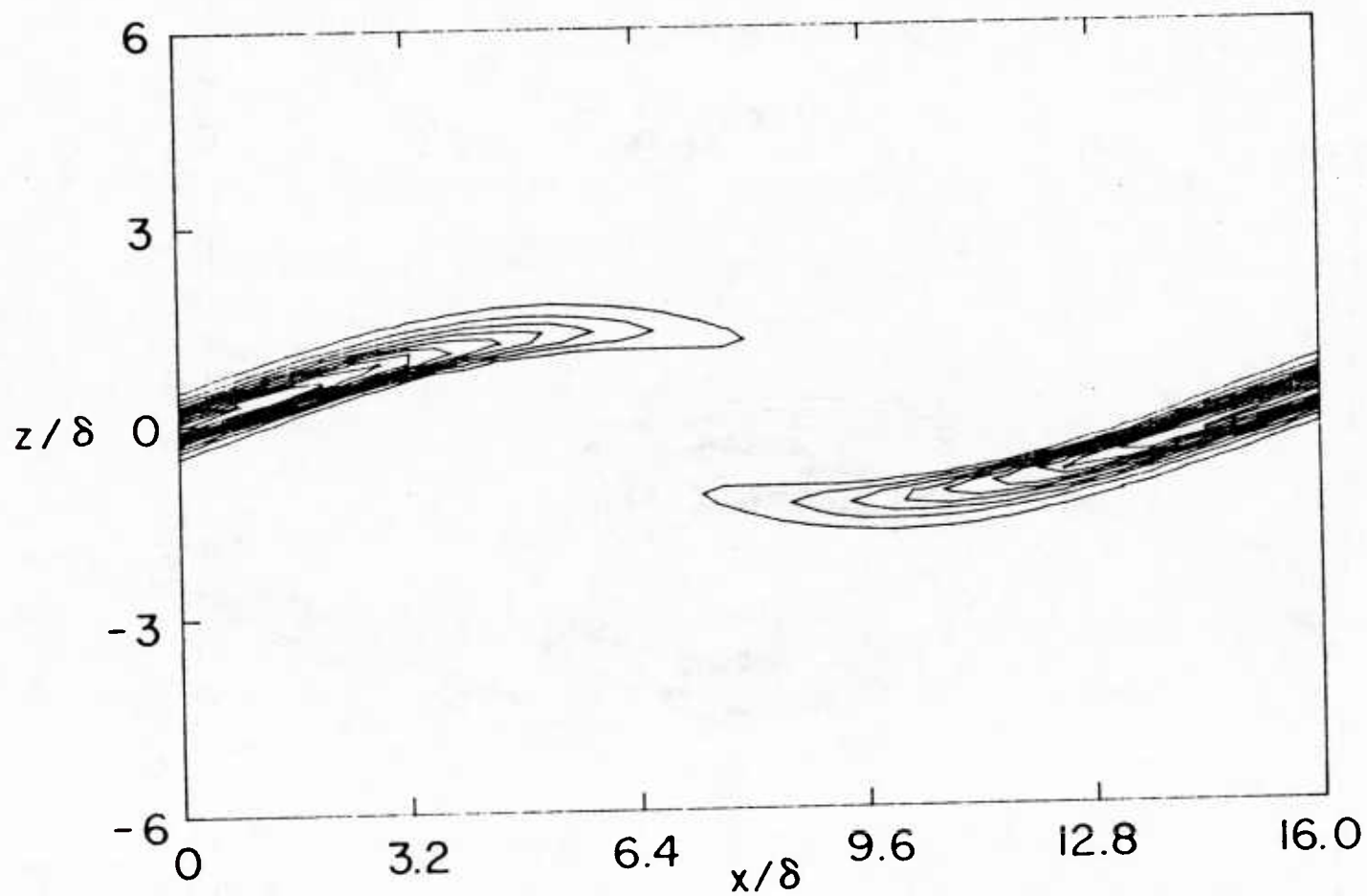


Figure 9 - Isopleths of dimensionless temperature variance  $\overline{\theta^2}/\Delta T^2$  for the case with  $Ri = 1$ . (a)  $\tau = 1.5$ , contour interval is 0.004.

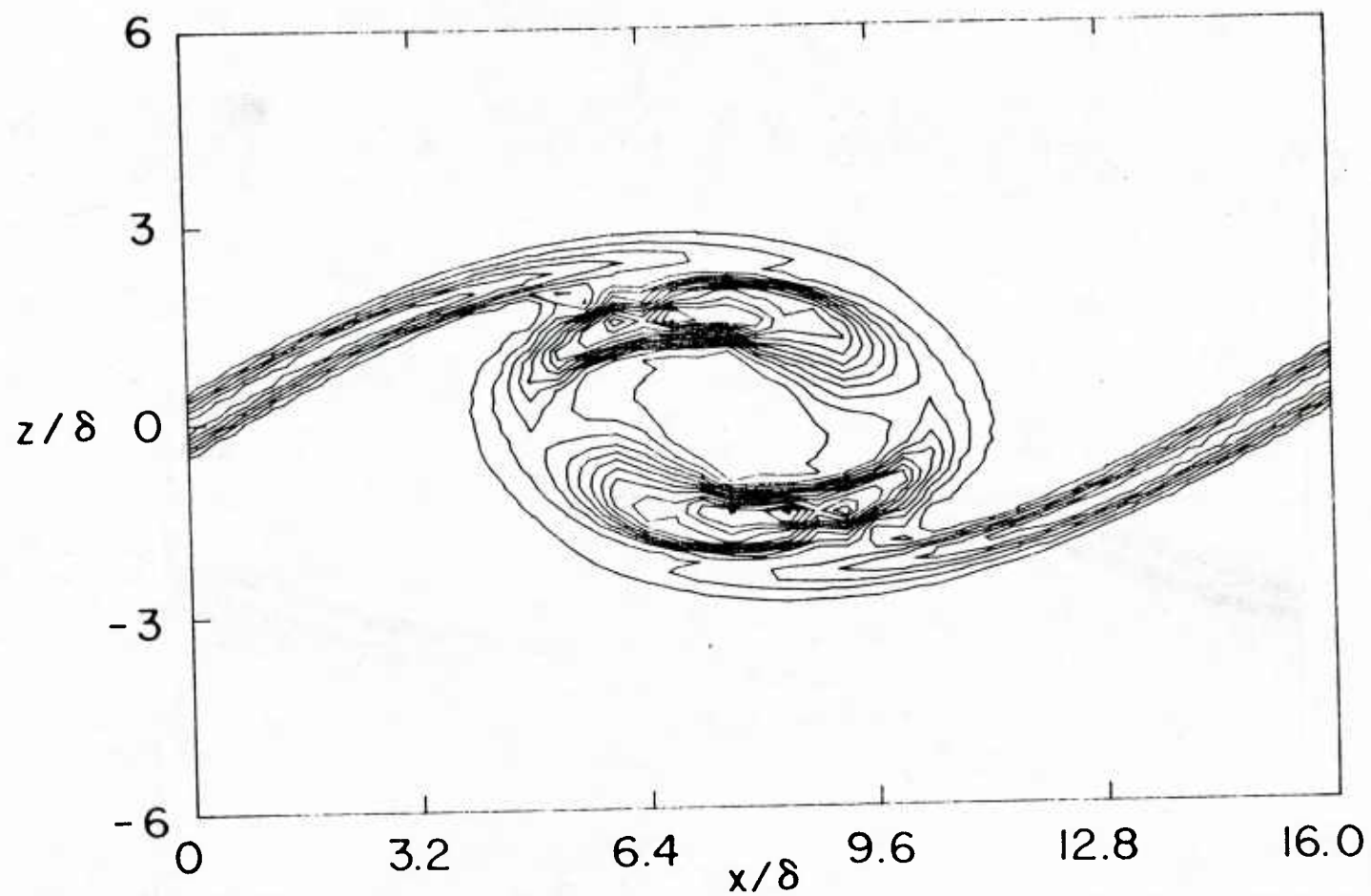


Figure 9(b) -  $\tau = 2.8$ , contour interval is 0.02.

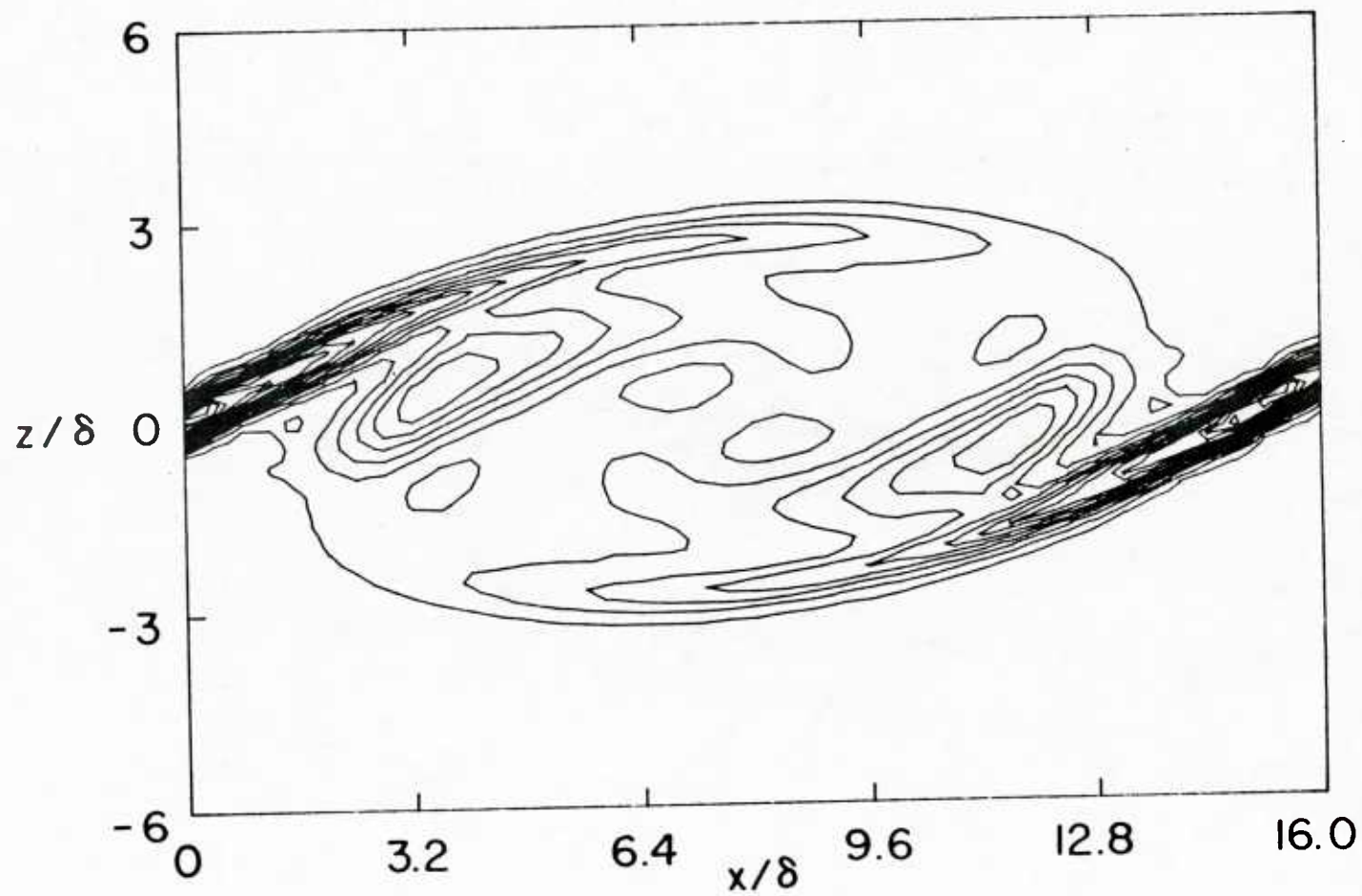


Figure 9(c) -  $\tau = 4.3$ , contour interval is 0.02

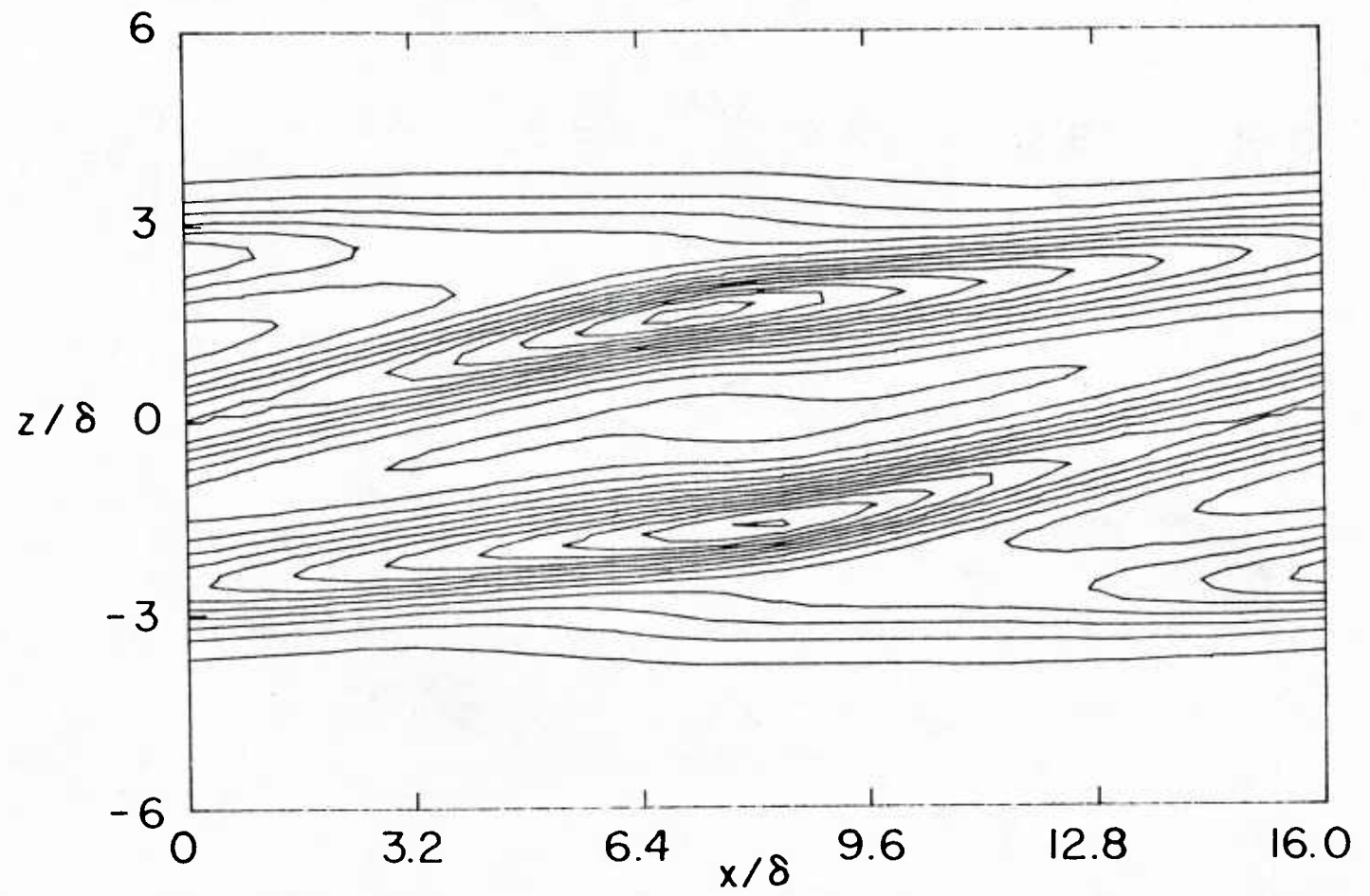


Figure 9(d) -  $\tau = 8.8$ , contour interval is 0.002.

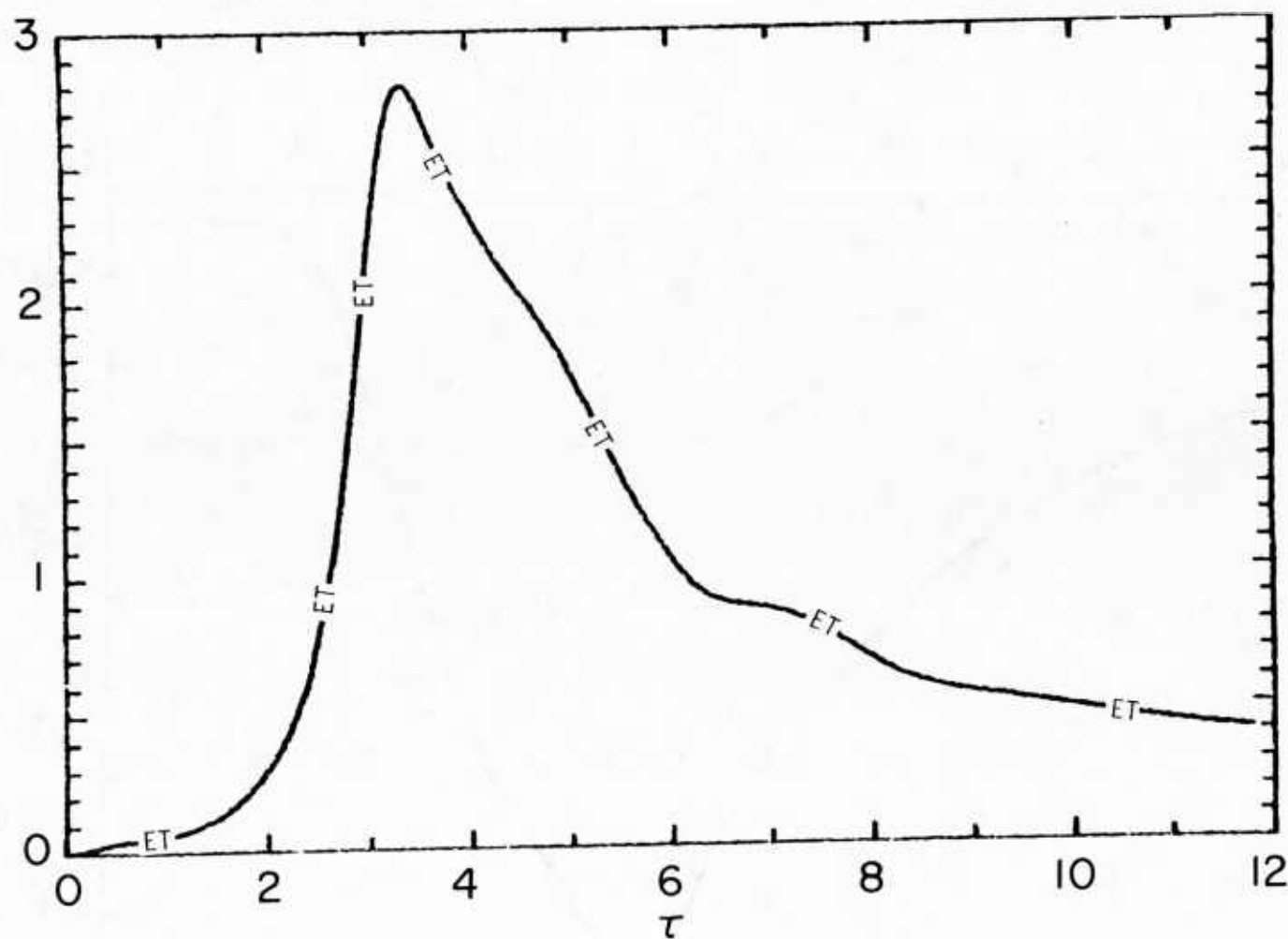
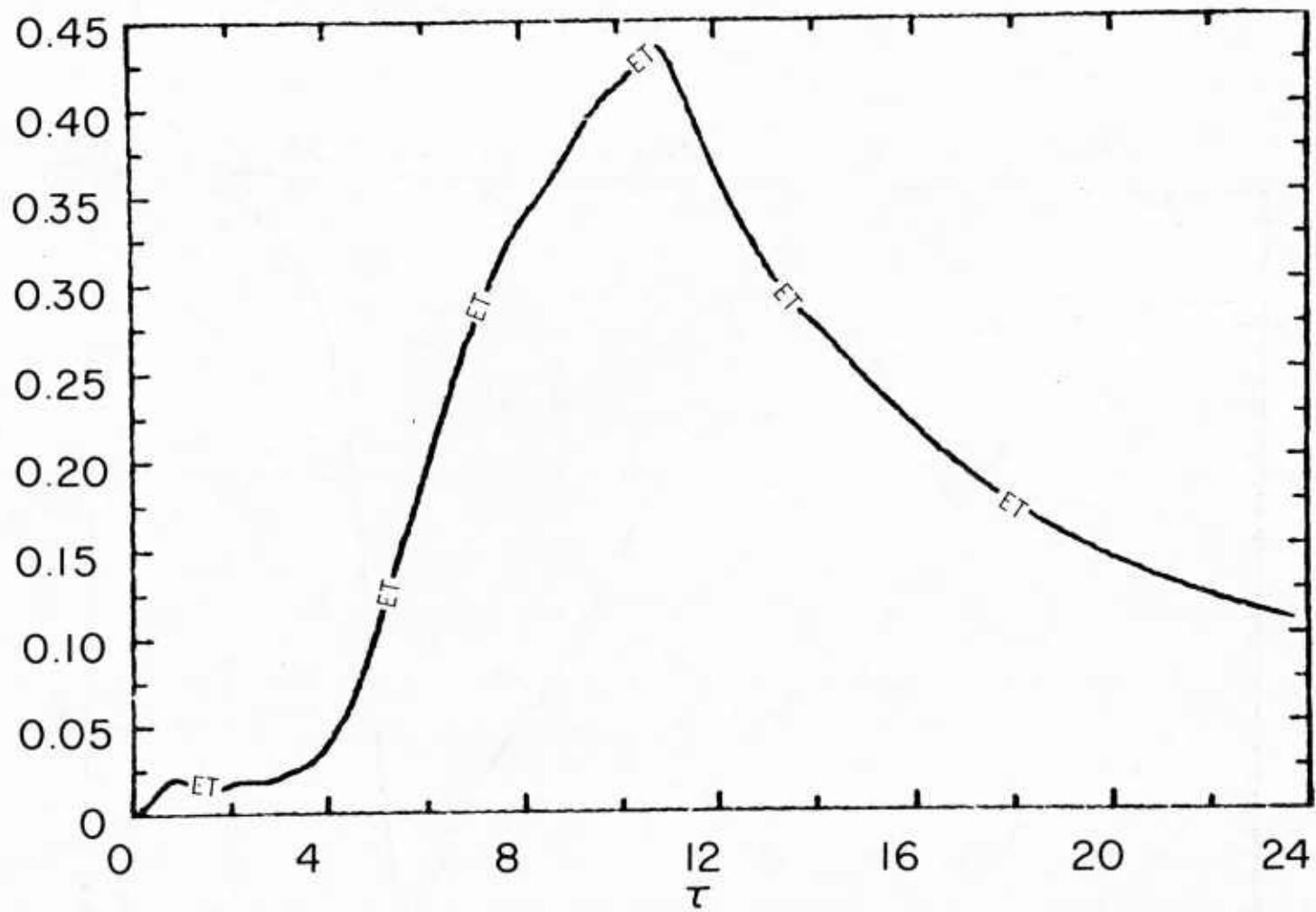


Figure 10(a) - Evolution of the total volume-integrated temperature variance,  $ET$ , for the case with  $Ri = 0.1$ .



Figure 10(b) -  $Ri = 0.2$ .

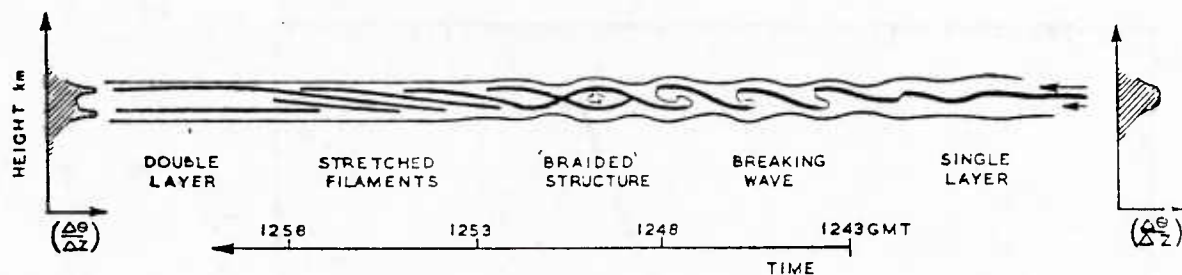


Figure 11 - Schematic representation of the life cycle of an individual Kelvin-Helmholtz billow based on the data in the earlier figures. Time progresses from right to left. Thick lines correspond to the detectable clear air radar echo, which started as a single layer at 1243 and finished as a double layer at 1258 GMT. Schematic vertical profiles of  $(\Delta\theta/\Delta z)$  are indicated before and after the occurrence of Kelvin-Helmholtz instability. (From Browning and Watkins, 1970.)

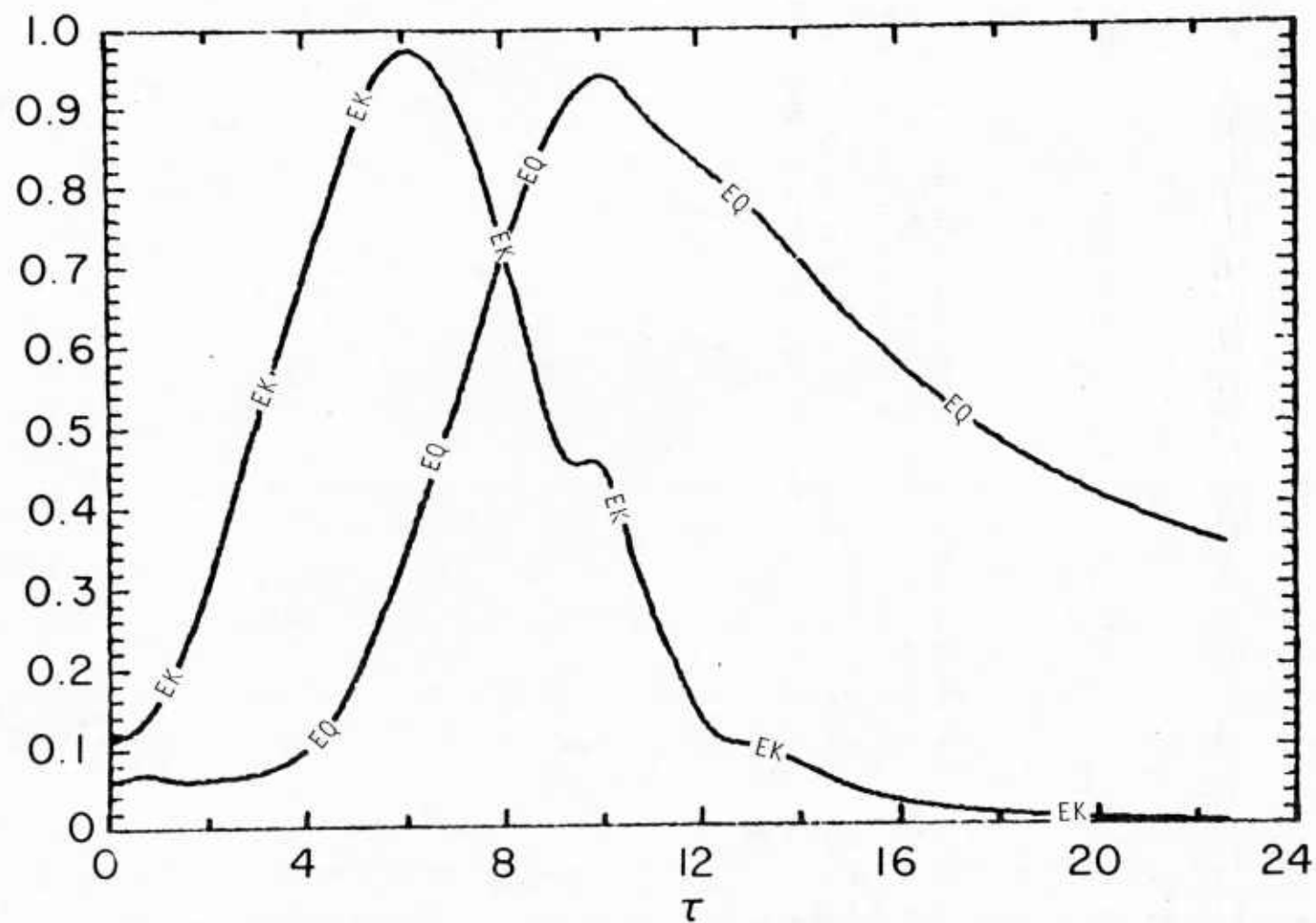


Figure 12 - Evolution of eddy kinetic energies for  $Ri = 0.2$  with (a) high resolution  $41 \times 61$ .

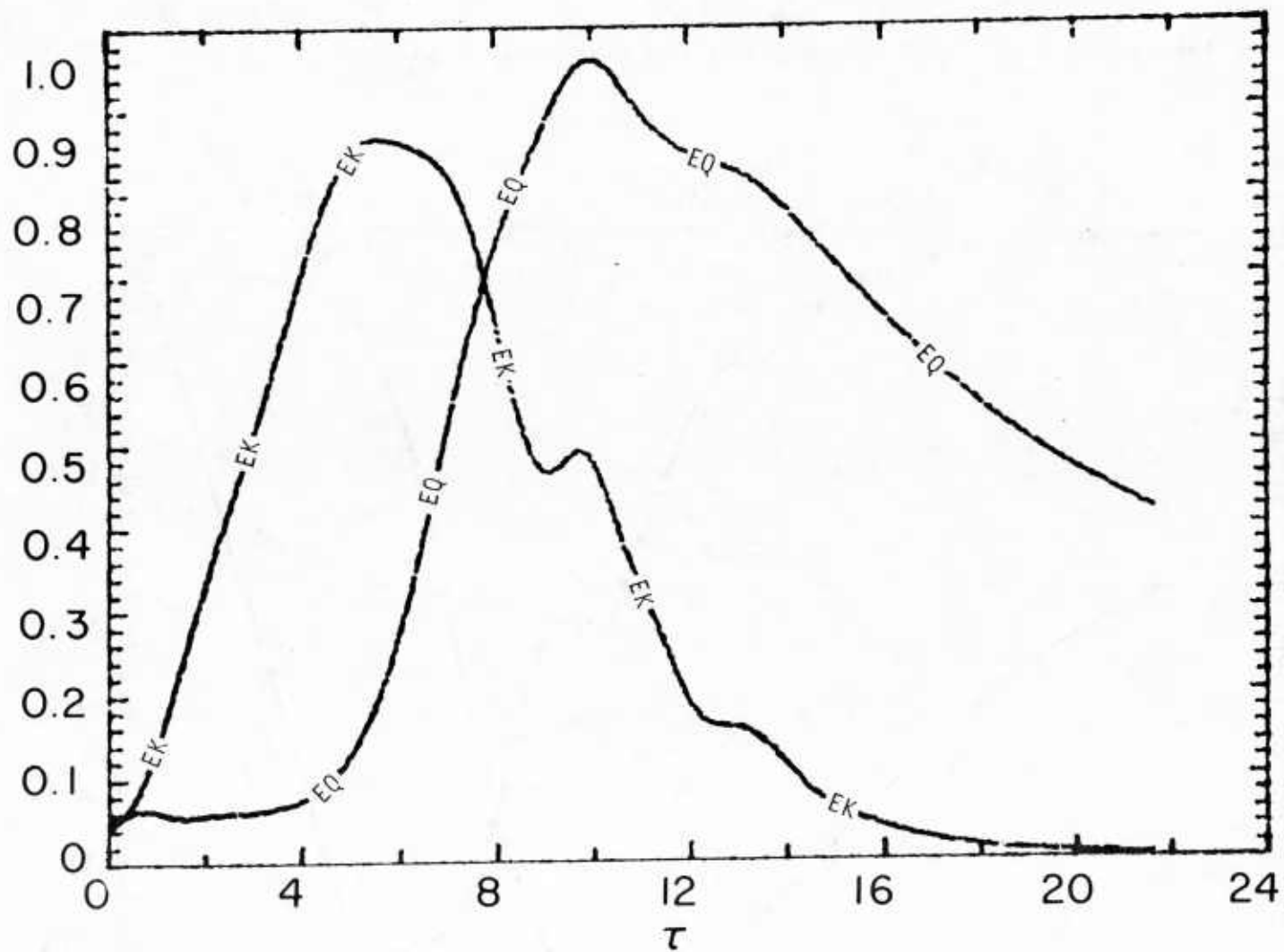


Figure 12 (b) - low resolution 32 x 40.

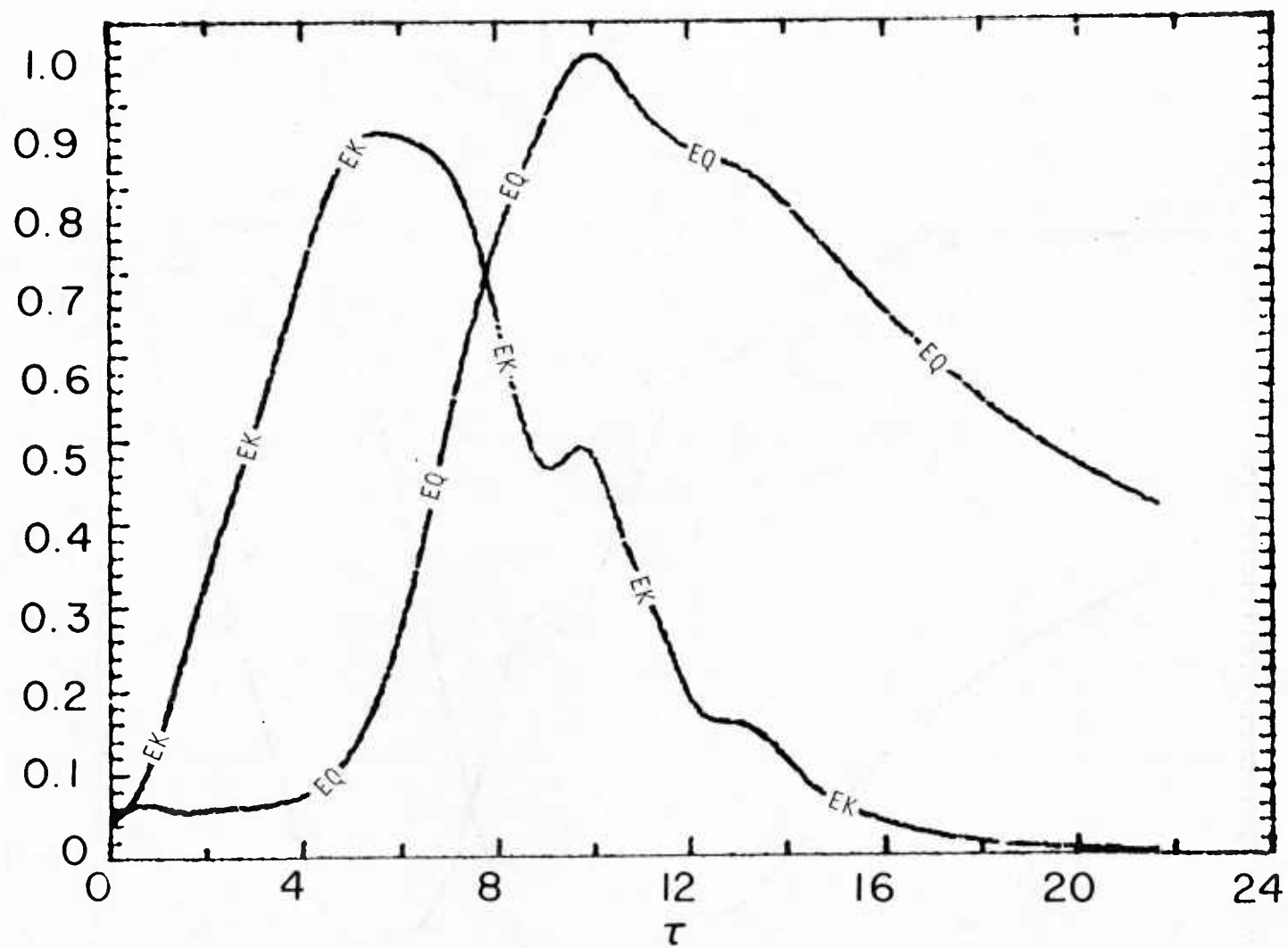
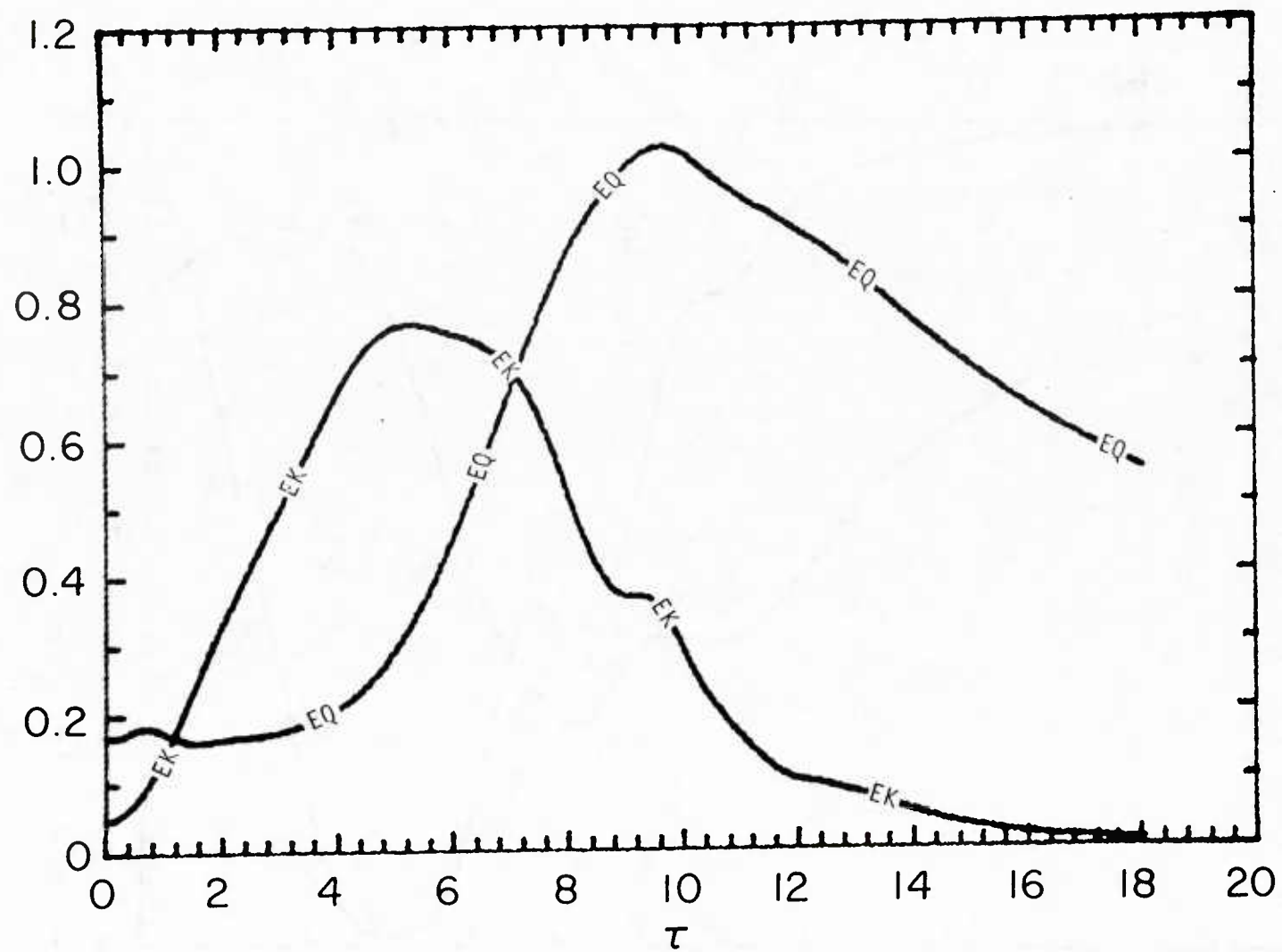


Figure 13 - Evolution of eddy kinetic energies for  $Ri = 0.2$  with different initial values of  $q^2/\Delta U^2$ , (a)  $10^{-3}$ .

Figure 13(b) -  $3 \times 10^{-3}$ .

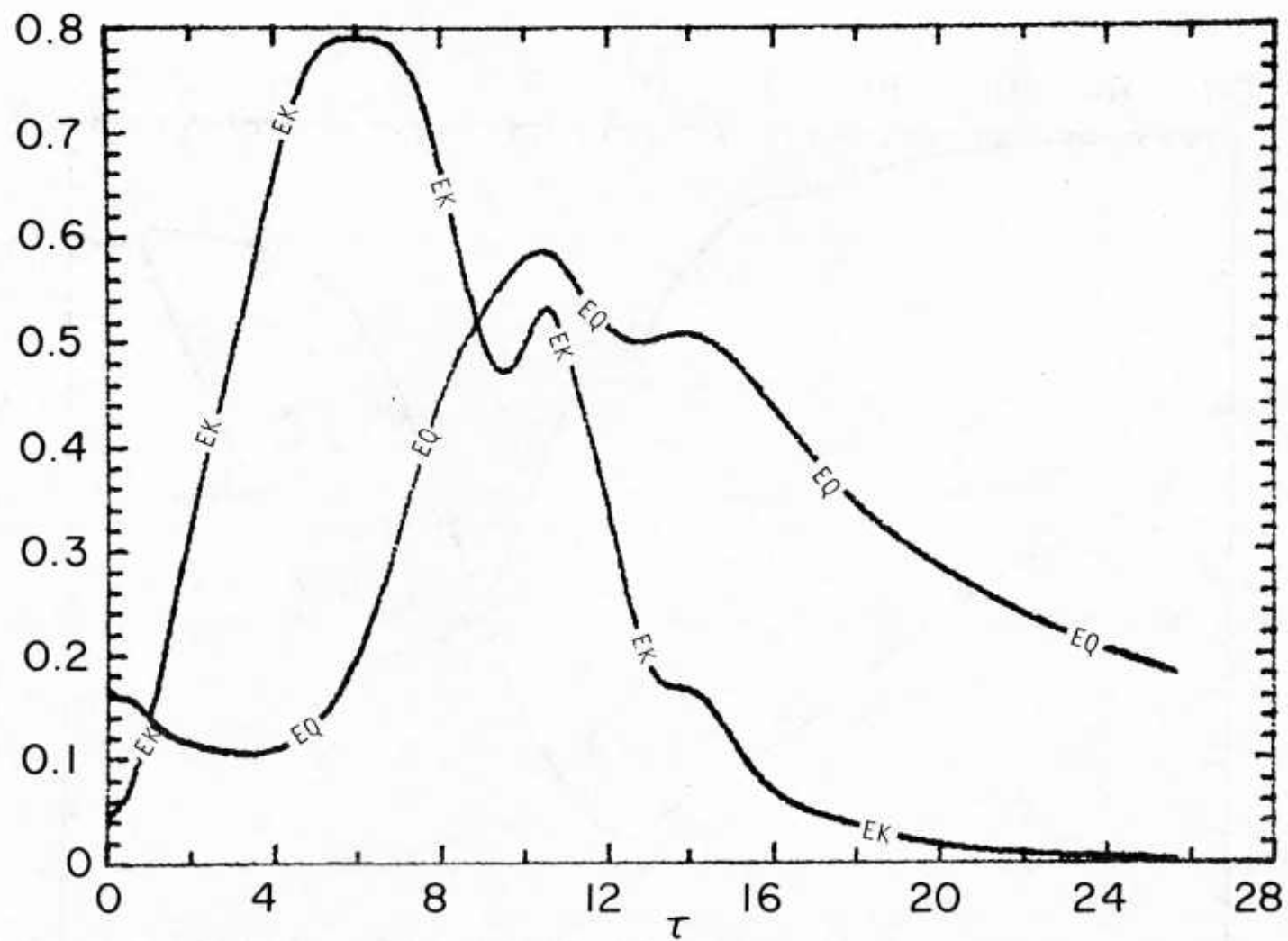


Figure 14 - Evolution of eddy kinetic energies for  $Ri = 0.2$  with different initial values of  $\Lambda/\delta$ , (a) 0.2.

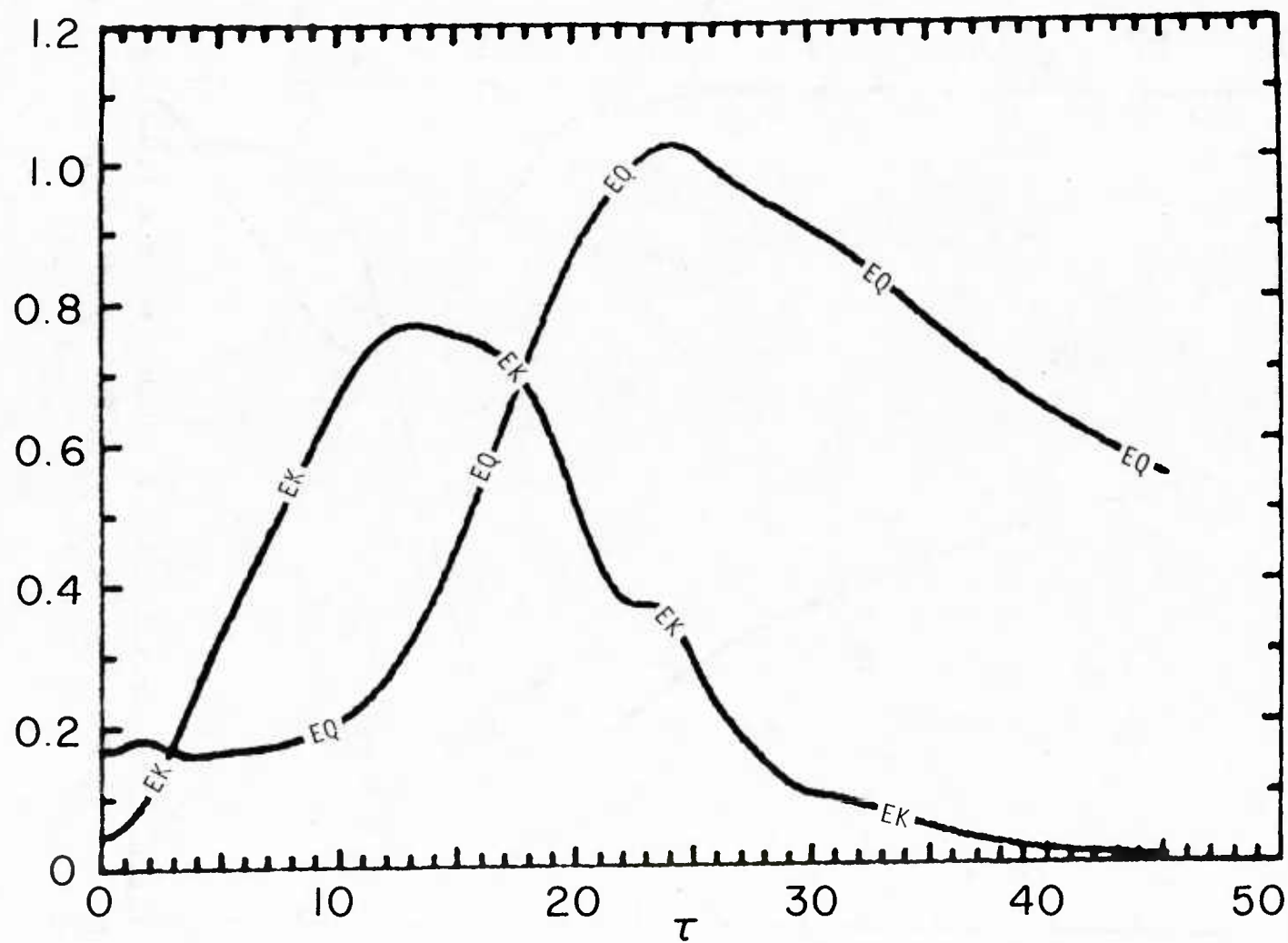


Figure 14(b) - 0.4



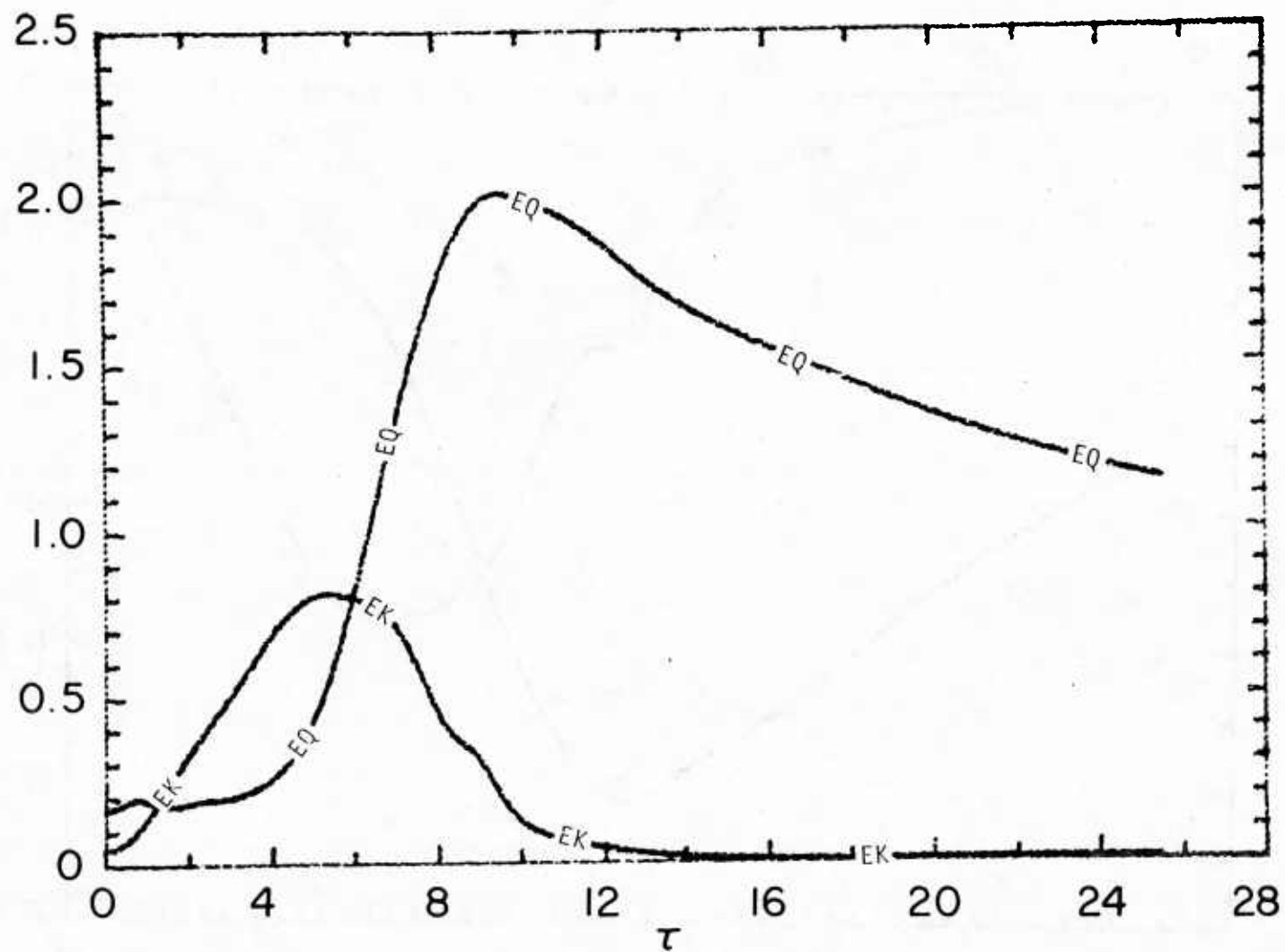
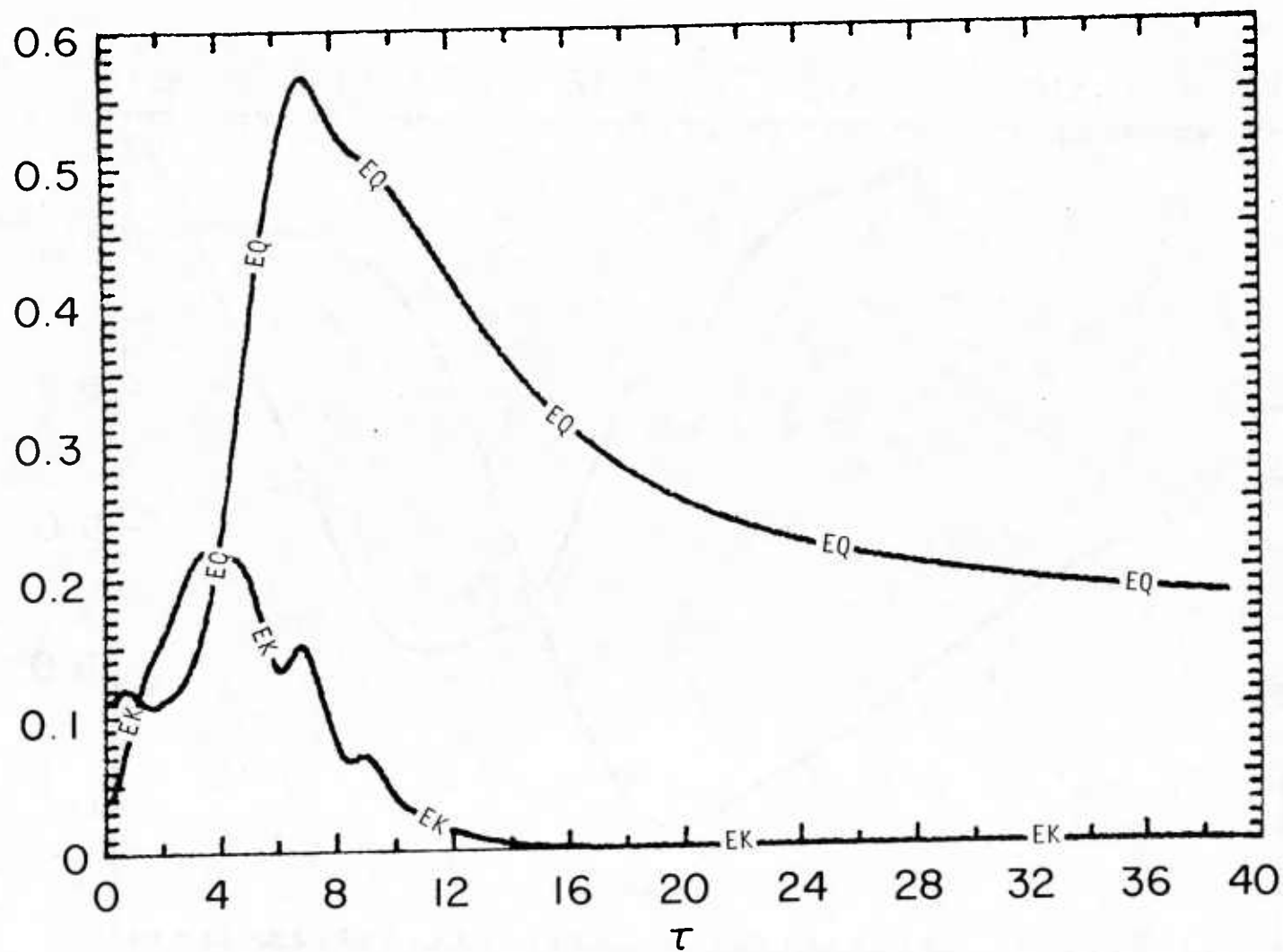


Figure 14(c) - 0.8.



Figures 15 - Evolution of eddy kinetic energies for  $Ri = 0.2$  with different domain lengths, (a)  $10\delta$ .

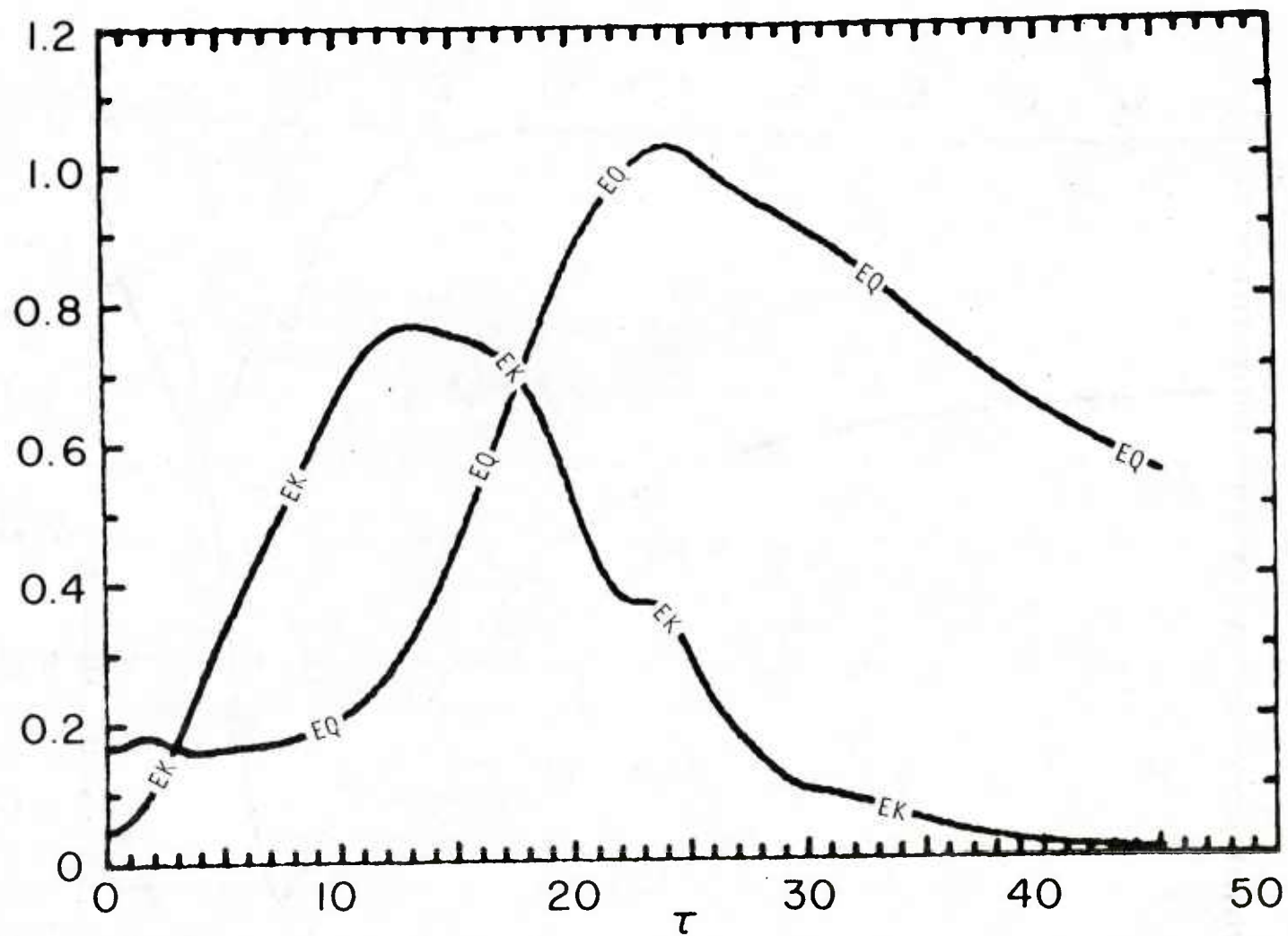


Figure 15(b) - 15s.

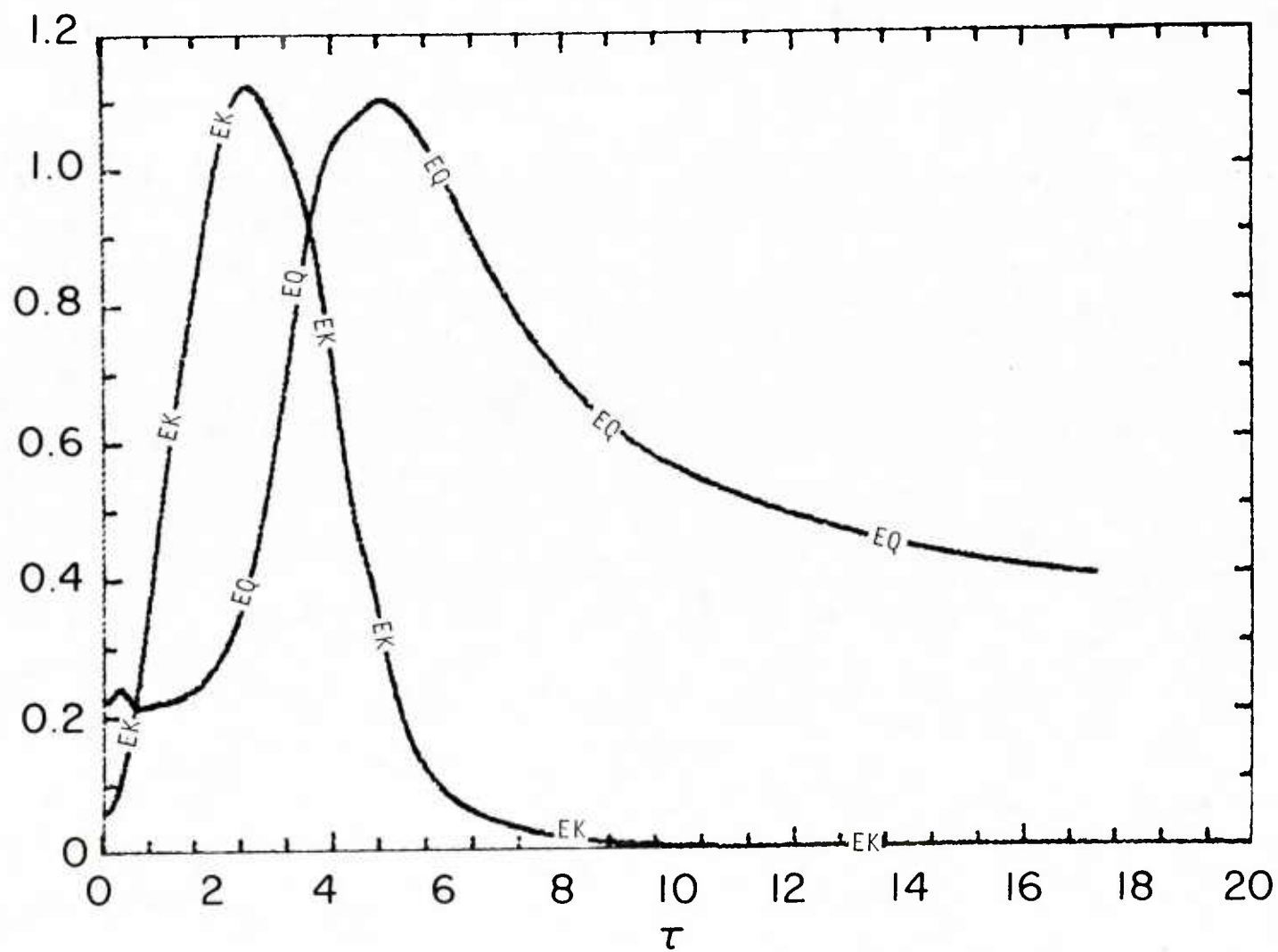


Figure 15(c) - 208.

U202082

